8. POLYMER COMPOSITES RESEARCH AND DEVELOPMENT

A. Automotive Composites Consortium Focal Project 4 (ACC007*)

Principal Investigators: Libby Berger
General Motors Corporation
Research & Development
MC 480-106-710
30500 Mound Road
Warren, MI 48090-9055
(586) 986-1177; fax: (586) 986-1207; e-mail:libby.berger@gm.com

John Jaranson
Ford Motor Company
Vehicle Design R&A
2101 Village Road MD 3137
Dearborn, MI 48121
(313) 390-5842; fax: (313) 337-5581; e-mail: jjaranso@ford.com

Field Project Manager, Composites: C. David Warren
Oak Ridge National Laboratory
P.O. Box 2009, Oak Ridge, TN 37831-8050
(865) 574-9693; fax: (865) 574-6098; e-mail: warrencd@ornl.gov

Technology Development Manager: Joseph Carpenter
(202) 586-1022; fax: (202) 586-6109; e-mail: joseph.carpenter@ee.doe.gov

Field Project Officer: Aaron D. Yocum
(304) 285-4852; fax: (304) 285-4403; e-mail: aaron.yocum@netl.doe.gov

---

Objectives

- Guide, focus, and showcase the technology research of the Automotive Composites Consortium (ACC) working groups.

- Design and fabricate structural automotive components with reduced mass and cost, and with equivalent or superior performance to existing components.

- Develop new composite materials and processes for the manufacture of these high volume components.

Approach

- Design, analyze, fabricate, and test a structural composite underbody, focusing on the following.

    — A 2 ½ minute cycle time (100k units per year [upa], 2 shift operation).

---

*Denotes Project 007 of the Automotive Composites Consortium, one of the formal consortia of the United States Council for Automotive Research set up by Chrysler, Ford, and General Motors to conduct joint, precompetitive research and development (see www.uscar.org).

— Methods of joining and assembly of the underbody to the vehicle.
— Processes for fabricating oriented reinforcement within the time window.
— Design, analyze, and fabricate a second row composite seat (with and without an integrated restraint system [SIR and STD, respectively]) which will combine the functions of a seat and a load floor.

Accomplishments

- Selected glass fabric sheet molding compound (SMC) with a high elongation core as our material and process system (M&P system) for the composite underbody.

- Developed design methodologies to achieve acceptable performance of the underbody in Full Frontal, Frontal Offset Deformable Barrier, Side, and Rear Offset Impact, and completed CAE stiffness, crash performance, and mass assessments.

- Conducted the initial testing of composite-to-steel weld-bond joints, using doubler strip (Applied for a U.S. Patent)

- Selected surrogate tool for the underbody for use in processing trials, fabric drape studies, and correlation of analytical and experimental dynamic testing. Designed appropriate test methodologies for correlations.

- Demonstrated vibro-thermography as a means of nondestructive evaluation of damaged weld-bonds.

- Achieved a seat design that meets worst-case load requirements for a vehicle seat, including front and rear impact and cargo retention with a cushion that is 30% lighter and a seat back that is up to 58% lighter than the comparator average.

- Cost modeling of the ACC seat design and a comparator thermoplastic P4 (programmable powdered preform process) (TPP4) design has been completed. While a weight save of greater than 50% can be achieved, the composite seat design is cost prohibitive due to the reliance on carbon fiber.

- A preliminary redesign of seat structure based on lessons learned in the Phase 1 work and the work done by Ecole Polytechnic Federal de Lausanne (EPFL) has been completed in carbon fiber reinforced nylon. Changes in the constraints placed on the design allow more efficient section properties.

- Constraint changes to the seat package include:

- 20% reduction in occupant body-to-metal clearance.

- Remove the kneeling feature of the seat.

- Allow trim panels.

Future Direction

- Selection of high elongation core material and demonstration of benefits to enable maximum weight savings of structural composite underbody.

- Further manufacturing demonstration of the selected M&P System, with fabric drape studies, cycle-time analysis, and determination of durability and high strain rate properties.

- Processing development and dynamic and durability characterization of composite-to-steel weld-bonded joints.

- Continued investigation of nondestructive evaluation (NDE) techniques for manufacturing quality and durability.

- Development of a manufacturing scenario for underbody and its assembly into vehicle.

- The seat redesign will continue with glass-fiber based composites to control costs while trying to achieve a goal of 50% weight reduction.

Introduction

This project encompasses two components, a composite underbody and a lightweight composite seat, with unique goals with respect to vehicle volume per annum, physical size, materials, and technology development. They both require structural performance with reduced mass and acceptable cost, and with equivalent or superior performance to existing components.

Structural Composite Underbody

The structural composite underbody is targeted to be part of the USAMP Multi-Material Vehicle (MMV) project, and will follow the MMV vehicle technical specifications. The primary research outcomes of this project are as follows.

- A 2 ½ minute cycle time (100k vehicles per year, 2 shift operation).
- Developing methods of joining and assembly of the underbody to the vehicle.
- Processes for fabricating oriented reinforcement within the time window.

Phase 1 of this project, completed in the first quarter of fiscal year 2008, was the selection of the materials and processes for the underbody, which involved the following.

- The development of a design concept, including a means of joining and assembly.
- The preliminary design of the concept using three material and process systems.
- The selection of an M&P System based on manufacturing considerations such as the following.
  — 2 ½ minute cycle time.
  — Technical feasibility of molding.
  — Joining and assembly feasibility.
- Technical cost model analysis.

Phase 2, which is now underway, is the full design of the underbody, based on a Large Rear Drive Vehicle (LRDV). This design includes the following.

- The whole underbody.
- Manufacturing plan for the component.

- Plan for joining and assembly to the vehicle structure.
- Validation of materials, processes, and analysis methodologies and assumptions.

Phase 3 will be fabrication and testing of the underbody.

In Phase 1, a preliminary composite underbody design was developed to replace the steel assembly from the donor vehicle. The preliminary design takes into account three proposed M&P System candidates, as well as the general vehicle packaging, and assembly and joining requirements. The vehicle level stiffness performance with the composite underbody is required to have equivalent performance to the donor, while crash performance is required to meet applicable government and industry requirements.

The concept design for Phase 1 must be suitable for predicting preliminary CAE-based structural performance and mass reduction, conducting technical cost modeling, and further Phase 2 detail design and development. The material and process system selected was a glass fabric sheet molding compound with a high elongation core (HEC). The glass fabric SMC has been demonstrated in several molding trials. However, the HEC is still under development. Our future processing, material evaluation, and design efforts will focus on this material system.

Our preliminary design and M&P system are based on the following set of assumptions.

- Analytical methodologies used to design the underbody for structural and crash performance are correct for this system.
- Material properties achieved with plaque testing will translate to properties in the complex underbody structure.
- Processing techniques can be developed to preform and mold the fabric SMC into the complex shapes needed.
- A high-elongation core material can be developed to maintain some continuity of the structure after crash.

- A production-feasible method of fabricating the composite-to-steel weld bonded joints will be developed, with necessary properties and durability.

Phase 2 addresses these assumptions as we move forward with the full design. Our primary means of doing this will be a structural surrogate with many of the challenges of the underbody. Chrysler has suggested a tub tool that can be used both in design and fabrication. Although this tub was designed for a Chrysler vehicle, it has not gone into production. The three-dimensional nature of this tool will allow testing of the material drape, preform and molding techniques, and property retention.

A composite-to-steel weld bonded joint has been designed and will be tested statically by the ACC, using super-lap-shear (SLS) specimens. Dynamic testing of the joint will be done at the Oak Ridge National Lab (ORNL) Test Machine for Automotive Crashworthiness (TMAC) facility; see 12.B. Physical testing methodologies for the surrogate structure, including the weld bonded joints, have been developed, to be compared with structural and crash analysis results.

One point of interest which has been raised about structural applications of composites is how to ensure quality, both after the initial manufacture and through day-to-day usage, or after low-energy crash events. This will require the development of NDE techniques that are low cost, robust, and easy to use. Examples of techniques which we will be evaluating for further development are thermal wave imaging (TWI), vibro-thermography, embedded microspheres or nanotubes encapsulating a fluorescent dye, embedded fiber optic mesh, and "coin tap" techniques.

Manufacturing a structural composite underbody and assembling it into a vehicle is a radical change in the vehicle assembly process. We are beginning to work on a scenario that will allow this assembly within a generic auto manufacturing facility.

Composite Design & CAD Model

Multimatic, the design and analysis supplier for Phases 1 and 2, examined the benchmark steel

vehicle underbody [see Figure 1(a)] to determine the basic construction, attachment requirements, parts count, material selection and gage.

Based on an evaluation of the steel design, and the results of Phase 1, the preliminary Phase 2 composite underbody CAD design model was developed to assess manufacturing and tooling requirements, and for further development [see Figure 1(b)]. The composite underbody design integrates 16 stamped steel components into a single molded floor with ribs, and utilizes both carry-over and modified mating components. The model represents the proposed joining concept and component integration. The overall dimensions of the underbody are approximately 1,640 × 1,470 × 445 mm with a variable material thickness ranging from 2.0 to 5.0 mm based on the selected M&P System and Phase 1 performance requirements.

(a) Baseline steel design
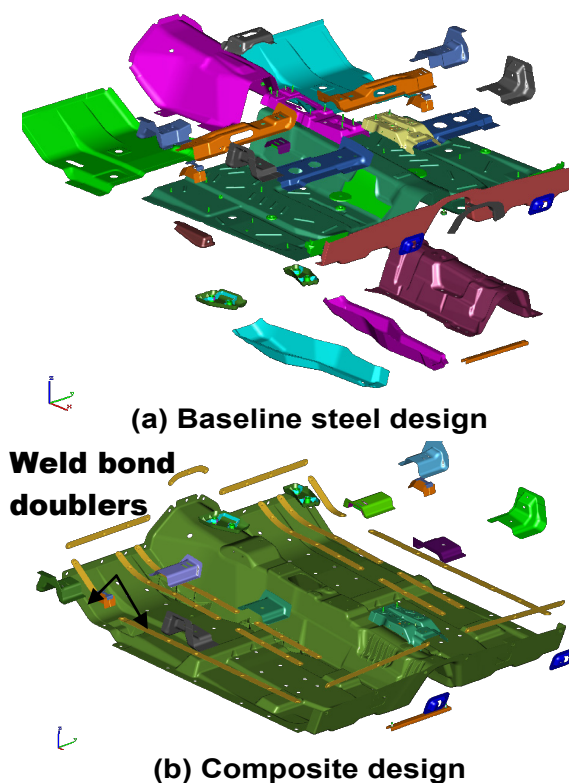
(b) Composite design

Figure 1. Baseline steel and composite design.

The expected mass savings using glass fabric SMC with a high elongation core is 14.9 kg, including 3.3 kg saved from the underbody rails, which is allowed by the increased structure of the floorpan. This translates to 33.2% mass savings.

An additional 1.6 kg could be saved by going to carbon fabric with an HEC. However, this would be at a cost of about $150/kg saved. This surprisingly high cost is due to the fact that this application is strength-driven, and must carry the crash loads. This is in contrast to most of the automotive studies of carbon-fiber composites to date, which focus on modulus-driven applications. For these, the higher modulus-to-strength ratio of carbon fiber composites is more beneficial.

Vehicle Assembly/Joining

Conceptually, the integration of structural composites into a primary metallic structure can be solved via adhesive utilization. This basic joining approach has been successfully implemented in many operations with slow builds, particular conditioning procedures and special care. In optimal, lightweight, multi-material designs, structural bonding provides enhanced seam integrity, gap bridging or tolerance functions and galvanic separation. However, for cyclic line rates and automotive body shop plant infrastructure, several process considerations and integrity qualifications present concerns and need solutions. In the high volume automotive environment, cycle time, body shop assembly process compatibility, and structural performance are all key requirements, and welding is a primary joining technique.

The combination of welding and bonding, weld bonding, is currently being implemented in some OEM body designs and assembly plants as a means of increasing stiffness, reducing mass, and improving durability. Weld bonding is currently envisioned as the primary joining process to meet the complex automotive requirements for the composite underbody. Specifically, the concept is to attach steel weld bond doublers (see Figure 1b) to the composite to enable spot welding to the surrounding steel structures as well as to attach the structural underbody rails to the composite floor (see Figure 2). The adhesive would be applied prior to spot welding. Not only would weld bonding provide compatibility with current body shop assembly and welding processes for installing the underbody itself, but the spot welds would also serve as peel stoppers in the adhesive joints, provide fixturing during adhesive cure, and

enhance overall joint durability and robustness. A typical weld bond joint at the rocker location is illustrated in Figure 3.
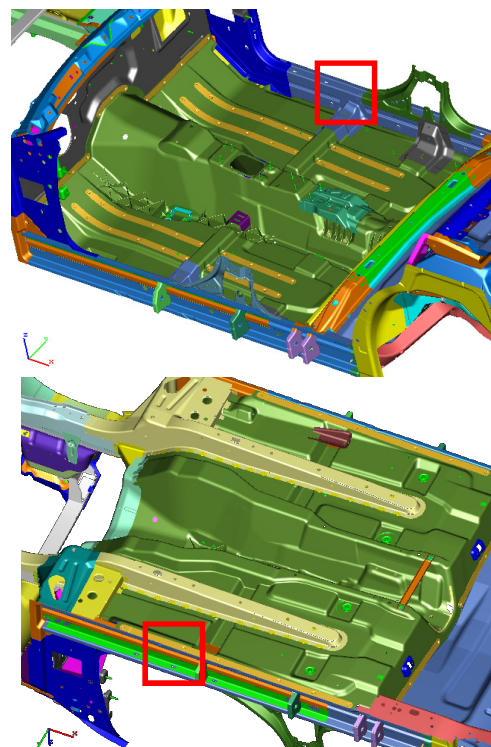
Figure 2. Composite underbody assembled into donor vehicle BIW.
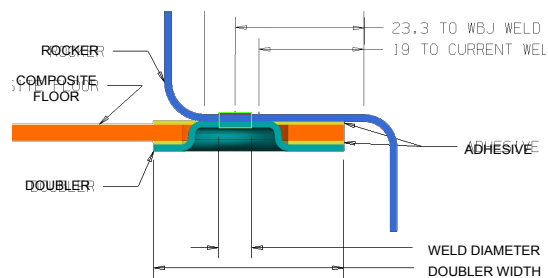
Figure 3. Typical weld bond joint section at rocker.

Phase 2 Performance Requirements

In Phase 1, the following key development load cases were considered.

- Body-in-White (BIW) static torsional and bending stiffness and modal response.
- NCAP 35 mph Full Frontal Impact.
- EuroNCAP/IIHS 40 mph Frontal Offset Deformable Barrier (ODB).

- FMVSS214 33.5 mph Side Impact.
- FMVSS301 50 mph Rear Offset Impact.

In Phase 2, additional performance requirements will need to be considered, including the following.

- FMVSS208 30 mph Frontal Impact at ±30°.
- IIHS 30 mph Side Impact.
- EuroNCAP 30 mph Side Impact.
- NCAP 38.5 mph Side Impact.
- FMVSS214 20 mph Dynamic Side Pole Impact.
- ECE R32 23 mph 100% Overlap Rear Impact.
- FMVSS207/210 Seat and seat belt anchorage strength.
- Vehicle shipping loads.
- Durability.
- Seat track modal response.

Material and Process System Development

As stated above, a glass fabric SMC with a high elongation core was selected as our material and process system. While molding trials in 2007 showed that this concept could work, further testing indicated that the originally selected HEC material would not withstand the processing temperatures needed for vehicle assembly. M&P System development in 2008 has focused on finding an acceptable core material. In a plaque molding trial, a variety of core materials were screened, including expanded mesh materials such as steel, poly ethylene terephthalate, and poly vinyl chloride, a polyester roofing fabric, a thermoplastic epoxy film, aluminum screening, and several types of cotton fabric. A number of these showed the desired failure mode of continued low level structural connectivity at high strain after failure. Several of these will be further evaluated in upcoming molding trials.

Experimental-Analytical Correlation Studies

As part of the development of the Phase 2 design input data, several experimental-analytical correlation studies are planned to develop the analytical material properties and models required for the detailed features of the Phase 2 underbody CAD design. These studies will be used to develop and validate analytical modeling techniques for materials, weld bonded joints, and structural components by correlating physical testing of coupons and surrogate components in environmental, static and dynamic loading conditions.

Surrogate Component

The surrogate tool mentioned above is illustrated in Figure 4, and has a nominal size of approximately 1365 × 785 × 285 mm with a nominal 3.5mm wall thickness and a 2.0 mm perimeter bond flange thickness. This is approximately 45% of the plan view size of the composite underbody with a similar part depth. The tool is a compression tool with shear edges designed for molding glass mat thermoplastics, which should be suitable for molding our glass fabric SMC material. The surrogate tool will be used for material and process development and to mold components for physical and analytical component level performance assessment trials.

Figure 4. Surrogate component.

Evaluation of Surrogate Tub Performance

As a first step toward assessing the impact performance of the surrogate tub, two component test configurations were developed to estimate the needed impact test mass and speed requirements to achieve "reasonable" tub deformations and loads. For this purpose, portions of the full tub were selected to represent impacted sections of the full vehicle (see Figure 5). The required initial mass and impact speeds were iteratively determined by means of a dynamic finite-element (FE) analysis

Frontal Impact Model

Side Pole Impact Model
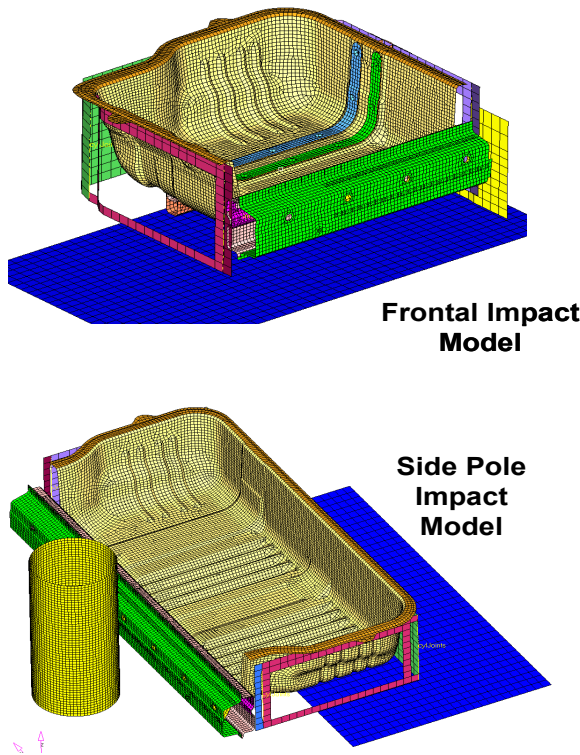
Figure 5. Surrogate component impact models.

to induce similar deformation modes (within the confines of the donor tub design) as observed in the full vehicle models.

Further analytical test development is planned once a suitable physical test facility is identified and test capabilities are established. Physical impact testing and performance validation is planned pending the availability of molded tubs. A similar approach is under development for the fatigue testing of the surrogate tub.

Material Drape Studies

One of the major issues for processing the underbody is the drape of the fabric SMC. The fabric will not deform as easily as a conventional SMC, but large deformations are possible via the shearing of the fabrics. The simulation of the complex fabric-SMC deformation behavior is possible and the drapability of the tub and the underbody has been studied. We have worked with the University of Massachusetts at Lowell to determine the drape characteristics of multiple layers of the fabric SMC, and to use this in computer models to determine appropriate layup,

blank size and shape, and preform configurations for the underbody. The models are applied to a simple shape, a double-dome with a connecting tunnel, as well as the surrogate tool and the full underbody design. The double-dome shape will be molded, and the fabric orientation will be analyzed to validate the modeling. This study includes the characterization of the SMC material (i.e., the frictional, tensile, and in-plane shearing behavior).

Material characterization

Shear Frame Test

Shear frame testing was performed to measure the force generated during shearing of the SMC fabric. Compounded fabric samples of specific geometry are tightly clamped in a custom-built frame and sheared. Figure 6 displays the loading, initial and final positions of the shear frame test as well as an example of resulting data.
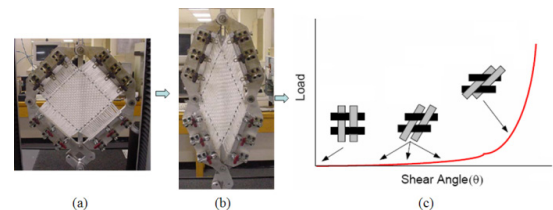
Figure 6. (a) Loading and initial position of shear frame testing. (b) Final position of sheared fabric. (c) Load vs shear angle plot and corresponding yarn positions.

Tensile testing

Conventional tensile tests on the dry yarns were performed to determine their stiffness and failure stress (Figure 7). Then, knowing the crimp ratio (the difference between the length of the fabric and the length of the yarn) and the yarn stiffness, the tensile behavior of the fabric can be assessed.
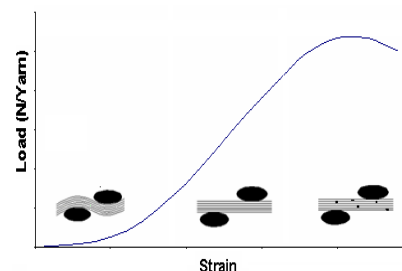

Figure 7. Typical tensile behavior of a woven fabric showing the decrimping phenomena.

Friction testing

A load-control friction test apparatus was used to capture the static and dynamic coefficients of friction at the tool/fabric and fabric/fabric interface. For the fabric/fabric friction characterization, the inner-fabric layer to be pulled out is placed between two additional layers of fabric clamped together on one end. The coefficient of friction was plotted against the pull-out displacement. Typically, these curves result in an initial peak, followed by a somewhat steady-state situation. The peak and the steady-state portions of the curves correspond to the static and dynamic friction coefficients, respectively. While the two outer layers of an SMC part will contact the heated tool, a thermal gradient will exist within the inner layers of a multilayered part. Therefore, tool temperatures of 25, 35, 45, and 90°C were selected to simulate different fabric temperatures in a multilayered part.

Figure 8 shows typical friction vs. displacement curves of the SMC material at the fabric/fabric
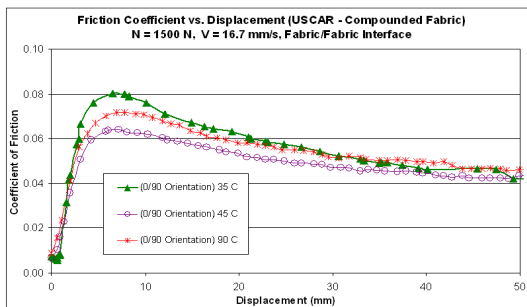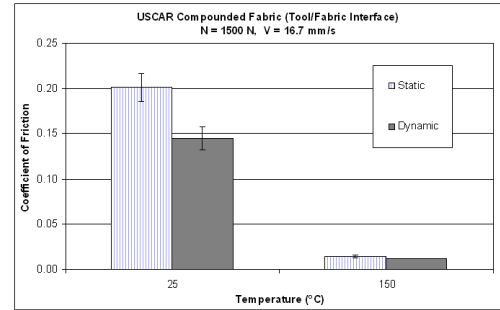

Figure 8. Coefficient of friction as a function of pull-out length.

interface, and Figure 9 compares the resulting static and dynamic friction coefficients of the SMC material at the tool/fabric interface. At high tool temperatures, as well as at the fabric/fabric interface, the lubricant resin film dominated the friction behavior and therefore, the coefficient of friction is essentially negligible for analytical modeling purposes.
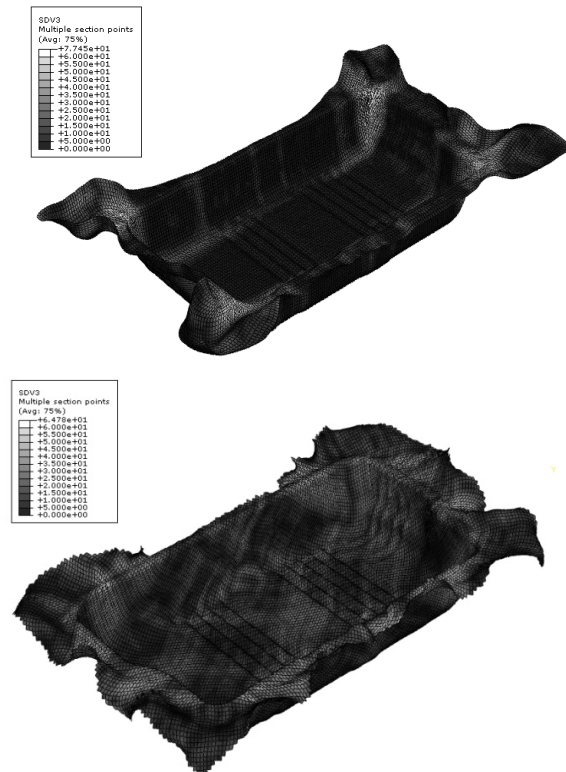
Draping Simulation

A mesoscopic/discrete approach using beams to model the yarns has been used, and shell elements are associated to the beams in order to model the


Figure 9. Coefficient of friction (tool/fabric) at low and high tool temperatures. The error bars indicate one standard deviation.

in-plane shear behavior. The drapability of both the tub and the floorpan has been studied for different fabric orientations (Figures 10 and 11). Tensile and shear properties for the beam and shell elements are provided from the materials characterization effort, as well as the friction layers and between the tool and the surface fabric layer.

Figure 10. Forming simulation of the Tub for a 90°/0° ply orientation (top) and a +45°/-45° (bottom). Shear angle contour (lighter areas show higher angles, with white above 60°).
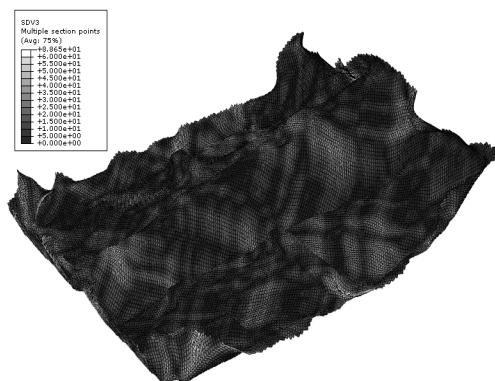
Figure 11. Forming simulation of the floorpan for a 45°/-45° ply orientation. Shear angle contour (lighter areas show higher angles, with white above 60°).

Based on these simulations, the initial orientation of a quasi-isotropic stack of plies within the mold were determined to achieve the best drapability. Valuable information was extracted from these simulations to further improve the drapability of the parts. For example it has been noted that ridges with sharp right angles lead to significant stress in the yarns that could lead to yarn failure (e.g., the flange or the bottom ridge of the tub part). A more filleted or curved edge would probably reduce this issue. In addition, the points of initial tooling contact can affect formability. For example, the corrugations at the bottom of the tub can lead to high tensions and fiber bridging across the channels if contact is first made across the peaks and the fabric must subsequently be forced into the channels. The simulation suggests that a preform that allows for more fabric in this region would improve formability.

Weld Bond Studies

A key element of the underbody design is the composite to steel weld bond joining concept as shown in Figure 3 (see joint location in Figure 2). To gain confidence in the vehicle level joint performance, quasi-static, impact, and fatigue loading conditions will be accessed via analysis and physical testing. Test-analysis correlation will be used to establish the best modeling practices and material models to be used for the prediction of weld bond joint performance.

Since it will be necessary for the underbody joints to carry dynamic loads, the adhesive used in the weld bonding must also be able to survive this loading. Two highly toughened adhesives, currently in use by the automotive industry for steel body-in-white weld bond applications, were trialed by the adhesive suppliers. In these trials, the adhesive suppliers were provided laser cut coupons of 50% random chopped glass SMC with the planned resin. They used these coupons for standard composite-to-composite lap shear testing using their adhesives. Both investigations reported positive results in that the failures noted occurred in the composite substrate and not the adhesive joint interface.

Super-Lap-Shear Coupon

The primary geometry for evaluating the joint performance is the SLS coupon. The SLS coupon was designed to evaluate quasi-static tensile joint performance, but it is also being considered as a candidate for evaluating dynamic tensile performance, as well as bending and torsional durability performance. Several SLS coupons have been fabricated to date for initial performance assessments and test method development. An early SLS coupon is shown in Figure 12.
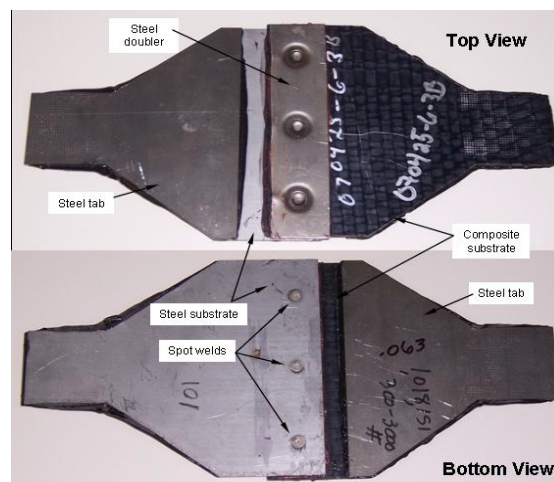

Figure 12. Super-lap-shear coupon.

Quasi-Static Performance

Several analytical studies were carried out to gain insight into quasi-static SLS tensile performance and to further develop the initial coupon design. The initial efforts were focused on:

- Mesh sensitivity
- Adhesive and weld modeling techniques
- Steel gage / grade effects
- Composite material effects (random and fabric SMC)
- Joint strength for tension, shear, bending, and torsion load cases

Preliminary quasi static tension, bending, and torsion testing have been carried out by ORNL and GM R&D for some early SLS coupons. Figure 13 shows the sample data for coupons made with a 7 ply 0/90 fabric and two gages of steel, 0.7mm GMW2 and 1.6mm DP590.
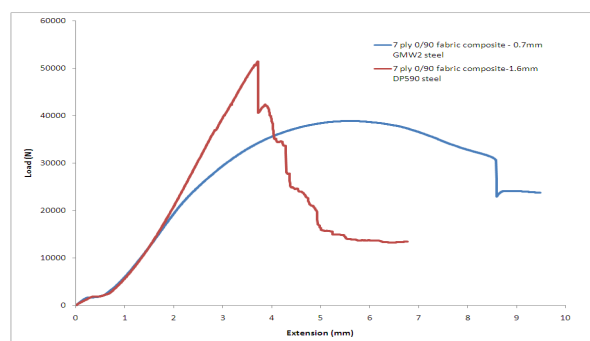
Figure 13. Load-extension curve of weld bonded composite to steel super-lap coupons in quasi-static tensile test.

The specimen with 0.7mm steel showed significant yielding of the steel before the joint failure. The specimens with 1.6mm steel, however, appeared to fail in the joint with composite shearing and tearing of weld nuggets accompanied by delamination. The sequence of the failure was unknown. A high-speed video camera will be used in the future to capture the failure sequence.

NDE found no clear evidence of cracks in the SMC, but did indicate the loss of continuity through the stacks and interply disintegration with debonds. Debonding at the steel-adhesive interface in the specimen with 0.7mm steel was found. Based on the overall results from preliminary tests, new test methods will be established for final quasi-static and dynamic evaluation.

Key variables in the matrix include grade and gage of the steel substrate, number of welds, type of adhesive, and test temperature. The data obtained from these tests will be used in structural test-analysis correlation and to develop the model for the tub tool.

Dynamic Performance

Dynamic tensile testing is planned at the TMAC facility at ORNL. The tensile tests will be carried out at higher strain rates derived from predicted rates observed in vehicle side impact. The initial test efforts will be focused on:

- Coupon, fixture and test methodology development
- Steel gage / grade effects
- Composite material effects (random and fabric SMC)
- Rate effects

To understand the general durability loading conditions in the proposed composite underbody, an early vehicle level finite element model was utilized to gain insight into the joint level loading modes. The vehicle model was subjected to simulated pothole loads and the resulting peel and shear forces were studied in the joint areas. From the analysis results, it was observed that localized mixed mode shear and peel stresses were induced in many joint areas of the underbody, but especially at the end of the weld bond joints and in the vicinity of the local geometric features.

Based on these observations, various loading conditions for the SLS coupons were investigated in an effort to generate a range of peel and shear stresses in the adhesive joint. The results of this coupon level study indicated that a range of peak shear and peel could indeed be achieved, depending on the gage of the steel substrate, and the loading condition. Preliminary tension-tension fatigue testing and quasi-static bending and torsion testing has recently been completed. The test results are being evaluated along with the analysis results and various practical considerations in an effort to select the most appropriate test methodologies and coupon configuration for further fatigue testing.

Nondestructive Evaluation

Several NDE techniques are being investigated to determine which would best fit the needs of

insuring the integrity of the composite underbody and it's joining to the rest of the vehicle structure.

Nondestructive techniques can be used to evaluate

- durability of preproduction designs,
- manufacturing operation quality, and
- possible repairs needed after a crash event.

Some of the desired attributes of NDE methods are as follows:

- robustness,
- low cost,
- ease of use,
- noncontact,
- no damage to part,
- full field,
- no or limited consumables,
- can be automated, and
- currently in use, with little technical development needed.

The level of importance for each of these criteria will be determined by where in the life of the underbody it is to be used. For example, an NDE technique for manufacturing quality assurance must be automated and high speed, but could require more capital expense than a technique that would be used to evaluate the need for repair in an independent body shop, where low cost and ease of use will predominate.

Several NDE tests were performed to analyze the failures in SLS joints, including TWI, vibro-thermography, X-ray radiography, ultrasonic scan, both through transmission (UT-TT) and pulse/echo (UT-PE). The super-lap coupons were difficult to inspect due to their geometry. The tests found no clear evidence of cracks in the SMC. UT-TT indicated the loss of continuity through the stacks and interply disintegration with debonds. UT-PE tests indicated debonding at the steel-adhesive interface in the specimen with 0.7 mm steel.

TWI was used to image the adhesive pattern as shown in Figure 14. The adhesive attached a doubling metal plate on the left side of the image. No contact to the part under test is required,
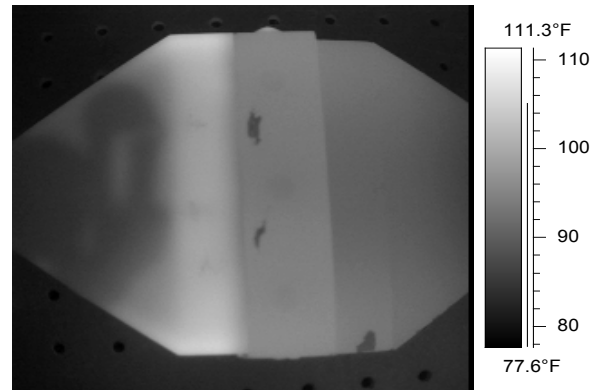
Figure 14. An example of infrared thermal wave imaging. The gray scale image shows the subsurface adhesive bead (left side of image) after construction of the composite weld bond. The construction consisted of an adhesive bead sandwiched between an SMC section and a sheet metal layer.

although line of sight to the area under test needs to be maintained.

Vibro-thermography was used to detect damage caused by striking a weld bond sample with a ball peen hammer... The three defects are easily detected, as indicated by the arrows in Figure 15.
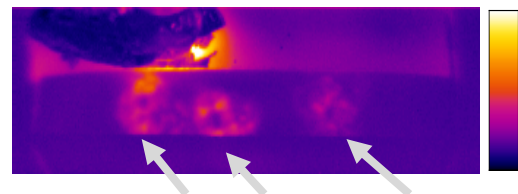
Figure 15. Arrows are pointing at each of 3 impact blows from a ball peen hammer on to the SMC layer of a composite weld bond sample.

TWI was also used to detect subsurface blistering on sheet molding compound (SMC) panels shown in Figure 16. The heat pulse in this TWI example was applied to the back side of the panel. The blisters prevented heat from reaching the front surface of the panel, thereby looking colder (darker gray scale) than the surrounding SMC material.

Other techniques which are under investigation include embedding a dye in the composite which would be visible upon fracture, coin tap methods, and enhanced visual inspection. Work is also underway to determine the degree of damage and size of damage areas that must be detected, for

Figure 16. Infrared thermal wave image showing three blisters present in an SMC test panel.

both the weld bond joints and the composite structure itself.

The end result may be that no one NDE technique has all of the desired attributes. A combination of several techniques may be required, including different techniques for preproduction validation, manufacturing monitoring, and post crash evaluation.

Underbody Summary

In Phase 1, glass fabric SMC, with a high elongation core was selected as our material and process system. A preliminary one-piece molded composite underbody design concept was selected, and its structural performance was analytically assessed assuming surrogate material properties and several stiffness and crash development load cases. In Phase 2, additional load cases have been considered along with M&P-specific material properties, leading to an overall mass savings of 14.9 kg, or 33%, including mass saved in the sled rails. To achieve the required level of confidence in the analytical performance and mass assessments, further considerations will be made for material rate dependency and environmental effects.

Further development of the fabric SMC is necessary, particularly for the manufacture of large parts, and for joining of these parts to the steel vehicle structure. Plaque molding trials have provided several materials showing the proper failure behavior for the HEC, which will be further investigated. Fabric drape analysis has shown

areas for which the design needs to be slightly modified.

A surrogate tool has been identified, to allow processing studies of a large structure and validation of design and analysis methodologies in a molded and weld bonded part. Dynamic evaluation of weld bond samples is underway, in cooperation with the ORNL TMAC facility. Investigations into NDE techniques to determine manufacturing quality and durability have shown promise and are being further developed.

Lightweight, Low-Cost Composite Seat

The primary objective of this part of FP4 is to develop materials, processes, and designs to yield a light-weight, low-cost composite seat structure.

Second row outboard stand-alone seats with volumes up to 340k upa are the target applications. Results from the comparator seat teardowns and testing have been used to develop average weights for a conventional steel seat frame that is used for comparison with the composite seats. The project will predominately investigate glass fiber reinforced composites, due to cost considerations, but will consider local reinforcement with carbon fiber and other materials, including metal, in order to achieve a 30% weight savings versus the components being replaced. Both thermoset and thermoplastic matrix material will be included. A design achieving a 50% weight savings utilizing carbon fiber reinforced composites is also being developed, although this may be cost prohibitive.
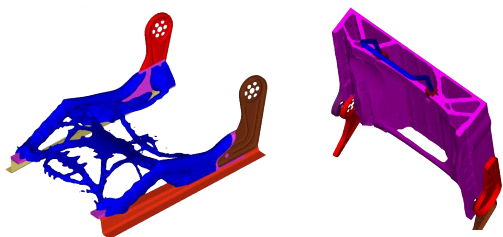
CAE Analysis

The original ACC seat design, shown in Figure 17, met the 120% loading requirements, required for the seatback to be used as a load floor, with only some minor local issues that are being addressed.

Recent activity has involved the redesign of the composite seat which began with topology optimization by Altair Engineering. Based on this redesign, only the back frame, cushion frame, and the pivoting recline/folding joint are included in the current project scope. The results of the topology optimization can be seen in Figure 18.
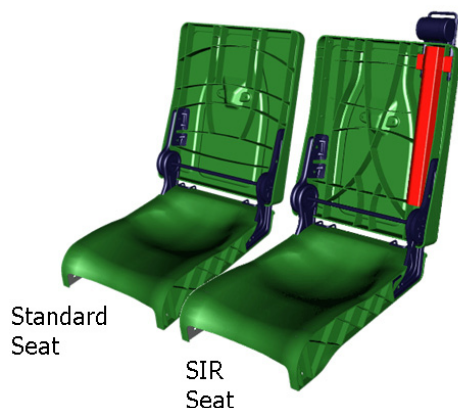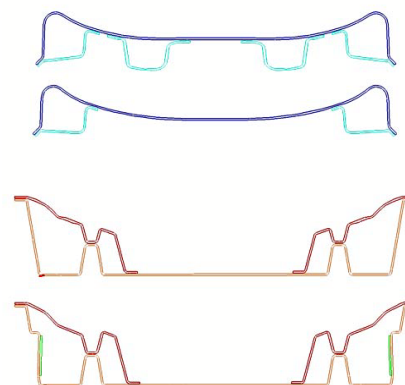
Figure 17. ACC seat designs—original.

Figure 19. Redesigned seat sections

Figure 18. Seatback topology results—redesign.

Figure 20. Adhesive paths and reinforcements.

The redesign resulted in inner and outer bonded shell designs for the seat back and seat cushion. This type of design allows much more geometric section modulus to be designed into the seat. Typical sections through the cushion and back are shown in Figure 19.
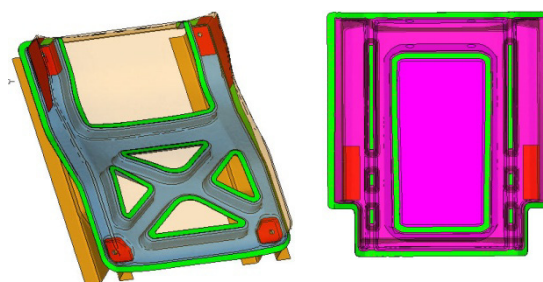
The design utilizes adhesive bonding to join the inner and outer shells. The adhesive paths are shown in Figure 20. The specific adhesive will not be selected until the final composite material choice has been made. The current redesign of the seat is shown in Figure 21.
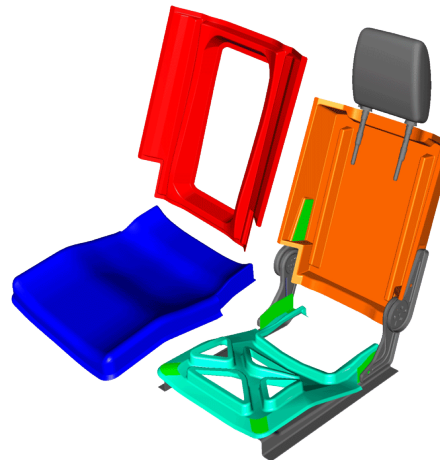
Weight Status

The original design of the ACC seat achieved a 30% weight reduction for the cushion pan. The seat back achieved an 18% weight saving, although some opportunity for further weight savings may exist with thickness optimization. However, EPFL used a different design approach for the seatback with carbon fiber, and achieved a weight saving of 58%.

Figure 21. Redesigned composite seat.

The redesigned ACC seat shows significant opportunity to save weight with a random chopped carbon fiber/nylon composite. The seat back is currently at a 41% weight save and the cushion is at 56% weight save. Further weight savings may be possible with localized directional reinforcements.

A glass based design is being developed to reduce the cost of a composite seat. Finite element analysis is ongoing to develop the design and thickness of the glass-based seat to meet the structural requirements of the application. The weight of the glass-based design will be calculated when it meets these requirements.

The details of the weight status can also be seen in Table 1.

Table 1. Composite seat weight status

	Cushion	Back	
	Weight (kg)	Weight (kg)	Cost [1] ($)
ACC Carbon Design	2.70	2.92	$73.76
% of Steel Comparator	-30%	-18%	738%
ACC Re-Design Carbon	1.71	2.11	TBD
% of Steel Comparator	-56%	-41%	
ACC Re-Design Glass	TBD	TBD	TBD
% of Steel Comparator			
EPFL Carbon Design	na	1.50	$41.51
% of Steel Comparator		-58%	415%
EPFL Glass Design	na	2.42	$15.74
% of Steel Comparator		-32%	157%
Steel Comparator	3.88	3.56	$10.00

[1] at 260k upa

Material Assumptions

The composite seat will be comprised of nylon 6 reinforced with chopped carbon fiber for the bulk of the molded composite part. The composite parts will be compression molded using DLFT compounded material. The inserts will be preformed from blanked, pre-laminated sheet stock and heated prior to being placed in the main molding tool. Robotic transfer will be necessary to meet the cycle times for the insert transfer.

Cost Modeling

Work has been completed with EPFL on developing a cost model for the composite seat. EPFL has designed a version of the seat back that utilizes the TPP4 process and materials. EPFL has also substituted the carbon/nylon material from the ACC seat design and reduced the material thickness to account for the improved mechanical properties. All three versions of the composite seat back have been used to understand the costs of a composite seat structure. Both of the carbon-based

seat backs are significantly more expensive than the steel comparator, as can be seen in Table 1. The ACC Seat back is over seven times the cost of the steel seat back. The carbon EPFL design is over four times as expensive. This cost discrepancy can be largely attributed to the material cost of the carbon fiber. The TPP4 design is the only seat that is close to the steel seat back at approximately 1.5 times the cost. This is largely attributed to the use of glass fiber reinforcement and low cost polypropylene.

EPFL's seat design can be seen in Figure 22. Additional trim parts and reinforcements may be necessary for the TPP4 seat and would need to be accounted for in a complete seat cost.
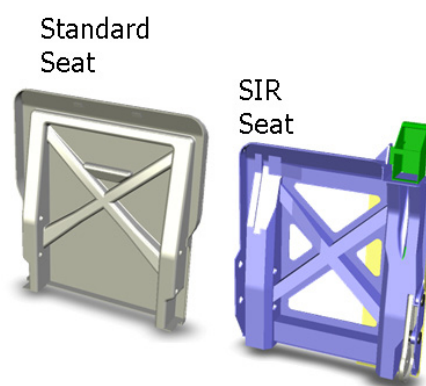
Figure 22. EPFL seat back designs.

Next Steps

The redesign of the composite seat structure will continue to be refined for carbon/nylon composites. It will also be designed with glass/PP and other glass fiber reinforced composites to reduce cost. The cost modeling exercise will need to be redone with the new designs.

Presentations/Publications/Patents

1. J. P. Fuchs, et al., "Automotive Structural Joint and Method of Making Same," US Patent Application 12119084, 5/12/2008.

2. H. Fuchs, "Initial Design of the Automotive Composites Consortium Structural Composite Underbody," SAMPE Fall Technical Conference, Memphis, TN, 9/10/2008.

3. L. Berger, et al., "Materials and Processes for a Structural Composite Underbody," SAMPE Fall Technical Conference, Memphis, TN, 9/10/2008.

4. L. Berger, et al., "Development of a Structural Composite Underbody," SPE Automotive Composites Conference and Exhibition, Troy, MI, 9/16/2008.

B.   Composite Underbody Attachment

Barbara J. Frame (Principal Investigator), Vlastimil Kunc
Oak Ridge National Laboratory (ORNL)
P.O. Box 2008, Oak Ridge, TN 37831-6053
(865) 576-1892; fax: (865) 574-8257; e-mail: framebj@ornl.gov
(865) 574-8010; fax: (865) 574-8257; e-mail: kuncv@ornl.gov

Automotive Composites Consortium (ACC) Joining Group
United States Council for Automotive Research (USCAR)
1000 Town Center Bldg., Ste. 300, Southfield, MI 48075
(248) 223-9000; fax: (248) 223-9021; e-mail: cphilpott@uscar.org

Technology Area Development Manager: Joseph A. Carpenter
(202) 586-1022; fax: (202) 586-1600; e-mail: joseph.carpenter@ee.doe.gov

Field Technical Monitor: C. David Warren
(865) 574-9693; fax: (865) 574-6098; e-mail: warrencd@ornl.gov

Objective

- Develop a method to predict the effects of environmental exposures and mechanical loadings on the durability of a composite-adhesive-metal (i.e., multi-material) joint. The focus application for this project is the joining of a polymer-matrix composite (PMC) underbody to an automotive body structure.

Approach

- Develop and validate the analytical models and tools capable of predicting multi-material joint performance and durability under multiple loading scenarios.

- Generate an experimental database on the multi-material joint's performance and durability under various loading and environmental conditions to support and validate the modeling approach.

- Establish and define the bounds of validity for the methodology.

Accomplishments

- Conducted a literature review of current best practices for joining structural automotive composites that included current domestic and foreign automotive technologies and recent technologies that have been developed and implemented in nonautomotive applications.

- Prepared and distributed to the working team data files containing geometry, material property, and other information necessary to describe and model the composite underbody joint.

- Prepared a conceptual test specimen design for simulation of individual load cases expected for the composite underbody joint during service. The conceptual specimen design has an advantage that representative global thermal stresses arising due to manufacturing or environmental exposures can be "locked in" to the specimen and thereby included as a part of the multi-material joint durability evaluation.

- Identified critical load cases (tension, bending, and torsion) for evaluation in joint durability tests and model validation efforts.

- Defined the durability cycle and environmental conditions (temperatures, humidity) to be used for joint durability testing.

- Identified the weld bonded "super lap shear" specimen geometry for initial joint durability testing and model validation efforts

- Conducted analyses to identify minimum specimen dimensions necessary to adequately capture the effects of thermal loading when using the super lap shear specimen design.

- Constructed an analytical model to estimate stresses in super lap shear, weld bonded geometry arising from manufacturing process temperatures.

- Identified an existing "tub tool" for the manufacture of the composite portion of the multi-material joint specimens to be evaluated in the second phase of this project.

- Conducted infrared (IR) thermography examinations of a weld bonded composite-to-steel super lap shear specimen.

Future Direction

- Conduct durability testing with super lap shear specimens tested in tensile mode.

- Modify and adapt super lap shear specimen geometry to accommodate testing via four-point-bending and torsion test methods.

- Prepare test fixtures and equipment to evaluate a weld bonded specimen via four-point-bending and torsion test methods.

- Evaluate validity of durability analytical models with weld bonded specimen test data and make modifications to models as appropriate.

- Design specimen, tests, fixtures, and equipment for evaluating multi-material joint durability using three-dimensional (3D) composite molded from "tub tool."

Continue validation and development of durability analytical models using test data from tub tool specimens as input.

Introduction

The objective of this project is to develop a method to predict the effects of environmental exposures and mechanical loadings on the durability of a composite-adhesive-metal joint. The focus application is joining a PMC underbody to an automotive body structure and validating the assembly's long-term durability and performance.

Technologies for attaching/joining PMC parts with other metallic components enable the wide-spread integration of composites into a predominantly steel vehicle's design and manufacture. This design strategy requires reliable technologies for joining components made of dissimilar materials. Issues associated with joint design include long-term reliability (durability) and ease of assembly (manufacturing cost). Multi-material joining also requires an understanding of the compatibility of

the joined members and means of attachment (adhesives, fasteners, etc.) under long-term service conditions.

Attempts have been made to characterize performance of such load-bearing joints in aerospace as well as some automotive applications in the past. However, those earlier results were specific to the geometries, materials, and joining techniques studied. Generic tools for predicting the performance of any composite design do not exist. Consequently, the joint and materials to be used in the PMC underbody must be studied for this particular application.

Because original equipment manufacturers need to minimize the number of developmental prototypes, validated modeling tools must be created to allow them to predict the durability of composite structures with the same level of

confidence as metal structures if they are to implement composite structures in vehicles intended to be produced in high volume using common program timing. This project is a step toward achieving that goal.

This project will validate the basic methodology for building computer-aided engineering (CAE) models capable of predicting the durability of composite-to-metal joints. Additional work will be required to expand the models to other types of multi-material joints. However, the tools developed as part of this project will be available for other joint designs, including other material combinations.

Technical Approach

A methodology for coupon-level testing of combined environmental and mechanical loading in a multi-material joint will be developed. The underbody geometry will be simplified to allow extraction of test data representative of the performance of this type of joint. Necessary size and scaling techniques to interpret test results will be established. CAE modeling will be conducted to aid in the design of the test specimens to best replicate real-life joint exposures and to allow for accelerated testing of environmental stressors and joint design due to differing load histories.

The validity of existing automotive CAE durability tools for this application will be evaluated. Inputs for model validation and development will be based on test results obtained as part of this project and previous research on similar materials. Test-program specifics will be determined in conjunction with the Automotive Composites Consortium (ACC) Focal Project 4, (see "Automotive Composites Consortium Focal Project 4," X.Y) design teams and relevant ACC working groups.

The key elements of this project include (1) design of the multi-material joint test, (2) material characterization, (3) test article manufacture, (4) mechanical performance of joint specimens for durability, (5) synergistic durability from multiple environmental stressors, and (6) CAE model validation. This project is a joint effort between ACC and ORNL.

Project Deliverables

Deliverables include a composite-to-metal joint coupon-testing protocol, test data, CAE model validation results, and final report. Recommendations to improve the methodology (testing and analytical) will be proposed as deemed appropriate.

Literature Review

A literature review of current best practices for joining structural automotive composites was conducted that included the current domestic and foreign automotive technologies as well as recent technologies that have been developed and implemented in nonautomotive applications (military, aerospace, industry, etc.). Technology gaps identified as part of this literature review included a general lack of durability modeling for composite-to-metal joints under automotive conditions.

Joint Specimen Concept

A multi-material joint specimen was designed incorporating previously analyzed super lap shear specimen dimensions and expected radii and flange sizes from the underbody geometry and surrogate tub (Figure 1). The specimen has the added feature of being able to "lock in" representative global thermal stresses arising due to manufacturing or environmental exposure.
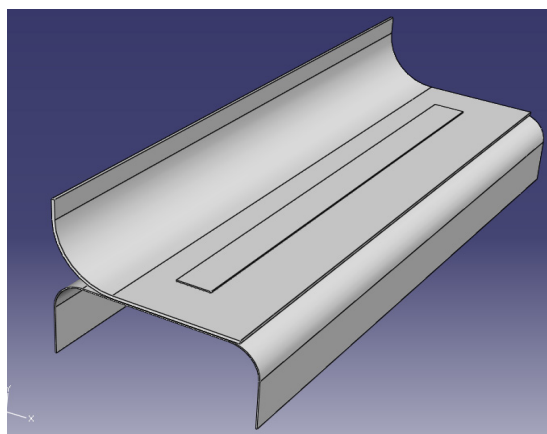
**Figure 1.** Conceptual design of multi-material joint specimen.

Six possible load cases were defined for the joint configuration, inducing various levels of peel and

shear along the concept joint specimen edges. Stress concentration factors, KvonMises and Kpeel, were devised to characterize the relative severity of the load cases, and are defined as

$$K_{vonMises} = \frac{\sigma_{vonMises}}{\sigma_{AJ}} \dots K_{peel} = \frac{\sigma_{peel}}{\sigma_{AJ}} \quad .$$

In this equation, σ_{AJ} is defined as the applied load divided by the area of the joint, and $\sigma_{vonMises}$ and σ_{peel} are, respectively, the vonMises and peel stresses.

Results of this analysis are summarized in Figure 2 and indicate that the most significant load cases were associated with peel along the long (L) length of the joint and across the width (E).
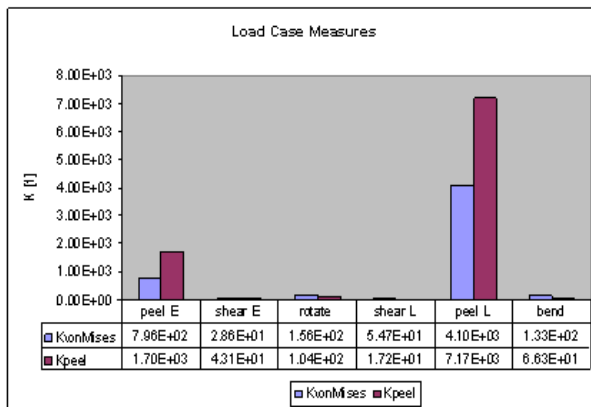
Figure 2. Analysis and severity ranking of load cases for conceptual joint specimen.

Experimental Test Parameters

Joint evaluations will be conducted through a combination of quasi-static and cyclic fatigue testing. The quasi-static tests are to determine the maximum joint strength and identify failure mechanisms. Fatigue testing will generate the S-N curves for each load case and environmental condition. The S-N curve is defined in high cycle fatigue as a graph of the magnitude of the cyclical stress (S) against the logarithmic scale of cycles to failure (N).

Fatigue-test parameters are 10% to peak load (sinusoidal) at 3 Hz. The environmental conditions include tests conducted at 25°C (ambient temperature), 80°C, −40°C, and 50°C and 85% relative humidity.

Super Lap Shear Weld Bonded Coupon Tests

The super lap shear weld bonded coupon, shown in Figure 3, was developed by General Motors for evaluating weld bonded metal joints. Since a significant amount of joint characterization has already been conducted using this geometry, this coupon was selected for the first phase of durability testing of a composite-to-metal joint.
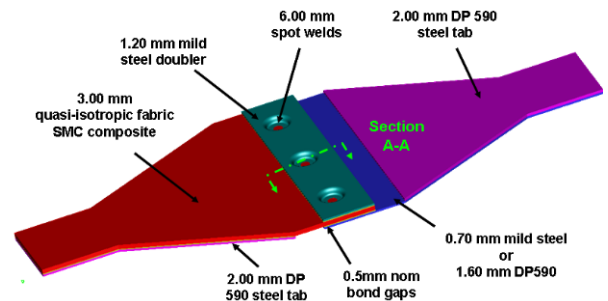
Figure 3. Super lap shear test weld bonded coupon developed by General Motors. (Image is courtesy of Multimatic Incorporated.)

Tested in tension, loading of the coupon's joint is primarily due to shear stresses (with a minor peel-stress contribution) leading (ideally) to failures that are shear dominated. The durability test data derived from these tests will therefore be used to validate simple durability models for prediction of shear dominated failures in a multi-material joint.

A goal of the project is to validate durability models for failure prediction of multi-material joints that are loaded in ways similar to what they would experience in the on-vehicle structure. In-service joints are typically subjected to mixed- or combined-loading conditions. Analyses conducted by Multimatic Incorporated show that in bending-mode tests (such as four-point bend tests), loading of the coupon joint is dominated by peel stresses. In torsion tests, loading is a combination of both shear and peel stresses.

Plans are to attempt to modify and adapt the basic components of the super lap shear specimen so that it may be used as both a four-point bend test specimen and a torsion test specimen. The data derived from these tests will be used to validate that the durability models are appropriate for

prediction of durability under these loading conditions as well.

Manufacturing Stresses Analysis

Linear finite-element analysis (FEA) was used to estimate the residual stresses in the composite-to-metal joint due to cooling after cure and spot welding.

A joint strip model was created with three welds along the length (see Figure 4) and geometry adopted from the super lap shear specimen model. The stresses were analyzed in the adhesive layer (Figure 5) of the composite.
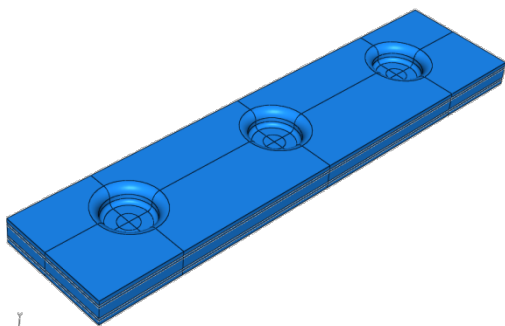
**Figure 4.** Representation of weld bonded joint used in residual manufacturing stress analysis.
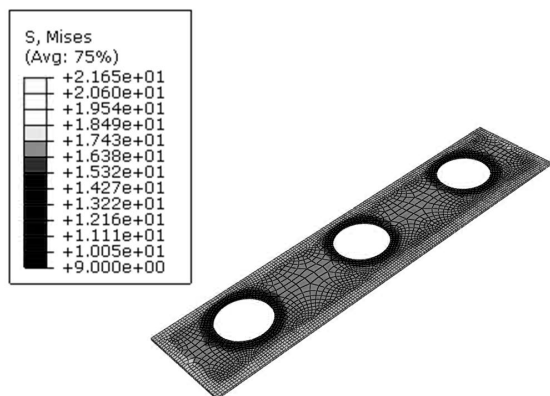
Figure 5. Analysis of residual manufacturing stresses in adhesive portion of weld bonded joint. The highest stresses are at the edges of the specimen.

Results of this analysis showed that the highest stresses were at the edges of the adhesive portion of the specimen. This type of analysis could be used to estimate an appropriate knockdown factor for a durability model.

"Minimum Length" Analysis

Analyses were conducted to establish the minimum specimen dimension required to ensure that the thermally driven stresses in a long, weld bonded, composite-to-metal joint are accurately represented by the test specimens. Stresses due to thermal loading were analyzed in flat specimens containing up to six welds. Figure 6 shows the mesh for one of the analyses and a path along which stresses were plotted in Figure 7.
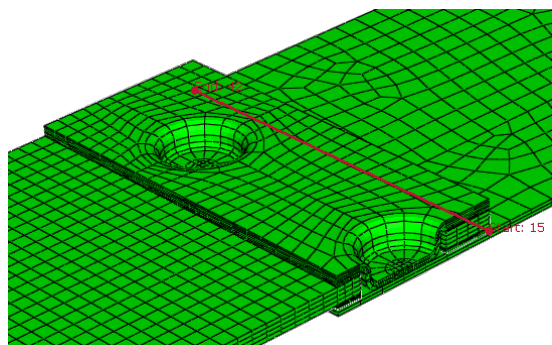
Figure 6. FEA mesh for analysis of thermally driven stresses in long weld bonded joint.
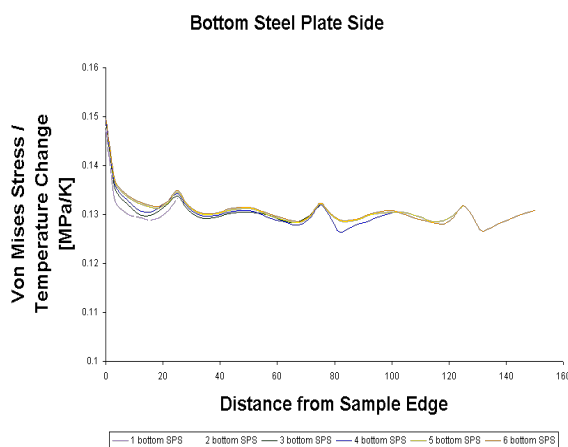
Figure 7. Thermally induced stresses versus distance from sample edge for multiple lengths of weld bonded specimens.

Upon examination of the results, it was concluded that specimens containing two or more welds experienced virtually identical stresses along the edges of the joint as those of longer specimens.

Surrogate Tub Specimens

Use of an existing tool for molding a composite tub was identified as a low cost way to obtain a

surrogate part for this project. This component will be used to provide the composite portion of the structure used in substructural-level testing in the second phase of this project. Composite tubs molded in the tub tool will possess many of the 3D features of the composite underbody design, including the flanges and corner details.

Design of the tub-tool test specimens is on hold pending results of the super lap shear coupon tests and model validation work.

Infrared Thermography Inspection of Weld Bonded Coupon

A super lap shear specimen was evaluated at ORNL using the IR thermography technique to determine whether the constituents of the joint (weld nugget, composite, and adhesive) could be examined nondestructively.

Figure 8 shows IR images of the coupon weld bonded region as a function of time following a thermal exposure applied to one side of the specimen using a xenon flash. An analysis of the measured IR intensity as a function of depth from the surface is shown in Figure 9.
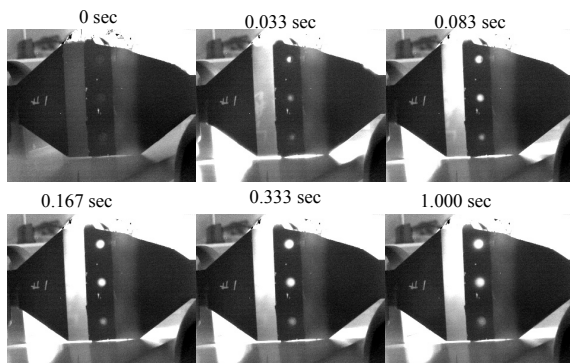
Figure 8. IR thermography images of composite-metal weld bonded coupon.

The preliminary data indicate that the details and size of the weld nugget could be deduced, and the weld nugget diameters in this specimen ranged between 5.78 and 6.50 mm (0.228 and 0.256 in.). Further work will be required to obtain information regarding the composite and adhesive.

IR thermography may provide a means to assess the quality and uniformity of weld bonded,
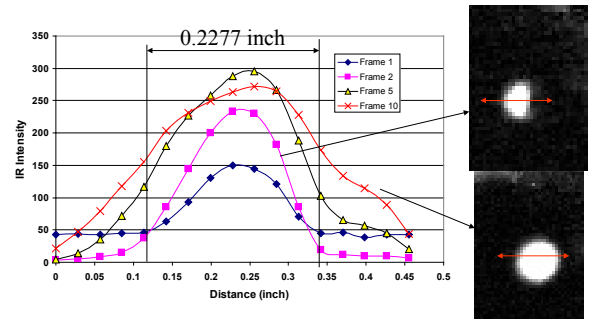
Figure 9. Estimated weld bond nugget size (0.228 in. or 5.78 mm) using IR thermography data.

composite-to-metal assemblies. It has the added potential to provide information on failure mechanisms for test specimens and structures where details of the failure (composite delaminations and cracks, weld nugget fractures, etc.) may be obscured by the outer facings of the specimen.

Summary and Conclusions

A literature review of current best practices for joining structural automotive composites was conducted. The results indicated a general lack of durability models for joints under automotive conditions, which this project addresses.

A conceptual multi-material joint specimen was designed incorporating previously analyzed super lap shear specimen dimensions as well as expected radii and flange sizes from the underbody geometry and tub tool. This concept specimen has the added feature of being able to lock in representative global thermal stresses arising due to manufacturing or environmental exposure.

Critical load cases to be studied for the joint durability test and model validation efforts have been identified, as well as the durability cycle and environmental conditions (temperatures, humidity) to be used during testing.

A super lap shear weld bonded coupon has been selected for the first phase of durability testing of a composite-to-metal joint. In addition to tensile tests, plans are to attempt to modify and adapt the basic components of the super lap shear specimen so that the weld bonded geometry can be evaluated in four-point bend and torsion.

Linear FEA was used to estimate the residual stresses in the composite-to-metal joint due to cooling after cure and spot welding. Analyses were also conducted to establish the minimum specimen dimensions required to ensure that the coupons experience thermally driven stresses during testing at temperature. Results showed that specimens containing two or more welds experienced virtually identical stresses along the edges of the joint as those of longer specimens.

An existing tool for manufacturing surrogate parts was identified. This tool will be used to manufacture the composite portion of the multi-material joint specimens to be evaluated in the second phase of this project. Design of the specimens based upon this component is on hold pending results of the super lap shear coupon tests and model-validation work.

A super lap shear specimen was evaluated using the IR thermography technique to determine whether the constituents of the joint (weld nugget, composite, and adhesive) could be examined nondestructively. Preliminary data indicate that the details and size of the weld nugget can be deduced. Additional work is required to obtain information regarding the composite and adhesive.

Acknowledgements

C.   Development of Next-Generation Programmable Preforming Process

Principal Investigator: Robert E. Norris Jr.
Oak Ridge National Laboratory
P.O. Box 2008, Oak Ridge, TN 37831-6053
(865) 576-1179; fax: (865) 574-8257; e-mail: norrisrejr@ornl.gov

Technology Area Development Manager: Joseph A. Carpenter
(202) 586-1022; fax: (202) 586-1600; e-mail: joseph.carpenter@ee.doe.gov

Field Technical Monitor: C. David Warren
(865) 574-9693; fax: (865) 574-6098; e-mail: warrencd@ornl.gov

Objectives

- Develop the next generation of low-cost fiber-preforming technologies based on programmable, robotic-controlled, directed chopped-fiber processes for the application of
    - low-cost carbon fiber (CF),
    - reinforced thermoplastics, and
    - hybrid glass-carbon.

- Develop the supporting technologies required to successfully implement the process technology including
    - preform characterization (e.g., permeability, areal-density uniformity) and
    - perform process modeling for process-effects analysis.

- Conduct parametric process studies to investigate fundamental process effects and establish process-property relationships.

- Conduct requisite molding investigations—experimentally and through modeling—to elucidate the relationship between preform characteristics and moldability.

Approach

- Use and expand the base-research, programmable, robotic preforming system for development and evaluation of advanced capabilities (e.g., new chopper designs).

- Use a highly instrumented and controlled research molding capability to isolate and investigate the effects of process variables on moldability and mechanical properties.

- Develop new severing technologies to facilitate the implementation of low-cost carbon-reinforced thermoplastics and hybrid glass-carbon products.

- Benchmark and incorporate process modeling in experimental work to guide parameter selection and to provide tools for longer-term implementation of preforming and related technologies.

Accomplishments

- Using commercially available industrial grades of CF and glass fiber, fabricated a number of test preforms with polypropylene and blends at various ratios of carbon and glass reinforcement to evaluate potential advantages of combining these materials to achieve performance and/or economic benefits. Although the focus of this approach is to facilitate evaluation of alternative material combinations, especially looking at hybrids, in situ blending may prove economically attractive as well. Since the variety of forms of commingled materials is

extremely limited, this allows evaluation of materials not available at all in commingled form and in a much broader array of blending alternatives.

— Significantly improved preforming and preconsolidation processes to allow evaluation in further processing.

— Demonstrated molding of hybrid panels made with the above processes. Results are encouraging, with the biggest issue being uneven distribution of the polypropylene through the panel thickness.

- Procured a refurbished urethane injection system to be installed in fiscal year (FY) 2009 to enable evaluation of various materials/forms in liquid molding processes, including hybrid blends and natural-fiber preforms, and early evaluation of lower cost CF.

- Developed and demonstrated capability to control prototype Wolfangel chopper in operations representative of those used in high-throughput preforming and specifically simulating a generic liftgate pattern. Established capability limits of original hardware and necessary parameters for scaling up the system.

- Designed, built, and characterized significant upgrades to Wolfangel chopper to simulate robotic-preforming operations at speeds exceeding those of the current chopper system and meeting economic goals established from earlier work.

- Achieved apparent improvements in cutter wear of Wolfangel blades coated with a thin layer of zirconium using the C3 International Metal Infusion Surface Treatment (MIST) process.

- Initiated effort to model image projection of the laser and fiber-optic delivery system being used in laser-severing experiments.

- Modified previously developed general modeling approach to handle various fiber types and improve realistic fiber-deformation predictions leading to enhanced capability to model void space and potential flow pathways.

Future Direction

- Continue improvements in preforming and molding through studies with hybrid carbon and glass reinforcement and polypropylene materials blended in situ at the preforming machine. Expand to consider various other product forms including forms with low-cost CF as available. Implement more industry-representative and effective means of heating and transferring blanks of reinforcing fibers mingled with thermoplastic fibers into the press for compression molding.

- Develop and implement required hardware modifications and control changes necessary to use Wolfangel chopper on the ORNL preforming machine while maintaining capability to switch back to the original chopper as necessary.

- Demonstrate technical and economic feasibility of higher-speed Wolfangel chopper in representative preforming manufacturing operations using the upgraded preforming machine.

- Demonstrate more durable chopping mechanisms using alternative blade materials and coatings and other hardware as appropriate, using both standard and higher-speed choppers. Continue monitoring/evaluating alternative chopping techniques for longer-term development.

- Evaluate preform process models relative to physical preform characteristics and expand model capability as resources permit.

- Continue developing and implementing tools for more-effective characterization of process variables and effects on final products.

Introduction

Polymer-matrix composite materials offer a number of benefits in lightweighting of automotive and heavy vehicles, including greater stiffness and strength per unit weight than conventional materials, easier formability, less corrosion susceptibility, the ability to tailor properties to specific load requirements, and enhanced noise and vibration damping. However, widespread implementation of CF composites, which are among the materials with the greatest weight-saving potential, will require lower-cost

materials and manufacturing processes than are currently available. Advanced preforming processes offer opportunities to facilitate the widespread use of carbon composites.

Robotic-controlled, programmable, directed-fiber preforming processes have demonstrated exceptional value for rapidly preforming large, glass-reinforced, automotive composite structures. Due to their unique features and flexibility and to their inherently low scrap rate, they are among the most viable candidate processes for making affordable CF preforms for a variety of structural automotive components. The Automotive Composites Consortium (ACC) has very successfully implemented the programmable powdered preform process (P4) with glass fibers in its truck box program—Focal Project 2 (FP2). Prototype B-pillars were also successfully fabricated with both carbon- and glass-fiber reinforcement and tested as part of the ACC's Focal Project 3 (FP3) composite-intensive body structure program). Original equipment manufacturers have transferred the technology to commercial applications such as the General Motors Silverado pickup box and the Aston Martin Vanquish body side.

Analyses have indicated a potential for greater than 60% weight savings for a CF-intensive body-in-white under the assumption of a thickness design constraint of 1.5 mm. The analyses also indicated the potential for saving an additional 15% if the thickness constraint is reduced to 1 mm. Unfortunately, evidence suggests that 1.5 mm may be a practical limit for liquid molding. However, thermoplastics preforms, in which the matrix and fiber are both deposited in the preforming step, offer a potential path to obtaining thinner sections and, consequently, additional weight savings as well as greater potential for recyclability. Hybrid-fiber preforms that can effectively take advantage of concurrently using carbon and glass fibers offer another potential benefit in terms of economics and property enhancement and may be a good route for actually introducing more CF at somewhat lower quantities than necessary for all-carbon components in automotive applications.

Preforming Developmental Approach

The objective of this project is to advance directed-fiber preforming processes to effect a further reduction in vehicle weight—relative to metals and conventional glass-fiber composites—while maintaining the economical advantages of net-shape preforming. The project is pursuing three focus areas corresponding to three materials systems: reinforced thermoplastics, CF, and hybrid glass-CF. Each focus area consists of four main tasks: (1) materials development, including introduction and evaluation of alternative and/or new fiber product forms and binders; (2) machine development, particularly new severing technology; (3) process development, for example, to control areal-density uniformity and preform anisotropy; and (4) supporting technologies development, including modeling and characterization techniques. This project will also include developing a deeper understanding of fundamental aspects of the process and their effects on preform quality and mechanical properties in the molded part. To summarize, this project will support, augment, and facilitate the current and future research activities undertaken in related ACC projects.

A research-focused preforming system has been installed in the polymer composites laboratories at ORNL to serve as the base for hardware and associated technology developments. A number of combinations of reinforcing fibers, binders, and/or matrix fibers have been obtained to establish materials baselines for comparison with and advancement of previous P4 work conducted by ACC. The P4 machine is currently being used to build preforms for evaluation using the Twintex product (glass fiber commingled with thermoplastic fiber to serve as the matrix), glass impregnated with thermoplastic resin using the Direct Reinforcement Fabrication Technology (DRIFT) process, and various forms of carbon and glass reinforcement in alternate independent and hybrid forms. Although the near-term focus is on demonstrating advances with glass fiber and existing industrial grades of CF, the long-term goal is to establish the groundwork for large-scale introduction of low-cost CF for significant impact in automotive lightweighting.

In Situ Blending to Evaluate Hybrid Carbon and Glass Compositions

Because it is believed that hybrid-fiber preforms can effectively take advantage of concurrently using carbon and glass fibers and offer potential benefits in terms of economics and property enhancement, ORNL has obtained standard, lower-cost CF alternatives from Zoltek and Toho to evaluate in conjunction with glass- fiber reinforcement previously acquired from Owens Corning. ORNL has also procured polypropylene fiber from Fiber Science to serve as the composite matrix in initial trials to evaluate and demonstrate in situ blending of these hybrid blends at the preforming machine.

A number of preforming and molding experiments has been conducted to establish the equipment setup requirements and process parameters necessary to evaluate the potential of these hybrid blends. As previously established in cutting the Twintex materials, the polypropylene is more difficult to completely sever than the carbon- or glass-fiber reinforcement, although it is less abrasive to the cutter blades themselves. Due to current polypropylene product availability, typically only in very small tow sizes, and the desire to maintain the capability to adjust the mix ratios to a large degree, the polypropylene was combined by the vendor to a larger tow size, which was still about half the size of the smaller glass and carbon tows on hand. Currently, the only packaging found immediately available was configured for outside unwind of this product versus the inside unwind configuration that works best for preforming. These limitations necessitated use of a multiple position creel to facilitate processing and mitigate entanglement. Still not being intermixed on a filament-to-filament basis with the reinforcement fibers as with the Twintex, the polypropylene also tends to "fuzz" a little more in handling than that with the Twintex. These factors have made the in situ-blended materials a little more difficult to cut while preforming and a little more difficult to preconsolidate into a preform having structural integrity for handling.

As we continued to make adjustments (e.g., to blade and roller configurations and placement of air purges and vacuum to reduce clogs) and improve chopability, significant effort was devoted to improving the preconsolidation process and developing necessary processing conditions for molding. We determined that one of the key problems in the preconsolidation process was that we were not able to get uniform air flow into the preform during compaction. Compaction is achieved by the dead-weight loading of the upper compaction table being let down on top of the lower table until the upper table weight is sustained by the combination of the pressure on the screen by the compressed preform and weight on the lower screen frame when the upper screen frame makes contact. Assuming that the screen-frame sections make contact (which had been the case for all preforms made until experiments described below), the greater the thickness of the preform, the greater the compaction pressure within each preform. It appears that the additional fuzziness of the in situ-blended materials probably impedes air flow and leaves more clumps of fibers and fibers extending out of the two-dimensional plane of the preforming screen. The air flow into the preform during the preconsolidation process is also not a self-stabilizing process (i.e., as the air flow encounters more resistance from the more densely packed regions in the preform, it actually concentrates flow through the less dense, lesser packed regions). The net result was that the initial preforms had holes where the hot air had created separation of all materials and some regions in which the polypropylene had been totally melted and flowed into almost a solid sheet and other larger regions with no signs of any consolidation. We were able to mitigate these effects by placing shims between the upper and lower screen-frame sections, thereby reducing the compaction pressure. Although this does allow some of the hot air intended for preconsolidation to escape, the upper screen still extends into the lower frame such that the thickness of the shims can be adjusted to balance escaping air flow and compaction pressure within the preform. Although still not optimal, this approach allows us to get preforms consolidated well enough for initial molding trials and is encouraging for further development.

To conduct initial molding experiments to evaluate the preforms and establish detailed

requirements for more optimal charge heating and transfer of the charge to the press, various heating and transfer techniques are being evaluated for this process. An existing laboratory curing oven is currently being used for charge heating. Due to the oven's relatively small air-flow capability and distance from the press, an aluminum plate has been used to maintain temperature while the preform is conveyed from the oven to the press. In addition, we have been using a single sheet of high-temperature release film large enough to fold and cover both the top and bottom of the preform to mitigate air exposure during oven-to-press transfer and to facilitate transfer of the charge from the aluminum sheet into the mold. Initial experiments indicate that we are approaching an acceptable preforming/molding process but that the distribution of the polypropylene is not uniform through the thickness of the panel, with the side of the panel that corresponds to the preforming screen much "wetter" than the "sprayed-up" side. We think that this could be due to the polypropylene being melted and flowing or being forced down to the screen due to the air flow in the preconsolidation process or problems with the initial blending. Although we have conducted a limited amount of mechanical testing, tests so far have been used to identify and direct process improvements (as discussed above) as opposed to generating reportable data.

During the latter portion of this period, experiments were conducted to evaluate different techniques to improve the intermixing of reinforcing fibers with the polypropylene. Several variations of the device shown in Figure 1 were used to evaluate injection of turbulent air flow into fibers before the chopping process, similar to the approach used in textiles for intentional yarn entanglement for splicing or other purposes. Although the different fibers were obviously better intertwined, initial experiments did not show significant improvements in the final panels after molding. We plan to investigate further entanglement in the preforming and changes in air flow and temperatures in the preconsolidation process. We are also evaluating whether we will go with an improved convection oven or a combination of convection and infrared for the charge preheating; either way, the oven will be

Figure 1. Prototype air injector for enhancing fiber intermixing.

placed significantly closer to the press to minimize transfer time.

As part of establishing supporting tools, a limited amount of effort was spent developing the capability to rapidly determine weight and volume ratios for mixtures of glass, carbon, and polypropylene. Typically, acid digestion processes for the composite matrix are used to determine ratios of carbon to resin in CF-reinforced composite parts. Typically, resin burn-off or acid digestion processes are used to measure glass and polypropylene ratios in glass-reinforced composite parts. Burn-off techniques are usually quicker, create fewer hazardous wastes, and are more practical for larger sections than acid digestion. However, if an inert atmosphere is not used, one has to be careful with CF to avoid oxidizing the fiber itself at high temperatures. The author and others have used combinations of acid digestions to determine resin content and then high temperatures in air (~800°C) to get the carbon : glass ratios for hybrid-type samples. We are conducting experiments to determine whether we can get ballpark numbers for resin content without oxidizing the CF at about 450–500°C. Alternatives include using an inert atmosphere and possibly higher temperatures to eliminate the resin. If so, this would be a much quicker and

more cost-effective tool for composition analysis for this work.

Although the current focus of this work is using polypropylene for demonstration purposes, the concept should also be applicable for other thermoplastic materials, including polyester and nylon. If successfully demonstrated, in situ blending would offer greater flexibility for manufacturers to tailor-blend ratios in-house to specific product needs without long lead times, inventory requirements, or dependence on the limitations of product variety from suppliers as is the case with the Twintex product manufactured by Saint-Gobain Vetrotex. It is believed that regardless of whether the in situ-blending process itself proves adequate for high-quality, thermoplastic matrix parts, the technology being developed could prove advantageous in blending glass and carbon reinforcement to a level adequate for use of hybrid reinforcement in general and could likely be extended beyond thermoplastics and applied to thermosets in sheet molding compounds or to preforming for structural reaction injection molding (SRIM). This could have significant impact on DOE and ACC goals as hybrids would appear to be an effective route for actually introducing more CF at somewhat lower quantities than necessary for all-carbon components in automotive applications and an effective means of reducing the component cost in CF by using only the minimum amount that is needed. To both expand the breadth of hybrid blend alternatives and facilitate evaluation of low-cost CFs being developed at ORNL, we have procured a refurbished urethane injection system, shown in Figure 2, to establish in-house SRIM capability for this program.

High-Speed Chopper Development and Demonstration

The ACC Materials and Processing working groups had initiated work with Ecole Polytechnique Fédérale de Lausanne (EPFL) in Switzerland to study processing effects and material properties of commingled glass and thermoplastic fibers leading to cost-model comparisons of various thermoplastic-composite processes. The focus of this work has been on the Twintex materials produced by Saint-Gobain

**Figure 2.** Urethane injection system capable of 110 pounds (lb)/minute and 33 lb shot sizes.

Vetrotex, incorporating glass and polypropylene fibers, but the basic evaluation process can be extended to a variety of materials and processes based on this concept. With the support of EPFL and an ACC representative, ORNL fabricated approximately 200 sample panels using various fiber lengths (25–75 mm) and preform thicknesses (2 mm–4 mm) along with variations in preforming compaction station time (10–60 s) and air temperature variables (180–240°C). Results so far have helped to establish initial thickness limits for processing at 3 mm without additional heat-stabilization modification to the materials. ORNL and ACC have each separately discussed with Vetrotex adding improved heat stabilization capability to the Twintex line. ORNL and Vetrotex have tentatively planned specific evaluation trials, but these trials have been on hold pending resolution of the sale of this business unit.

Material properties of the ORNL panels processed by EPFL are competitive with similar materials and, in some cases, significantly improved. Overall economics for this process were shown by EPFL analysis to approach targets as chopping speeds improved, leading to additional near-term focus on demonstrating the technical and economic feasibility of higher-speed chopping processes.

To potentially improve preforming throughput, ACC purchased a prototype chopper unit from Wolfangel. This chopper was designed to process up to 5 tows of fiber at a maximum peripheral speed of ~892 meters (m)/minute (min), which for

the 1,870 tex Twintex tows amounts to ~8.3 kilograms (kg)/min of throughput. For comparison, the P4 chopper is designed to process 2 tows at up to 625 m/min, which for 1,870 tex tows translates to ~2.3 kg/min. We were able to run 2 tows through each tube of the P4 chopper, which would effectively double the throughput, but this was difficult to sustain and certainly could not be exceeded with the current configuration. Economic goals were to be able to achieve 12 to 15 kg/min, which would require similar doubling of at least some of the tows through each position of the Wolfangel chopper, speeding up the peripheral speed, or combinations of both. The Wolfangel chopper, shown in Figure 3, allows chopping at two distinct fiber lengths, determined by blade spacing in either the inside or outside half of the cutter wheel, which is then controlled by manually switching the positioning of the cutter roller with respect to the fiber stream passed through the cutter. The P4 chopper allows selection of an infinitely variable fiber length within a relatively wide range, but use of more than two lengths within a single production operation has been very rare.
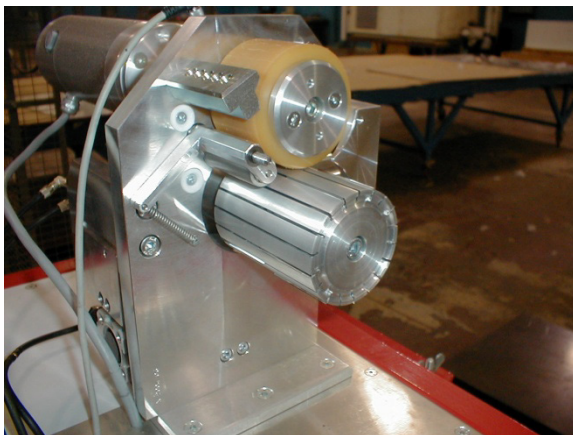

Figure 3. Wolfangel chopper showing cutter wheel extended. Cutting takes place on inner portion of the wheel in contact with the rubber roller.

Working with the ACC Processing Working Group, trials were conducted to check out the chopper using the supplied manual chopper controls and to capture representative chopper-control signals from the P4 machine to approximate simulation of the fabrication of a preform suitable for fabrication of a liftgate similar in shape to that shown in Figure 4.
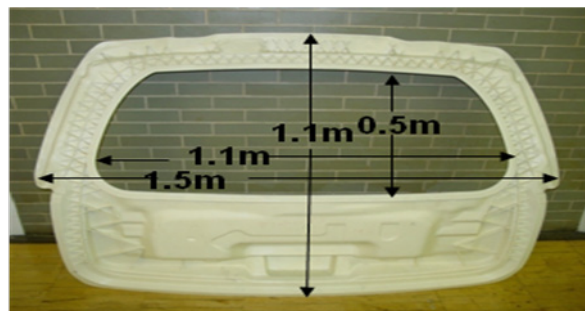

Figure 4. Approximate liftgate dimensions used in simulation program.

In typical processing, the chopper starts and stops very abruptly in tight coordination with the robot movement as the robot traverses across each pass and then indexes though multiple passes in uniformly spraying up the part profile. Obviously, the economics of the process are improved as speed of the preforming process is increased up to the repeatability and capabilities of the preforming system. A program was written in LabView to capture signals from the robot that could then be used to control the chopper for evaluation independent of operation of the entire preforming system. A separate LabView program was written to provide the necessary control signals to the chopper using the data previously captured, as shown in Figure 5. Also, hardware and program capability was provided to automatically switch fiber length during processing.
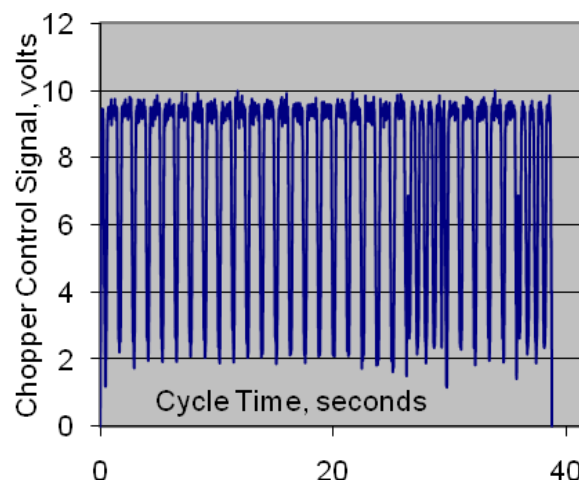
**Figure 5.** Chopper control signals in simulation program.

A larger set of trials was conducted at ORNL with ACC support to evaluate the Wolfangel chopper in liftgate fabrication simulations. During these trials, a number of enhancements were made to processing conditions and fiber handling as shown in Figure 6. It was determined that the chopper could easily handle up to 3 tows at close to the upper speed limit (892 m/min) to deliver about 5.0 kg/min but that the chopper did not have adequate torque to handle more tows due to the pressure required to fully sever the tows. However, it appeared that achieving both higher speeds and higher torque with a larger motor would be feasible with relatively minor modifications.
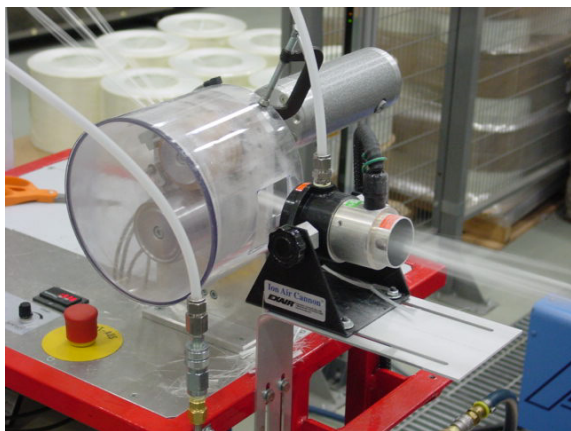
Figure 6. Photo showing ORNL-ACC trials which demonstrates improved fiber-processing techniques.

The existing Servowatt motor was rated at 0.75 Nm (Newton meter) maximum torque and 4,000 revolutions per min (rpm). An Allen Bradley MPL-B430 motor and drive system was located that rated at 20 Nm maximum torque and 5,000 rpm. With this motor operating at its speed rating, it should be able to achieve 12 kg/min using about 6 tows with a maximum output of more than 18 kg/min using 9 tows. The system was reconfigured with the new motor while using as much of the existing chopper hardware as possible, although a number of components had to be modified to use this higher-powered motor system.

The upgraded system, shown in Figure 7, has been characterized in extensive trials. It has been shown capable of achieving more than 18 kg/min instantaneous output when using 9 tows. Very
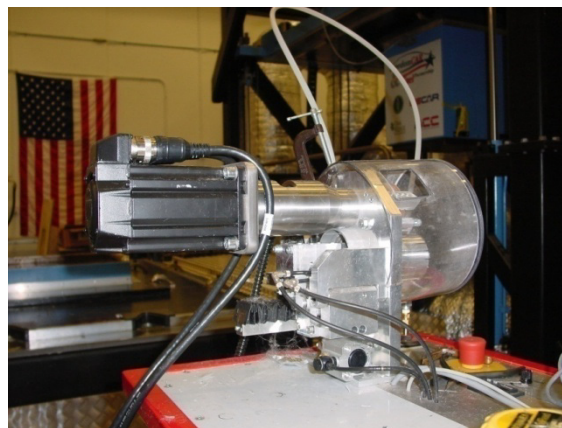
**Figure 7.** Chopper retrofitted with more powerful motor and adapters.

good severing was achieved at these conditions when using 150 pounds per square inch air pressure on the cutter/rubber roller interface for the 1-inch cut length, while the 3-inch length at these conditions was largely, but not completely, cut. (Typically, when not completely severed, the glass is more fully cut than the polypropylene.) This trend toward better cutting at the shorter length was essentially replicated for all conditions at which any difference was noted. As expected, improved severing was achieved at higher air pressures for essentially all speeds regardless of the number of tows being processed. Also expected was the finding that cutting quality decreased with the number of tows. However, we unexpectedly found that cutting quality actually improved with increased speed regardless of the number of tows being cut or interface pressure. Plans for FY 2009 are to further characterize the durability of this chopper. If the results continue to be as promising as those thus far, ORNL will make necessary hardware modifications and controls upgrades to mount the high-speed chopper to the robot to demonstrate the economic and technical feasibility for making preforms representative of those required to fabricate the liftgate shown in Figure 4.

As another part of the current focus on thermoplastics, ORNL has been working with Polycomp (inventor of the DRIFT process for making thermoplastic prepreg) and Fiberform (a key licensee) to evaluate the possibility of chopping the DRIFT product form in the ORNL preforming machine as well as providing one route

to evaluating the DRIFT material, in general. In the most recent work, a basic processing envelope, including both preforming and molding, adequate for fabricating evaluation panels was established and demonstration panels fabricated. Plans are to repeat the process to fabricate panels for testing. However, similar to problems with getting air flow into the preform for the compaction of the hybrid materials, the most recent ribbonized DRIFT form was very difficult to preconsolidate. We may get some improvement by reducing the compaction pressure as with the hybrid panels, but in this case, we feel that this could possibly be addressed by returning to the more oval-shaped form that was difficult to chop in the P4 chopper and instead use the upgraded Wolfangel chopper. With data from these experiments, plans are to focus efforts on developing more optimal processing techniques, taking into account material forms and chopper configurations that might be economically feasible for implementation. Discussions between ORNL and Polycomp are continuing concerning putting a prototype DRIFT line at the end of a low-cost CF pilot line to demonstrate and evaluate the technical and economic potential for various automotive applications of the DRIFT process.

Fiber-Severing Technology

ORNL is continuing to study mechanical chopping for various materials forms and techniques and also plans to continue evaluation of the potential for laser severing for rapid fiber cutting. In addition to evaluating the output capabilities of the Wolfangel chopper previously mentioned, we are also evaluating modifications to the chopper equipment including cutting wheels and blades for both units. As part of the extensive cutting experiments already completed involving a large amount of Twintex material, blades coated with thin layers of zirconium implanted with the C3 MIST were used alongside the standard stainless-steel blades supplied by Wolfangel. (MIST is a low-cost process that recently won an R&D 100 award.) Examination of the surface of the blades at the conclusion of these tests indicated that those blades coated with the MIST process showed fewer signs of wear, as shown in Figure 8. Conversely, use of MIST-coated carbon steel blades in the P4 chopper did not have immediately positive results. We had been experiencing
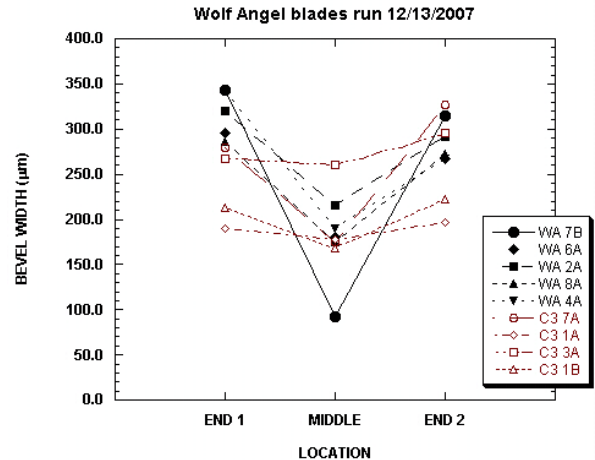
Figure 8. Comparison of wear on C3-coated and noncoated Wolfangel blades. Wear is indicated by difference of readings from the ends to the middle.

chopper jams and eventual blade breakage with the standard blades when cutting the hybrid materials in the P4 machine, largely due to binding of the polypropylene. When the standard blades were replaced with coated blades, the blades bent very quickly. It was apparent that although the MIST process is considered to be a relatively low-temperature process, it was indeed changing the steel properties. Additional data from upcoming tests using the Wolfangel chopper to cut a large amount of material under nearly identical conditions should afford a good opportunity to more fully evaluate these and several other blade options and other system components.

We will continue to work with C3 to better exploit the gains achieved with the Wolfangel blades and to better understand and use the information gained from failure of the P4 blades.

We have limited experience with the tungsten carbide blades in the original P4 chopper. Our initial experience was that binding of the polypropylene fractured these brittle blades; however, with changes in techniques and cutting of other materials, we may be better able to take advantage of the potentially higher wear capabilities of this blade material.

We are pursuing other sources for commercial blades and efficient, economical coatings. One of these is the low-temperature carburization process developed by Swagelok, which we found is not

directly applicable to blades manufactured from the carbon and stainless steels we have on hand. Nevertheless, we believe we will be able to find some blades made from the preferred alloys that will fit in our cutters.

Based on test data and other input, recommendations will be developed for enhancing the durability of cutter assemblies. This may include changing to more durable materials, changing the surface finish, changing design of the cutters or holders, and applying coatings or surface treatments to existing or alternative materials. With a better understanding of chopping mechanics and more experience with varying blade designs, blade materials, and cutting mechanisms, we will be able to better address a variety of cutting issues associated specifically with CFs as well as with other materials and material blends including somewhat unique products such as the DRIFT materials.

Due to significant differences in the physical properties of various reinforcement fibers as well as their available product forms, chopping technology that has been successful for glass-fiber systems has demonstrated less satisfactory results for the CF products that are currently available. It is expected that similar results will occur for reinforced thermoplastics and hybrid glass-carbon products. Accordingly, consideration has been devoted to identifying alternative severing technologies. Literature and patent searches were undertaken previously to assess promising technologies for benchtop investigation. Possibilities identified include mechanical-based, laser-based, CO_2 pellet, liquid nitrogen, water-jet, and ultrasonic. Based on the information available in the literature and consideration of project-team experience in related activities, laser-based choppers appear to offer the most promise for development and eventual deployment.

Although laser severing was demonstrated earlier in this project with Nd:YAG (i.e., neodymium-doped yttrium-aluminum-garnet) laser pulses, this took more energy than originally estimated. Even with modification to the delivery optics, we have not yet been able to demonstrate a pathway to a practical, cost-effective laser and optics system for this application in our experimental and limited

modeling efforts to date. Although we still believe that this approach is likely technically feasible and intend to continue monitoring development of lower-cost laser systems and alternative means for optical delivery, we have halted active work in this area in the near term. We intend to revisit this technology and others that may have applicability at a later point.

Modeling of Preforming Processes

A process model has been established to analyze the effect of process variables on preform characteristics that affect further processing and performance of molded parts. The computer program can simulate deposition of long fibers and accounts for various processing conditions in automated manufacturing of fibrous preforms for automotive composites. The model accounts for different fiber types (e.g., glass, carbon, polymer) of different geometries and process deposition conditions (e.g., vacuum pull, fiber orientation and clustering, substrate traversal paths). The program uses a graphical user interface that allows the user to avoid mathematical details of the modeling process and concentrate on the physical aspects.

Recent improvements to the model include implementation of additional computational models that are relevant to the transport properties of the fiber preforms and therefore directly relevant to molding applications. A new method has been implemented for determining particle caging volumes. The topology of the fiber and void spaces can be related to physical measurements of tortuosity, porosity and characteristic lengths (viscous and thermal). The current model goes well beyond percolation-type and simple regular capillary geometry models. The transition between spanning connectivity, spanning cluster size, and fiber-particle-network caging capacity can also be used in preform permeability characterization. Realistic fiber deformation is a key provision along with strict enforcement of spatial rules (e.g., fibers are not penetrating as is the case in several commercial products). The basic consolidation model has been implemented and will be further developed based on particular processing conditions.

Near-term plans include correlating the capability to simulate fiber layups made of multiple fiber types deposited concurrently with experimental work in progress. We will compare predictions of the performance of the in situ blending with what is achieved and make comparisons with the theoretical predictions for offline commingling for different deposition scenarios. Longer-term plans include expanding the models and using these tools along with experiments for evaluation of manufacturing feasibility of the above preforming processes through consolidation and/or molding.

Summary and Conclusions

The Next-Generation Programmable Preforming Process project is continuing to build on past development and application of directed-fiber preforming processes, namely, those of the baseline P4, to extend the process to new material systems. Developments are expected to facilitate the use of lower-cost CF-reinforced thermoplastics and glass-carbon hybrid materials as effectively as with the current state-of-the-art glass-fiber technology. Using these materials is expected to lead to further reductions in vehicle weight in a more cost-competitive scenario than is currently possible.

A research-focused preforming system installed in the polymer composites laboratories at ORNL is currently being used to build preforms for evaluation. The system uses both glass fiber commingled with thermoplastic fiber and glass fiber preimpregnated with thermoplastic resin (DRIFT) as the composite matrix. EPFL and ACC evaluations of a large number of ORNL-fabricated preforms from off-the-shelf and the commingled Twintex product have been both technically and economically encouraging, especially if the projected speed increases can be achieved with the modified Wolfangel chopper. These modifications have been completed and the chopper characterized to establish capabilities and optimal operating parameters. Plans are to complete durability testing of this chopper in FY 2009 and, assuming results continue to be as promising as those thus far, to make necessary modifications and mount the high-speed chopper to the robot to demonstrate the economic and technical feasibility for making preforms representative of those

required to fabricate a generic liftgate type structure.

During the first half of FY 2008, preforming and molding experiments were conducted to establish the necessary equipment setup requirements and process parameters to evaluate the potential for on-the-fly commingling of CF and glass fiber with polypropylene fibers to achieve hybrid blends. We were able to establish fiber intermixing, chopping, and preconsolidation techniques adequate for initial molding trials, which is encouraging for further development of this process. We investigated various techniques for charge heating and transfer of the charge to the press and demonstrated that we can mold panels fairly well using a relatively primitive setup before finalizing a design for better temperature control and faster transfer to the mold. Work to improve these techniques will be continued in FY 2009.

Severing investigations have been conducted in two areas: mechanical chopping and laser severing. The mechanical-chopping investigations included blade materials and coatings and various cutter configurations. Preliminary results indicate that low-cost C3 MIST coatings may improve blade life for specific applications, and this work is continuing. Since we have not yet been able to demonstrate a pathway to a practical, cost-effective, laser and optics system for this application, we intend to continue monitoring development of lower-cost laser systems and alternative means for optical delivery but have halted active work in this area in the near term with plans to revisit this technology and others that may have applicability at a later point.

Modeling of the fiber-deposition process continues through the development of an in-house code. It has unique characteristics compared to existing models reported in the literature and can simulate deposition of long fibers of various types and geometries and accounts for various processing conditions in automated manufacturing of fibrous preforms for automotive composites. Work is underway to evaluate the recently implemented capability to simulate layups made with multiple fiber types and to compare differences in manufacturing techniques.

Collectively, the technologies under development in this project will advance low-cost processing on two fronts. First, they will provide the opportunity to use additional materials in the net-shape preforming process, which is expected to lead to additional weight reduction and/or better performance. Second, they will provide the requisite tools to evaluate the effects of process parameters on the utility and performance of preforms and molded parts.

D. Low-Cost Carbon-Fiber Composites for Lightweight Vehicle Parts

Principal Investigator: Mark A. Janney
Materials Innovation Technologies LLC
320 Rutledge Road, Fletcher, NC 28732
(828) 651-9646; fax 828-651-9648; e-mail: mjanney@emergingmit.com

Technology Area Development Manager: Joseph A. Carpenter
(202) 586-1022; fax: (202) 586-6109; e-mail: joseph.carpenter@ee.doe.gov

Objectives

- Develop at pilot scale the Three Dimensional Engineered Preform (3-DEP) process, a slurry-based, low-cost, high-volume production process for making net-shape, carbon-fiber preforms for use in polymer composite automobile parts.

- Optimize 3-DEP tooling development and evaluate how it influences fiber placement in the preform.

- Optimize carbon-fiber slurry development and determine how it affects preform properties.

- Develop process capabilities to include material handling, preform molding, preform drying, and reducing preform variability.

- Demonstrate the utility of 3-DEP preforms to make an in-production, thermoset composite, automotive component using production tooling (Corvette wheelhouse support).

- Build a process cost model for composites made using 3-DEP preforms.

- Write training and quality manuals.

Approach

- Investigate effects of processing parameters on properties of flat plate parts and Corvette wheelhouse support parts produced in the 3-DEP machine.

- Demonstrate ability to control part weight during a 3-DEP production run.

- Demonstrate ability to control within-part areal weight distribution (i.e., fiber areal density).

- Collaborate with a current Tier 1 automotive supplier to demonstrate the applicability of 3-DEP preforms in an existing production process.

Accomplishments

- Conducted a mock Part Qualification Test Protocol at Molded Fiber Glass (MFG) per the standard approach that MFG would use to qualify any new process or product for General Motors (GM).

- The Corvette wheelhouse supports made by the 3-DEP process passed the Part Qualification Test Protocol which demonstrated that the 3-DEP process can be used to make automotive-quality parts.

- Preforms were manufactured at two basis weights, which yielded molded parts at 20 and 23 % fiber volume fraction.

- Fabricated a total of 355 preforms (105 wheelhouse supports and 250 flat plaques) for the qualification test.

- Part-to-part coefficients of variation (COVs) for the preforms were between 2 and 4%; these COVs were lower than what MFG usually experiences.

Future Direction

- Develop preforming technology to achieve higher fiber loading (>50 vol %) in molded composites.

- Develop preforms having higher resin permeability to make infusion easier.

- Combine 3-DEP preforms with continuous fiber face sheets to make true structural composites.

- Identify opportunities within the automotive, industrial, and aerospace communities to commercialize the 3-DEP technology.

- Expand our forming capabilities to other fiber-reinforced composites including fiberglass, aramid, natural fibers, and hybrids of these.

Introduction

This work is being conducted under an SBIR Phase II project. The goal of the project is to develop at pilot scale a potentially low-cost, high-volume production process for making net-shape, carbon-fiber composites for use in polymer composite automobile parts. The main technical focus of the project is making components and optimizing their manufacture using the 3-DEP fiber forming process.

The overall objective of the Department of Energy (DOE) SBIR Phase II project is to complete the development of the technology started in the Phase I SBIR project by focusing on a complex-shaped component that will be commercially viable. The part chosen for the Phase II project is the front wheelhouse lower support for the Corvette (Figure 1).

Figure 1. Corvette wheelhouse lower support demonstration part molded at MFG using a carbon fiber preform made by the 3-DEP process.

This part is currently manufactured by our partner in the project, the MFG companies of Ashtabula, Ohio.

The specific technical objectives of our Phase II project are as follows.

1. Develop at pilot scale the 3-DEP process, a slurry-based, low-cost, high-volume production process for making net-shape, carbon-fiber preforms for use in polymer composite automobile parts.

2. Optimize 3-DEP tooling development and how it influences fiber placement in the preform.

3. Optimize carbon-fiber slurry development and how it affects preform properties.

4. Develop process capabilities to include material handling, preform molding, preform drying, and reducing preform variability.

5. Demonstrate the utility of 3-DEP preforms to make a thermoset composite, in-production automotive component using production tooling (Corvette wheelhouse support).

6. Build a process cost model for composites made using 3-DEP preforms.

7. Write training and quality manuals for the 3-DEP process.

Results and Discussion

Based on the excellent preforming and compression molding results we obtained in the first year of the project, we decided to conduct a full-scale mock qualification run for the Corvette

wheelhouse support part. The qualification runs were conducted using the same set of criteria that MFG would use for any new part or new process being considered for production for the Corvette. The qualification runs were conducted between March and July 2008. Preforms were made by Materials Innovation Technologies (MIT) LLC in March and April; molded flat plaques and Corvette wheelhouse support parts were made at MFG in April and May; testing was conducted at MFG and at Ashland, Inc. from April through July.

Preform Fabrication

Preforms were fabricated in six lots and at two different fiber loadings, which produced two different fiber volume fractions in the molded polyester parts (20 vol % and 23 vol %). A "lot" comprised a totally independent set of fabrication conditions. For each lot, the following procedure was used at MIT-LLC:

1. The 3-DEP machine was completely drained of water and carbon fiber.

2. The equipment was given a "super" cleaning to ensure that there was no carryover of fiber from one lot to the next.

3. The system was charged with fresh water (heated to 70°F), fresh carbon fiber, and fresh binder fiber.

4. This operation was conducted six times (six lots) for each fiber loading level.

Tables 1 and 2 summarize the preform runs that were conducted during this qualification run. For each volume fraction, Lot #1 comprised 50 wheelhouse support parts and a group of 23 or 60 flat preforms. For Lots #2 through #6 at each volume fraction, at least 15 flat preforms were run. The part-to-part COVs were between 2 and 3% for the 20 vol % preforms, and between 2.5 and 4.5% for the 23 vol % preforms. COVs in this range are considered excellent according to our contacts at MFG and GM. Figure 2 shows the probability distribution of part weights for Lot 1 runs for both 20 vol % and 23 vol % fiber loadings. The normal distribution of part weights demonstrates that the preforming process was in statistical control.

**Table 1.** MFG wheelhouse and flat preforms at 20 vol % carbon

Lot	Part Type	Number	Mean Wt	COV
			(g)	(%)
Lot 1	Wheelhouse	50	110	2.59
Lot 1	flat	23	117	2.10
Lot 2	flat	22	114	2.14
Lot 3	flat	16	117	2.99
Lot 4	flat	16	115	2.88
Lot 5	flat	16	114	2.92
Lot 6	flat	15	115	2.13

Mean - 23 vol % flats (6 runs)	115 g
Std Dev - flats - all 6 runs	3.18 g
COV - flats - all 6 runs	2.77 %

Table 2. MFG wheelhouse and flat preforms at 23 vol % carbon

Lot	Part Type	Number	Mean Wt	COV (%)
			(g)	
Lot 1	Wheelhouse	55	127	4.17
Lot 1	flat	60	137	3.20
Lot 3	flat	15	131	3.32
Lot 4	flat	20	127	4.28
Lot 5	flat	17	127	4.03
Lot 6	flat	15	131	3.25
Lot 7	flat	15	127	2.79

Mean - 23 vol % flats (6 runs)	132	g
Std Dev - flats - all 6 runs	6.38	g
COV - flats - all 6 runs	4.83	%
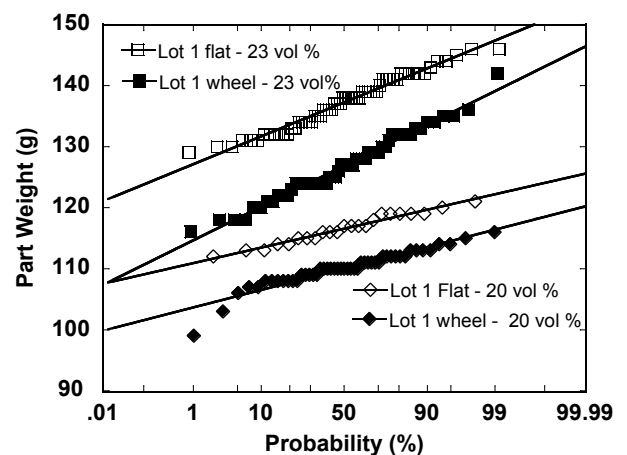
Figure 2. Probability plot of dry part weight for Lot 1 (20 vol %) and Lot 1 (23 vol %) parts showing that the part weights were normally distributed throughout the qualification runs.

Molding and Testing Activities

Flat coupon test specimens are required for acquiring basic material physical properties. In order to compare measured properties to existing material specifications, several tests on several lots were run to account for standard deviation adjustment to test average values. These test plans closely resemble a Qualification Run such as General Motors would likely require in the course of releasing a new material specification.

Flat plaque molding and Materials Testing was conducted at MFG Research. Adhesive testing was conducted at Ashland Inc., Analytical Services & Technology Division (http://ashlandanalytical.com).

MFG Research fabricated the 12 in. × 12 in. × 2.5 mm plaques by compression molding them in a hydraulic press with 500 tons capacity. The plaque tool is constructed of steel and has controlled heat in both halves. The edges of the plaque are produced by a telescoping shear feature in the mold which produces consistent molding pressure and a finished edge.

The test plan was designed to mimic a new material qualification submission plan such as General Motors would require prior to release of a new process into their Materials Specification System. An example of a GM Material Specification is GMP.UP. 011 (see Table 3). It is widely used in production at MFG in parts compression molded with directed fiber glass preforms and an unsaturated polyester resin filled with calcium carbonate and glass microspheres. The current production Corvette wheelhouse support falls under this GM Material Specification.

The GM procedure requires a minimum of six lots of test material. The test data are averaged, the standard deviation (STD DEV) calculated, and a final minimum specification is calculated by subtracting (STD DEV) × 3 from the mean value. This testing strategy enables us to make a direct comparison to approved materials than are presently in production at MFG.

Another feature of the GM Materials Specification is paragraph "1.1 Bondability." MFG offered that the question of bondability is always raised and would be important to the GM Materials Engineer in the consideration of new material specifications. To address this issue, sufficient preforms were supplied to MFG to construct plaques that were submitted to Ashland. Ashland screened the plaques with several surface preparation techniques as well as lap-shear strength testing and issued reports to MFG.

Table 3, Comparison of 3-DEP Properties to Other Molding Compounds, summarizes the physical test data gathered from 12 in. × 12 in. × 2.5 mm plaques molded and tested at MFG Research Company. In general, the mechanical properties of the parts molded from 3-DEP preforms compare favorably with the requirements of GMP.UP. 011.

Table 3. Comparison of 3-DEP material properties with GM molding compound specs

Material Description	Carbon Fiber 3-DEP Preform	GMP.UP.011 Directed fiber preform - lite
Fiber type	carbon	glass
Fiber length	25mm	25 mm
Fiber mass fraction %		40-48
Fiber volume fraction %	20%	
Resin type	polyester	polyester
Filler type	none	glass
		microsphere
Tensile Strength D-638	87.5 MPa min	85 MPa min
(Mean - 3σ)		
Tensile Modulus D-638	11012 MPa min	10100 MPa min
(Mean - 3σ)		
Flexural Strength D-790	176 MPa min	207 MPa min
(Mean - 3σ)		
Secant Modulus D-790		
(Mean - 3σ)		
At 22C Average	8727 MPa min	9200 MPa min
At 70C Average	6340 MPa min	6900 MPa min
Un-notched Izod D-4812	75 J/m min	10 J/m min
(Mean - 3σ)		
Specific Gravity D-792	1.32 max	1.50 max
(Mean + 3σ)		
Water Absorption D-570	0.90% max	0.95% max
(Mean + 3σ)		
Dynatup Impact D-3763		
Energy to Max Load	1.9 J	NA
Total Energy	6.6 J	NA

Molded Three-Dimensional Parts

The molded Corvette Parts were built into bonded assemblies in the same form that MFG supplies parts to the General Motors assembly plant at Bowling Green, Kentucky. That assembly consists of the front wheelhouse outer, front wheelhouse inner and the front wheelhouse lower reinforcement. Those assemblies were evaluated by collecting dimensional information and by performing destructive bond evaluations at Ashland.

General Comments from MFG regarding the qualification runs

- The properties the preforms were satisfactory for the type of molded parts that MFG produces.

- The consistency of the preforms was good; the part-to-part COVs were lower than what MFG usually experiences.

- The carbon preforms were more difficult to impregnate with polyester resin than are the customary air-laid fiberglass roving preforms. Molding trials on the 23 vol % flat plaques were successful in the flat tool press in their laboratory. However, in molding tests for the wheelhouse support part (run in the production tools at MFG's Premier Molding Company) the molding engineers and operators encountered difficulty in getting complete resin coverage with the 23 vol % preforms.

- Molding tests were rerun with the 20 vol % preforms; those preforms performed much better – the resin flowed through the preform satisfactorily.

- The bonded assemblies (comprising the wheelhouse inner, wheelhouse outer, and wheelhouse lower support) measured within production tolerances. The carbon 3-DEP based parts appeared the same as the production fiberglass parts.

- The bonded assemblies performed the same as production in the bond destruct evaluations. Fiber tear was observed at the bond sites.

- The adhesive screening report from Ashland Inc., Analytical Services & Technology

Division indicates that the carbon parts perform as well as their current production parts. Three different surface preparation techniques were evaluated and all three produced satisfactory bonding.

Summary Comments Regarding the Qualification Runs

Engaging MFG to perform the physical testing of the 3-DEP carbon preforms had several advantages. MFG has more preform manufacturing and molding activity than any molder in the world. They have been developing air-directed, glass-fiber preforming for 50+ years. They have evaluated using that process to make a carbon-fiber preform and can appreciate the challenge of performing with very lightweight fibers. As an automotive and commercial truck supplier they have an interest in supplying new materials when their customers request them. Their willingness to provide access to a production molding tool and comments from their engineers gave this project more depth than had we just contracted with a prototype shop.

Summary and Conclusions

We have demonstrated that the 3-DEP process can be used effectively to make chopped fiber preforms in carbon fiber. Those preforms have been molded into final parts that would be acceptable to the automotive industry. Our demonstration part, the Corvette front lower wheelhouse support, was run through a mock **Part Qualification Test Protocol** at MFG per the standard approach that they would use to qualify any new process/product for GM. The protocol simulated the testing that would be required for a new production part including adhesively bonding the part into a test assembly. A total of 355 preforms (105 wheelhouse support preforms and 250 flat plaque preforms) were fabricated for the qualification test. The part-to-parts COVs for these preforms The Corvette wheelhouse support made by the 3-DEP process passed the **Part Qualification Test Protocol** which indicates that the 3-DEP process can be used to make automotive-quality parts.

The variability of the preforms made by the 3-DEP process is significantly lower than that

obtained for preforms made by competing processes such as air-laid, directed-fiber preforming. This is true for both within-part variation and part-to-part variation. The COV for both of these measures is consistently below 5% of the mean.

MIT LLC is moving forward with the commercialization of this technology with both government and industrial partners. We have won SBIR contracts/grants with the Department of Defense for manufacturing helicopter spare parts (Phase II) and with the National Science Foundation to investigate natural fiber-reinforced composites (Phase I). We were awarded a Phase II Supplemental contract with DOE for this project. We have process/product development contracts in place with Boeing, Plasan Carbon Composites, and Toho Tenax Americas. The Automotive Composites Consortium—Materials is conducting a third-party cost model evaluation of the 3-DEP process.

Presentations/Publications/Patents

1. Mark A. Janney, "Making Composites Using the Three Dimensional Engineered Preform (3-DEP) Process," presented at the AATCC Medical, Nonwovens, and Technical Textiles Symposium, Raleigh, NC October 6–7, 2008.

2. Mark A. Janney, "Manufacturing Composites Using the Three Dimensional Engineered Preform (3-DEP) Process," presented at the NDIA 9th Annual Science & Engineering Technology Conference DoD/Tech Exposition, Charleston, SC, 15–17 April 2008.

3. Mark A. Janney, "Interlayer Hybrid Composites of Chopped and Woven Carbon Fiber," presented at the SAMPE Fall Technical Conference, Memphis, September 8–11, 2008.

E.   High Volume Processing of Composites (ACC115*)

Principal Investigator: Daniel Houston
Ford Motor Company, Manufacturing & Processes Department
2101 Village Road, Dearborn, MI 48121
(313)323-2879; fax 313)390-0514; e-mail: dhousto2@ford.com

Technology Area Development Manager: Joseph A. Carpenter
(202) 586-1022; fax: (202) 586-1600; e-mail: joseph.carpenter@ee.doe.gov

Field Project Officer: Aaron D. Yocum
(304) 285-4852; fax: (304) 285-4403; e-mail: aaron.yocum@netl.doe.gov

Objective

- Develop and demonstrate high-volume manufacturing (molding) processes to produce lightweight composite automotive components.

- Expand the scope of the Automotive Composites Consortium (ACC) composite projects into the thermoplastic area.

Approach

- Work with a Tier One automotive composites supplier to investigate and develop an improved carbon-fiber sheet molding compound (SMC) material amenable to cost-effective high volume applications.

- Continue exploration of the root causes of bond-line read-through (BLRT) through application of developed quantification tool to enable use of reduced thickness panels.

Accomplishments

- Provided process support for Focal Project 4, the Composite Underbody and Composite Seat.

- Upgrade an existing SMC compounder at Tier One supplier, Continental Structural Plastics (CSP). Developed carbon-fiber chopping apparatus and successfully chopped carbon-fiber roving.

- Continued work on BLRT by the molding, bonding, and analysis of assemblies to develop understanding of the impact of various factors on BLRT severity.

Future Direction

- High volume processing of lightweight structural thermoplastic composites.

- Carbon-fiber SMC materials for structural automotive applications:

- Continue working with fiber and resin suppliers through the Tier One supplier (CSP) to develop a superior material with improved manufacturability within cost and supply constraints.
    — Demonstrate material on potential applications.

---

*Denotes Project 115 of the Automotive Composites Consortium (ACC), one of the formal consortia of the United States Council for Automotive Research (USCAR) set up by Chrysler, Ford, and General Motors to conduct joint, precompetitive research and development.

- Initiate development of a modeling tool for predicting BLRT in the component design phase using experimental data obtained through this project to validate the model.

- Provide process support to Focal Project 4, Composite Underbody/Seat (ACC 007).

Introduction

The purpose of this project is to develop the high volume composite molding technologies germane to automotive production. The direction of ACC115 is to collaborate with suppliers to develop low cost – high volume molding processes that enable production of minimal weight components using materials and processes compatible with the material property and processing requirements of the automotive industry.

Two processing investigations are under way.

1. BLRT continued with studies of plaques molded with specific variations to assess the impact of various factors on the severity of the resultant surface distortions.
2. Develop high performance, cost-effective carbon-fiber SMC materials and associated processing techniques in conjunction with a Tier-1 supplier.

Bond-Line Read-Through

Phase 1
The focus of the fiscal year (FY) 2008 work in Phase 1 was evaluation and refinement of the procedure for converting raw curvature data into a quantitative measurement. The quantitative measurement needs to correlate to the visual perception of the severity of BLRT defects. The algorithm for converting the characteristics of a defect into a numerical value was established in FY 2007. The focus in FY 2008 was to identify the filters that would distinguish the regions on a panel that would be considered to be visible surface distortions from those that are not visible or that are due to defects other than BLRT. A large number of filtering schemes were evaluated and an initial combination of smoothing and thresholding filters was selected. The resulting severity scores and "score maps" (i.e., visual representations of the areas on a panel that were identified as visible distortions) for the reference panels were found to correlate well with visual assessments.

Unfortunately, application of the filtering procedure to assemblies constructed in Phase 2 of this work showed that the filters selected were not robust to high levels of orange peel in paint. When a high level of orange peel was present on an assembly, the score maps contained high levels of noise and the severity scores no longer adequately represented the severity of BLRT on the assembly. A number of other filtering combinations were evaluated, but filtering combinations that removed the orange peel also removed too much of the BLRT signature so that the severity scores obtained from those filtering combinations no longer reflected the apparent visual severity of the BLRT distortion. As a result, the team had to revert to the original algorithm and accept that the poor quality paint will impede the system's ability to acquire meaningful data.

The team also initiated gage repeatability and reproducibility (Gage R&R) evaluations in FY 2008. Since the ONDULO system that the ACC purchased for this project is a transportable system designed to be used on a wide variety of parts, very little of the system is fixed. As a result, the Gage R&R for the system was found to be unable to meet the expected level of repeatability and reproducibility. As an interim solution, the team is now repeating the measurements three times on every part and averaging the measurements. In FY 2009 the team intends to complete a Gage R&R using our parts, filtering procedure, and algorithm using a more production representative system. If that Gage R&R shows substantially better results than our system, the team will likely upgrade the existing system to improve its repeatability and reproducibility.

Phase 2
The objective of Phase 2 of this project is to conclusively determine which material and processing factors are the root causes of BLRT through the completion of multiple designed experiments. The measurement tool developed in Phase 1 of the project provides the objective data to quantify the change in BLRT severity in the

manufactured assemblies. The team made three trips to Meridian Automotive Systems' Shelbyville, IN plant in FY 2008 to complete designed experiments. The first trip consisted of a single experiment while multiple smaller experiments were completed during the second and third trips.

The first experiment was a screening experiment designed to determine whether any of the factors included in the experiment affect BLRT severity. The factors and factor levels included in this experiment are summarized in Table 1.

Table 1. Factors and Factor Levels Included in the First Screening Experiment

Factor	Low Level	High Level
Adhesive Modulus	364 MPa (Urethane)	3296 MPa (Epoxy)
Variation in Bond-line Thickness	None	3mm
Adhesive Application Pattern	Continuous	Drops
Warp in the Inner Panel	None	Warped
Outer Panel Substrate Stiffness	2.5mm SMC	0.7mm 210BH Steel
Bonding Temperature	RT	300°F
Degree of Cure of the Outer Panel	Undercured SMC	Fully Cured SMC
Bond Nest Configuration	Skeletal Nest	Full Nest

In Table 1, a "skeletal nest" refers to a bonding fixture in which only the bond lines are supported and heated whereas a "full nest" refers to a bonding fixture in which the entire panel is both supported and heated. These two types of fixtures are illustrated in Figures 1 and 2.
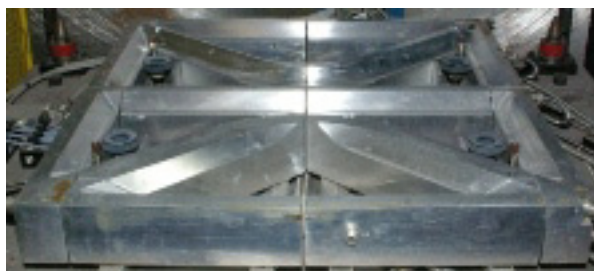
Figure 1: The bonding fixture in the "skeletal nest" configuration.

Figure 2: The bonding fixture in the "full nest" configuration.

The factor found to have the strongest effect on BLRT severity in the first experiment was the temperature at which the adhesive was cured in the bond cell. The type of material used for the outer panel was also found to have a strong effect. While the outer panel material was characterized by material type in this experiment, the team has since concluded that the bending stiffness of the outer panel, in which both the material stiffness and thickness of the panel are factors, has a greater effect on BLRT severity than the material stiffness itself. Finally, the bond nest configuration was not found to have an effect on BLRT severity. The team feels this result, however, is potentially misleading. The percentage of this assembly that is supported and heated in the skeletal configuration is substantially higher than what would typically be seen in a production application. Consequently, further investigation into the effect of the fixture design is planned. The effect of the other factors appeared to have been confounded by uncontrolled squeeze-out. Squeeze-out occurs when the adhesive bead intrudes into the radius of the bond flange and does not maintain a consistent, defined thickness.

The team chose to build a production representative bond fixture and bond press and to partner with Meridian Automotive Systems so that assemblies could be manufactured using a process as representative of production conditions as possible in order to reduce part-to-part variation. In the first screening experiment, only one assembly was made at each factor level combination, except for one combination. Four assemblies were manufactured for that combination, using what were assumed to be identical manufacturing conditions. Unfortunately,

there was a large difference in the BLRT severity within this set of assemblies. As a result, the team has manufactured three replicate assemblies at each condition in all subsequent experiments.

The results from the first experiment were used to determine the content and format of the majority of the following experiments. The primary experiment completed during the second trip to Meridian-Shelbyville attempted to determine the specific relationship between the temperature at which the adhesive was cured and BLRT severity. This experiment was a two- factor, full-factorial experiment. The factors and factor levels for this experiment are summarized in Table 2. The time required for the adhesive to reach handling strength varies with both adhesive and cure temperature. The time the assemblies were cured in the fixture for each combination of adhesive and cure temperature are summarized in Table 3.

Table 2. Factors and factor levels for the effect of cure temperature experiment

Factor	Factor Levels
Type of Adhesive	Urethane, Epoxy
Adhesive Cure Temperature	RT, 120°F,[a] 240°F, 270°F, 300°F

[a]Assemblies were not made at 120°F using the epoxy adhesive. Since the adhesive required three hours to cure at this temperature, there was not sufficient time allotted in the experiment to manufacture these assemblies.

Table 3. Cure time and temperature used in the effect of cure temperature experiment

Cure Temperature	Cure Time	
	Urethane	Epoxy
RT	2 hours	Overnight
120°F	25 min	3 hrs (est)[1]
240°F	120 s	300 s
270°F	105 s	180 s
300°F	90 s	120 s

Unfortunately, assembly-to-assembly repeatability in this experiment was insufficient to generate good data. The adhesive was dispensed at a volume that was intended to produce a 15 millimeter (mm) wide, 1-mm tall bead on all flanges, regardless of flange width. Since one

bond flange is only 12 mm wide, this bead size was expected to always produce read-through on that flange. Unfortunately, either the adhesive volume and/or the bead location on the flange varied sufficiently to result in a high level of panel-to-panel variation and no statistically significant effect of cure conditions could be detected.

In addition to the primary experiment completed during the second trip to Meridian-Shelbyville, the team also built six assemblies with twice the normal amount of urethane adhesive. In one set of three replicates, the bond gap was left at 1 mm. The bond gap was increased to 3 mm for the other set of three replicates. All of these assemblies were bonded at 300°F for 90 seconds(s). The BLRT severity on these assemblies was then compared to the BLRT severity on the urethane assemblies bonded at 300°F for the primary experiment completed during that trip. The filtered curvature maps for one panel of each type are shown in Figure 3.

The images in Figure 3 suggest that BLRT severity is more strongly related to squeeze-out than to the volume of adhesive dispensed. This finding will be important when developing CAE models for predicting BLRT severity.

The third trip to Meridian-Shelbyville included two smaller experiments. The first experiment completed during that trip investigated the relationship between the amount of the bond flange that was covered with adhesive and BLRT severity. In addition, two different outer panel thicknesses (2.5 mm and 3.0 mm) were used to manufacture assemblies made with epoxy adhesive. While the fact that increasing outer panel thickness reduces BLRT severity is well established, building these assemblies provided data for validating CAE modeling results later in Phase 3 of this project. Assemblies with the thicker outer panel were made only with one adhesive to reduce the number of assemblies that had to be manufactured and analyzed. The factors and factor levels for this experiment are summarized in Table 4. Flange coverage was controlled by the amount of adhesive dispensed. Figure 4 illustrates the urethane adhesive dispensing patterns developed for each intended

(a)

(b)

(c)
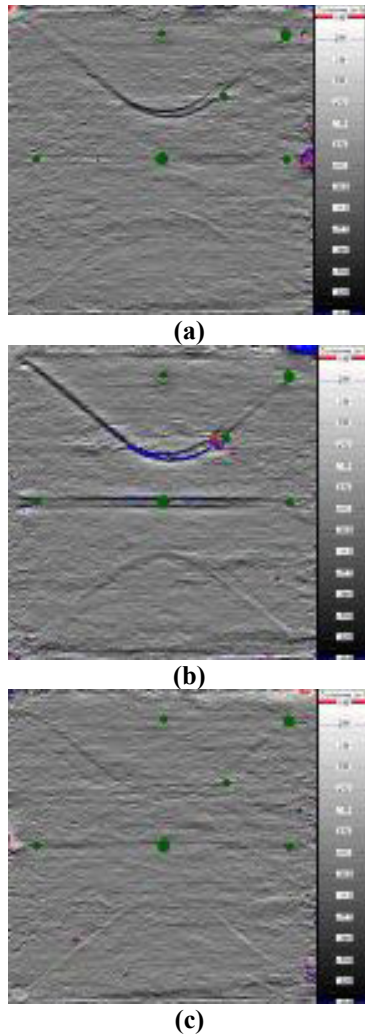
Figure 3. Curvature maps for raw assemblies bonded with differing amounts of urethane and differing bond gaps: (a) Standard adhesive volume and 1-mm gap, (b) 2X adhesive volume and 1-mm gap, (c) 2X adhesive volume and 3-mm gap.

Table 4. Factors and factor levels for the effect of cure temperature experiment

Factor	Factor Levels
Type of Adhesive	Urethane, Epoxy
Flange Coverage Level	25–50% 75–100% Assured Squeeze-out
Outer Panel Thickness	2.5 mm, 3 mm[a]

[a]3-mm outer panels were used only to manufacture assemblies bonded with epoxy adhesive.

(a)

(b)

(c)
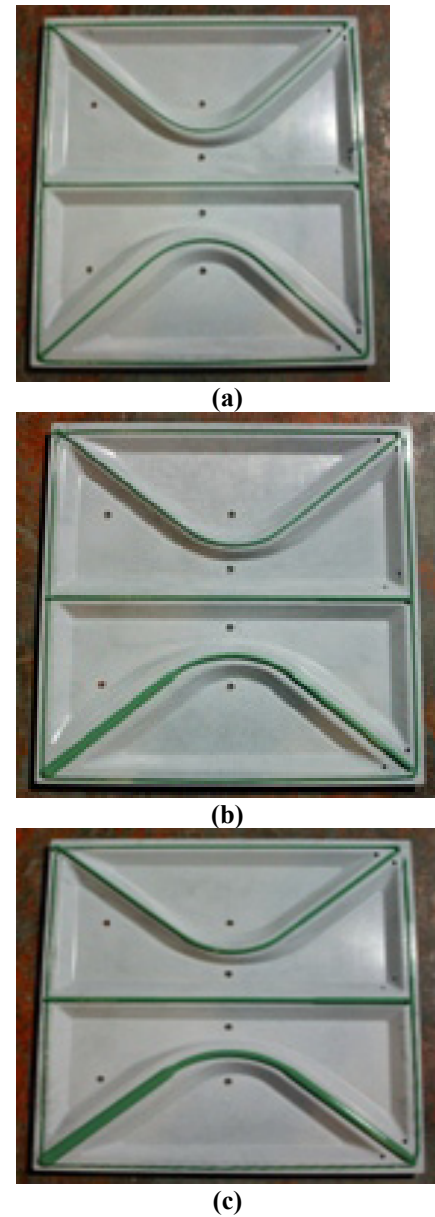
Figure 4. Adhesive dispensing patterns in the flange coverage experiment: (a) bead pattern for 25–50% flange coverage, (b) bead pattern for 75-100% flange coverage, (c) bead pattern for assured squeeze-out.

flange coverage. The dispensing patterns for the epoxy adhesive are similar.

The relationship between flange coverage and BLRT severity was evident even in the as-bonded (i.e., "raw") assemblies. The relationship is illustrated by the filtered curvature maps shown in

Figures 5 and 6. These figures show one assembly made with 2.5mm outer panels, each flange coverage level, and each adhesive. The maps for assemblies made with urethane adhesive are shown in Figure 5. The maps for the assemblies made with epoxy are shown in Figure 6.

(a)

(b)

(c)
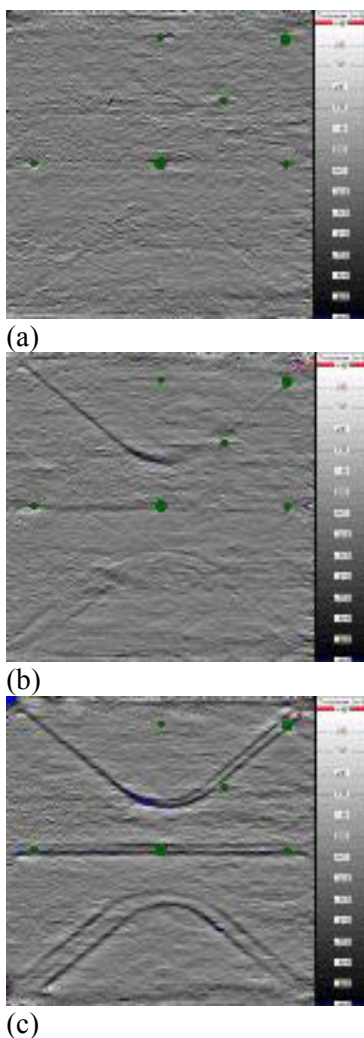
Figure 5. Curvature maps for raw assemblies bonded with urethane and differing levels of flange coverage. The percent of the flange surface covered by adhesive: (a) 25–50%, (b) 75–100%, and (c) assured squeeze-out.

These figures clearly show the strong relationship between the amount of the flange that is covered by adhesive and BLRT severity. While these assemblies have not been sectioned to

(a)

(b)

(c)
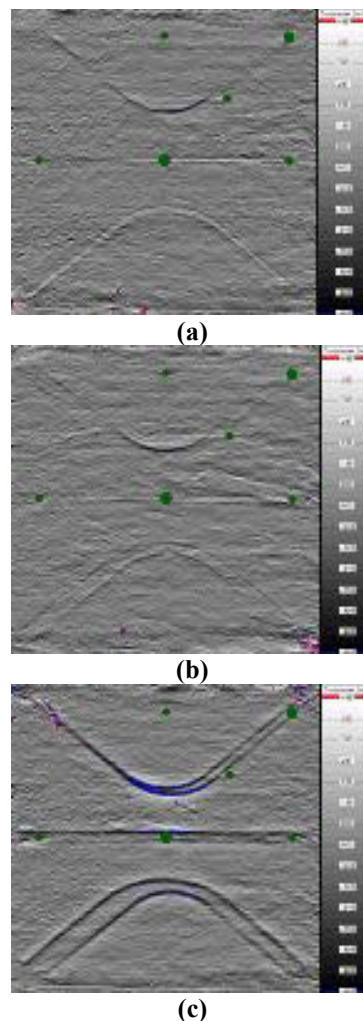
Figure 6. Curvature maps for raw assemblies bonded with epoxy and differing levels of flange coverage. The percent of the flange surface covered by adhesive: (a) 25–50%, (b) 75–100%, and (c) assured squeeze-out.

conclusively verify this, Figures 4(c) and 5(c) imply that the BLRT is particularly severe when the adhesive enters the radius of the flange. Combining the inferences from the assemblies made in the second trip that varied both the amount of adhesive dispensed and the bond gap with inferences that can be drawn from these assemblies, it appears that the BLRT visible in these assemblies' results from the presence of adhesive in the flange radius rather than the volume of adhesive dispensed. In addition, while the type of adhesive appears to have an effect on

BLRT severity, BLRT severity appears to be much more sensitive to the presence of adhesive in the radius of the bond flange than to the type of adhesive.

All of the inferences from the third experiment must be drawn from the data collected on the raw (i.e., as-bonded) assemblies. This is because the paint application process used to apply paint to these assemblies resulted in a very high level of orange peel in the paint. Consequently, the BLRT severity data from these assemblies was confounded by the variation in curvature caused by orange peel. The curvature due to orange peel could not be filtered out of the data without also filtering out too much of the curvature caused by BLRT. As a result, no meaningful data could be captured from these panels after painting.

The second experiment completed during the third trip to Meridian-Shelbyville was a screening experiment designed to investigate the relationship between the degree of softening of the outer panel during the painting process, the degree of cure of the adhesive, and the paint oven temperature. The factors and factor levels for this experiment are summarized in Table 5.

Table 5. Factors and factor levels for the substrate softening vs. paint temperature experiment

Factor	Factor Levels
Substrate Softening during Painting	SMC, GTX973[a]
Adhesive Degree of Cure	Uncured Partially Cured Fully Cured
Paint Oven Temperature	Simulated E-coat (365°F for 30 min) Low Bake (250°F for 25 min)

[a]GTX973 is an e-coat capable thermoplastic available from SABIC Innovative Plastics. This material is designed for electrostatic, on-line painting in automotive body shops.

GTX973 panels were molded at Husky in Novi, MI using the ACC injection molding tool. That tool is the same size as the compression molding tool. Unfortunately, the injection molding machine used to mold these panels did not have sufficient clamp tonnage to completely pack out the tool with this material and very few good quality panels were manufactured. In addition, the assemblies built by bonding a GTX973 outer panel to an SMC inner panel warped significantly. The high warpage made these assemblies unusable. Consequently, this experiment did not provide the team with the desired data.

Two additional trips to Meridian-Shelbyville in FY 2009 are planned at this time. The fourth trip will complete a screening experiment to investigate many of the factors evaluated in during the first experiment, but this time using mastic (a.k.a. anti-flutter) rather than adhesive. The primary experiment during the fifth trip will determine whether the density of the SMC inner and outer panels impacts BLRT severity. That experiment will also vary the inner panel thickness to determine how that factor affects BLRT severity.

Carbon-Fiber SMC

The objectives of this program are to develop high performance, cost-effective, carbon-fiber SMC materials and associated processing techniques for high-volume automotive components. The technical emphasis is to optimize properties, improve consistency of the properties, and to optimize the manufacturability of the compound. The project assumptions are that the material could be used for all current structural and Class-A SMC applications; that the current SMC compounding, molding processes, and equipment can be utilized; and that the thickness of the new materials will be in the range of 1.0 to 3.0 mm. In addition to the technical issues and constraints, business challenges have been addressed by working with CSP to leverage their production knowledge of what it takes to develop a marketable system. Zoltek (a low-cost carbon-fiber manufacturer) has agreed to work with CSP supplying appropriate carbon fibers and developmental sizing systems suitable for automotive resin systems.

The CSP SMC compounder was upgraded to provide carbon-fiber compounding capability. Early carbon-fiber chopping issues were resolved

and the fiber chopping system now performs flawlessly.

Initial compounding trials have consistently shown marginal wet-out of the 50K carbon fiber bundles. Future compounding trials will develop methods to open up the carbon-fiber bundles and resin system changes. Additionally, compounding with much smaller carbon-fiber bundles will be done, leveraging work done on an earlier P4 process. Similar fiber bundle wet-out improvements are expected, which should result in significantly improved material properties.

Conclusions

ACC115 explores different approaches to the high-volume processing of composites. Two programs are in progress, each with the objective of researching ways to save weight in automobiles, at the volumes appropriate to the industry. BLRT continued with studies of plaques molded with specific variations the impact of various factors on the severity of the resultant surface distortions. Carbon fiber SMC research is progressing well against constraints of cost and supply. Acquisition of new equipment specifically owned by ACC will speed research by eliminating time needed to move tools between suppliers, and will also provide the benefit of reducing variation in the test results.

F.   Natural Fiber Composite Retting, Preform, Manufacture, and Molding

Principal Investigator: James Holbery
Pacific Northwest National Laboratory
P.O. Box 999, Richland, WA 99354
(509) 375-3686; fax: (509) 375-2379; e-mail: james.holbery@pnl.gov

Principal Investigator: Dan Howe
Pacific Northwest National Laboratory
P.O. Box 999, Richland, WA 99354
(509) 376-2923; e-mail: daniel.howe@pnl.gov

Principal Investigator: Kevin Simmons
Pacific Northwest National Laboratory
P.O. Box 999, Richland, WA 99354
(509) 375-3651; e-mail: kevin.simmons@pnl.gov

Principal Investigator: Leo Fifield
Pacific Northwest National Laboratory
P.O. Box 999, Richland, WA 99354
(509) 375-6424; e-mail: leonard.fifield@pnl.gov

Technology Area Development Manager: Joseph A. Carpenter
(202) 586-1022; fax: (202) 586-1600; e-mail: joseph.carpenter@ee.doe.gov

Field Technical Monitor: Mark T. Smith
(509) 375-4478; fax: (509) 375-4448; e-mail: mark.smith@pnl.gov

---

Objective

- To develop, build, and demonstrate an economical, lab-scale, automated fiber retting process and apparatus suitable to bast-based fibers, including hemp, kenaf, and flax.

- To develop and demonstrate a thermoset polymer preform compression molding process and produce panels to develop a mechanical and thermal natural fiber polymer composite database.

Approach

- Explore existing and new fiber preparation approaches, including decortication techniques, high-speed fiber separation, steam explosion, chemical treatment, and modified extrusion methods.

- Develop the fundamental understanding of bast fiber structure that will provide direction for fiber separation.

- Conduct several lab-scale process trials of fiber preparation-retting processes enabling the development of the most appropriate process and instrumentation.

- Develop and construct a non-aqueous natural fiber preforming process capable of integrating surface modification and hybrid fiber and preform geometries.

- Explore alternative material forms, including sheet-molding compounds from natural fiber and hybrid reinforcements.

- Conduct full mechanical, thermal, and environmental characterization of manufactured panels.

Accomplishments

- Completed fiber analysis lab apparatus, developed fiber analysis procedure, and conducted fiber analysis on major natural fiber varieties.

- Procured several pieces of hardware assembled into the mechanical fiber preparation line, including fiber cutting apparatus, extruder modification, decorticator, and Wiler Mill.

- Completed supercritical fluid delignification study.

- Conducted fundamental research on ionic liquid delignification of natural fibers.

- Explored several natural fiber non-aqueous preform manufacture strategies and are currently exploring two further with mock-up, with construction of a prototype line in fiscal year (FY) 2009.

- Completed panel tool (approved by the Automotive Composites Consortium [ACC] and built by PNNL) and have produced sheet molding compound (SMC) panels from the tool.

- Established relationships with U.S. kenaf farm, Kengro Inc.; planted, harvested, and delivered 2 tons of kenaf.

- Developed relationships with resin suppliers (including AOC, Reichold, and Ashland Chemical) and processing companies (including Material Innovation Technology, TimTek, Inc., and Canadian hemp supplier, Stemergy).

Future Direction

- Integrate fiber decortication, separation, and preparation-retting techniques into a lab-scale fiber preparation unit.

- Deliver process and lab-scale unit to our customer in FY 2009.

- Determine the most economical approach to prepare fibers for surface modification.

- Explore non-aqueous natural fiber preforming processes capable of scaling to industrial volumes.

- Determine the most appropriate method to integrate fiber surface modification technology into the preform manufacture process.

- Interface with resin suppliers concerning SMC formulations for producing panels.

- Develop natural fiber SMC and hybrid-fiber architectures; produce panels and characterize in mechanical, thermal, and environmental.

Introduction

The objective of this project is to develop critical capability in the area of natural fiber retting, preform manufacture, and composite manufacture to enable the large-scale insertion of natural fiber reinforcement into the automotive industry. The benefits of natural fiber reinforced composites are well known, including lightweight, energy savings, cost reduction, carbon capture, recycling, and the environmental benefits from using renewable resources. However, several technical milestones must be met before the full confidence of engineering, manufacturing, and commercial sectors will embrace natural fiber reinforcement as a viable replacement for glass fiber. In this effort, three critical barriers restricting natural fiber usage in automotive manufacture are addressed: (1) develop an inexpensive, rapid, environmentally friendly mechanical process to remove natural fibers from plant stalks; (2) develop a rapid cost-effective method to create natural fiber preforms suitable for infusion of a thermoset polymer matrix; and (3) develop a natural fiber polymer composite molding process adaptable to hybrid

fiber composites and ester, soy, and urethane resin.

Retting is a fiber preparation process that traditionally has involved separating fibers via moistening or soaking fibers in water and partially rotting the fiber binders. This process consists of up to four methods: dew retting, water retting, warm water retting combined with heat, and chemical retting involving alkali solutions. Preparation should ideally prepare a fiber to be surface modified to promote bonding and adhesion and provide both dimensional stability and thermo-plasticity. Surface modification of natural fibers can be employed to optimize properties of the fiber-matrix interface and integrated within the fiber preform manufacturing process to produce a preform that may be stored for long periods of time before composite manufacture without a loss of properties (or more importantly excessive moisture uptake) with compromised composite interfacial properties.

Fiber Preparation

PNNL received 1,000 lbs of contractually grown kenaf fiber from Kengro, Inc. (Charleston, MS) in the beginning of FY 2008. In addition, research concentrated on the following fibers: (1) fresh water retted kenaf (Bangladesh), (2) un-retted from Kafus, Inc. (Raymondville, TX), (3) industrial hemp from Stemergy (Ontario, Canada), and (4) chemically modified kenaf from Professor Brian Baldwin (Agriculture Department, Mississippi State University).

PNNL personnel researched and developed the following processes and apparatus in an effort to develop a novel, mechanical-based fiber preparation process.

Decortication

Decortication (removal of kenaf core) using parallel rollers on a simple screw apparatus [see Figure 1(a)] appears to be a robust means of removing bast core; the method was originally developed at Georgia Pacific but was sold to TimTek to use in making wood panel board. The process unit consists of two offset screws turning at the same rate with a conveyor belt between the screw units that moves material. The unit has the
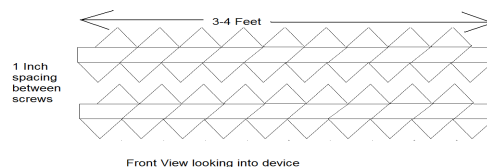
(a)

(b)

Figure 1. Decortication: (a) artist's rendering of apparatus and (b) decorticated kenaf fiber strands.

ability to vary the process speed up to >160 feet per minute of green material. Fibers are "dehusked" but need to be pulled off core by hand; PNNL has developed a design that eliminates this task.

The final decorticated fibers appear as fiber bundle "strands" as depicted in Figure 1(b).

Subsequently, PNNL procured a lab-scale roll laminator and has adapted it to perform the decortication process. The roll laminator and modification design are depicted in Figures 2 and 3. The decorticator rollers have been machined, and the unit is near operation.
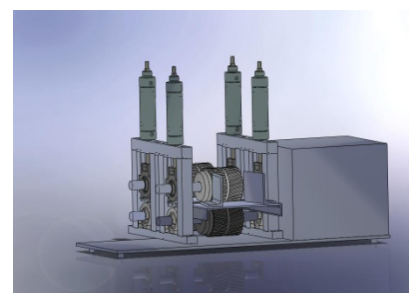

Figure 2. Solid model of decorticator.
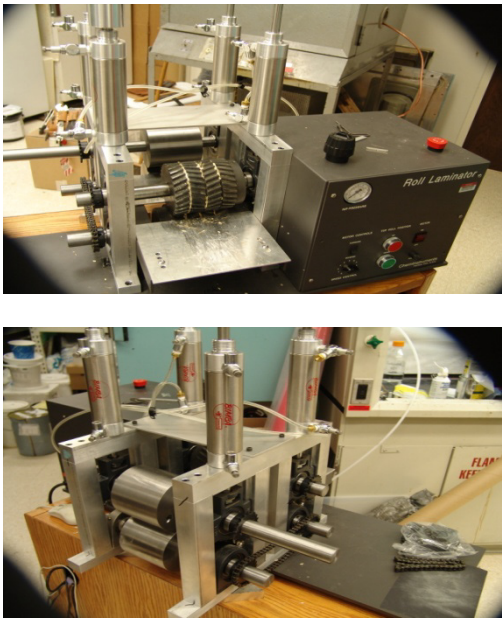
Figure 3. Front and rear views of the PNNL decorticator near completion.

To determine the pressure needed to decorticate the fibers, a set of experiments was designed and run to determine the compressive strength of the kenaf stalks as a function of the position along the stalk and its diameter (Figure 4). Moisture uptake experiments were also performed in order to evaluate maximum uptake of the whole stalk material and the effect moisture absorption has on the compressive strength of the material. This information is necessary to set the decorticator pressure applied to the material. It has been found that the kenaf stalk strength decreases as a logarithmic function the further from the butt end of the stalk the sample is cut, corresponding to decreasing lignin contents along the length of the stalk.
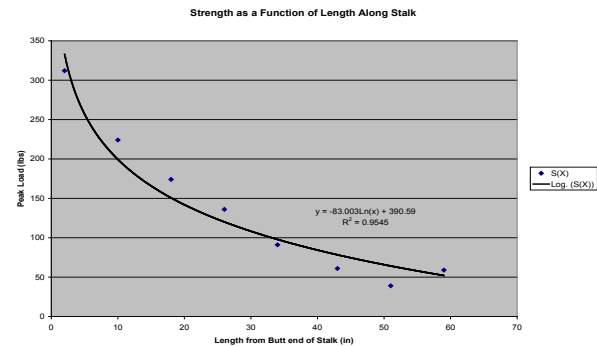
Figure 4. Fiber strength as a function of position along the fiber stalk.

The diameter of the stalk also plays a role in the force required to separate the core from the fiber sections. Up to a diameter of 0.7 in., the force required is near constant at ~115 lbs (Figure 5). At that point, however, the failure load begins to vary linearly.
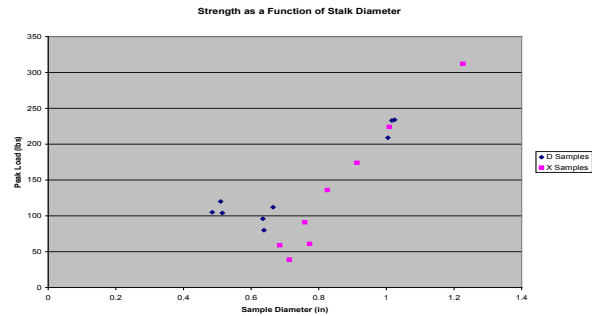
Figure 5. Strength as a function of stalk diameter.

Finally, it was demonstrated that whole stalk kenaf is capable of absorbing a large amount of water (up to 250% the weight of the sample; Figure 6). As water is absorbed, the strength of the material decreases; Figure 7 indicates the strength drops off due to soaking with an asymptote obtained at ~24 hours of soak time.
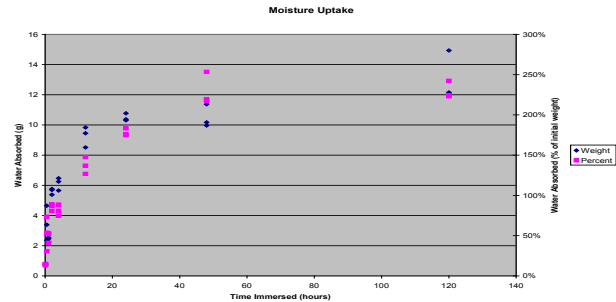
Figure 6. Moisture uptake in grams (g) (left y-axis) and % of original weight (right y-axis) with time.
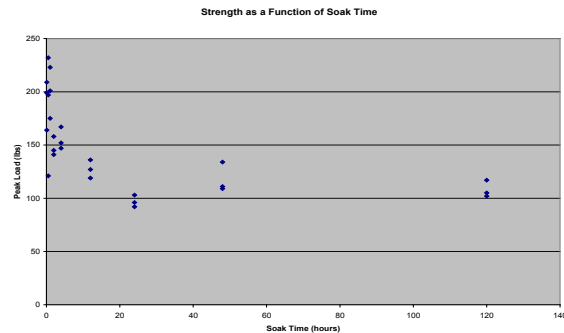
Figure 7. Strength of the stalk/core as a function of soak time.

Fiber Cut/Chop to Length

A pelletizer, which will be used to chop the fibers to the required length, was purchased from a used equipment vendor. Electrical work, including new switches and a face plate, was necessary to meet safety codes. The work was accomplished on July 31, 2008, and the unit has been tested. Fiber tests are planned in the immediate future, but preliminary tests show that the machine works well and produces material uniformly 1/8-2 in long (Figure 8).

Figure 8. Pelletizer used to chop fiber into specified lengths.

Ionic Liquid Delignification

A chemical process wherein diaza(1,3) bicyclo-undecane (DBU), sulfur dioxide gas, hexanol, and water are used to remove chemically the lignin present in lignocellulosic material has been tested and is shown to be effective. A salt that is liquid at room temperature, DBU is mixed with hexanol and then sparged at 0°C with sulfur dioxide (SO_2) gas (Figure 9). This liquid is then pumped under a vacuum to remove any non-chemically bound sulfur dioxide groups and added to a fiber or wood sample and water. It is stirred and heated to 90°C in a reaction chamber. The lignin is dissolved by a process where the sulfur groups chemically bound to the DBU form sulfurous acid, which hydrolyzes the lignin. These sulfurous acid groups then recombine with the water to reform the ionic liquid. The mixture is cooled down, and the pulp is washed with water, which removes all reactants from the delignified pulp (Table 1). Acetone washes may also be employed to remove residual hexanol. Due to low vapor pressure of the ionic liquid separation and consequent reuse of the reactants, creation of a completely closed loop system is possible. As a proof of concept, this method was used on the Pulp and Paper Research Institute of Canada (PAPRICAN) reference soft wood pulp.

Figure 9. DBU+1-hexanol with (from left to right): CO_2, COS, CS_2 and SO_2.

Table 1. Ionic liquid delignification. Numbers are reported as percentages on an oven-dry basis. Lignin is quantified according to TAPPI–T222.

Type	Start Lignin	End Lignin	Delignification
PAPRICAN Pulp/ CS_2 IL	4.16%	1.52%	63.50%
	4.16%	2.76%	33.55%
	4.16%	2.83%	32.05%
PAPRICAN Pulp/ SO_2 IL	4.16%	1.52%	63.55%
	4.16%	1.40%	66.43%
	4.16%	3.23%	22.40%

Ethanolysis of Kenaf Lignin

Supercritical fluids, solvents controlled at temperatures and pressures above their critical point, can have liquid-like densities and solvation characteristics while exhibiting vapor-like diffusivities. Thus, reactants and solvents in the supercritical phase may effectively access a wide range of the micro and macro pores in a porous material to deposit chemical functionality or to extract material. In addition, the tuneability of supercritical solvent characteristics by temperature or pressure adjustment can enable ease of separation of dissolved species from reactant solutions. These promising functions of supercritical fluids have the potential to extract components (such as lignin from biomass) selectively to simplify clean up of lignin processing solutions and facilitate recycling of reaction solvents.

Motivated by the potential of supercritical fluids as processing solvents and the observation of selective lignin removal from woody biomass using supercritical alcohols by Shiro Saka's group at Kyoto University, ethanol as a supercritical reactant/solvent for lignin removal from kenaf fibers is being pursued.

Batch-type reactions of 1.5 in. long decorticated kenaf bast fibers with pure ethyl alcohol (ethanol) were carried out using a Parr-heated, high-pressure reaction system (Figure 10). Two grams of cut fiber and 50 mm of ethanol were added to the Hastelloy-C reaction vessel before it was sealed and inserted into a heating mantle. A thermocouple is connected to the vessel, where the temperature is maintained to a programmed set point using an attached controller. The reaction mixture was held at various temperatures from 20–300°C for two hours from the point at which the heated vessel reached 95% of the desired reaction temperature. After the set reaction time, the heated vessel was removed from the heating mantle and allowed to cool to 50°C. After cooling, the reaction solution was recovered from the fibers by filtering through a glass pre-filter and retained. The recovered fiber was rinsed with fresh ethanol and set aside to air dry. Recovered reaction solutions were analyzed to determine components being removed from the kenaf fibers at various reaction temperatures. Mass of recovered fiber was recorded to determine mass loss due to the reactions. Larger batch reactions of 12 g of fiber in 50 ml ethanol were carried out with two reaction temperatures to produce samples of adequate mass for the soxhlet-based total fiber analysis.

Figure 10. Parr high-pressure reaction system (left) and 1.5-in. decorticated kenaf fibers.

In Figures 11–12, the effect of treatment of the kenaf fibers in ethanol is visibly apparent. The fiber reacted with ethanol at 300°C was completely degraded into a dark powder.

Lignin is unique among the majority constituents of kenaf fiber (lignin, hemicellulose, and cellulose) in that its monomers contain aromatic functional groups. This feature provides a unique

Figure 11. Darkening of the fibers due to treatment.
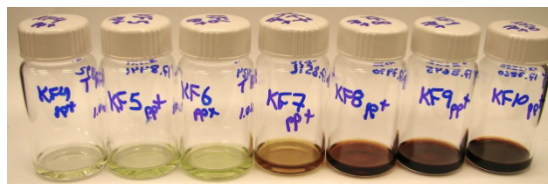
Figure 12. The portions of the recovered reaction solvents indicate a darkening of the solution beginning at 150°C increasing above 200°C.

signature for lignin that enables its spectroscopic detection and quantification in component mixtures. In the spectrophotmetric traces of recovered reaction solutions (Table 2), the characteristic lignin absorbtion at 280 nm is seen to increase with increasing reaction temperature. This trend continues up to 200°C, temperatures above which the lignin degrades during reaction. At 300°C, the characteristic lignin peak is no longer visible in the ultra-violet to visible spectrum.

**Table 2.** Change in initial fiber mass with reaction temperature.

20°C	50°C	100°C	150°C	200°C	250°C	300°C
0.6%	1.6%	4.2%	12.4%	29.4%	51.2%	82.0%

Some proton nuclear magnetic resonance (NMR) spectra of reaction solutions from selected process temperatures are portrayed. The axis displays 0–9 ppm chemical shift, with chloroform NMR solvent peak visible at 7.2 ppm. Note the absence of aromatic content from 6-7 ppm corresponding to extracted lignin in the lower temperature reactions. Increasing levels of lignin, hemicellulose, and cellulose decomposition products are visible above 200°C (Figures 13–14).
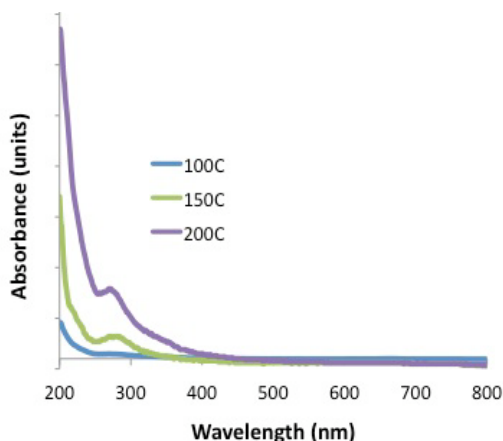
Figure 13. An increase in lignin absorption at 280 nm with increasing temperature.
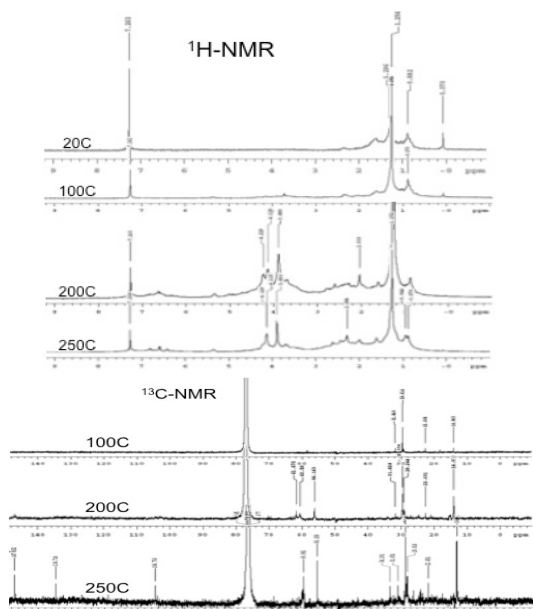
**Figure 14.** Carbon 13 NMR spectra of reaction solutions displayed with axis 0–150 ppm chemical shift.

High performance liquid chromatography (HPLC) was used to identify some of the components in the kenaf/ethanol reaction solution in addition to lignin. A few major observed species are displayed in Figure 15. Compounds identified in the effluent trace as glucose and fructose are the largest fractions observed at lower reaction temperatures. As glucose in alpha-cellulose is strongly bound, it is not expected that this observed sugar comes from that fraction of kenaf structure. Xylitol and arabanose (not shown) are detected in solutions reacted above 150°C. These
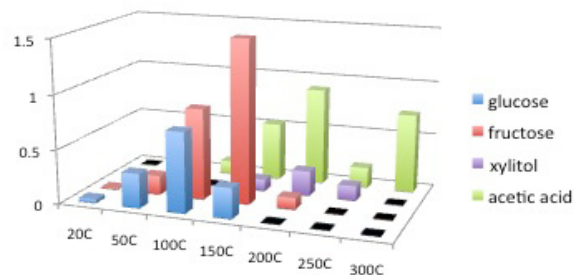
Figure 15. Kenaf/ethanol species from the effluent trace as a function of temperature.

compounds are indicative of hemicellulose breakdown. The small molecule degradation products are observed (not shown) in solutions reacted above 200°C and constitute in entirety of the mixture at 300°C.

If mass loss with temperature of reaction is plotted with lignin observed in the recovered and xylitol content in the reaction solution (Figure 16), information may be obtained regarding temperatures at which reaction under conditions used results in lignin (and hemicellulose) removal with minimum destruction of cellulose.
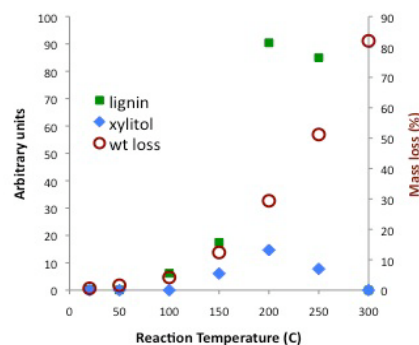
Figure 16. Mass loss at different reaction temps.

It is apparent from the characterization techniques used that the kenaf fiber undergoes signficant structural degradation at temperatures above 150–200°C under the reaction conditions used. Significant lignin removal is observed at reaction temperatures exceeding 100°C. Therefore, larger batches (>10g) of fiber were processed at 100 and 150°C for total fiber analysis to determine the effect on lignin, cellulose, and other fiber contents using the soxhlet method. The reaction time used in these experiments (2 hours) is long relative to 30 minute reaction time used by the Saka group.

At 270°C, that group observed the cellulose content in their beechwood sample a decrease of <10%, while lignin in their sample decreased to <20% of its original value. A 30% total mass loss was observed (Yamazaki M and S *J Wood Sci* 2006 [52]:527-532). At 350°C, they observed almost total loss of their beech wood after 30 minutes. No mention is made by those authors that their work is performed anaerobically. In addition to ethanol, there is air present at the sealing of the reaction vessel and adventitious moisture present on the fiber. It is perhaps a combination of oxidants included in the system and longer reaction times that lead to degradation of the samples at lower temperatures.

The supercritical temperature of ethanol is ~240°C. Therefore, ethanol in reaction systems is subcritical at temperatures below which significant structural degradation of the fibers is observed. If the presence of a supercritical fluid is desired in the current work at temperatures below those that give fiber degradation (<200°C), then one option is to use a cosolvent mixture of ethanol and carbon dioxide instead of ethanol alone. The supercritical temperature of carbon dioxide is less than 40°C, and ethanol is commonly added to supercritical carbon dioxide to improve its solvating characteristics for polar compounds (and the two are significantly soluble in one another). Combinations of the two would be expected to have intermediate supercritical temperature relative to the pure fluids. In the case of delignification of kenaf fiber, carbon dioxide may provide the attractive pore penetration, while the ethanol provides the reactant for ligning depolymerization and enable solubility of the lignin fragments in the reaction solution.

Additional options to achieve a supercritical reaction solvent without fiber destruction in the current system include shorter reaction times (<30 min) at high temperature (~250°C). In a continuous process, the residence time in the hot part of the reactor may be controlled short enough to prevent thermal degradation, though it is difficult in a batch pot reactor process. Another option may be to try to perform the reaction in a more anaerobic environment by flushing the fiber and ethanol with nitrogen before heating. It would be expensive and impractical to remove

completely all the water from the fiber before the reaction for high volume processing of fibers.

Use of ethanol at an elevated temperature may remain an effective way to remove lignin from kenaf fiber while leaving cellulose chains intact. Reaction temperature between 100–200°C may be optimum for achieving this goal. Small amounts of additives can make these reactions more effective for lignin and other desirable components for removal. These additives may increase the effectiveness of ethanol alone in achieving the goal of a simple method for cellulose fiber preparation from kenaf bast fiber.

High-Energy Delignification

Numerous forms of high-energy delignification have been examined, and the two most promising methods seem to be ultrasonics and tunable microwaves. Ultrasound possesses the ability to form both OH* and H* radicals, which are the main components of the various chemical delignification systems. In addition, the mechanical stresses imparted during cavitation can possibly serve to pull depolymerized lignin away from the bulk material, negating any rinsing steps. Any OH or H radicals not utilized in the reactions will recombine almost instantly into water, negating the use of expensive and capital intensive recycling and cleaning processes. PNNL has recently designed an ultrasonic system capable of processing volume elements, as opposed to the industry standard ultrasonic horns that operate only at the fluid/horn surface area interface. Meanwhile, microwaves allow a specific frequency of energy to be focused on a sample. Since maximum power transfer occurs when energy input equals the resonance frequency of specific bonds, tuning the microwaves to the frequency of the β-O-4 ether linkages holding lignin together is possible.

Extruder Delignification

The use of an extruder to mimic steam explosion processes has been examined, but the currently available nozzles are incorrect geometry. A device has been designed (Figure 17) that will attach to the current extruder that consists of a collection chamber and a Venturi nozzle to screw together and allow for introduction of high pressure steam
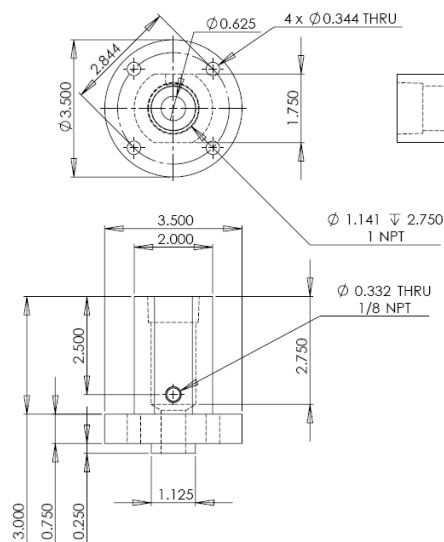
Figure 17. Newly designed device allowing for high pressure steam introduction.

once the fiber slurry has left the extruder. The Venturi nozzle will allow for a pulsing effect without the need for release valves. PNNL is currently exploring this process, which will continue into FY 2009 (Figure 18).

Figure 18. Current extruder apparatus with adapted tip. This work continues into FY 2009; results will be reported upon determination of the process viability.

Bast Fiber Structural Characterization

The structure of several bast fibers has been explored to determine the composition. This is important because process changes affect fiber structure and the separation of fiber from core fiber-fiber interaction, enabling fiber separation for follow-on steps (i.e., preform manufacture). To analyze these fibers, PNNL constructed a fiber structural analysis laboratory that will enable the

structural analysis of *any* natural fiber. This consists of a six soxhlet extractor columns combined with a Rotovap to remove solvent. PNNL designed and built the table, had the glassware produced and assembled, and purchased columns for HPLC analysis of the organics. This is a beneficial addition to PNNL capabilities; coordinated tests are being conducted with the University of Idaho to verify process set-up and calibration (Figure 19).

Figure 19. PNNL fiber analysis lab apparatus.

Additionally, in support of this effort PNNL procured a used Wiley mill and adapted it to be used to produce small fiber fragments suitable for analysis (Figure 20). With a 7.5 in. cutting chamber, this 2 hp mill is used for grinding fiber samples to the specified size before analysis. The unit was successfully modified to meet safety regulations. Dust created when samples are ground was also a cause for concern. In order to minimize this hazard, a containment box was designed and built with a snorkel hood attached to a filter to provide negative pressure during operation to minimize the possibility of inhaling fiber dust. The polycarbonate enclosure will serve as both a blast shield in case of catastrophic failure of the unit and a fire containment device in the unlikely event of ground fiber ignition.

The characterization of kenaf acquired from KenGro in Mississippi has been completed. Previous experiments with KenGro material mechanically decorticated showed mass balances of ~65%. However, manual decortication of kenaf from the same planting gave much better balances. KenGro material that had been dew retted and mechanically separated also showed a mass balance above 90%. Average characterization results of several fiber test batches are given in Table 3.

Figure 20. Wiley mill with polycarbonate containment enclosure.

Table 3. Chemical characterization of natural fibers and reference pulp. All numbers reported as percentages of total mass on an oven-dry basis.

Fiber	Ash	Extrac-tives	Klason Lignin	Acid Soluble Lignin	Cellu-lose	Hemi-cellulose
Hemp	2.42	0.59	8.12	N/A	71.43	8.43
Bangladesh	1.24	0	12.39	N/A	63.11	19.96
Mechanically separated dew retted Kengro kenaf	1.39	0.15	7.75	5.19	63.65	21.01
Hand separated non-retted Kengro kenaf	4.11	1.39	12.10	5.19	45.98	18.63
Texas Kenaf	4.35	0.27	8.36	N/A	57.28	25.35
PAPRICAN (standard)	0.5	0.26	4.16	0	83.04	9.99

Preform Processing

The goal of this task is to develop a preforming process to produce natural fiber reinforced preforms of a variety of geometries without an aqueous solution. This task is underway and will continue throughout FY 2009. At this time, two concepts are being explored, though others are under consideration.

The first process that has been conceptualized and mocked-up involves infrared heaters that set the kenaf to a sheet form via a micro-scale thermoset resin particulate which is subsequently stamped into the desired shape.

The first set of kenaf fiber preforms were produced and are shown in Figure 21.

Figure 21. Preform hat section and curved pieces.

Another approach under consideration is one that will utilize a fluidized bed to produce a series of layers of natural fiber on a conveyer, transported to the preform stamp station with the fibers bound by a surface modifier. This concept is still under development and will be further refined in FY 2009.

Composite Manufacture and Characterization

The compression molding tool was built and is fully operational (Figure 22). Trial panels produced from SMCs that have been made on this tool from glass and kenaf fibers are shown in Figure 23. In the near future, sandwiched kenaf and glass sheets will be molded. These will be characterized by measuring moisture uptake and mechanical properties, comparing straight glass and kenaf SMC.

Figure 22. PNNL SMC plaque tool (in press), producing kenaf-reinforced panel.
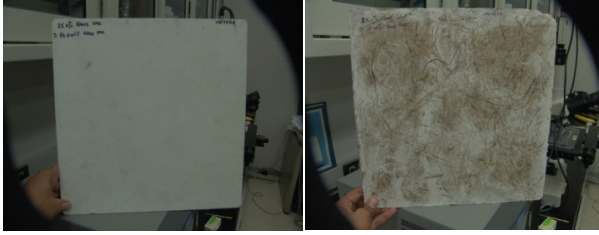
Figure 23. On the left, a 25 vol % SMC of glass fibers; on the right is a 25 vol % SMC panel of kenaf fibers. As fibers are produced from the processes developed, full characterization will take place using PNNL personnel and outside vendors, as necessary. The focus will be on mechanical, thermal and environmental properties.

Conclusions

Begun on July 1, 2007, this effort has focused on the fiber preparation-mechanical retting process for industrial scale. A prototype line is near completion. The fiber preform line has been conceptualized and a mock-up has been assembled. A tool has been completed to produce SMC panels, and good progress has been made toward the fiber preparation steps necessary to produce quality repeatable natural fiber reinforced composite panels. Thus far, the focus has been on kenaf fiber; in FY 2009, hemp fiber will be incorporated into the testing and analysis. Fiber structural analysis capability is fully operational, and this will aid in process development. Fibers this year were grown by contract at the USDA WSU Prosser Irrigated Agriculture Research and Extension Center.

G. Natural Fiber Composites for Structural Component Design

Principal Investigator: Sheldon Q. Shi
Assistant Professor
Forest Products Department
Mississippi State University
Franklin Center, Rm. 222
100 Blackjack Road, Starkville, MS 39759
(662) 325-3110; fax: (662) 325-8126; e-mail: sshi@cfr.msstate.edu

Co-Principal Investigator: Jilei Zhang
Associate Professor
Forest Products Department
Mississippi State University
Franklin Center, Rm. 113
100 Blackjack Road, Starkville, MS 39759
(662) 325-9413; fax: (662) 325-8126; e-mail: jzhang@cfr.msstate.edu

Co-Principal Investigator: Yibin Anna Xue
Assistant Professor
Mechanical and Aerospace Engineering,
Utah State University
4130 Old Main Hill, Logan, UT 84322
(435) 797-2867; http://www.mae.usu.edu/personnel/faculty.php

Co-Principal Investigator: L. Catherine Brinson
Department of Materials Science and Engineering
Northwestern University
2220 Campus Drive, Evanston, IL 60208-3108
(847) 491-3537; fax: (847) 491-7820; e-mail: cbrinson@northwestern.edu

Technology Development Manager: Joseph Carpenter
(202) 586-1022; fax: (202) 586-6109; e-mail: joseph.carpenter@ee.doe.gov

Objective

- Obtain material data on biomaterials (e.g., kenaf) by investigating microstructural characteristics, establishing fabrication methods (i.e., retting and formatting), and quantifying mechanical properties for use in automotive structural design.

Approach

- For automotive exterior applications, natural fiber-reinforced polymer-based composites are investigated in the following primary steps: (1) develop natural fiber retting technology and recommend solutions aiming at cost reductions of fiber retting processes, (2) use nanotechnology to enhance composite mechanical properties by improving the interfacial bond strength, (3) evaluate natural fiber composite processing techniques, and (4) develop micromechanical models for natural fiber composites.

Accomplishments

- Fiber retting/treatment—Developed a rapid chemical retting process with the aim of increasing the retting speed and reducing the cost; the inorganic nanoparticle impregnation process was optimized for the kenaf bast fiber obtained from the chemical retting process.

- Composite fabrication—Developed an innovative laminated sheet molding compound (LSMC) process with the aim of having a large natural fiber loading capacity and comparable properties to the commercial sheet molding compound (SMC) products with synthetic fibers.

- Fiber testing—Quantified the heat and time effects on the tensile properties of the kenaf bast fiber bundles.

- Micromechanical simulations—Applied a Drucker-Prager model to evaluate the effect of fiber waving and kinking on fiber properties; a three-dimensional Mori Tanaka model was applied for kenaf-epoxy composites with random fiber orientations and dispersed carbon nanotubes.

Future Direction

- Evaluate more environmentally friendly fiber retting options such as thermomechanical processes, bio-retting processes, and innovative fiber formatting methods.

- Continue to develop cost-effective bio-composite sheet molding process methods using different fiber/fiber bundle forms from different retting processes (such as chemically retted, mechanically retted methods).

- Conduct physical and mechanical tests on the fabricated composites, including bending, water absorption, impact resistance, etc.

- Obtain strength properties of single fibers and fiber bundles of kenaf bast fibers for composite modeling.

- Continue the effort of dispersing nanophase additives into the composites for property enhancement.

- Continue updating the present micromechanical models to better account for the physical factors, such as water absorption capacities and the spiraling angle of the fibers.

Chapter One: Chemical Retting, Inorganic Nanoparticle Impregnation, and Composite Fabrication

Sangyeob Lee, Sheldon Q. Shi, Jinshu Shi, H. Michael Barnes, and Mark F. Horstemeyer

Introduction

Kenaf bast fiber consists of cellulose, hemicellulose, lignin, and pectin, whose contents are 44–57%, 21%, 15–19%, and 2%, respectively [1]. However, the cellulose component of kenaf fibers contributes to the reinforcement in polymer-matrix composites [2, 3, 4, 5, 6, 7, 8, 9]. In general, lignin and pectin components hold the cellulose fibrils together so that fiber bundles are formed. To obtain fibers with high cellulose content, a chemical retting process can be used [10, 11, 12, 13, 14]. The removal of lignin and hemicellulose generates micropores in cell walls [15]. Inorganic nanoparticles can fill up the micropores and minimize the air in composites. The inorganic nanoparticles can also act as a modifier for the interfacial compatibility between natural fibers and polymer matrixes [16, 17]. The impregnation process is also an environmentally friendly and cost-effective process as it uses two ionic salts [18, 19].

The objectives of this study were: (1) to refine the rapid pressurized chemical process for the kenaf bast fiber retting, (2) to obtain an optimum inorganic nanoparticle impregnation condition for the kenaf bast fiber, and (3) to investigate a processing technique for the natural fiber—polymer composite fabrication.

Experimental

The flow charts of experimental steps are depicted below for retting, impregnation, and lamination processes (Figures 1–3).
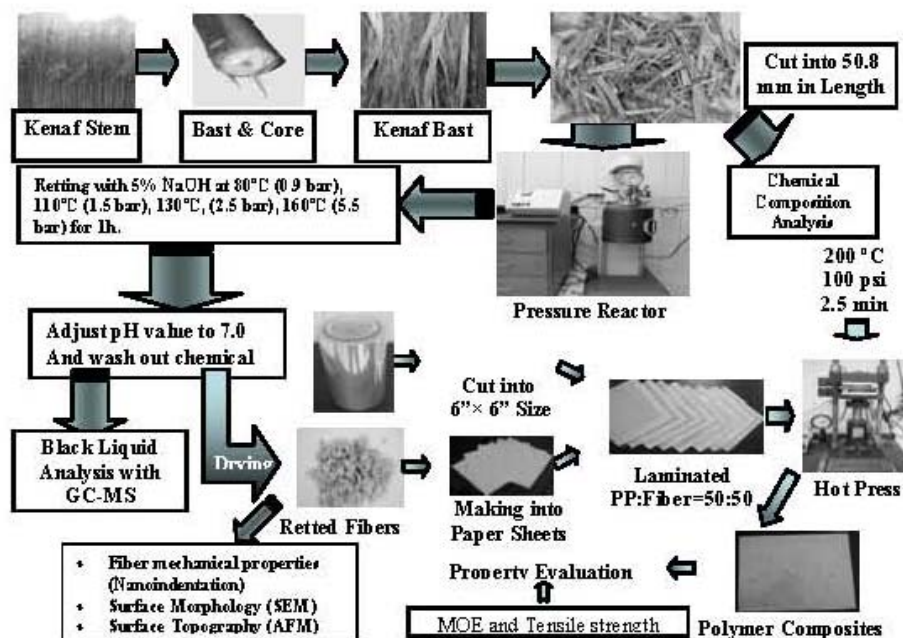
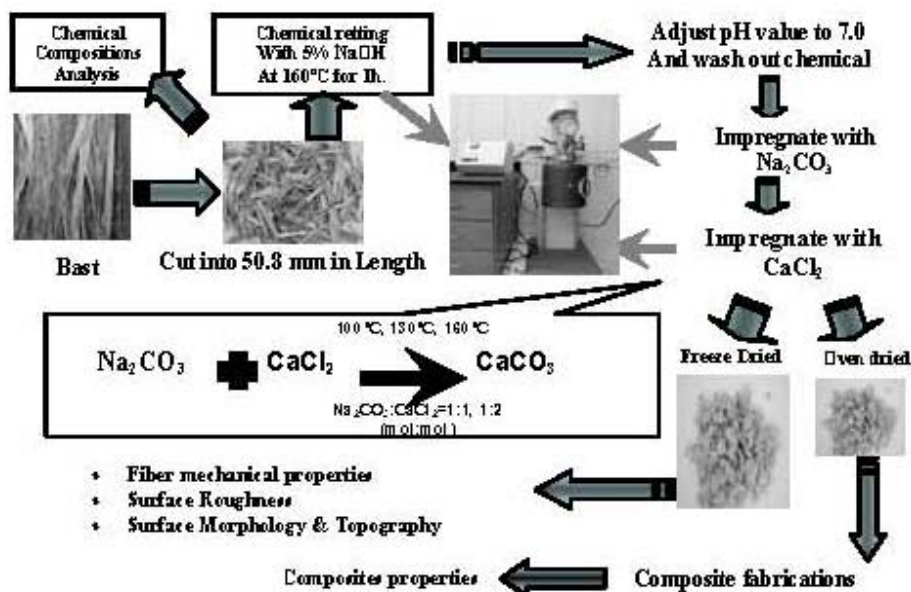**Figure 1.** Chemical retting and characterization.

Figure 2. Inorganic nanoparticle impregnation and characterization.
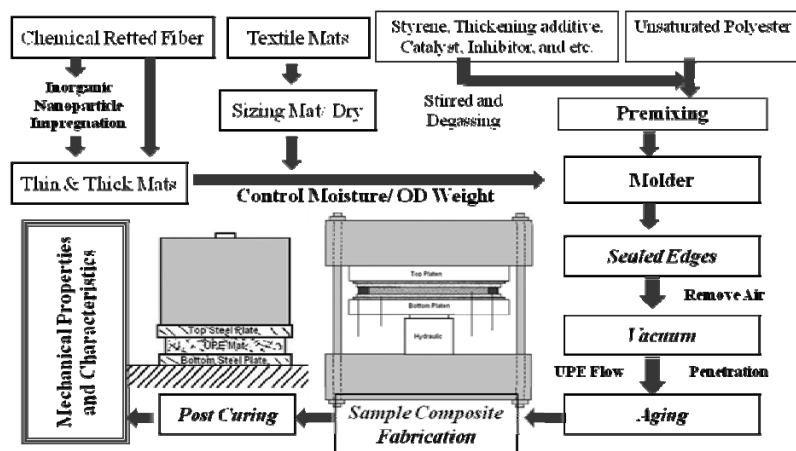
Figure 3. Lamination process for natural fiber-polyester composites.

Table 1 shows the chemical compositions, solvent extractives, and water solubility of the kenaf bast fibers. Figure 4 shows the fiber yields from retting at four different conditions. As shown in Figure 4, the fibers retted at 160ºC (0.55 MPa) gained 44.6% fiber yield, which was about equivalent to the α-cellulose content (45.95%) of kenaf bast fiber.

Table 1. Chemical compositions of kenaf bast fiber

Components	Content (%)
Moisture content	7.40
Ash	5.07
Klason Lignin	19.10
Holocellulose	75.83
α-cellulose	45.95
Extractives	
Hydrogen peroxide extractives	8.57
Methylenechloride extractives	0.99
Ethanol extractives	4.61
Hot water solubility	9.76
Cold water solubility	7.21

Py-GC/MS Analysis of the Black Liquid

Figure 5 shows the mass spectra (MS) from pyrolysis-gas chromatography/MS (Py-GC/MS) analysis on black liquid. The main peaks with a relative molar area greater than 1% were identified from the Py-GC/MS. The different levels of residue among the products suggested that the extraction of hemicellulose and lignin compounds was improved at higher retting temperatures and pressures. As shown in Figure 5, the majority of
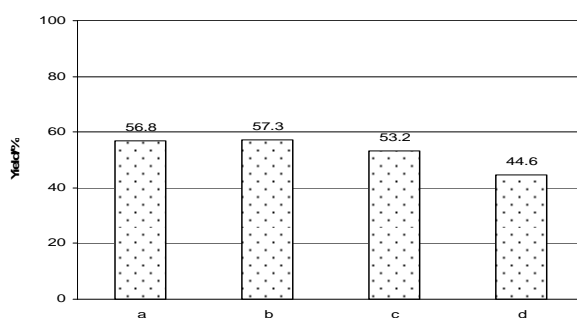
Figure 4. Fiber yield strength from the retting processes. a = 80ºC (0.09 MPa), b = 110ºC (0.15 MPa), c = 130ºC, (0.25 MPa), and d = 160ºC (0.55 MPa).
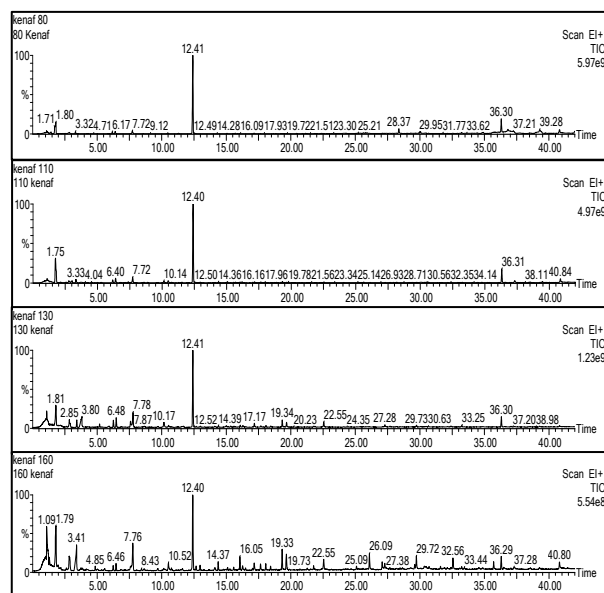
Figure 5. Retting rejects analysis using Py-GC/MS and identification of main peaks with relative molar area ≥1%.

the chemical compounds in the black liquid from chemical retting were lignin based.

Figure 6 shows the loading percentage of $CaCO_3$ in kenaf fibers. It indicates that the fibers impregnated at 130°C, with a molar ratio of 1:1 (Na_2CO_3 to $CaCl_2$), gave the highest $CaCO_3$ loading. However, a little increase of $CaCO_3$ nanoparticles in kenaf fibers could result in significant changes in fiber surface characteristics because of the large specific surface area of $CaCO_3$ nanoparticles. A small number of $CaCO_3$ nanoparticles can generate a large surface area, which may have a significant effect on composite properties.
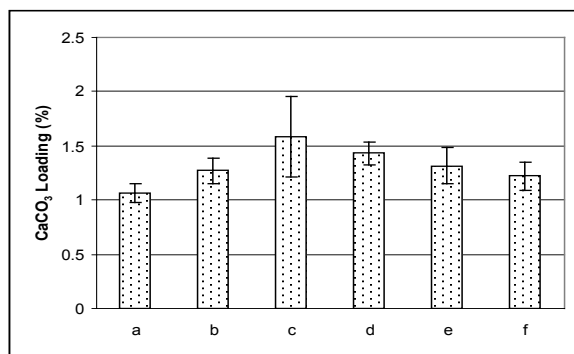
Figure 6. Percentage of $CaCO_3$ loading in the cell wall structure of weak chemical retted kenaf fiber. (a) = 100°C (0.15 MPa) at 1 : 1 ionic salt ratio, (b) = 100°C (0.15 MPa) at 1 : 2, (c) = 130°C (0.30 MPa) at 1 : 1, (d) = 130°C (0.30 MPa) at 1 : 2, (e) = 160°C (0.70 MPa) at 1 : 1, and (f) = 160°C (0.70 MPa) at 1 : 2.

Surface Characteristics

Figure 7 shows the microstructures of the retted and impregnated kenaf fibers examined with a scanning electron microscope. For the fibers generated at a retting temperature of 160°C, the micropores appeared in the fiber cell wall. As the retting temperature and pressure increased, more lignin and hemicelluloses were pyrolyzed and extracted from the fiber cell wall. More nanoparticles were shown on the fiber surface impregnated with the 1:2 molar ratio compared to that with the 1:1 ratio. Some particles generated at 160°C grew to a diameter of 100 to 500 nm (Figure 7[g] and [j]). The nanoparticles were found at the inner micropore structure in the kenaf fiber cell wall.
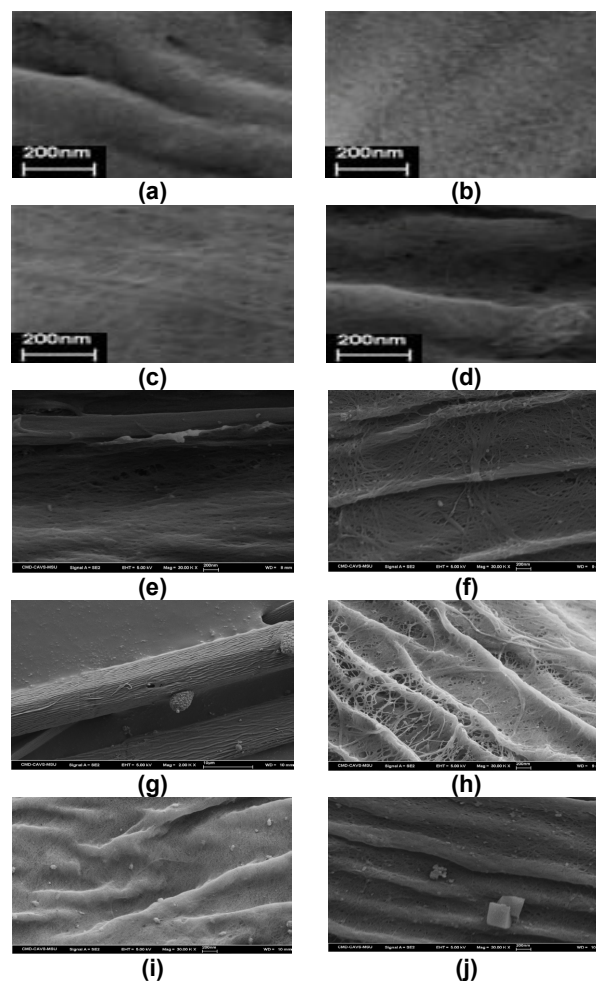
Figure 7. Surface morphology of kenaf fibers alkaline retted and impregnated with $CaCO_3$. (a) = 80°C, 0.09MPa; (b) = 110°C, 0.15MPa; (c) = 130°C, 0.25MPa; (d) = 160°C, 0.55MPa; (e) = 100°C (0.15 MPa) at 1 : 1 ionic salt ratio; (f) = 130°C (0.30 MPa) at 1 : 1; (g) = 160°C (0.70 MPa) at 1 : 1; (h) = 100°C (0.15 MPa) at 1 : 2; (i) = 130°C (0.30 MPa) at 1 : 2; and (j) = 160°C (0.70 MPa) at 1 : 2.

The porous structure at the inner cell wall held the inorganic nanoparticle crystals in position (Figure 8). Smaller nanoparticles (50 to 100 nm) were also formed on the surface of bigger inorganic particles. Root mean square (RMS) surface roughness of kenaf fibers retted with an alkaline solution and impregnated by the inorganic nanoparticles is shown in Table 2. The higher the retting temperatures, the lower the fiber surface roughness. The surface roughness of impregnated fibers increased due to the $CaCO_3$ particles deposited on the fiber surface.

(a)

(b)
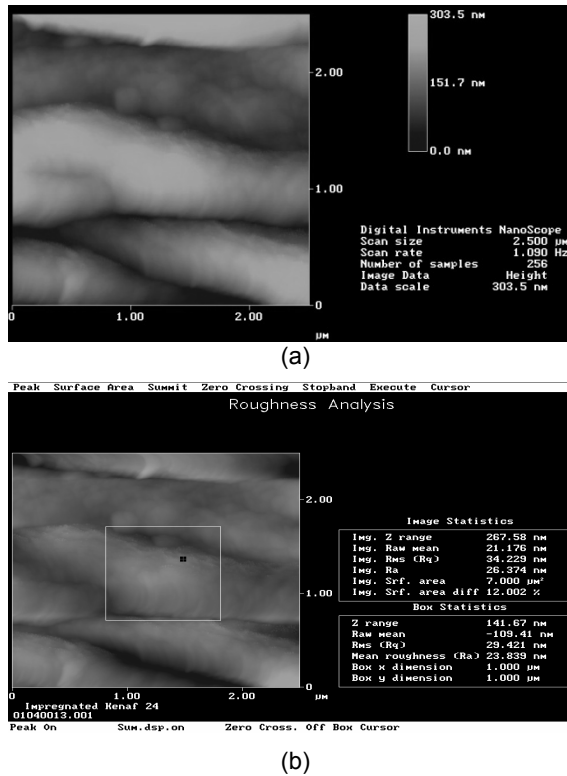
Figure 8. Surface roughness analysis of nanoparticle impregnated kenaf fibers (160°C, Na_2CO_3 : $CaCl_2$ = 1 : 1) using atomic force microscopy. (a) = 2.5 µm scan size and (b) = roughness analysis.

Table 2. RMS surface roughness of kenaf fibers retted with an alkaline solution and impregnated using two ionic salts.

Temp.	Pressure	Na_2CO_3 : $CaCl_2$ (mol : mol)	Scanning Size 2.5 µm	Scanning Size 1 µm
80°C		N/A	73.2	32.6
110°C	Retting fibers (5%NaOH)	N/A	71.1	22.3
130°C		N/A	43.7	25.4
160°C		N/A	31.3	11.2
100°C	0.15 MPa	1:1	39.5	21.9
		1:2	29.8	20.4
130°C	0.30 MPa	1:1	40.2	19.0
		1:2	48.8	30.5
160°C	0.70 MPa	1:1	24.9	20.8
		1:2	40.1	23.1

Nanoindentation on Fiber Surfaces

Figure 9 shows the surface hardness and modulus of retted kenaf fibers and inorganic nanoparticle impregnated kenaf fibers tested using the Hysitron NanoIndenter instrument. The reduced modulus and surface hardness of kenaf fibers retted at

(a)　　　　　　　　　　　(b)

(c)

(d)
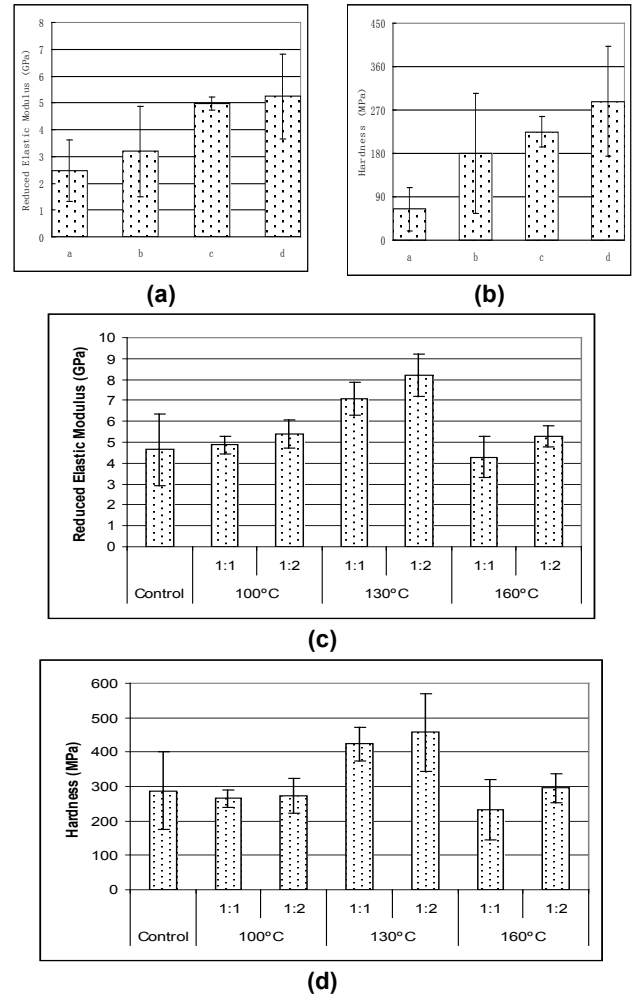
Figure 9. Surface hardness and elastic modulus of retted and nanoparticle impregnated kenaf fibers. The y-axes indicate (a) and (c) are elastic modulus and (b) and (d) are hardness; a = 80°C, 0.09 MPa; b = 110°C, 0.15 MPa; c = 130°C, 0.25 MPa; and d = 160°C, 0.55 MPa.

160°C were more than two times higher than those retted at 80°C. This may be due to a higher cellulose content obtained at the retting temperature of 160°C. Kenaf fibers impregnated with $CaCO_3$ at 130°C, with the two molar ratios of Na_2CO_3 to $CaCl_2$, yielded a 53–77% reduction in bending modulus and a 47–59% increase in hardness. From the surface image shown in Figure 7, lesser and smaller $CaCO_3$ nanoparticles were observed for the fibers impregnated at 100°C than those impregnated at 130°C, which reduced the elastic modulus.

Mechanical Properties of Composites

Figure 10 shows the bending modulus and tensile strength of the composites fabricated with retted and inorganic nanoparticle impregnated kenaf fibers. The tensile strength and bending modulus of composites were increased as the retting temperature and pressure increased. The composites reinforced with the kenaf fiber retted at 160ºC, 5.5 bar, resulted in a 33% increase in tensile strength and 16.7% in modulus of elasticity (MOE).

(a)   **(b)**

(c)

(d)
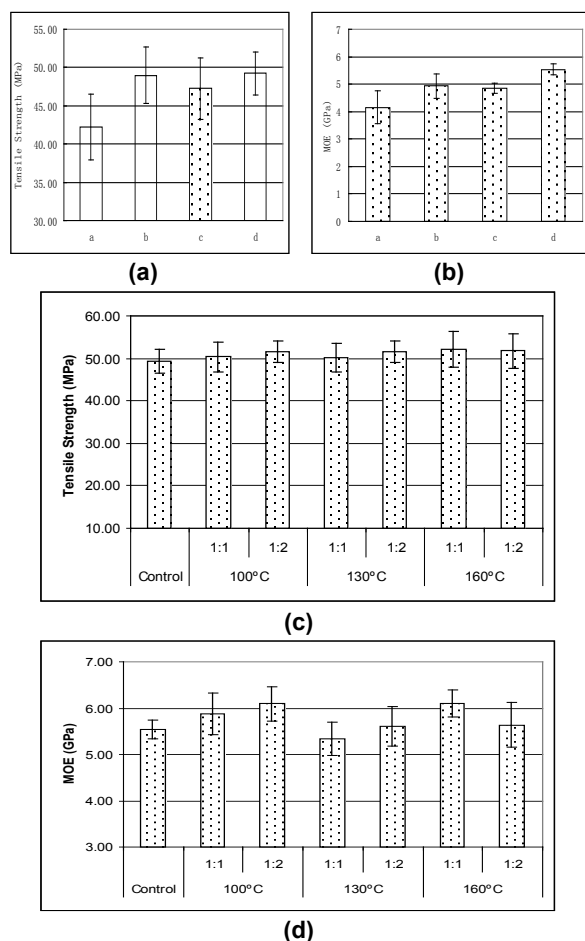
Figure 10. Mechanical properties of retted and impregnated kenaf fibers reinforced polypropylene composites. The y-axes indicate a and c are tensile strength and b and d are MOE ; a = 80ºC, 0.09 MPa; b = 110ºC, 0.15 MPa; c = 130ºC, 0.25 MPa; and d = 160ºC, 0.55 MPa.

The fibers with the highest surface hardness and modulus would not necessarily result in the highest elastic modulus [Figure 10(d)] for the composites because the contribution to the

composite properties is not only from the fiber strength, but also from other factors such as fiber-polymer interfacial compatibility, microfibril angle, etc. The inorganic nanoparticle impregnation treatment gave about 10% improvement on the MOE property (Figure 10 [d] for the treatment conditions of 100°C with $Na_2CO_3 : CaCl_2 = 1 : 2$ [mol : mol] and 160°C with $Na_2CO_3 : CaCl_2 = 1 : 1$ [mol : mol]). Inorganic nanoparticle impregnation may improve the interfacial compatibility between the fiber and matrix and thus improve the bending performance of the composites. However, the impregnation treatment does not show a significant improvement on the tensile strength of the composites (Figure 10 [c]). The contribution to the tensile strength of the composites from some enhancements at the fiber-polymer interface may not be too significant compared with other factors such as fiber orientation and fiber network in the polymer.

Preliminary tests were conducted on the composites fabricated from the developed LSMC process using the unsaturated polyester resin matrix and a series of natural fiber loading (15–60%). The initial bending modulus for the composites was obtained as over 8 GPa, which is very close to the commercial SMC composites with 25% synthetic fiber glass, 8.5–14.0 GPa for SMC R25 (European Alliance for SMC 2001).

Conclusions

Alkaline retting at high temperature and high pressure generated micropores in fiber cell walls. The surface roughness of retted fibers decreased as the retting temperature and pressure increased. The removal of lignin and hemicellulose resulted in an improvement of fiber surface hardness and modulus. The polypropylene composites reinforced with the kenaf bast fibers retted at 160°C showed the highest MOE and tensile strength among the retting conditions investigated. Among the impregnation conditions used in this study, the highest nanoparticle loading in the fiber cell wall was obtained at 130°C. The $CaCO_3$ loading increases the surface hardness and elastic modulus. Improvement on the MOE of composites was observed at a 1.32% nanoparticle loading. The composites reinforced with the kenaf bast fiber

impregnated with $CaCO_3$ at 100°C
($Na_2CO_3 : CaCl_2 = 1 : 2$) and 160°C
($Na_2CO_3 : CaCl_2 = 1 : 1$) show about 10%
improvement on MOE. The developed LSMC
process may be suitable for natural fiber
composite fabrication.

Presentations/Publications/Patents

1. S. Q. Shi, S. Lee, and J. Shi, "Lamination
   Process for Chemical Retted Kenaf
   Fiber/Thermoplastic Polymer Composites,"
   23rd Annual American Society for
   Composites Tech. Conf., September 9–11,
   2008, Memphis, Tennessee.

2. S. Lee et al., "Inorganic Nanoparticle
   Impregnated Kenaf Fibers as Reinforcement
   for Polypropylene Matrix Composites in the
   Automobile Application," Intern. Cong. Nano-
   Bio Clean Tech 2008, October 27–30, 2008,
   San Francisco, California.

3. B. G. Lee et al., "Influence of surface
   morphology of the kraft pulp fibers on the
   growth of the transcrystalline layer of
   polypropylene," *J. Appl. Polym. Sci.* (2008) In
   Press.

4. S. Lee et al., "Nanoparticle Impregnated
   Kenaf Fibers for the Reinforcement for
   Polymer Matrix Composites, 4th Intern. Conf.
   Adv. Engin. Wood Hybrid Composites, **Bar
   Harbor, Maine, July 6–10, 2008.**

5. S. Lee, S. Q. Shi, and J. Shi, "High Pressure
   Chemical Retting for Kenaf Bast Fiber, Forest
   Products Society, 62nd Intern. Conv.,
   St. Louis, Missouri, June 22–24, 2008.

6. J. Shi et al., Inorganic Nano-Particle
   Impregnation for Kenaf Bast Fiber, Forest
   Products Society, 62nd Intern. Conv.,
   St. Louis, Missouri. June 22–24, 2008.

7. S. Q. Shi and S. Lee, 2008, "Laminated sheet
   molding compounding (LSMC) process from
   accelerated weak chemically retted natural
   fibers" (patent disclosure).

References

1. L. Mwaikambo, *African J. Sci. Tech.,* Sci.
   Eng. Ser., **7**(2), pp. 120–133 (2006).

2. B. Aleksandra, et al., *J. Mater. Sci.* **42**,
   pp. 6501–6509 (2007).

3. T. Bullions et al., *Composites Sci. Tech.* **66**,
   pp. 102–114 (2006).

4. R. Anand et al., 6th Intern. Conf. Wood fiber
   and plastic composites (2001).

5. C. Clemons, and A. R. Sanadi, *J. Reinforced
   Plasti. Composites,* **26**(15), pp. 1587–1602
   (2007).

6. J. Park, et al., *Composite Interf.,* **13**(2–3),
   pp. 105–129 2006).

7. T. Nishino et al., *Composites Sci. Tech.,* **63**,
   pp. 1281–1286 (2003).

8. S. Shibata, Y. Cao, and I. Fukumoto, *Polymer
   Testing,* **25**, pp. 142–148 (2006)

9. S. Aziz et al., *Composites Sci. Tech.,* 65,
   pp. 525–535 (2005).

10. K. H. Song and S. K. Obendorf, *Textile Res.
    J.,* **76**(10), pp. 751–756 (2006).

11. S. Keshk, W. Suwinarti, and K. Sameshima,
    Carbohyd. Polym., **65**, pp. 202–206 (2006).

12. H. Lee, et al., *J. Korean Soc. Clothing
    Textiles,* **27**(9/10), pp. 1144–1152 (2003).

13. G. Ramaswamy, C. Ruff, and C. Boyd, *Texile
    Res. J.,* **64**(5), pp. 305–308 (1994).

14. J. Wang and G. Ramaswamy, *AATCC Review,*
    06, pp. 22–26 (2005).

15. A. P. Deshpande, M. B. Rao, and C. L. Rao, *J.
    Appl. Polym. Sci.,* **76**, pp. 93–92 (2000).

16. S. Lee, Ph.D. Dissertation, Louisiana State
    Univ., Baton Rouge, Louisiana, 2006.

17. S. Y. Lee et al., in T.F. Shupe (Ed.) (Forest
    Products Society, Madison, Wisconsin, 2006).

18. G. G. Allan, Y. C. Ko, and P. Ritzenthaler, *Tappi J.,* **74**(3), p. 205 (1991).

19. J. Kuusipalo, et al., *Tappi J.,* **4**(8), pp. 17–21 (2005).

Chapter Two: Temperature-Time Effects on Tensile Properties of Kenaf Bast Fiber Bundles

Yicheng Du, Jilei Zhang, and Yibin (Anna) Xue

Introduction

Typical processing temperatures for injection molding and compression molding for automotive part fabrication are 170ºC and 180ºC, respectively, with 1 hour duration, and the severe service conditions in automotive front-end structural application can be mimicked by conditioning the parts at 130ºC for 24 hours [1–2]. In addition to the process requirements, there are different testing procedures among automotive manufacturers for evaluating material strength performance under long-hour, high-temperature situations (Figure 11). This study was carried out to investigate temperature and time duration effects on the tensile properties of bacteria-retted kenaf bast fiber bundles (KBFBs) subjected to temperatures up to 190ºC, with different durations up to 9 hours.
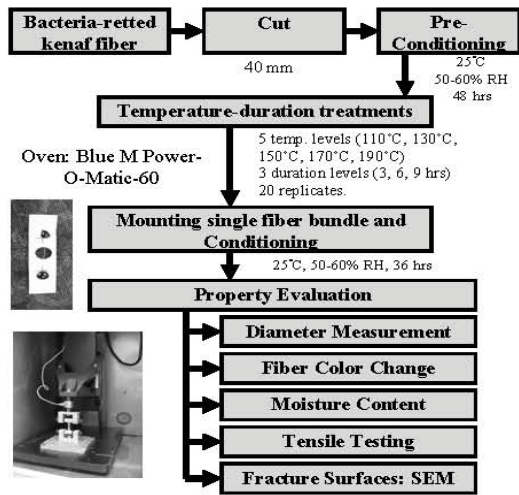
Figure 11. Experimental flow.

Experimental Procedure—Results and Discussion

Failure locations and modes

Under tensile loading, KBFBs had three main locations of failure: fiber breakage at the grips, fiber breakage in the middle of the specimen, and fiber explosion fracture (Figure 12). Table 3 summarizes the levels of KBFB failure for each of the three failure locations. The specimens of each combination had different average equilibrium moisture contents (MC), and in general, MC decreased as heat-treated temperature increased.
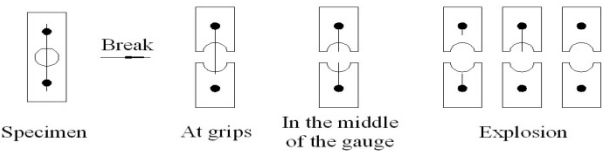

Figure 12. Failure modes of kenaf fiber bundles under tensile load.

Table 3. Failure locations and total number of kenaf fiber bundles tested in tension for each temperature-duration combination and moisture content (MC) of specimens after testing.

Temp. (°C)	Duration (hours)	Failure mode			Total	MC (%)
		Middle	Grip	Explosion		
	3	5	8	3	16	10.3
110	6	2	4	13	19	12.6
	9	6	10	3	19	10.3
	3	6	10	3	19	10.6
130	6	2	7	11	20	12.5
	9	8	4	7	19	9.9
	3	11	5	4	20	10.7
150	6	5	8	6	19	10.4
	9	2	10	7	19	9.2
	3	4	7	7	18	9.7
170	6	4	9	3	16	9.4
	9	1	6	3	10	9.5
	3	3	6	0	9	8.1
190	6	2	2	0	4	8.4
	9	2	2	0	4	8.8

Splintering mode was observed in specimens heated at 1,100°C, the combined splintering and brash modes were found in specimens heated at 150°C and 170°C, and brash mode occurred in specimens heated at 190°C (Figure 13). The failure modes were related to fiber color changes (from light blond to golden brown, then to brown). Changes indicated thermal degradation in chemical components (cellulose, hemicellulose, and lignin) of KBFBs.
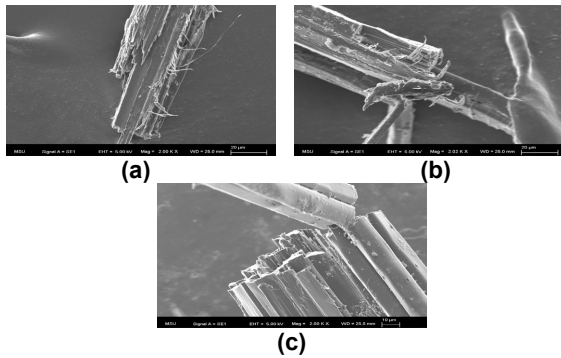
Figure 13. Scanning electron microscope micrographs of tensile fracture surfaces of KBFB specimens: (a) splintering tension, (b) combined splintering and brash tension, and (c) brash tension.

Data Analysis

Table 4 summarizes the mean values of the tensile modulus, tensile strength, and failure strain of tested specimens. A two-factor unbalanced analysis of variance general linear model procedure was performed for individual data, adjusted for the MC effect, to analyze the main effects and interaction factors on the mean values of the tensile modulus, tensile strength, and failure strain, respectively. The least square means a multiple comparison procedure was performed to determine the mean differences of the treatment combinations.

Table 4. Means of mechanical properties of tested kenaf fiber bundles for each combination of temperature and time. (COV=Coefficient of variance, N= Number of measurements)

Temp. °C	Duration Hour	Tensile Modulus			Tensile Strength			Failure Strain		
		Mean GPa	COV %	N.	Mean MPa	COV %	N.	Mean	COV %	N.
110	3	12.0	22	16	136.5	40	8	1.17	23	8
	6	15.3	23	19	214.0	34	15	1.39	34	15
	9	13.0	19	19	176.6	26	9	1.33	11	9
130	3	13.8	21	19	162.6	34	9	1.13	22	9
	6	14.2	18	20	173.2	29	13	1.20	20	13
	9	14.3	16	19	166.7	30	15	1.24	28	15
150	3	14.4	22	20	140.1	33	15	1.05	28	15
	6	13.4	14	19	152.7	26	11	1.13	14	11
	9	13.7	18	19	146.3	28	9	1.02	14	9
170	3	15.0	25	18	147.8	36	11	0.92	31	11
	6	15.3	17	16	133.1	33	7	0.83	20	7
	9	14.3	22	10	91.3	50	4	0.57	38	4
190	3	9.2	47	9	49.7	39	3	0.72	23	2
	6	8.0	42	4	72.8	16	2	0.81	38	2
	9	6.8	59	4	41.4	42	2	0.47		1

Temperature effects

When the temperature increased from 110°C to 170°C, no significant change was observed in the KBFB tensile modulus. However, significant drops in tensile modulus occurred when the temperature increased from 170°C to 190°C. The average drops in tensile modulus were about 39%, 47%, and 55% for duration times of 3, 6, and 9 hours.

For the 6- and 9-hour tests, the tensile strength declined as the temperature increased and different declining rates were observed as the temperature increased (Figure 14). For the 6-hour test, the tensile strength declined at an average rate of 1.19 MPa per degree Celsius from 110 to 170°C. The average declining rate reached 3.07 MPa per degree Celsius from 170°C to 190°C, with 44% drop in tensile strength. Tensile strength had a significant drop of 51% from 150°C to 190°C. The significant drop in tensile strength can be explained by the severe degradation of the three major components of the KBFBs, cellulose, hemicellulose, and lignin, especially cellulose at the high temperature, plus long duration. The temperature had a significant effect on the tensile failure strain of KBFBs (Figure 15). It was noticed that a significant decline in strain started at about 150°C. The strain continued to drop significantly from 150°C to 170°C, but no further decline was observed at 190°C.

Duration Effects

There were no significant changes in tensile modulus, strength, and failure strain for temperatures ranging from 130°C to 190°C for a 3- to 9-hour duration (Table 5). A significant effect of duration on tensile modulus and strength was observed at 110°C for 3–6 hours of thermal exposure. The tensile modulus had a significant 28% increase, followed by a significant 16% drop as the duration increased from 6 to 9 hours. In the case of temperature at 190°C, the tensile modulus decreased as the time increased, although the decrease was not significant.
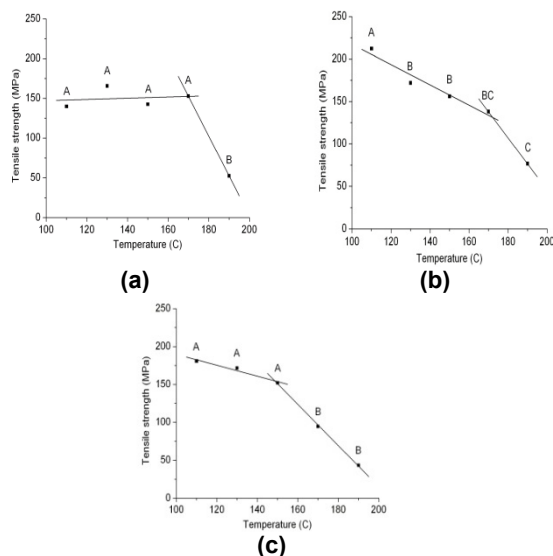
Figure 14. Mean comparisons for temperature effects on tensile strength for each duration of (a) 3, (b) 6, and (c) 9 hrs (values with the same capital letter are not statistically different at 0.10 confidence interval).
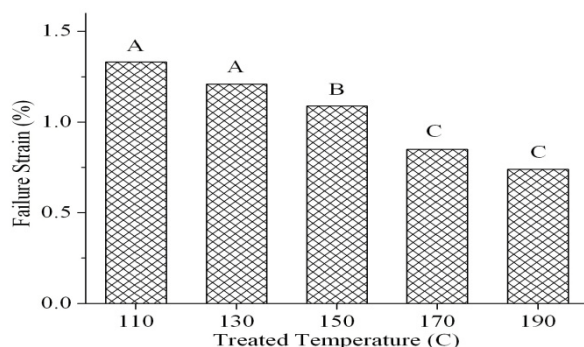
Figure 15. Effect of temperature on the ultimate strain of the kenaf fiber bundles (values with the same capital letter are not statistically different at the 10 percent significance level).

Table 5. Duration on tensile modulus and strength for each level of temperature.

Temperature	Duration (Hour)					
°C	3		6		9	
Tensile modulus (GPa)						
110	12.0	B	15.3	A	12.9	B
130	13.8	A	14.3	A	14.2	A
150	14.4	A	13.4	A	13.7	A
170	15.0	A	15.2	A	14.2	A
190	9.2	A	8.0	A	6.7	A
Tensile strength (MPa)						
110	139.9	B	212.3	A	181.0	A
130	165.7	A	172.0	A	171.7	A
150	142.6	A	156.1	A	152.2	A
170	152.7	A	138.0	AB	94.5	B
190	52.5	A	76.7	A	43.2	A

Values with the same capital letter are not statistically different at $\alpha = 0.10$.

Conclusions

A significant decrease in tensile modulus started when temperature increased from 170°C to 190°C, and the decreases in tensile moduli were 39%, 47%, and 55% for durations of 3, 6, and 9 hours, respectively. The tensile failure strain was significantly affected by temperature, but not by time duration. A significant decline in KBFB failure strain started at 150°C. The exposure duration seemed to have no significant effect on the tensile strength and modulus at temperatures of 130°C and above. The different stiffness behavior of the KBFBs can be explained by the degradation process of its major component, cellulose.

Presentations/Publications/Patents

1. Du, Y., J. Zhang, and Y. Xue. 2008. "Temperature-duration effects on tensile properties of kenaf bast fiber bundles," Forest Prod. J., 58(9) pp. 59–65.

2. Zhang, J. Y. Du, Y. Xue, and S. Q. Shi. 2008. "Temperature-duration effects on tensile properties of kenaf fiber bundle," Forest Products Society 62th Intern. Conv., Hyatt Regency Union Station, St Louis, Missouri, June 22–24, 2008.

References

1. Holbery J, Houston D. JOM 2006:80–6.

2. Sellers Jr T, Reichert Nancy A, Mississippi State University; 1999.

3. Bhuta M, Hall HL, Ziimmernman JM, Burcham TN, Columbus EP, Fuller MJ. In: Sellers Jr Terry, Reichert Nancy A, Eds. Mississippi State University; 1999. p. 401–20.

4. Roger RM, Sanadi A, Jacobson R, Caulfield D. In: Sellers Jr Terry, Reichert Nancy A, editors. Mississippi State University; 1999. p. 381–92.

5. Mohanty AK, Misra M, Dizal LT, Boca Raton, FL–CRC Press; 2005.

6. Mori T, Tanaka K. Acta Metall 1973;21:571–4.

7. Han JS et al. In: Sellers Jr Terry, Reichert Nancy A, Eds. Mississippi State University; 1999. p. 149–67.

8. Xue Y, Du Y, Elder S, Shame D, Horstemeyer M, Zhang J. In: Proc. 9th Intern. Conf. on wood and biofiber plastic composites, May 21–23, Madison WI; 2007.

9. Suzuki K, Kimpara I, Saito H, Funami K. J Soc Mater Sci Jpn 2005;54(8):887–94.

10. Standard test method for tensile strength and Young's modulus of fibers. ASTM C 1557-03. ASTM, West Conshohocken, PA; 2003.

11. Benveniste Y. Mech Mater 1987;6:147–57.

12. SAS Version 9.1.3, SAS Institute Inc., 100 SAS Campus Dr., Cary, NC.

13. Kollmann Franz FP, Cote Jr Wilfred A. New York: Springer; 1968.

14. Kocurek MJ et al. The pulp and paper manufacture series, vol. 3; 1987.

15. Mura T. Martinus Nijhoff, Hague. Netherlands; 1982.

16. Cox HL. J Appl Phys 1952;3:72–9.

17. Tucker III CL, Liang E. Compos Sci Technol. 1999; 59:655–71.

Chapter Three: Natural Fiber Composite Modeling

Section A: Kenaf-Epoxy Composite with Carbon Nanotubes

L.C. Brinson, S. Narayanan, and A. Schoch

Introduction

Composite materials can be analyzed at different length scales due to the different failure mechanisms. A micromechanical scale analysis helps to give us insightful knowledge of the local states of deformation and stress of the composite constituents (matrix and reinforcing fiber) and their interaction. This inspired us to follow micromechanical modeling approaches for the kenaf-epoxy composite and try to compare our results with the experimental results of its elastic moduli obtained by Xue et al. [1]. In the beginning phase of this project we were successful in modeling the kenaf-epoxy composite using the Mori-Tanaka model for the unidirectionally aligned composites and randomly oriented composites [2]. In the second phase of the project

we were interested in investigating the enhancements in mechanical properties of the kenaf-epoxy composite when carbon nanotubes were randomly dispersed in it. The modeling for this was done by suitably extending the Mori-Tanaka model. The details of these two works and the ongoing and future works are presented in this report.

Modeling of Kenaf-Epoxy Composites

As mentioned previously, a three-dimensional Mori-Tanaka model (Figure 16) was used for modeling the kenaf-epoxy composite. The values of the mechanical properties required by the model were adopted from the available literature [1]. Justifiable assumptions were made for the mechanical properties whose values were not found in the literature.
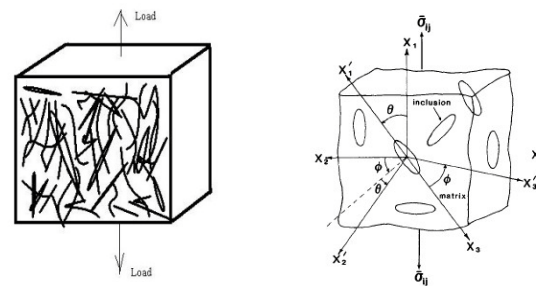
Figure 16. Comparing the schematic representations of the actual kenaf-epoxy composite sample and the 3D Mori-Tanaka model for randomly oriented fibers.

The moduli of elasticity were computed using the model, and their variation with fiber volume fraction was studied for a representative range of fiber aspect ratios (FARs) ranging from 100 to 1,000, as shown in Figure 17. The Young's modulus values obtained were very much comparable with the experimental values of 9.53 GPa (Yarn) and 4.76 GPa (Sliver), obtained by Xue et al [1]. It could be observed that there was no appreciable difference in the Young's modulus and the shear modulus for various aspect ratios of the fiber, due both to the small difference between Kenaf modulus and matrix modulus, as well as the single order of magnitude appropriate for the range of aspect ratios.
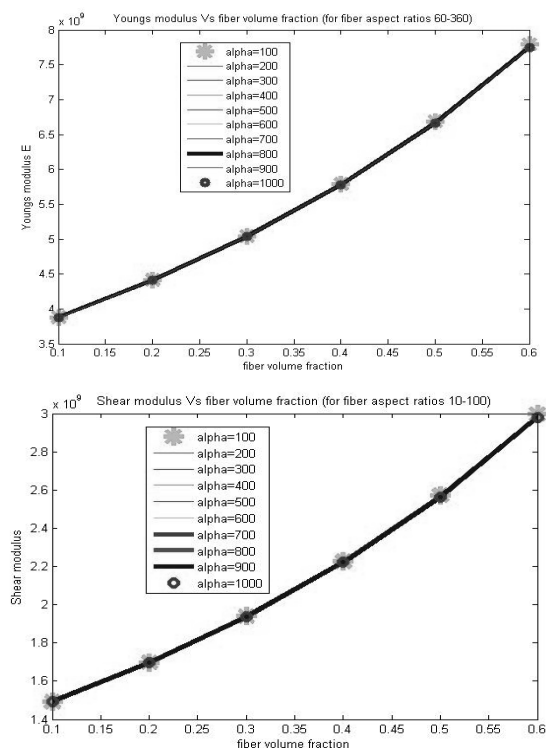
Figure 17. Young's modulus and shear modulus vs fiber volume fraction for various aspect ratios.

Modeling of Kenaf-Epoxy Composite With Carbon Nanotubes Dispersed

A small quantity (2%) of carbon nanotubes is embedded in the kenaf-epoxy composite. Note that both the Kenaf fibers and the nanotubes are embedded randomly in the matrix. The conventional Mori-Tanaka model is suitably extended to model the present case. The aspect ratio is chosen to be 100 for kenaf fibers and 1,000 for the nanotubes. The variation of Young's modulus with fiber volume fraction was studied for this case and compared to the earlier case, without nanotubes (Figure 18). For a fiber volume fraction of 0.6, the Young's modulus calculated was observed to be 21.94% greater than the case when nanotubes were not dispersed. This clearly indicates the possible advantages of introducing carbon nanotubes into the composite matrix in terms of enhanced modulus, strength, and other nonmechanical properties like thermal conductivity, electrical percolation, etc.
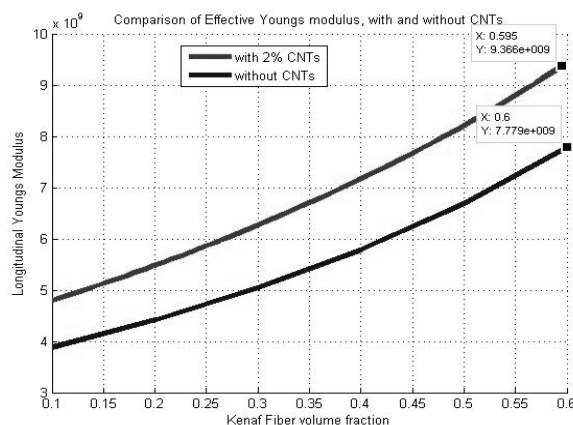
Figure 18. Effective Young's modulus of the kenaf-epoxy composite, with and without dispersed carbon nanotubes .

Presentations/Publications/Patents

1. K. Wakabayashi et al., "Polymer-Graphite Nanocomposites: Effective Dispersion and Major Property Enhancement via Solid-State Shear Pulverization," Macromolecules, 41(6) pp. 1905–1908 (2008).

2. L. M. Hamming et al., "Mimicking mussel adhesion to improve interfacial properties in composites," *Composite Science and Technology,* 2008 (in press).

References

1. Y. Xue et al., "Statistical tensile properties of kenaf fibers and composites," 9th Intern. Conf. Wood Biofiber Plastic Composites, May 21–23, 2007, Madison Wisconsin.

2. G. P. Tandon and G. J. Weng, "Average stress in matrix and effective moduli of randomly oriented composites," *Composites Sci. Tech.,* **27**, pp. 111–132 (1986).

3. G. P. Tandon and G. J. Weng, "The effect of aspect ratio of inclusions on the elastic properties of unidirectionally aligned composites," *Polym. Composites,* **5**(4) (October 1984).

Section B: Effects of Fiber Waving and Kinking On the Composite Performance

Yibin Anna Xue (MAE, USU), Scott Fletcher, Kunpeng Wang

Introduction

Linear and nonlinear elastic behaviors of wood fiber-plastic composites with discontinuous straight fibers arranged in regular and staggered arrays were obtained at various wood fiber volume fractions [1]. In this report a series of micromechanical simulations was conducted to predict the elastic and nonlinear elastic behaviors of wood-fiber-reinforced plastic composites (WPCs), considering the effects of fiber waving and kinking forms on the stress-strain relations, with the wood fiber volume fraction at 50%, a popular target volume fraction for automobile applications. The fiber kinks were presented as localized kinks in the middle of the fiber, uniform waving forms, and nonuniform waving forms. Figure 19 shows the unit cells contained fibers as (a) straight, (b) in a wave form, and (c) in a kinking form.

(a)   **(b)**   **(c)**
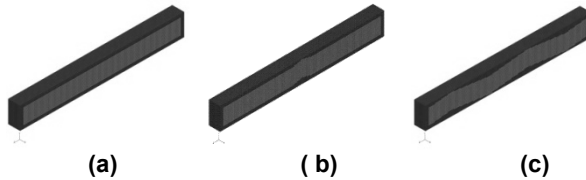
Figure 19. The unit cells of wood-fiber-reinforced polypropylene composites at the wood fiber volume fraction of 50%: (a) straight fiber, (b) uniform waving fiber, and (c) with local kink in the middle.

Composite Stress-Strain Relations

Figure 20 shows the stress-strain relations for WPCs with the wood FAR ranging from 5 to 100. For the particular WPC studied, when the fiber aspect ratio is 100, the stress-strain relation is very close to the case of that of continuous fibers when the total deformation is less than 4%.

Effects of Waving and Kinked Fibers

Numerical simulation of waving and kinked fibers demonstrates that the stress-strain relations of the composites are not sensitive to the forms of the wood fibers, as shown in Figure 21. Figure 22
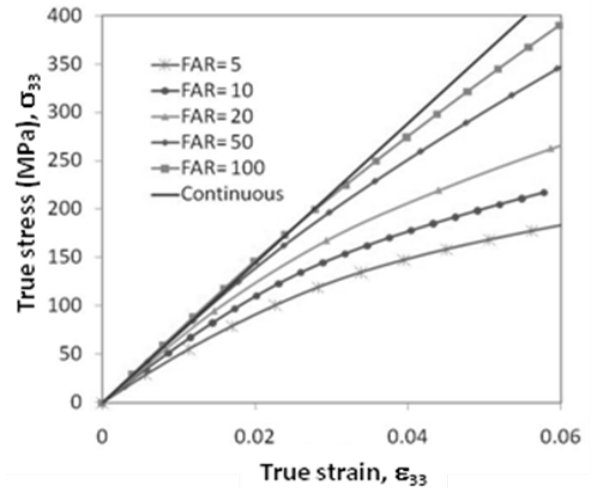
Figure 20. The true stress-strain relations for wood-fiber-reinforced polypropylene composites as a function of FARs.
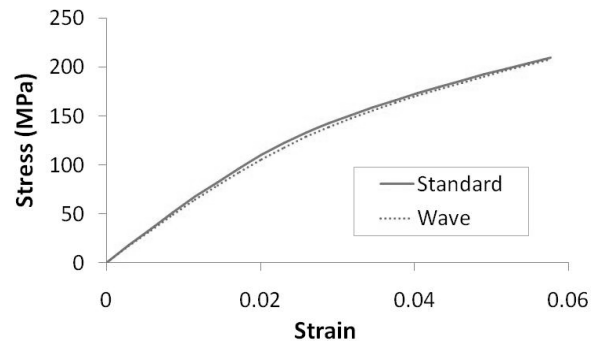
Figure 21. The true stress-strain relations for wood-fiber-reinforced polypropylene composites of uniformly distributed straight (standard) and waving fibers (wave).
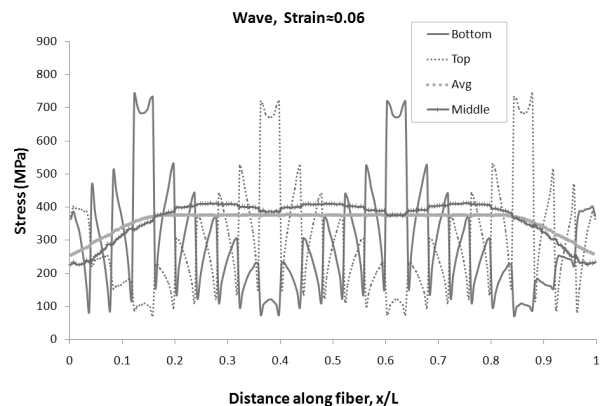
Figure 22. The distribution of stress along the length of fiber in the middle plane at the middle, top, and bottom of the fiber, in addition to the stress averaged over the cross-sectional area for waving fibers.

shows the normal stress distributions in the middle plane of the fiber at the top, center, and bottom of the fiber in composites with uniformly waved fibers. The stresses at the middle of the fiber in straight and waving fiber forms are similar. The most significant effect of the fiber forms relies on the local stresses in the fiber, especially the stresses on the top and bottom surface of the wood fiber. Figure 22 shows the stresses in the fiber at the peak of the waving fiber are more than twice the average of the stresses in the fiber at the corresponding points. The earlier surface failure of the wood fiber might induce fracture-type of stress intensity and cause earlier failure of the wood fiber.

Conclusions

1. For straight fibers, the high fiber aspect ratio enhances both the elastic modulus and nonlinear hardening of the composites. However, high fiber aspect ratio (greater than 50) may also induce high stresses in fiber, especially under loading greater than 4%, when the maximum stresses in fiber are greater than the tensile strength of the wood fiber.

2. For waving and kinked wood fibers (with the fiber aspect ratio of 10), the constitutive relation is not affected significantly by the fiber form. However, the local stress concentration on the surface of the wood fiber at the peak of wave and kink is more than double compared to the average stresses in the fiber, which may cause earlier failure of fibers.

Presentations/Publications/Patents

1. Y. Xue, S. A. Fletcher, and K. Wang, "Micromechanical simulations on waving and kinked natural fiber-reinforced plastic composites," Proceedings of IMECE2008, 67462, 2008 ASME International Mechanical Engineering Congress and Exposition, Boston, Massachusetts, October 31–November 6, 2008.

2. Y. Xue and K. Wang, "Micromechanical Simulations on Hydro-Mechanical Properties of Bio-Fiber Composites," MRS 2008 Spring Meeting Proceeding, 1097-GG-4-20, San Francisco, California, March 24–28, 2008.

3. Y. Xue and K. Wang, "Micromechanical Simulations on Hydro-Mechanical Properties of Bio-Fiber Composites," MRS 2008 Spring Meeting (poster).

4. Y. Xue, S. A. Fletcher, and K. Wang, "Micromechanical simulations on waving and kinked natural fiber-reinforced plastic composites," 2008 ASME International Mechanical Engineering Congress and Exposition (podium).

5. Z. Q. Zhang, D. Ward, and Y. Xue, "Molecular dynamics simulation on interfacial behavior of carbon nanotube and polyethylene," Micro/Nano Technology Society Function—2008 ASME International Mechanical Engineering Congress and Exposition (poster).

References

1. Y. Xue and K. Wang, K., "Micromechanical Simulations on Hydro-Mechanical Properties of Bio-Fiber Composites," MRS 2008 Spring Meeting Proceeding, 1097-GG-4-20, San Francisco, California, March 24–28, 2008.

H.   Evaluation of Composite Natural Fiber/Resin Compatibility

Principal Investigator: Leonard S. Fifield
Pacific Northwest National Laboratory
P.O. Box 999, Richland, WA 99354
(509) 375-6424; fax: (509) 375-2186; e-mail: leonard.fifield@pnl.gov

Technical Contributor: Cheng Huang
Pacific Northwest National Laboratory
P.O. Box 999, Richland, WA 99354
(509) 375-6424; fax: (509) 375-2186; e-mail: cheng.huang@pnl.gov

Technical Contributor: Kevin L. Simmons
Pacific Northwest National Laboratory
P.O. Box 999, Richland, WA 99354
(509) 375-6424; fax: (509) 375-2186; e-mail: kevin.simmons@pnl.gov

Technology Area Development Manager: Joseph A. Carpenter
(202) 586-1022; fax: (202) 586-1600; e-mail: joseph.carpenter@ee.doe.gov

Field Technical Manager: Mark T. Smith
(509) 375-4478; fax: (509) 375-4448; e-mail: mark.smith@pnl.gov

---

Objective

- To develop surface modification strategies applicable for industrial applications of woven and nonwoven natural fiber molding compound reinforcements.

- To manufacture thermoset polymer composite coupons for mechanical, thermal, extent-of-cure and environmental characterization.

- To develop material characterization data of composite material forms at the micro- and macroscopic scales with particular emphasis on fiber swelling, polymer-fiber interfacial adhesion and the effects of environmental exposure on composite mechanical properties.

Approach
- Develop a fundamental understanding of the natural fiber architecture to inform and tailor fiber surface modification strategies.

- Explore inexpensive and effective moisture barrier approaches for natural fibers including papermaking wet-end chemistry sizing agents and bio-based surface modifiers.

- Conduct lab trial iterations combined with screening tests to define the modification approaches best suited to natural fibers.

- Produce panels from modified natural fiber reinforcements to determine mechanical and moisture uptake characteristics relative to panels produced using unmodified natural fiber and glass fiber.

- Combine PNNL knowledge on sheet molding compound (SMC) materials with PNNL expertise in surface chemistry to develop new natural fiber materials capable of impeding moisture ingress as a function of time while providing advantageous specific mechanical properties.

Accomplishments

- Developed four unique surface modification strategies to combat moisture absorption in fibers and improve fiber-resin compatibility in natural fiber polymer composites.

- Performed initial experiments using two sizing agents from the papermaking industry to modify bast-type natural fibers from domestic and international fiber suppliers.

- Investigated the effect of surface treatments on the microscopic structure of fibers using scanning electron microscope (SEM) imaging.

- Used diffuse reflectance infrared spectral imaging on powdered samples of modified fibers to evaluate the effect of sizing type and reaction conditions on sizing efficiency.

Future Direction

- Complete evaluation trials of proposed natural fiber surface treatments.

- Develop new fiber surface modification strategies.

- Characterize moisture uptake and wettability of modified fibers to identify moisture resistance and polymer compatibility.

- Fabricate composite test samples from down-selected surface treatments to investigate strength of fiber/polymer interface.

- Produce SMC panels from modified natural fibers for mechanical and environmental characterization.

- Integrate developed surface treatments with fiber forms produced by the independently developed lab-scale fiber preparation unit.

Introduction

This project investigates the compatibility of natural fiber reinforcements with polymer systems that are of interest and applicable to automotive structural and semi-structural composite components. The project will evaluate and characterize composite strength, failure modes and time-dependent properties of select candidate natural fiber reinforced material systems. Novel fiber surface treatments and material processing variables will be designed and evaluated in an effort to optimize the compatibility and durability of the natural fiber composites. The project will focus on a limited number of natural fiber and polymer systems that meet requirements for automotive applications, including fiber cost and availability, strength and stiffness of fibers, and high-volume processing compatibility.

Plant-based natural fibers constitute a category of renewable biomass categorized as lignocellulosic; the major components of the fibers are cellulose, hemicellulose and lignin. Lignocellulosic fibers have appealing potential for use in polymer composite reinforcement and include bast, leaf and seed fibers, fruit fibers, wood fibers, grasses and reeds. A paramount challenge for the use of lignocellulosics as engineering materials is their inherent tendency to absorb moisture. The polar character of the fiber surface, which makes them hygroscopic, also limits utility of the fibers as reinforcement in common non-polar polyolefin thermoplastic matrices. Both physical and chemical methods have been used in attempts to control the interface of natural fibers and polymer resins to improve the performance of their composites. High moisture absorption, however, remains a barrier to widespread use of these materials. Moisture ingress causes fiber swelling, which leads to composite dimensional instability and a decrease in both fiber and composite mechanical properties.

The mechanical properties of fiber reinforced composites depend on the properties of individual components, including the fibers and the resin, and on the interfacial compatibility of the components. Plant fibers have a cellular composition that provides

mechanical support for the organism. The rigid cell well is made up of crystalline cellulose microfibrils glued together with amorphous lignin macromolecules. Bast fibers such those from flax, jute, kenaf and hemp are ~45-75wt% cellulose and ~5-25wt% lignin. Hydroxyl groups, acetyl groups and ether groups on the fiber molecules give the fiber is polar nature and inherent incompatibility with non-polar polymers such as polypropylene.

The moisture content inherent in lignocellulosic fibers is an important consideration in a chemical strategy to make the fibers compatible with a polymer resin. A large amount of energy is required to fully dry the fibers, but residual moisture can interfere with the coupling process by hydrolyzing reactants before they can add to the fiber. There remains significant opportunity for new methods to control fiber surface chemistry and minimize energy input required for fiber treatment.

An additional important consideration for fiber treatment methods is the temperature stability of natural fibers. Unless placed in an inert atmosphere, lignocellulosic fibers are generally limited to $150^{\circ}C$ for longer processing durations and $200^{\circ}C$ for brief exposures in order to prevent degradation of the fiber structure. Longer exposure can lead to discoloration of the fibers, volatilization of fiber components, and can have an adverse effect on fiber mechanical properties. The widespread use of lignocellulosic fibers in composite materials will require the development of scalable, low temperature fiber surface treatment methods.

Approach

Surface Modification Methodology

At the start of this project in July 2008, a thorough analysis of current modification strategies was conducted. Among the techniques that were considered include the following:

Mercerization

Mercerization is a process developed in the 19th century for improving the properties of cotton fiber for use in textiles. It involves treatment of fibers in a caustic solution containing sodium hydroxide. The concentration of solution, temperature, and process duration determines the extent of reaction. The treatment serves to swell the fiber bundles, lower the overall crystallinity of cellulose in the fibers and decrease hydrogen bonding in the fibril network structure. Though it can improve interfacial strength between the fiber and a polymer matrix, the mercerization process can lead to an increase in the tendency of fibers to absorb moisture.

Hydroxyl Group Blocking

Common reactions aimed to reduce the affinity of natural fiber to moisture involve blocking hydroxyl groups on the cellulose chains through the formation of esters. The yield of these reactions generally tracks with the dryness of the fiber.

$$\text{Fiber-OH} + \text{HOOC-R} \rightarrow \text{Fiber-OO-R}$$

Silane Coupling Agents

Organosilanes are the major coupling agents used for glass fiber reinforced polymers. Alkoxysilanes used for this purpose contain three alkoxy groups on a silicon atom that also contains a functional group for interfacing with the polymer. The alkoxy groups on the silane are hydrolyzed by residual moisture then displaced by the hydroxyl group's resident on the glass or natural fiber surface to form a silyl ether bond. After reaction the surface is less hydrophilic and more compatible with the polymer matrix.

$$\text{Fiber-OH} + \text{(RO)}_3\text{-Si-R}^2 \rightarrow \text{Fiber-O-Si(OR)}_2\text{-R}^2$$
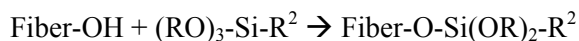
Treatment with Isocyanates

Isocyanates, another common class of coupling agents, have N=C=O functional groups that can react directly with hydroxyl groups on the fiber surface.

$$\text{Fiber-OH} + \text{O=C=N-R} \rightarrow \text{Fiber-OO-CH-N-R}$$
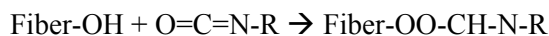
Graft Copolymerization

An effective method of surface chemical modification of natural fibers is graft copolymerization. Redox initiation has been successfully implemented to graft

vinyl monomers onto natural fibers for composite application. Among the redox initiating systems, $CuSO_4$ - $NaIO_4(Cu^{2+}\text{-}IO_4^-)$ is particularly interesting because no acid is used during the graft polymerization reaction; utilizing acid in a graft reaction degrades natural fiber properties. Optimized vinyl grafted natural fibers that consist of an orderly arrangement of grafted moieties act as compatible reinforcing fibers with several resin systems in obtaining better fiber-matrix adhesion.

The development of surface modifiers is critical to the success of this project. From the PNNL analysis of current technology, potential surface modifiers range from small molecules for blocking moisture to long-chain coupling agents that promote polymer matrix adhesion. An effective developed process with maximize reaction with bound –OH to minimize the lignocellulose moisture content prior to composite processing. This could potentially include a process deploying super critical CO_2.

All approaches seek to protect the entire surface with the goals of gaining moisture resistance, increasing fungal resistance, reducing processing temperatures and reducing of drying costs, simultaneously increasing physical and mechanical properties through improved fiber/resin compatibility and fiber/matrix bonding.

Surface Modification Plan

In this effort, innovative surface modification techniques outlined in the following paragraphs will be explored due to their potential for inexpensive, robust and effective application:

- Low molecular weight molecules currently used as paper sizings modified for structural composite applications.
- Bio-based, soy-derived modification strategies.

Sizing Chemistry and Paper Sizing Analogy

In this approach, we apply "papermaking wet-end chemistry" to natural fiber surface modification design. Paper sizes are designed to control moisture penetration into paper through modification of wood pulp fibers. The paper sizing mechanism can analogously be applied to control moisture of natural fibers for polymeric composite reinforcement. Commercial paper sizes are relatively inexpensive and available in quantities of tons per day. An example of one common sizing, alkylketene dimer (AKD), is depicted in Figure 1.
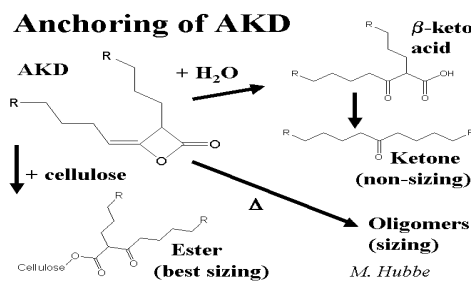
Figure 1. AKD paper sizing (www4.ncsu.edu/~hubbe/AKD.htm).

Bio-inspired Coupling Agents

Many plant biopolymers such as soy flour protein are being developed as sizes for natural fibers. Working with Professor Kaichang Li at Oregon State University's Department of Wood Science and Engineering, PNNL is investigating bio-based surface modifiers for natural fibers. Professor Li is exploring bio-inspired cure agents based on soy protein and other bio-molecules. Professor Li has issued patents for bio-derived adhesives. It is anticipated that new technology developed will utilize wet chemistry methods.

It is believed that these strategies will lead to a novel approach that will remain within the stringent process and economic parameters of the auto industry. Fibers that will be used as a baseline are hemp (Stemergy) and kenaf (Kengro).

Outlined below are two test methodologies that will be undertaken, one for screening different modification approaches and the other for more in-depth testing on those candidates that appear via screen testing to be viable natural fiber surface modification strategies.

A. Screening Tests
1. Fourier Transform Infrared (FTIR)—Surface Chemistry
2. Contact Angle (Packed Cell Method)—Surface Energy
3. Zeta Potential—Surface Charging
4. Moisture Uptake Tests

B. Advanced Testing
1. Produce Panels—24 Hour Boil Test
2. Produce Panels—Tensile Test
3. SEM—Microscopic Structure

Experimental Testing and Analysis

Experimental characterization of the material surfaces will be undertaken utilizing several analytical techniques to determine the raw and surface treated natural fiber properties.

FTIR

Infrared spectra will be generated of the raw and surface-treated natural fibers to determine the surface-deposited chemistry and functionalization.

Moisture Absorption

Treated and untreated fiber samples will be characterized for moisture absorption, as will polymer composites produced from the fibers.

Panel samples first dried by heating will be weighed (W_1) and then soaked in a bath of deionized water at room temperature for a prescribed time (W_2). Water absorption, WA(%), will be determined by the following:

$$WA(\%) = \left(\frac{W_2 - W_1}{W_1}\right) \bullet 100$$

.

Thickness swelling (TS) will be calculated on the fibers as follows:

$$TS(\%) = \frac{(t_c - t_o)}{t_o} \bullet 100$$

,

where t_c is the sample thickness after immersion and t_o is the thickness prior.

Scanning Electron Microscopy

SEM analysis will be conducted to reveal the effect of modification on the fiber surface structure (Figure 2). This will be particularly important for analysis of composite fracture surfaces to determine failure modes in composites produced and tested using the treated fibers.
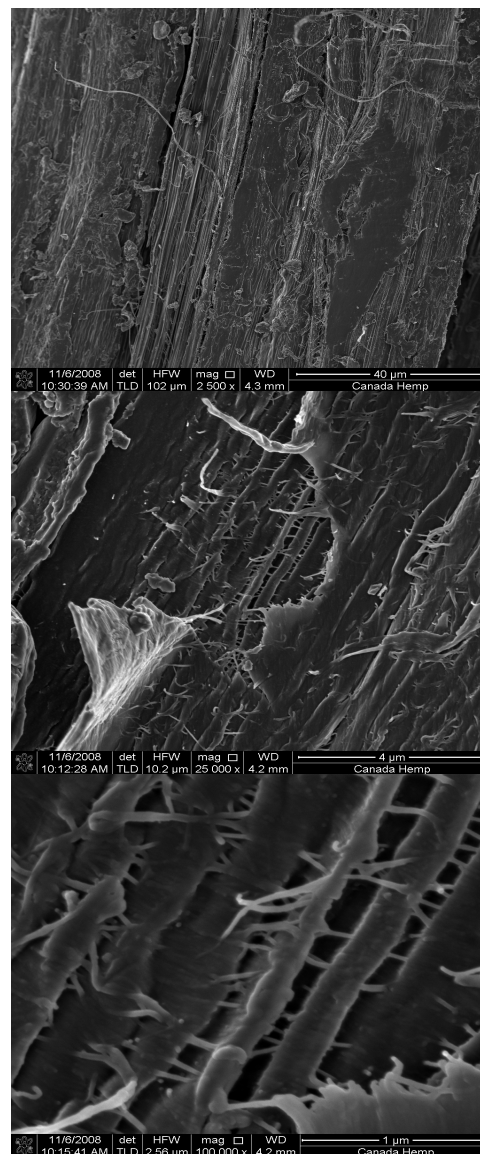
Figure 2. SEM images of Stemergy hemp with 40 μm, 4 μm and 1 μm scale bars.

Zeta Potential (ζ-Potential)

Due to the known hydrophilic character of cellulose-based materials, suitable methods that allow characterization of the wet state of these materials are

typically applied to study their surface properties. For this reason, the Zeta Potential (ζ-Potential) measurements have been established to characterize the potential difference in an otherwise uniform medium between a point some distance from the surface and a point on the plane of shear. The plane of slip between the electrochemical double layer and the medium involved (in this case, water) may be interpreted in terms of charge density. Thus, changes in surface composition and in the water uptake behavior due to fiber separation and subsequent surface treatment may be quantified by measuring the ζ-Potential. Additionally, it will be useful to quantify trends in the ζ-Potential as a function of pH and subsequent fiber swelling.

Sample Trials

SEM characterization of surface modification effects on natural fibers is ongoing. Below are SEM images of surface morphology of Kengro kenaf natural fibers without surface modification (Figure 3), obtained from FIB (Focused-Ion-Beam)-SEM, which exhibits clear fibrous textile microstructures, including microfibrils and lignin globules.

At this time, PNNL is conducting a series of experiments to determine the effect of paper sizing on surface chemistry. Kenaf and hemp samples have been modified with two sizes; in the future, size concentration, exposure time, temperature and fiber platform preparation will be explored.

Diffuse Reflectance Infrared Fourier Transform Spectroscopy (DRIFTS) for the identification of chemical modification of the natural fiber surface was applied (Figure 6). DRIFTS is an efficient, quasi-accurate (especially under Kubelka-Munk conversion) and convenient method for natural fiber surface modification analysis. Although the peak intensity ratios can be reliable for semi-quantitative determinations of functional groups, this technique will mostly be relied upon for qualitative evaluation of relative changes in surface chemistry.
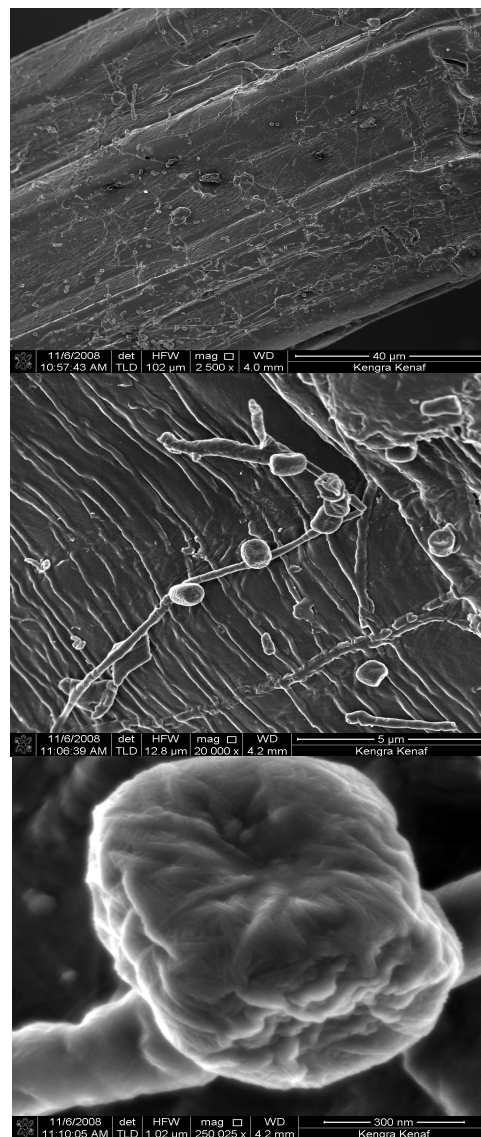
Figure 3. Kengro kenaf imaged with 40 μm, 5μm, and 300 nm scale bars.

With work newly begun mid-year, the next fiscal year will require a dedicated effort to move judiciously through the strategies outlined in this report to proceed with the most appropriate methods.
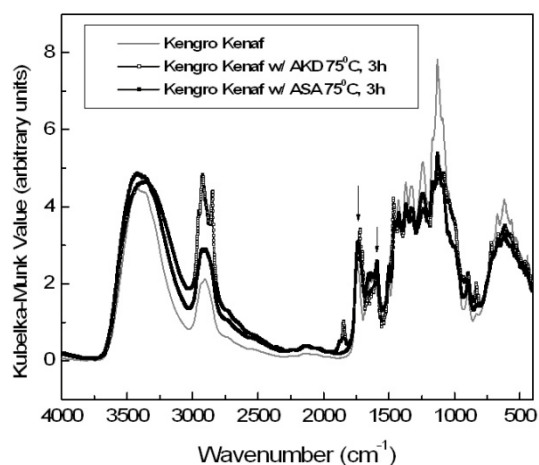
Figure 4. FTIR peaks of kenaf (Kengro, Charleston, MS), indicating change in fiber surface bonding sites with treatment.

Conclusions

Commenced in July 2008, this program had an initial focus on developing fiber surface modification strategies that will scale to the auto industry. At this time, PNNL has investigated several concepts and will be finalizing the experimental plan in the next quarter.

I.   **Composite Crash Energy Management (ACC100*)**

Principal Investigator: Khaled W. Shahwan, Ph.D.
Chrysler LLC
Chrysler Technology Center—Scientific Labs.
800 Chrysler Drive (CIMS: 483-05-10)
Auburn Hills, Michigan 48326
(248) 576-5609; e-mail: kws8@chrysler.com

Technology Area Development Manager: Joseph A. Carpenter
(202) 586-1022; fax: (202) 586-1600; e-mail: joseph.carpenter@ee.doe.gov

Field Project Officer: Aaron D. Yocum
(304) 285-4852; fax: (304) 285-4403; e-mail: aaron.yocum@netl.doe.gov

---

Objective

- Develop, verify, and validate efficient, robust, and physics-based modeling and analysis tools for predicting damage initiation, progression, energy absorption, and overall crush behavior of composite components in lightweight vehicle structures using micromechanical, phenomeno-logical, or hybrid computational approaches.

- Develop design, testing, modeling, and analysis guidelines for advanced lightweight automotive composites for safety and crashworthiness applications in vehicle development.

Approach

- Conduct extensive experimental tests to characterize the quasi-static and dynamic properties of selected structural composite materials and micro-architectures, including damage modes and progression mechanisms.

- Develop advanced models based on phenomenological and micro-mechanical approaches to predict the material and structural response during the full regimes of behavior including ascending branch, peak strength, post-peak and softening, and plateau characteristics of the stress-strain and force-displacement of coupons as well as structures.

- Verify and validate the computational tools by predicting quasi-static and dynamic behavior of experimental tests at the coupon and structural levels. Further validate by predicting structural crash performance of lightweight automotive composites.

Accomplishments

Carbon composites, especially braided textiles which exhibit mass density of about 1400 kg/m^3 (~ 80% lighter than common structural steels), have been characterized as viable materials for automotive structural applications. Their low densities as well as other characteristics such as equivalent structural stiffness, strength, and energy absorption, are well suited to meet many of the contemporary lightweighting challenges. The following specific accomplishments are aimed towards achieving that:

---

*Denotes Project 100 of the Automotive Composites Consortium (ACC), one of the formal consortia of the United States Council for Automotive Research set up by Chrysler, Ford, and General Motors to conduct joint, precompetitive research and development (see www.uscar.org).

- Demonstrated via extensive testing and modeling that post-peak softening in quasi-brittle textiles cannot be considered a constitutive property especially in homogenization techniques (as is commonly done), and the coupled local material-structural behavior plays a major role in characterizing such softening and overall response envelope.

- Demonstrated via extensive testing and modeling that the employment of models which contain mostly physically-defined and measurable quantities (non-phenomenological) is possible and achievable in order to predict the post-peak and softening behavior of such materials. Using such required fundamental understanding of the underlying physics and mechanics, and the full reliance on purely abstract mathematical concepts to quantify damage, is not sufficient.

- Identified the dominant mechanisms responsible for influencing the strength, post-peak softening response, and plateau (residual) strength in braided textiles. Extensive experimental and computational tests have been used to qualitatively characterize them.

- Revealed that modeling damage initiation and progression in braided textile composites necessitates the objective utilization of the concept of representative unit cell (RUC) as well as the inclusion of some measures for local/global imperfections. Because of the nature of damage, the minimum number of RUCs needed to accurately predict the damage zone and its progressions may not be known a priori and does depend on a host of factors.

- Exposed the dependence between compressive and bending strain fields and damage. Due to the multi-axial nature of damage, damage initiation and progression depends on the nature of the local stress field as well as remote applied loads.

- Experimental tests and computational analyses revealed that local in situ properties in textile composites can differ appreciably from their presumed virgin (bulk) values. Test-validated models (using optical techniques and nano-indentation) have quantified the dependence of the final elastic properties on cure time, cure temperature level, and distribution.

- Developed test-validated modeling (preliminary) techniques to study size effects in braided (quasi-brittle) composites. Recently, completed tests have confirmed and quantified size effects on the strength in such composites which is of importance for using finite-element modeling (FEM) techniques as well as designing sample sizes for laboratory tests.

- Completed a phase of study aimed at using multiscale modeling and analyses techniques to model and predict the damage initiation and progression during the quasi-static and dynamic crush of braided carbon tubes. A multiscale design system (MDS) was also developed to model the micromechanics including interface degradation and debonding, and couple the analysis procedure with a commercial software package.

- Completed and validated an automated FEM procedure for modeling random distribution of carbon fibers within a given spatial volume using a commercial software package to statistically investigate the influence of the RUC size on the elastic properties of the homogenized material.

Future Direction

- Develop a modeling database encompassing all models, associated material modules, coupled material-structural data, and special finite elements. This modeling database will serve as a central point for all predictive analyses and modeling developments for understanding and quantifying the strength and crashworthiness of lightweight automotive composites.

- Expand the current multiscale design system (MDS) to complete its functionality by including additional rate sensitivity effects, delamination, RUC optimization (with some adaptive capability), and size effects in order to enhance its proven predictive abilities.

- Investigate ways to minimize (or even mitigate) size effects in such quasi-brittle textile composites. Having characterized and quantified such important and inherent size effects within braided carbon textiles further investigations would provide important insights on how to minimize such effects at the early

material/architecture design/selection stages so that predictive tools, computational modeling and laboratory testing can be further simplified and streamlined.

- Material properties' changes with service/environmental factors (e.g., fatigue, high-frequency high-amplitude pulses/vibrations, moisture, and large thermal fluctuations, etc.) and their influence on energy absorption, mechanical response, and crash performance during a component's life-cycle. This could be focused on characterizing the in situ properties of in-service structural components and studying which factors influence (and to what degree) mechanical response and energy absorption capacity of lightweight carbon textile composites for automotive applications.

- Develop a demonstration project in which all completed accomplishments will be utilized to show the viability of carbon fiber-reinforced composites as a primary structural material in an actual automotive subassembly (e.g., front end), as well as the validity of the modeling and predictive tools developed thus far.

Introduction

The purpose of the Crash Energy Management Program is to develop and demonstrate the technologies required to apply production feasible structural composites in automotive crash and energy management applications. Projects within the program are intended to understand the mechanisms of polymer composite crash, develop analytical tools for use in design, and build a knowledge base for the application of lightweight polymer composites. The projects relate to materials, molding, and assembly process and design configurations that are useful in realistic applications. Design analysis methods will be developed that can be used at several different steps in the design process. These steps require different levels of precision and speed of use and the appropriate tools are expected to include both micro-mechanical and phenomenological approaches.

Multiscale Modeling for Crash Prediction with Interface Debonding

The previously developed multiscale composite crash prediction software system has been enhanced with the development of an interface model consistent with new experimental data. In addition, in situ inelastic phase properties of matrix and tows have been recalibrated to the coupon test data from the transverse tension, longitudinal tension, and longitudinal compression—all conducted on the 45° braided composite architecture.

The reduced-order multiscale model with interface debonding has been verified against an analytical solution on a model problem. Finally, the reduced order multiscale model with interface debonding has been validated against quasi-static tube crush experiments on various braid architectures (45°, 30°, and 60°) and different cross-sectional shapes of tubes (circular and square).

A close investigation of the experimental work performed at South Dakota School of Mines & Technology (see Figures 1 and 2) shows little or no interphase. The nanoindentation tests confirm this observation as well. Therefore, in the reduced-order multiscale model, the interface (rather than interphase) was modeled using a traction-separation law. In the traction separation law adopted, the value of fracture toughness in modes I, II, and III measured in quasi-static tests was used. The interface strength values were assumed to be identical to those of the matrix strength in the corresponding direction. These values were taken from the prior tests conducted elsewhere.
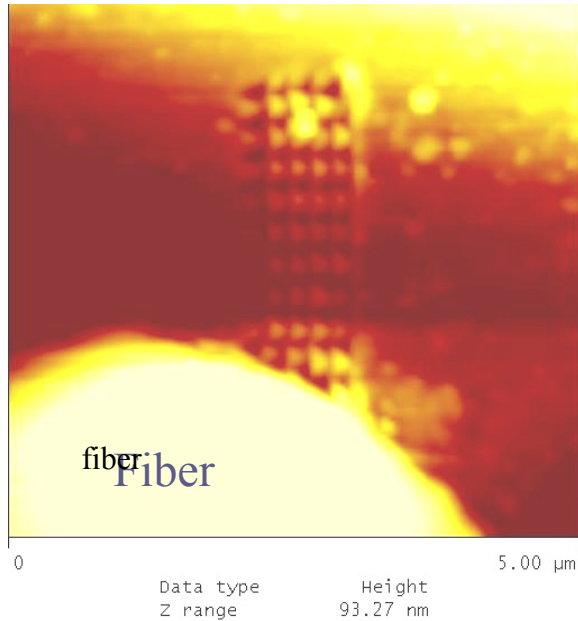
Figure 1. Fiber-matrix interface.
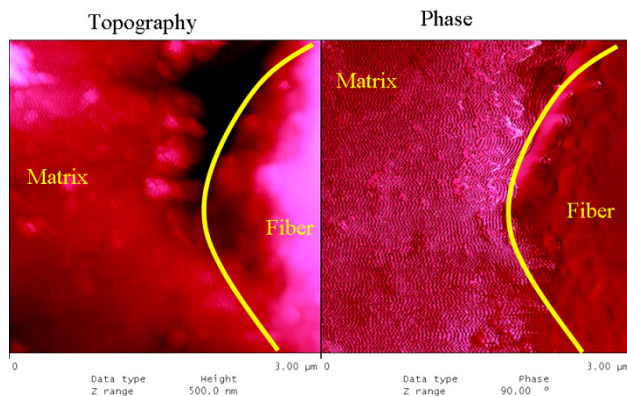
Figure 2. Close-up of an Atomic Force.

The theoretical aspects of the reduced-order multiscale model have been presented in past reports. It is instructive to comment on the computational complexity of the reduced-order multiscale model with interface debonding. The reduced-order multiscale model with interface debonding consists of 46 state variables, which include: six eigenstrain components times four phase partitions = 24, three components of eigenseparations times three interface partitions = 9, one phase damage state variable for each phase partition = 4 and three interface damage state variable for each of the three interface partitions = 9.

Microscopy (AFM) Phase Image of a Fiber-Matrix Interface

We now discuss the comparison of the simulation results on the ¼ tube model to the experimental results. We consider two layers of braided composite, an initiator plug with a specific fillet radius and loading rate of 0.5 in/min. Figure 3 compares the test data to the simulation results of the reduced-order multiscale model with and without interface debonding for 45° braid architecture.
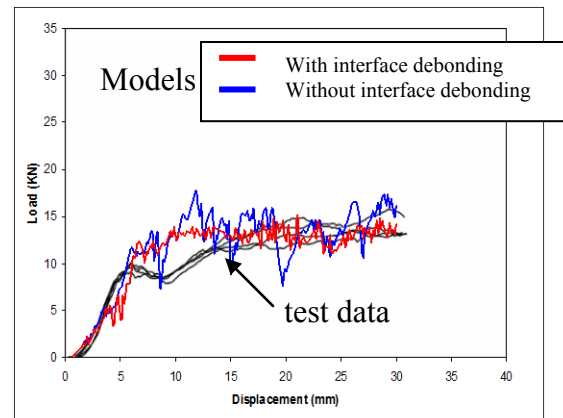
Figure 3. Predictions vs test for 45° carbon braided quarter tube.

It should be noted, however, that calibrated braid and matrix properties are different in the two simulations, i.e., in each case they have been calibrated to fit the test data in the transverse tension, longitudinal tension and longitudinal compression of the 45° braided composite architecture. Nevertheless, it can be observed that a notable improvement is obtained when the interface damage is considered in the model.

Figure 4 shows the comparison of the simulation and test data for the 60° braid architecture. In this case, the agreement between the experiment and simulation results is less remarkable and the improvement obtained due to modeling of interface damage is less pronounced, if any.

We suspect that the main reason for this less dramatic improvement is due to the fact that phase properties were calibrated based on the coupon tests of 45° braid architecture. This hypothesis can
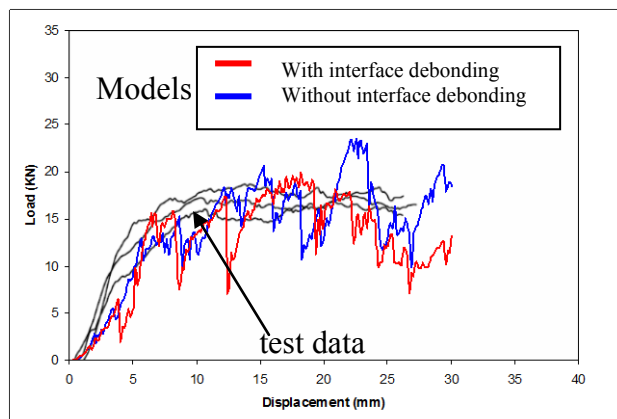
Figure 4. Predictions vs test for 60° braided quarter tube crush.

be easily verified if coupon tests on 30- and 60° architectures were available. Possible other reasons that will be investigated in the future are: consideration of a three-scale analysis (so far, the braid was assumed to have isotropic damage) and consideration of full-scale tube models.

Size Effects in Textile Composites

This project is focused on developing a qualitative and quantitative understanding of the important topic of meso- to macro-size effects in automotive structures made of quasi-brittle textile composite materials. Such an understanding plays a role in the accurate modeling and characterization of structural crashworthiness and energy absorption in components made of lightweight quasi-brittle materials (such as textile composites). Obtaining an understanding and useful insights of size effects, along with verifiable experimental evidence and clarification of the implications of the size effects for finite element (computational) modeling of structures made of two-dimensional triaxially braided composites (2DTBC), is the major goal of the project.

It is important at this point to clarify what is meant by "size" and what are the "effects." "Size" refers to the size of specimen/structural dimensions relative to the size of the damage zone and/or micro-structure. "Effects" refer to those effects on damage characteristics, nominal strength, and post-peak regime in materials exhibiting such strength–size dependence.

This project is motivated by the following fundamental question: What is the relationship between the measurements of energy released and dissipated (i.e., fracture properties and material nonlinearities) carried out in the laboratory at the coupon level of a 2DTBC, and their manifestations at the structural level in a real crash setting of a structure made of the same 2DTBC i.e., do the measured overall material/ structural properties change when different size specimens are tested? It is important to note that the primary interest in this topic (relating specimen size effects on measured material properties) does not stem from the well-known statistical distribution of micro-flaws in a material based on Weibull theory, but rather from an energetic consideration driven by the relatively recent findings that quasi-brittle materials exhibit size effects because their fracture process-zone is not negligible (in size) compared with the overall structural dimensions.

The work is focused on designing, manufacturing, testing and modeling different-size structural plaques using one matrix/resin system and three carbon fiber-braid architectures (+/-30°, +/-45°, and +/-60°). Various sizes of plaques were made encompassing a certain numbers of RUC as determined by the project's plan. Each plaque made was multi-layer (up to 8 layers), each having axial tows as well as braider tows exhibiting one the above angles. The main objective is to provide the sponsors with insights and guidelines on how best to model and test such materials in order to accurately model their true behavior under static and dynamic loads. It is worth noting that such an effort has not received significant attention in the past especially for this type of materials, architecture and manufacturing process.

Thus far, several tasks have been accomplished. Tests have been carried out on small samples and a larger one representing multiple RUCs. Based on the preliminary experimental data and observations, such braided carbon-fiber textiles exhibit strong and rapidly evolving size effects. i.e., the emergence of size effects, as one tests and compares one RUC vs multiple RUCs, is apparent and changes rapidly as larger-size plaques are tested.

The principal investigators (PIs) have proposed and developed a simplified way to model large

number of RUCs (e.g., 9, 14, 25… etc.) using "rugged" instead of "smooth" boundary condition per RUC (Figure 5). This resulted in a significant reduction in the number of finite elements (FE) needed to model each RUC. While it has been typical to have 5,000 FE or even 30,000 FE per RUC to achieve certain level of validity and accuracy, the current approach employs only 30 FE (approx.) and achieves similar results when compared to other models as well as laboratory experiments. This is a remarkable improvement and could be very useful once large, full-component or full-systems are modeled using FEM/finite-elelent analysis (FEA). Figure 5 also shows a modeled plaque with a total of 25 RUCs using the above technique.
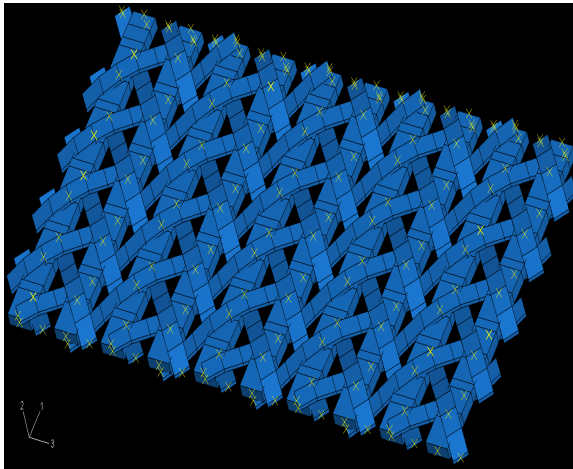
Figure 5. A full plaque modeled using multiple RUCs. There are 25 RUCs. Each RUC is made up of three-dimensional (3D) elements and irregular (rugged) boundary/edges. Only axial and braider tows are shown for clarity.

Figures 6 and 7 show the strong size effects that are present in such quasi-brittle textiles. This implies that strength characteristics depend not only on the material properties but also on the size of the specimen being tested and/or modeled. Ongoing work is focusing on developing an enhanced version of the popular Microplane Models used for modeling and analyzing damage and fracture in various types of materials (Figure 8).
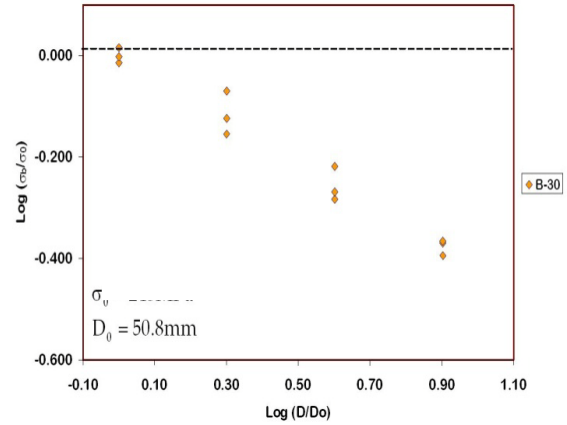
Figure 6. Experimental tests showing the change of the log of normalized strength (σ_N/σ_o) vs change in specimen size (shown as log D/D_o). The above results are for 30° braided-carbon fiber specimen.
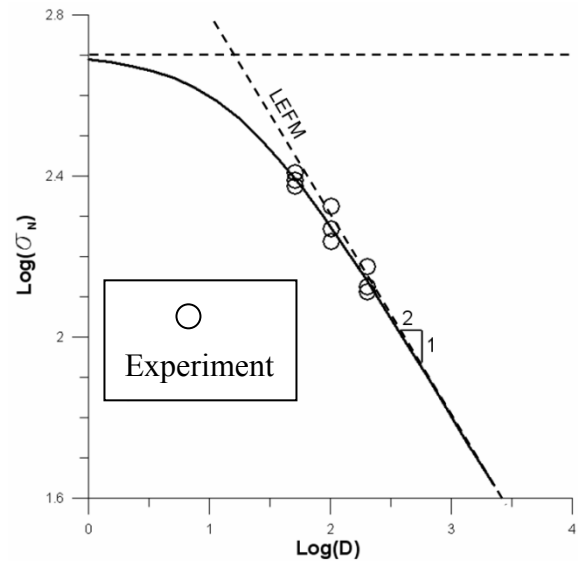
Figure 7. Experimental tests and fitted numerical predictions (solid line) showing the change of the log of normalized strength (σ_N) vs change in specimen size (shown as log D) for 30° braided carbon-fiber specimen.

Modeling of the Manufacturing Process Induced Effects (MPIE) on the Matrix Properties of Textile Composites

During the manufacturing process of textile reinforced composites (TRCs) the material properties of the polymer resin (matrix) change remarkably over the curing cycle. Resin's liquid-to-solid transition is accompanied by volume change. Coupled with mismatches in thermal
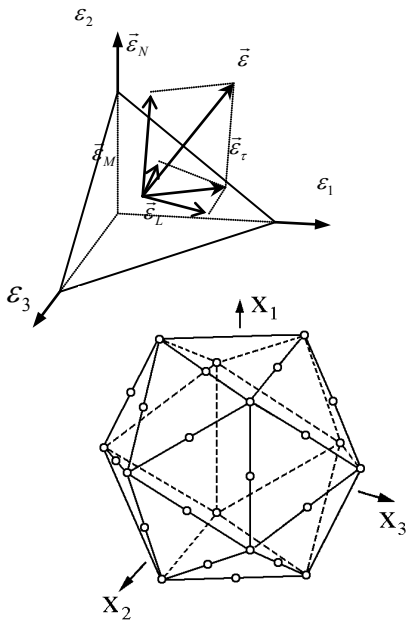
Figure 8. Microplanes modeling technique in which the stress-strain relationships at a material point are mapped onto a sphere with infinite tangent surfaces, and then simplified by selecting a finite number of surfaces.

coefficients between fibers and resin, and applied mechanical stresses, will result in inhomogeneous curing of TRCs structural specimen with built-in local residual stresses and pre-existing micro-cracks. Such local field-variations within the cured material can result in significant differences between virgin material properties and the actual in situ material properties.

The actual response of a structural component made of TRCs can be accurately predicted using only in situ material properties NOT the virgin properties which are typically the presumed input values into an analysis code. Such a practice can introduce inaccuracies which are typically attributed to other sources. It is the primary objective of this project to develop qualitative and quantitative methodologies (and modeling tools) to better understand and predict the in situ properties within a fully cured structural component made of TRCs.

Figure 9 shows the difference in response of one RUC model of a tri-axially-braided carbon-
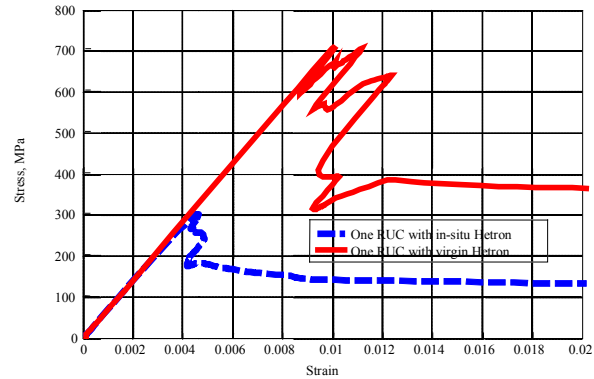
Figure 9. The effect of using virgin matrix properties vs their in situ counterparts on the response of an RUC using finite-element method. The RUC represents a triaxially braided carbon-composite material specimen.

composite material specimen. The figure demonstrates the effects of using virgin matrix properties vs their in situ counterparts on the response of an RUC using a nonlinear finite-element method. Figure 10 shows one of the major sources for such a difference in response which is mostly attributed to differences between (presumed/virgin) and in situ properties.
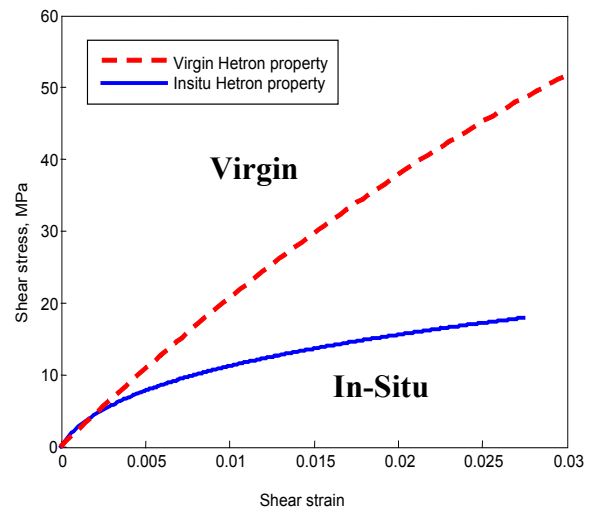
Figure 10. Shear stress vs shear strain of virgin matrix (dashed) as tested in the lab. However, the in situ matrix shear strength and stiffness properties (as shown in the solid blue stress vs strain curve) differ significantly for this specific case. Note that the in situ properties are back-calculated using test data and elasto-plastic theories.

TRC materials are quasi-brittle systems whose energy-dissipation characteristics are dominated

by micro-cracks which are controlled by local geometry and in situ properties. A need exists to develop a robust computational predictive tool which uses as input only stress-relaxation, evolution of extent-of-cure, and thermal conductivity properties measured/calculated from simple mechanical tests without resorting to back-calculations using full nonlinear finite element analysis (FEA) simulations.

Currently, the in situ properties are typically back-calculated using several laboratory tests as well as elasto-plastic analytical theories (in conjunction with computer models). Although this process has been verified and validated, and is based on well established theories from mechanics of materials, it is not efficient especially during the preliminary design process.

This project involves three major aspects: a) spatial material characterization of cured matrix in resin-rich locations, adjacent to fibers within a tow, as well as in between fibers and tows; b) temporal and thermal evolution of constitutive properties (using state-of-the-art optical techniques) as functions of time, extent-of-cure, as well as imposed thermal conditions at the boundaries; and c) development and validation of predictive tools which model the manufacturing and curing processes including mechanical and thermal stresses, visco-elasticity, and visco-plasticity.

More specifically, resin-filled cylinders will be subjected to temperature variations based on manufacturer curing profile. Time and radial variation of temperature, extent of cure, strains and stresses will be measured and calculated.

The cured resin will be removed and subjected to additional mechanical tests. The above detailed procedure will be repeated but with a fiber tow (simulating TRCs) placed concentrically in the cylinder prior to curing and repeated tests. A complete set of experimental results using nano-indentation [Figure 11(a)], Brillouin light scattering (BLS) and Raman light scattering (RLS) [Figure 11(b)], including refined resin properties during curing, and a FE code capable of simulating the MPIE (no flow simulation) are deliverables. The effects of process cure

parameters and their effects on matrix cracking modeled through the thermomechanical FE code is a deliverable.
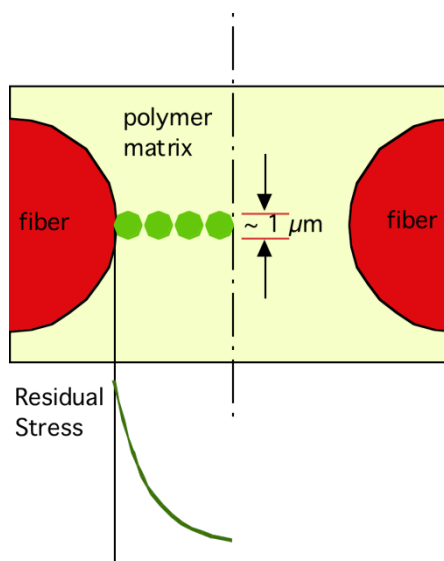

Figure 11(a). Schematic showing examples of locations (four green circles) where nano-indentation may be used to extract values for the modulus distribution near and away from the fiber as well as within resin-rich regions.
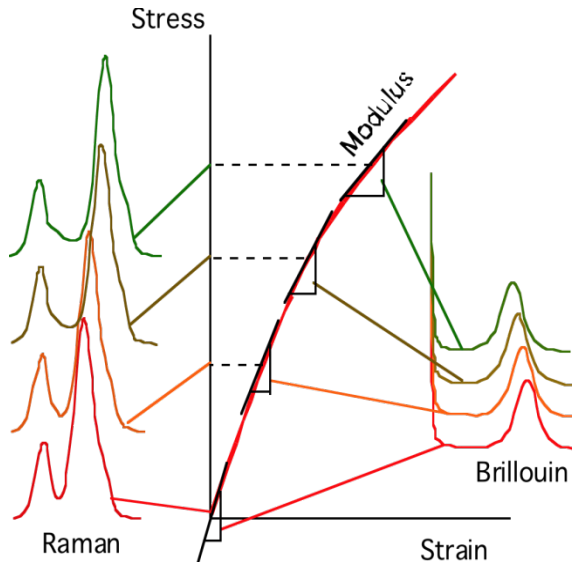
Figure 11(b). Schematic showing the basic idea of using BLS and RLS to estimate the mechanical properties via optical methods.

Figure 12 shows the preliminary results from laboratory tests designed to measure elastic modulus of an Epon resin sample while it is curing (plotted vs time) at different imposed boundary
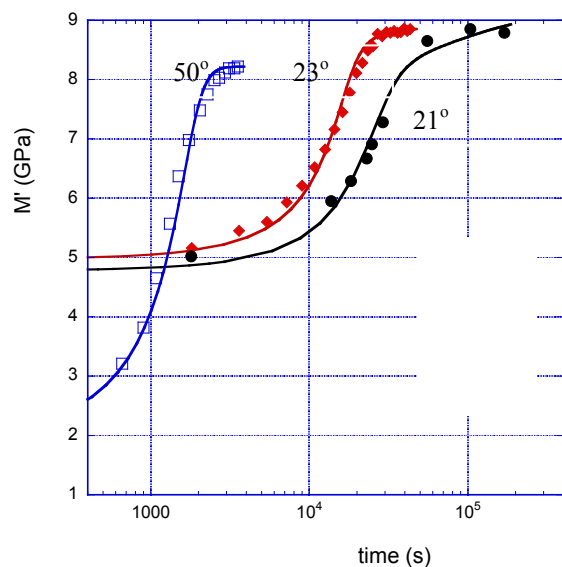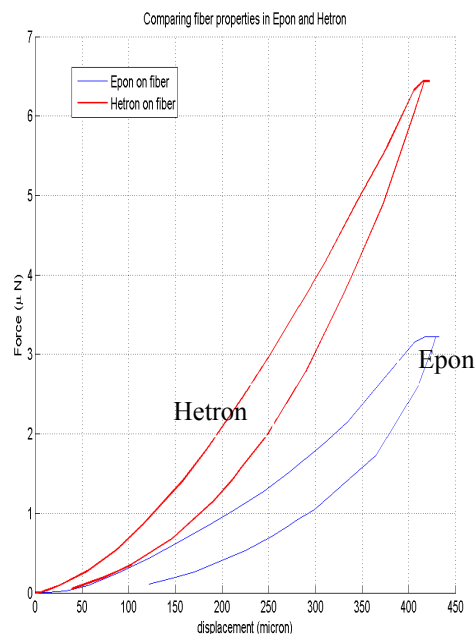
Figure 12. Preliminary laboratory test measurements of elastic modulus (M') vs curing time at different boundary temperatures (21°, 23° & 50°C) for Epon resin. AT higher temperature the resin sample cured faster however it attained a lower final elastic modulus. The tests used optical techniques to measure M'.

temperatures. The tests used optical techniques to measure the modulus.

One of the main outcomes of the project is the development of a predictive tool which can be incorporated into any existing composite material-damage model. Such a tool will eliminate the need for carrying out parallel (and additional) tests as well as extensive nonlinear FEA (as currently is the practice) in order to "back-out" the actual in situ material properties which influence the structural response and local damage characteristics.

Another important contribution of the project is to expose the main factors contributing to such in situ properties and their evolution during the manufacturing and curing process. For example, using nano-indentation it was found that not only matrix properties vary with time (while curing) and with location (i.e., how close to a fiber/tow) but also that because of the very nature of chemical curing, the apparent fiber properties within a tow differ depending on the type of resin (Figures 13 and 14). Here, the somewhat expected preliminary results highlight the importance of

Figure 13. Preliminary laboratory test measurements show the results of using nano-indentation to measure the transverse force-displacement response of two carbon fibers each embedded in a different (cured) resin.
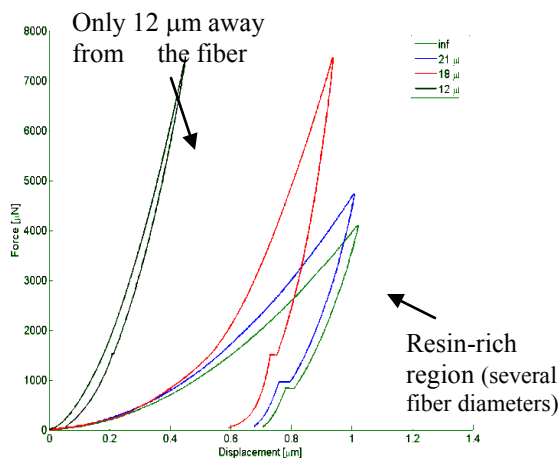
Figure 14. Preliminary laboratory test measurements show the results of using nano-indentation to measure the force-displacement response of the cured matrix as a function of the distance away from the edge of a single carbon fiber embedded in the cured matrix.

understanding the time history, the manufacturing process, and spatial variation of material properties within a cured structural component.

Crashworthiness Assessment of Tubular RaFCs Structures Based on Micro and Interfacial Mechanics

An integrated experimental-computational research program is carried out with the aim of creating a novel Hierarchical, Micro-Experimental and Computational Characterization (HiMECC) algorithm for Random fiber composites (RaFCs). This will be realized through the following four deliverables:

1. Develop computational tools for RaFCs micro-scale material characterization and damage modeling (Figure 15),
2. Conduct experimental work to determine required material parameters and validate numerical analysis tools,
3. Determine key mechanisms responsible for macro-scale damage, and
4. Determine key mechanisms responsible for interfacial damage.
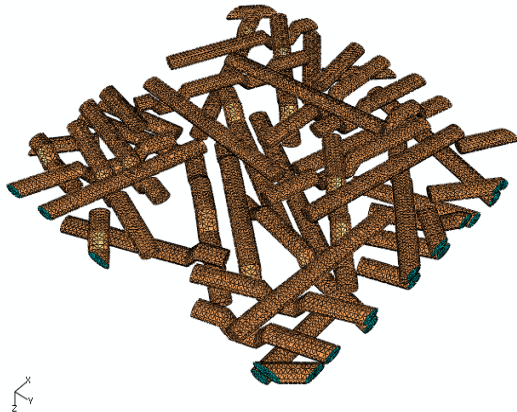
Figure 15. A finite element model of a network of random fibers.

The following milestones have been reached thus far:

1. Completion of an automated FEM analysis procedure using a commercial software package, to statistically investigate the influence of the representative volume element (RVE) size on the elastic properties of the homogeneous material.
2. Validation of the FEM results through comparison with analytical and semi-analytical approaches. In particular we

compared our results with several validation algorithms and models.
3. Scanning Electron Microscopy (SEM) and optical characterization of Glass and Carbon/Urethane specimens.
4. Modeling of a fiber bundle with elliptical fiber bundle cross-section to accurately represent composite materials. We determined the shape of the cross sectional area of the fiber bundles with the aid of optical microscopy and SEM experiments. For the modeling part of the project, a dodecagon inscribed in the ellipse that covers 95.5% of the ellipse area. The 3D fiber bundle was formed by sweeping the ellipse into the 3D space. Moreover, we performed spline modeling, with 3D bundle intersection checks carried out by employing convex optimization algorithms.
5. RVE generation with curved and straight fiber bundles. We were able to generate RVEs (that correspond to real material parameters) with the following characteristics: (1) use of both straight and curved, (2) non-circular fibers, no intersection between fibers, and (3) volume fractions in the 35.1–36.7 % range.
6. We performed tensile experiments to fracture point on the following material systems:
    (1) E-Glass - vf 38%, and
    (2) Carbon/urethane–vf 35%, where vf denotes volume fraction.
7. Performed single fiber debonding simulations. It is well established that the interfacial strength of fiber and matrix affect the performance of fiber composites. We modeled the fiber debonding using cohesive elements. Simulations were run for single fiber composite (SFC) with perfect interface (Figure 16) and SFC with finite interfacial strength (Figure 17).

Each fiber is modeled with hundreds of finite element as well as cohesive elements near the interface. This is used to model the response of a fiber with infinite interfacial strength as well as finite one.
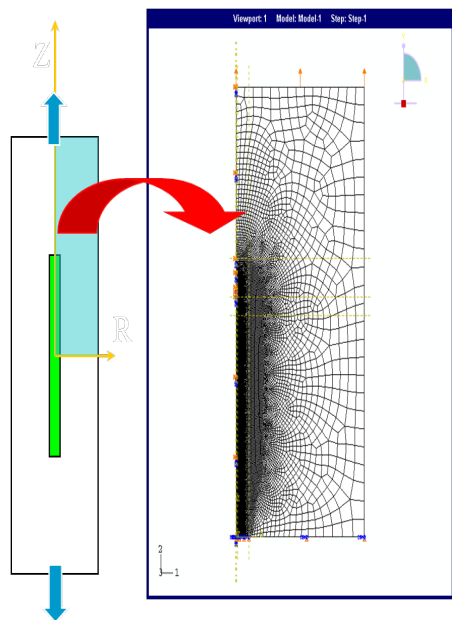
Figure 16. A finite element model of a single fiber, surrounding matrix, and interface.
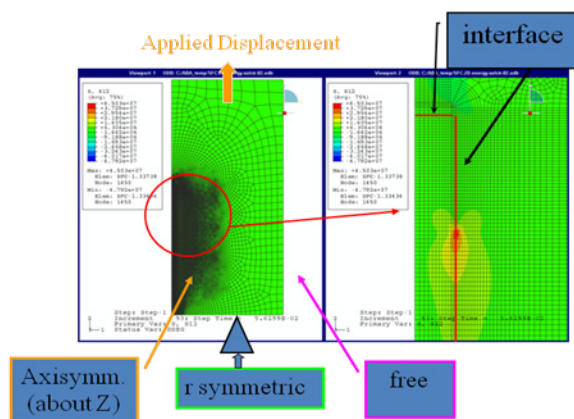
Figure 17. This figure provides an expanded view detailing the regions of interest, as well as the onset of damage initiation at the single-fiber-matrix interface (with finite bonding strength). The figure also shows the finite element modeling and analysis user-interface.

Publications/Presentations

1. Z. Bazant, F. Caner, and C. Hoover (2008), *Mesomechanical Multiscale Elastic-Fracturing Model for Braided Polymer Composites*, **49ᵗʰ AIAA/ASME/ASCE/ AHS/ASC Structures, Structural Dynamics & Materials Conference**, AIAA paper 2008-1932, April 7–10, Schaumburg, IL, p. 6.

2. K. W. Shahwan (2008), *Thinking Out of the Metallic Box—ACC Activities and Challenges*, 2008 Plastic and Composite Intensive Vehicle (PCIV) Safety Workshop, US-DOT/RITA Volpe Center, Cambridge, MA, August 4, p. 27. (http://www.volpe.dot.gov/safety/pciv/ pcivagenda.html)

3. S. Song, A. Waas, K. Shahwan, O. Faruque, and X. Xiao (2009), *Effects of Matrix Microcracking on the Response of 2D Braided Textile Composites subjected to Compression Loads*, **J. of Composite Materials**, paper in print.

4. S. Song, A. M Waas, K. W. Shahwan, O. Faruque, and X. Xiao (2009), *Compression Response, Strength and Post-Peak Response of an Axial Fiber Reinforced Tow*, **International Journal of Mechanical Sciences**, paper in print.

5. S. Song, A. M Waas, K. W. Shahwan, O. Faruque, and X. Xiao (2008), *Compression Response of 2D Braided Textile Composites: Single Cell and Multiple Cell Micromechanics Based Strength Predictions*, **J. of Composite Materials**, Vol. 42, No. 23, pp. 2461–2482.

6. B. Shan, A. A. Pelegri, and Y. Pan (2008), *Interfacial Crack Kinking Subjected to Contact Effects*, **J. of Mechanics of Materials and Structure**s, 3(4):591–605.

7. A. A. Pelegri, L. Iorga, and Y. Pan (2008), *Analysis of 3D Random Chopped Fiber Reinforced Composites Using FEM and Random Sequential Adsorption*, **NSF CMMI Engineering Research & Innovation Conf.**, Knoxville, Tennessee, January 1–10.

J. Engineering Property Prediction Tools for Tailored Polymer Composite Structures

Principal Investigator: Ba Nghiep Nguyen
Pacific Northwest National Laboratory
P.O. Box 999, Richland, WA 99354
(509) 375-3634; fax: (509) 375-6736; e-mail: ba.nguyen@pnl.gov

Principal Investigator: Vlastimil Kunc
Oak Ridge National Laboratory
P.O. Box 2009, Oak Ridge, TN 37831
(865) 574- 8010; fax: (865) 574-0740; e-mail: kuncv@ornl.gov

Technology Area Development Manager: Joseph A. Carpenter
(202) 586-1022; fax: (202) 586-1600; e-mail: joseph.carpenter@ee.doe.gov

Field Technical Manager: Mark T. Smith
(509) 375-4478; fax: (509) 375-4448; e-mail: mark.smith@pnl.gov

---

Objective

- Enable the optimum design of lightweight automotive structural components using long-fiber reinforced injection-molded thermoplastic composites.

Approach

Phase I: Technical feasibility assessment (9/1/05 to 3/31/06)

- Perform a technical assessment of current process models and computational methods for short-fiber polymer injection-molded composites in order to determine their accuracy, limitations and potential applications to long fiber thermoplastics (LFTs).

- Identify the research directions needed to develop process and constitutive models for LFTs.

- Understand and examine the LFT emerging microstructure, characterization techniques and material processing.

- Characterize fiber orientation in LFT samples.

- Examine the molding behaviors of glass and carbon fibers.

Phase II: Research and development (4/1/06 to 9/31/09)

- Develop an integrated approach that links process to structural modeling allowing the optimum design of LFT composite structures. This work includes:

  — Develop process models for LFTs that allow simulations of LFT structures in order to predict flow-induced fiber orientation and other microstructural features.
  — Develop and implement LFT constitutive models for structural finite-element analyses that make use of the composite microstructure predicted by process modeling. These constitutive models will predict the composite thermoelastic properties and its nonlinear behaviors due to damage, fatigue, creep and impact.
  — Develop characterization methods for LFT materials.
  — Injection-mold larger samples and complex geometries.

— Conduct experimental testing to determine the model parameters and validate the process and constitutive models.

Accomplishments

- Injection-molding of long-glass-fiber/polyamide 6,6 (PA6,6) plaques was planned with DuPont, Inc. and RTP Co., which then injection-molded these plaques for the project.

- A new fiber orientation model termed as the anisotropic rotary diffusion-reduced strain closure (ARD-RSC) developed for LFTs was implemented into the ORIENT and Molflow codes.

- ORIENT and Moldflow simulations of the injection-molding of glass/polypropylene (PP) and glass/PA6,6 samples were carried out using the ARD-RSC model.

- A mapping technique was developed to map fiber orientation results from a Moldflow analysis to an ABAQUS finite-element mesh for subsequent structural analyses.

- The elastic-plastic and strength prediction model for LFTs developed last year and implemented in ABAQUS was used to analyze the stress-strain responses of long-glass-fiber/PP specimens.

- An article on microstructural modeling and elastic property prediction for LFTs has been published in the *Journal of Composite Materials*. Another article on the prediction of the elastic-plastic response of LFTs has been accepted for publication in this journal.

- A creep model for LFTs was developed and implemented in ABAQUS, which has been validated against the experimental creep responses of glass/PP specimens.

- A theoretical framework for fiber breakage during injection molding was established.

- A damage model for LFTs was developed and implemented in ABAQUS, which has been validated against the experimental stress-strain responses of long-glass-fiber/PP specimens.

- An integrated approach linking Moldflow's process modeling to an ABAQUS structural analysis was demonstrated in the damage analysis of a holed glass/PP plaque subjected to tensile loading.

- Novel technique for through-thickness fiber length distribution measurement was developed.

- Fiber length distribution was found to vary through the thickness of LFTs.

- Creep properties of LFTs and polypropylene have been characterized.

- Miniature samples for detection of damage on microscopic level have been designed and analyzed.

- Digital image correlation technique was adapted to measure strain in X-ray mechanical tests.

- Injection-molded glass/PA6,6 plaques were X-rayed and analyzed.

- Fiber length distribution and fiber orientation were measured for glass/PA6,6 specimens.

- Quasi-static tests were performed on glass/PA6, 6 samples at -40, 25 and 80°C for 34.3 and 50% fiber weight fractions for 2.8 and 5.85 mm thick samples in flow and cross-flow directions.

- Fracture surfaces were examined using optical and scanning electron microscopy.

- Quasi-static, creep and fatigue tests on PA6, 6 were performed to provide input data for property prediction models.

Future Direction

- Complete the development of a fiber length attrition model.

- Integrate the ARD-RSC fiber orientation model into the fiber length attrition model, implement the integrated model into Moldflow and apply Moldflow to simulate more complex LFT parts.

- Develop a fatigue model and an impact damage model for LFTs.

- Characterize fiber architecture of new materials.

- Characterize creep, fatigue and impact behavior of LFTs.

- Acquire and analyze unique data on damage and plasticity in LFTs.

Introduction

Last year, a new fiber orientation model for long-fiber reinforced injection molded thermoplastic composites (LFTs) termed the anisotropic rotary diffusion-reduced strain closure (ARD-RSC) model was developed allowing fiber orientation in LFT samples to be predicted correctly [1]. This model was implemented in the ORIENT and Moldflow processing codes and was then used in the injection-molding simulation of LFT samples. Fiber orientation predictions using the ARD-RSC model reasonably agreed with the experimental results. Predicted fiber orientations were also used in the elastic-plastic computation of the stress-strain responses of glass/PP specimens loaded to failure. These results were reported in an article accepted for publication in the *Journal of Composite Materials* [2]. This article extends the modeling methodology developed in our previous article [3] to predict elastic-plastic LFT behavior.

Next, progressive damage due to monotonic loading was modeled as both damage and plasticity control the composite stress-strain response. An elastic-plastic damage model based on continuum damage mechanics was developed that accounts for matrix damage coupled with plasticity and fiber/matrix debonding [4]. The response of the composite was obtained using an incremental Eshelby-Mori-Tanaka approach (EMTA) similar to that developed in [2].

Creep modeling of LFTs was also performed that uses an incremental EMTA accounting for elastic fibers embedded in a nonlinear viscoelastic matrix [5]. The viscoelastic behavior of the matrix is described using Schapery's model [6].

A procedure was developed to map Moldflow fiber orientation results into an ABAQUS mesh accurately [7]. This work has enabled an ABAQUS analysis to be performed using orientation results predicted from a Moldflow analysis. Additionally, a theoretical framework for fiber length attrition model for injection-molding of LFTs was developed [8]. This

highly challenging work started with the analysis of the forces due to fiber-fiber contacts that cause fiber breakage. A fiber breakage rate model was sought and will be used to predict fiber length distribution.

Experiments were performed on several material systems for model input and validation. Two molding trials were performed with glass/PA6, 6 materials. RTP Co. molded 15.2 × 15.2 cm plaques of 3 and 6.35 mm thicknesses. DuPont molded 30.5 × 30.5 cm plaques of 2.8 and 5.85 mm thickness with four fiber weight fractions. Initial fiber length measurements revealed significant fiber length attrition in the smaller plaques; therefore, subsequent measurements were performed on the larger samples.

Fiber architecture was analyzed by performing fiber orientation measurements, fiber length measurements and analysis of X-ray images of molded plaques. Quasi-static tests were performed at –40, 25 and 80°C for 34.3 and 50% fiber weight fractions for two thicknesses. Quasi-static tests for neat PA6, 6 samples were performed at identical temperatures along with creep tests to provide input data for model validation. Additional experiments were carried out to characterize creep behavior of glass/polypropylene (PP) material as well as the PP matrix. A novel method for fiber length measurement through the thickness was developed. Initial measurements confirmed prior qualitative observation of variation in fiber length distribution as a function of thickness [9].

Analysis of miniature specimens was carried out so that damage could be isolated from creep on a microscopic level. It was found that optical strain measurement was necessary at the specimen gage length to interpret material response [10]; therefore, a novel measurement technique was developed.

## Approach

Modeling Fiber Orientation

The Folgar-Tucker model [11] has become the standard model for implementation in mold-filling simulation software. However, the reduced strain closure (RSC) model [12] has shown to give more accurate results for short-fiber thermoplastics. During fiscal year 2007, Phelps and Tucker [1] developed the ARD-RSC model for short-/long-fiber thermoplastics. This model was able to predict more accurately all the components of fiber orientation in long-glass-fiber/PP samples. More recently, the ARD-RSC model has been further validated against the experimental orientation data obtained for glass/PA6, 6 samples injection-molded by DuPont. Figures 1 and 2 present the through-thickness fiber orientation distributions predicted by the RSC and ARD-RSC models for a glass/PA6, 6 composite having 40% fiber weight fraction. The z-coordinates normalized by the specimen thickness h are used in Figures 1 and 2. The predictions agree well with the measured fiber orientation also shown in the same figures.
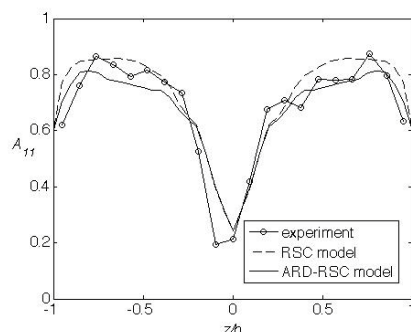
Figure 1. Predicted and measured fiber orientation tensor component A_{11} for a glass/PA6, 6 composite.

Modeling Fiber Length Attrition

Paramount to developing a model for fiber breakage rate is an understanding of the loads placed on fibers. Good models exist for the hydrodynamic loading of fibers in suspension [13], sliding forces arising from fiber-fiber contacts [14] and fiber-fiber contact statistics [15]. At this time, there are no good models for other loading modes such as normal fiber-fiber contact forces that give rise not only to bending (a
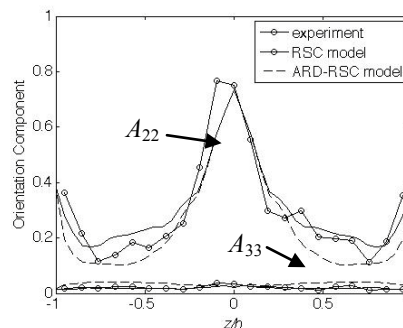
Figure 2. Predicted and measured fiber orientation tensor components A_{22} and A_{33} for a glass/PA6, 6 composite.

suspected fiber failure mode) but also fiber networking. Finally, features in the injection molds such as sharp bends in the runner system or contractions at the gate cause high-stress regions in the flow of the melt and can trap fibers. Both a fiber breakage rate model that incorporates hydrodynamic fiber loading and a conservation equation for total fiber length have been developed. These two models give an evolution equation for the fiber length distribution. If experimental fiber length data suggest the necessity, other breakage rate models incorporating different modes of fiber loading and feature based breakage models may be developed later.

An Elastic-Plastic Damage Model

An elastic-plastic damage model for LFTs was developed that accounts for both plasticity and damage of the matrix material as well as fiber/matrix bonding [4]. Three stages of damage are considered. First, the initiation stage involves both matrix damage and fiber/matrix debonding that can occur simultaneously. Second, the development stage involves the evolution of both mechanisms up to the point of failure due to excessive matrix cracking and fiber/matrix debonding leading to fiber pull-out and rupture (final stage). The final stage corresponds to rupture of the composite.

In the first and second damage stages, the elastic-plastic and damage behavior of the thermoplastic matrix is described by the modified Ramberg-Osgood relation, which expresses equivalent stress in terms of the matrix-effective using the principle

of strain equivalence [16]. Further, using the three-dimensional damage model in deformation [17], a damage evolution law for the matrix material associated with the *J*-2 deformation theory of plasticity, is obtained. Fiber/
matrix debonding is accounted for using the modified Mori-Tanaka model by Qu [18]. While Qu assumed slightly weakened interfaces with constant and low values of the interface compliance, progressive debonding is considered from an eventual perfect interface to a complete debonding state where total frictional fiber/matrix sliding can occur. In addition, a linear relation-ship between the matrix damage variable and damage parameter controlling fiber/matrix interfaces is assumed.

The next step is to compute the current tangent modulus of the matrix material that is affected by both plasticity and damage, and then to use it in incremental EMTA [2, 4] to compute the composite stress increment due to an overall strain increment. Damage can evolve to a critical state characterized by the critical values of the damage variables. Rupture of the composite is predicted to occur when the damage variables attain their critical values. This final stage of damage is modeled by a vanishing element technique that reduces the stress and stiffness of the composite to zero at the locations where rupture occurs.

This elastic-plastic damage model implemented in ABAQUS was used to compute the stress-strain response of LFT specimens up to failure. Figures 3 and 4 shows the flow- and cross-flow direction stress-strain responses of specimens removed from injection-molded glass/PP center-gated disks. The predicted curves using the predicted fiber orientation by the ARD-RSC model reasonably agree with the solutions based on measured fiber orientation and with the experimental results.

An Integrated Approach Linking Process to Structural Modeling

The incremental EMTA has been implemented in ABAQUS by means of user subroutines for structural analysis, an integrated process called EMTA-ABAQUS. In addition, a mapping technique was developed to map fiber orientation results from a Moldflow analysis into an
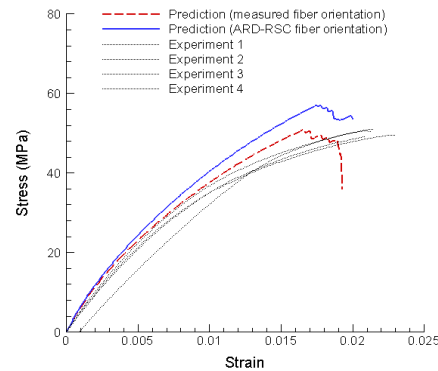

Figure 3. Predicted and experimental flow-direction stress-strain responses of specimens removed from glass/PP center-gated disks.
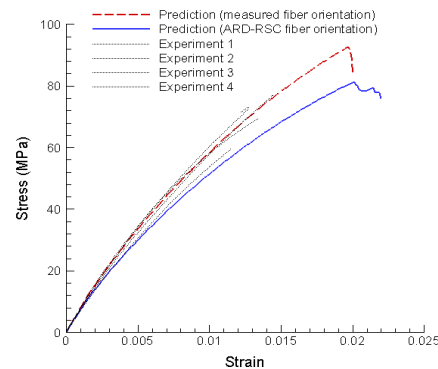

Figure 4. Predicted and experimental cross-flow-direction stress-strain responses of specimens removed from glass/PP center-gated disks.

ABAQUS mesh for subsequent structural analyses [7]. Figure 5 illustrates the position of an open-hole specimen removed from a glass/PP International Standards Organization (ISO)-plaque for an ABAQUS analysis. Figure 6 shows the contour of the orientation tensor component A_{11} for a shell layer that was mapped into the ABAQUS finite element mesh created for analyzing the open-hole specimen.

The ARD-RSC model was used in Moldflow for prediction of the fiber orientation distribution. Next, the elastic-plastic damage model implemented in ABAQUS was used to analyze this holed plaque subjected to tensile loading along its longitudinal direction. Figure 7 shows the contour of the matrix damage variable *D* in this plaque when the applied displacement has attained 0.58 mm. The critical value of this damage
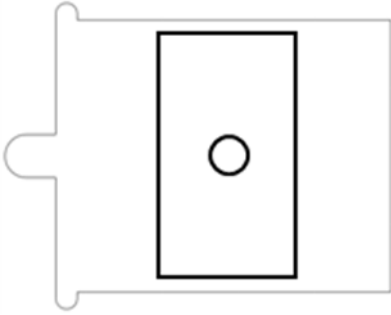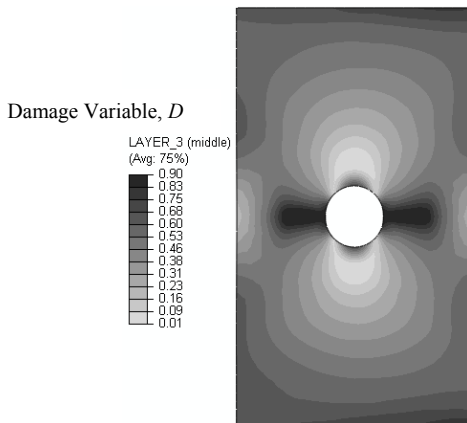
Figure 5. Position of the open-hole specimen removed from a glass/PP ISO-plaque for an ABAQUS analysis.
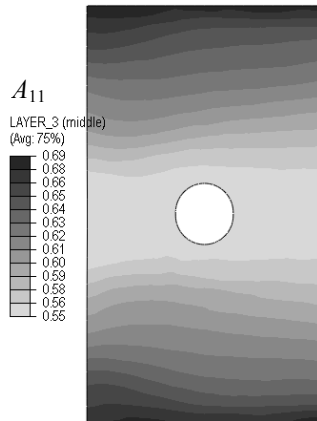
Figure 6. Mapping technique used to obtain the distribution of A_{11} in a shell layer of the open-hole specimen.
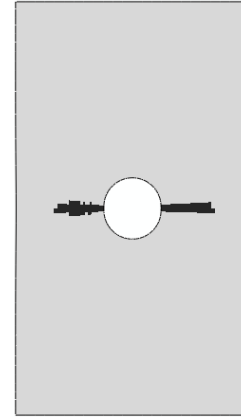
1.

Figure 7. Contour of the matrix damage variable in a shell layer for the applied displacement of 0.58 mm.

variable is 0.9. Damage is predicted to occur from the hole and to expand perpendicularly to the loading direction. Figure 8 shows the crack

propagations in the same layer that were captured by a vanishing element technique.

Figure 8. Prediction of crack propagations (black areas) in a shell layer for the applied displacement of 0.58 mm.

A Creep Model for LFTs

A creep model for LFTs was developed [5] that considers elastic fibers embedded in a nonlinear viscoelastic matrix obeying Schapery's model [6]. The computational procedure is as follows: the composite is first loaded to an overall stress level. The EMTA and fiber orientation averaging technique are then applied to compute the composite stiffness and resulting stress in the matrix. For a given time increment, the viscoelastic matrix experiences a creep strain increment and an increase in creep compliance according to Schapery's model. The stiffness of the composite is then updated at the end of the increment by EMTA using the current properties of the matrix. While the overall applied stress level is maintained constant, the composite experiences a creep strain increment during this time increment. The creep deformation process continues for the next time increment and the composite creep response for the whole period is then determined. The incremental EMTA for creep of LFTs was implemented in ABAQUS via user subroutines. It has been validated using the creep data obtained for glass/PP specimens.

Figure 9 presents the creep responses predicted for the specimens removed along the flow direction of a glass/PP center-gated disk. The computation
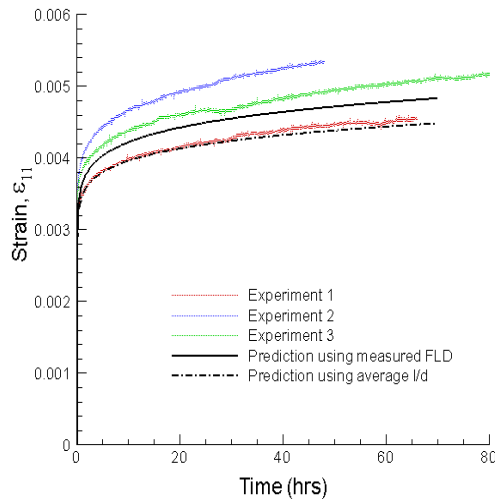
Figure 9. Flow direction glass/PP specimens' creep responses to the applied stress of 15 MPa.

used the experimental fiber length and orientation distributions. To study the effect of fiber length distribution (FLD) on creep response, computation was also performed using the average fiber aspect ratio *l/d* (*l/d*=125 for this composite). The applied stress level used in the experimental tests and computation was 15 MPa. Figure 9 also presents the experimental creep curves obtained for these specimens. Good agreements are found between the prediction using the FLD and experimental results. The solution using the average fiber aspect ratio under-predicts the creep strains. The scatter of the experimental creep results reflects the variation in the LFT microstructure that is strongly governed by fiber length and orientation distributions.

Microstructural Characterization of Glass/PA6, 6 Plaques

X-rays of 30.5×30.5 cm glass/PA6, 6 plaques of 2.8 and 5.85 mm thicknesses molded by DuPont were performed. Segmented X-ray image of the molded plaque in Figure 10 shows a significant size of border regions where filaments did not appear to be distributed uniformly and fiber orientation appeared to differ significantly from that of the center of the plaque. Thicker plaques exhibited higher degree of radial flow compared to thinner plaques.
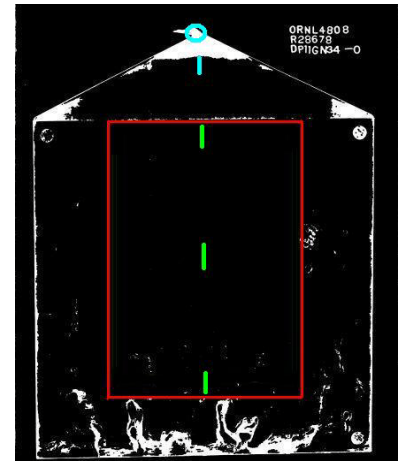
Figure 10. Segmented X-ray digital image of glass/PA6.6 plaque with border regions and sampling locations marked.

Results of fiber length measurements presented in Figure 11 show a notable percentage of fibers less than 1 mm in length regardless of plaque thickness or fiber content. The fraction of short fibers in glass/PA6, 6 samples was significantly higher compared to glass/PP samples.
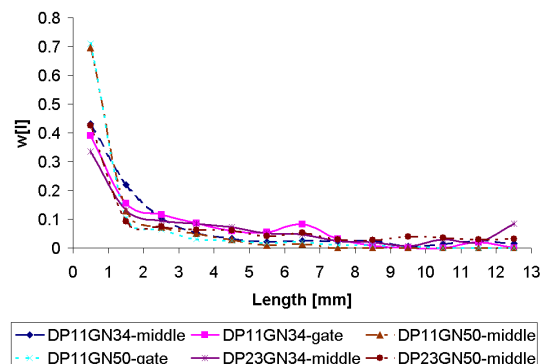
**Figure 11.** Fiber length distribution for glass/PA6, 6 samples.

Fiber orientation measurements were performed using the Leeds method [19]. Typical fiber results as a function of thickness were given in Figures 1 and 2. Distinct core and shell regions could be readily identified by visual observation.

Mechanical Properties of Glass/PA6, 6 Plaques

Mechanical tests were performed on both thin and thick plaques with 34.3 and 50% fiber weight fractions. The 34.3% glass/PA6,6 and previously

examined 40% glass/PP samples have the same fiber volume fraction; therefore, the validity of models developed to date could be checked with different matrix materials before examining materials with higher fiber volume fractions.

Quasi static tests at -40, 25 and 80°C have revealed the expected material behavior with stiffness and ultimate stress increasing with decreasing temperature. Five replicates for each material/thickness/temperature combination were tested in the flow and cross-flow directions in the dry state. Samples were dried in a vacuum at 50°C with periodic weight loss checks. Once their weight had been stabilized, the samples were kept in a vacuum at room temperature. Additionally, a few samples were tested under as-machined condition to check the effect of moisture presence in the material on its mechanical properties. Figure 12 shows typical stress-strain curves of the glass/PA6, 6 samples with flow-direction samples having higher stiffness and strength compared to cross-flow samples.
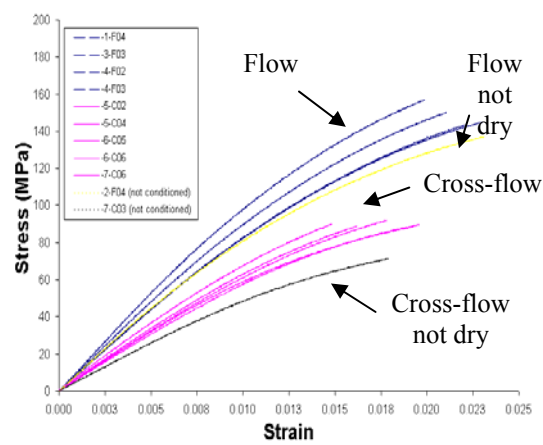
Figure 12. Stress strain curves for 2.8 mm thick glass/PA6, 6 specimens with 34% fiber weight fraction tested at 25°C (F-flow, C-cross-flow).

This behavior is opposite to that observed in glass/PP samples and reflects the difference in relative sizes of shell and core layers resulting from differing fiber length distributions. Plasticization of the matrix material due to moisture is also apparent from the material response. Figure 13 shows the fracture surface of a failed sample with distinct shell and core regions. Fracture surfaces were perpendicular to the
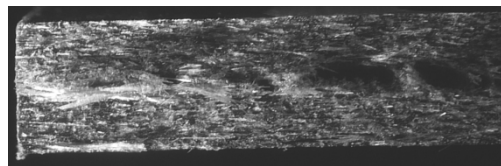
Figure 13. Fracture surface of 2.8 mm thick glass/PA6, 6 specimens with 34% fiber weight fraction tested at 25°C showing distinct shell and core region.

direction of loading with some samples exhibiting considerable post-failure fiber bridging.

Fiber surfaces on the fracture faces were also examined with scanning electron microscopy to determine the nature of fiber-matrix adhesion. Figure 14 shows a typical fiber extending from the fracture face with matrix residuum on the fiber surface. These observations confirmed that the mechanical properties were not diminished due to poor fiber matrix adhesion.
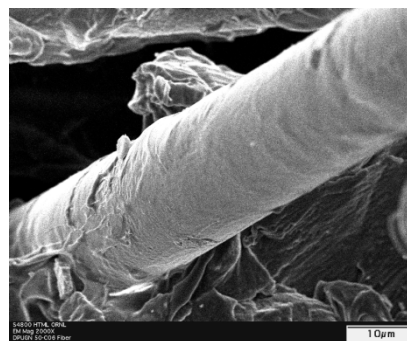

Figure 14. Scanning electron microscope image of a fiber extending from a fracture surface of glass/PA6, 6 material.

In addition to tests on fiber-filled material, mechanical tests were also performed on neat PA6, 6 samples to provide input data for the property prediction models. Quasi-static tests on PA6,6 specimens at -40, 25 and 80°C showed expected increase in strength and stiffness with decreasing temperature, with dry samples attaining greater modulus, strength and lower strain at failure compared to samples containing moisture. Failures were brittle at -40°C and localized necking was observed at room temperature, while extensive material stretching in the gage length was observed at 80°C. Some specimens did not fail at 80°C before reaching the displacement limit of available equipment.

Creep tests on PA6, 6 plaques were performed at room temperature in the dry and as-machined states. The creep response of PA6, 6 was strongly dependent on conditioning.
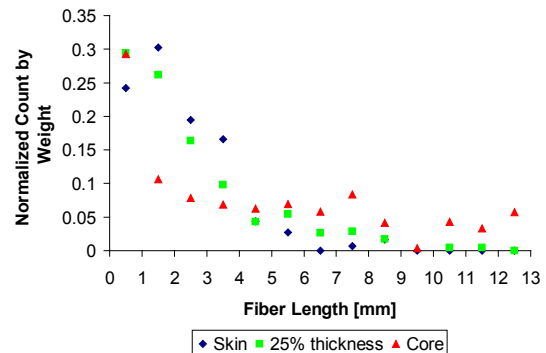
Through Thickness Fiber Length Measurement

Previous measurements and models of FLD assumed no variation in the distribution as a function of thickness. This assumption appeared reasonable; however, it was observed that this assumption may not reflect reality. A method allowing measurement of the FLD at various locations through the thickness of a sample [9] relies on the expansion of the LFT fiber network during burn-off, which increases the sample thickness. The profile of expansion is characterized by measuring the relative displacement of thin wire pieces located through the thickness of a test sample. The location of wires before and after burn-off can be obtained by taking an X-ray and analyzing resulting image. Figure 15 shows the profile of expansion, which appears to be linear with the thickness of the fiber mat being three times that of the original sample thickness. Once the expansion profile is known, one can choose a desired location in the thickness of the original sample and extract fibers for measurement from the corresponding location in the expanded fiber mat. A well defined region of approximately spherical shape can be extracted by depositing a small drop of epoxy through a hypodermic needle in the fiber mat and curing the epoxy.
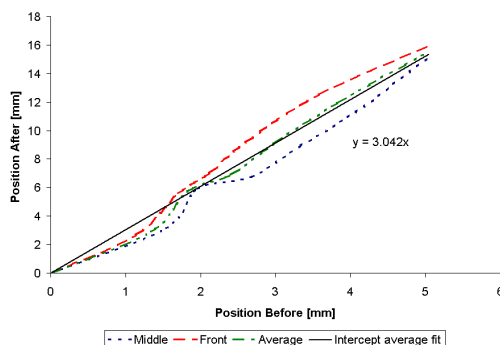
Figure 15. Linear expansion profile in burned-off samples.

Figure 16 shows the FLD measured in a 3 mm-thick long-glass-fiber/PP injection molded disk. Three locations were considered: skin - surface of the sample, 25% of the sample thickness, and core - middle of the sample. It is apparent from the experimental data that the core of the sample retains significantly longer fibers compared to the regions closer to the specimen surface. While the variation of FLD through the thickness should not influence in-plane property prediction, models with an accurate FLD distribution through the thickness should provide better property prediction for out-of-plane loading. These results should also be instrumental in the development and validation of predictive fiber length attrition model.

Figure 16. Fiber length distribution measurements through the thickness of three millimeter long glass/polypropylene disk sample.

Creep Testing of Glass/PP

Creep tests have been performed on a set of glass/PP samples to support the development of the creep model discussed above. Center of dogbone samples coincided with the location of previous fiber orientation and fiber length distribution measurements. A load level of 30% of the average ultimate tensile strength was selected so that the effects of plasticity would be negligible and only visco-elastic effects would be considered. The load level was 21 MPa for specimens with the longitudinal axis aligned in the cross-flow direction and 15 MPa for specimens with the longitudinal axis in the flow direction.

All samples were tested at room temperature, and the given load was ramped to the final value and held for one day. Samples were subsequently unloaded in ramp and held at zero load to observe

recovery. Three replicates of each specimen orientation and mold fill speed were obtained. The property prediction models use fiber and matrix material properties as input. While creep in the fibers can be neglected, it is essential to obtain the visco-elastic properties of the matrix in order to predict viscoelastic response of the composite material. Stress levels in the polypropylene matrix were estimated for the 30% load level. It was determined that adequate load levels of 1, 5, 7 and 10 MPa are adequate for determining the coefficients of Schapery's model for the neat PP [6], and tests were performed in the same manner as for composite samples.

Miniature LFT Specimens – Design and Analysis

The objective of upcoming experiments in this unit is to separate the effects of matrix plasticity and material damage such as micro-cracking and fiber-matrix interface slippage on the stress strain response of the composite material.

Due to inherent physical limitations, samples in these experiments must be very small. A shoulder loaded double-dogbone specimen with 1 x 1 mm cross-section has been designed. Two phenomena have been investigated using finite- element analysis. First, the effect of mismatch in shoulder radius between the sample and the grip due to imprecision in manufacturing of these miniature samples from fiber-reinforced thermoplastic was considered. It was concluded that the stress profile within the sample and its load-displacement response vary significantly as a function of the shoulder radius mismatch [10]. It is therefore imperative to measure deformation of the material in the gage length optically, because displacement measured at the sample shoulder will not provide useful information. Second, relaxation of the sample during pauses for imaging has been studied because the load loss during imaging has been significant in preliminary tests. It was determined that load loss of the sample is influenced by the shoulder radius mismatch; therefore, correlation between load shedding of the sample and material relaxation will not provide useful results. Since optical measurement of gage length deformation along with load data has to be considered in order to describe material response, a digital image

correlation technique has been adapted to provide localized strain measurement in the sample gage length. Fiber crossings X-rayed at appropriate angle have been shown to provide an appropriate pattern for digital image correlation. This technique allows not only average strain measurement of the gage length but also provides information about the strain variation within the gage length.

Conclusions

Process and constitutive models as well as computational tools have been developed and integrated to predict the flow-induced fiber orientation successfully and the resulting linear and nonlinear responses of LFTs. The relevant nonlinear behaviors of LFTs that were studied are elastic-plastic, progressive damage and creep behaviors. An elastic-plastic damage model and a creep model for LFTs were developed and implemented in ABAQUS. Accounting for both plasticity and damage has enabled better predictions of the LFT stress-strain responses up to failure. The creep response of LFTs was modeled, and our analysis has shown important

effects of fiber length and orientation on the creep response. Fiber architecture was characterized via X-ray imaging, optical fiber orientation measurement and fiber length distribution measurement. The quasi-static response of LFTs was measured at three temperatures and the creep response was obtained at room temperature. Properties of the neat polymer were measured to provide input for property prediction models. Experimental characterization was coordinated with model development and validation to improve specific areas of predictive capabilities of process as well as property prediction models. Novel experimental techniques were developed for fiber length measurement as a function of thickness and for local strain measurement during a tensile test with X-ray imaging of LFTs. These techniques provide unique insight into the architecture and response of LFTs.

An integrated approach linking process modeling to structural analysis with support of microstructural characterization has been developed and improved in an ongoing effort to

enhance predictive capabilities for lightweight automotive structures using LFTs.

Presentations/Publications/Patents

1. See Reference 1.

2. See Reference 3.

3. See Reference 2.

4. See Reference 4.

5. See Reference 7.

6. See Reference 5.

7. Nguyen B. N. et al. 2008. "An Elastic-Plastic and Strength Prediction Model for Injection-Molded Long-Fiber Thermoplastics." Proceedings of the 23rd Technical Conference of the ASC, Memphis, TN.

8. Phelps J. H. and C. L. Tucker III. 2008. "An Anisotropic Rotary Diffusion Model for Fiber Orientation in Short- and Long-Fiber Thermoplastic Composites." American Regional Meeting of the Polymer Processing Society, Charleston, SC.

References

1. J. H. Phelps and C. L. Tucker III (2008). "An Anisotropic Rotary Diffusion Model for Fiber Orientation in Short- and Long-Fiber Thermoplastics," *J. Non-Newt. Fluid Mech.*, in press.

2. B. N. Nguyen, V. Kunc, J. H. Phelps, C. L. Tucker III, and S. K. Bapanapalli (2008). "Prediction of the Elastic-Plastic Stress-Strain Response for Injection-Molded Long-Fiber Thermoplastics," *J. Compos. Mater.*, in press.

3. B. N. Nguyen et al. (2008). "Fiber Length and Orientation in Injection-Molded Long-Fiber Thermoplastics – Part I: Modeling of Microstructure and Elastic Properties," *J. Compos. Mater.*, **42**:1003–1029.

4. B. N. Nguyen and V. Kunc (2008). "An Elastic-Plastic Damage Model for Long-Fiber Thermoplastics," *Int. J. Damage Mech.*, submitted.

5. B. N. Nguyen et al. (2008). "Creep Modeling for Injection-Molded Long-Fiber Thermoplastics," Proceedings of the ASME IMECE 2008, Boston, MA, paper # IMECE2008-66335.

6. R. A. Schapery (1969). "On the Characterization of Nonlinear Viscoelastic Materials," *Polym. Engn. Sci.*, **9**(4): 295–310.

7. B. N. Nguyen et al. (2008). "An Integrated Approach Linking Process to Structural Modeling with Microstructural Characterization for Injection-Molded Long-Fiber Thermoplastics," Proceedings of SAMPE 2008, Memphis, TN.

8. J. H. Phelps and C.L. Tucker III (2008). "Processing-Microstructure Modeling for Long-Fiber Thermoplastics," Internal Report submitted to PNNL.

9. V. Kunc et al. (2008). "Techniques and Results for Fiber Length Distribution Determination as a Function of thickness in Long fiber reinforced injection molded thermoplastics," Proceedings of 8th-Annual SPE Automotive Composites Conference & Exhibition, Troy, MI.

10. V. Kunc et al.(2008). "Design of Fiber Reinforced Polymer Specimens for Examination with Micro-tomography under Tensile Loading," Proceedings of SAMPE 2008, Memphis, TN.

11. F. Folgar and C. L. Tucker III (1984). "Orientation Behavior of Fibers in Concentrated Suspensions," *J. Reinf. Plast. Comp.*, **3**: 98–119.

12. J. Wang et al. (2008). "An Objective Model for Slowing Orientation Kinetics in Concentrated Fiber Suspensions: Theory and Rheological Evidence," *J. Rheol.*, **52**:1179–1200. See also: U.S. Patent 7,266,469 (2007).

13. S. M. Dinh and R. C. Armstrong (1984). "A Rheological Equation of State for Semi-Concentrated Fiber Suspensions," *J. Rheol.*, **28**(3): 207–227.

14. M. Djalili-Moghaddam, and S. Toll (2005). "A Model for Short-Range Interactions in Fiber Suspensions," *J. Non-Newt. Fluid Mech.*, **132**: 73–83.

15. S. Toll (1998). "Packing Mechanics of Fiber Reinforcements," *Polym. Engn. Sci.*, **38**: 1337–1350.

16. J. Lemaitre (2002). "Introduction to Continuum Damage Mechanics," in: *Continuum Damage Mechanics of Materials and Structures*, Allix, O. and Hild, F., eds., pp. 235–258, Elsevier Science Ltd, Oxford, United Kingdom.

17. J. Lemaitre and J. L. Chaboche (1985). "Mécanique des Matériaux Solides," Dunod, Paris, France.

18. J. Qu (1993). "The Effect of Slightly Weakened Interfaces on the Overall Elastic Properties of Composite Materials," *Mech. Mater.*, **14**:269–281.

19. A. R. Clarke et al. (1990). "A Multitransputer Image Analyzer for 3D Fibre Orientation Studies in Composites," *Trans. Roy. Microsc. Soc.*, **1**: 305.

K.   Predictive Modeling of the Structure and Properties of Polymer-Matrix Composites: NSF/DOE Grant Projects

DOE Technology Area Development Manager: Joseph A. Carpenter
(202) 586-1022; fax: (202) 586-1600; e-mail: joseph.carpenter@ee.doe.gov

National Science Foundation (NSF) Grant Monitor: Joycelyn S. Harrison
(703) 292-7088; e-mail: j-harris@nsf.gov

Objective

- The objective of the six projects in this program, jointly funded by NSF and DOE and administered by NSF as grants, is to perform fundamental development of modeling, simulation and processing of polymer composite materials. These projects support the DOE-funded "Engineering Property Prediction Tools for Tailored Polymer Composite Structures" project being conducted jointly by Oak Ridge National Laboratory (ORNL) and Pacific Northwest National Laboratory (PNNL) (see report 8.J). The NSF/DOE-funded projects are intended to investigate alternate modeling and processing approaches that can contribute to more fundamental understanding of the mathematical and physical behavior of fiber-reinforced polymer composites. The following sections provide a high-level summary of one grant's objectives and work progress during 2008. Full reports on four others are found in reports 8.L–8.O.

Comparative Determinations of Orientation in Injection-Molded Thermotropic Liquid-Crystalline Copolyester (TLCP) Plaques

Principal Investigator: Robert A. Bubeck
Michigan Molecular Institute (MMI)
1910 West St. Andrews Road
Midland, MI 48640
(989) 832-5555; fax: 989-832-5636;
e-mail:Bubeck@mmi.org

Co-Principal Investigator: Wesley R. Burghardt
Northwestern University
Robert McCormick School of Engineering and Applied Science
Dept. of Chemical Engineering
2145 Sheridan Road, Evanston, IL 60208-3120
(847)-467-1401;
e-mail: w-burghardt@northwestern.edu

NSF Award No. DMI-0521771

Objective

Thermotropic liquid crystalline polymers (TLCPs) offer considerable promise as high strength, lightweight engineering materials. Understanding, manipulation and control over the evolution of molecular orientation during injection molding is a necessary prerequisite towards optimized fabrication of TLCP net-shaped parts. Based upon knowledge gained in this and previous work, we shall implement new modeling strategies to predict orientation development, coordinated with cutting-edge synchrotron techniques to characterize the resulting orientation state.

Approach

1. The development and application of *in situ* capabilities to perform x-ray scattering measurements of molecular orientation *in real time* within the injection molding cycle.

2. Exploitation of novel spectroscopy techniques (Near Edge X-ray Absorption Fine Structure (NEXAFS) and Attenuated Total Reflectance Fourier Transform Infrared (ATR-FTIR)) that offer new capabilities for unprecedented three-dimensional (3-D) characterization of the molecular orientation distribution within the surface layer of moldings.

3. Formulation of new modeling strategies to predict orientation development employing so-called 'polydomain' description of orientation which facilitates direct connection to experimental measurements of orientation.

Research and Education Activities

The influences of molding parameters and mold thickness on the anisotropy, skin-core morphology, and mechanical properties of injection-molded commercial TLCPs are being studied. Key observations and milestones for the year 2008 include the following commentary.

A comprehensive NEXAFS characterization was performed on a selected 76 mm x 51 mm narrow-gated injection-molded plaque surface using the new 6-axis manipulator in the experimental chamber of the soft X-ray materials characterization beam line, U7A, at the National Synchrotron Light Source (NSLS) at Brookhaven National Labs. The narrow-gated plaques are of great interest because of their flow complexity. The samples were fabricated of commercially-available VECTRA A950 TLCP. Our graduate student on the project (Mr. Fang) gained further expertise in NEXAFS under the direction of Dr. Bubeck and wrote the driver routine that controlled the position and angles of the manipulator and sample programmatically while collecting an extensive set of NEXAFS spectra. Both the maximum orientation and its direction on the plaque surface were mapped for nine positions. This was the first time that so large a sample (38 mm $\times$ 51 mm) had been investigated using the manipulator in the U7A sample chamber.

A Herrick Seagull Variable Angle Reflectance ATR-FTIR dichroism accessory was used to determine maximum surface orientations and their directions corresponding to the positions interrogated using NEXAFS at the NSLS. An undergraduate student (Ms. Burgard), who is in cooperative employment at MMI and biology major at Saginaw Valley State University assisted us in performing the ATR-FTIR measurements. The agreement between the NEXAFS and ATR-FTIR mapping of surface orientation was excellent for magnitude and very good for directional maxima. This effort represents the first time that two surface spectroscopy techniques have been used in conjunction to determine the surface orientation of an injection-molded part.

Simulations of injection molding have been and continue to be performed by Mr. Fang under the

direction of Professor Burghardt at Northwestern University using process parameters provided via the injection molding efforts undertaken at MMI to prepare plaques for mechanical, 2-dimensional wide angle X-ray scattering (2-D WAXS), and surface spectroscopy characterizations. The surface techniques and 2D-WAXS have been used to map orientation in the "skin" and "core", respectively. The simulation strategy drawing upon Folgar-Tucker concepts within the Moldflow modeling platform has yielded results that mimic the experimental orientation mapping of the plaques.

Findings

Extensive mapping of the surface orientation of a complex injection-molded part (narrow-gated plaque) has been done for the first time. Two surface spectroscopy methods were utilized (NEXAFS and ATR-FTIR) with very good agreement between the two techniques. Computer simulations for our two plaque configurations predict the "skin" orientation fields, as well as those obtained via 2D-WAXS for the "core" very well.

Future Direction and Project Completion

- Complete any remaining required ATR-FTIR measurements.

- Perform "short shot" injection molding experiments to verify some predictions for mold filling derived from our simulations.

- Coauthor with Northwestern University colleagues and submit an extensive paper that will tie together the orientation mapping with the molding simulations.

Acknowledgments

Journal Publications

1. J. Fang, W. R. Burghardt, and R. A. Bubeck; "Polydomain Model Predictions of Molecular Orientation in Isothermal Channel Flows of Thermotropic Liquid Crystalline Polymers"; *Poly. Eng. Sci.*, 2259 (2008).

2. S. Rendon, J. Fang, W. R. Burghardt, and R. A. Bubeck; "An Apparatus for In-situ X-ray Scatting Measurements during Polymer Injection Molding"; Submitted to *Review of Scientific Instruments*, December, 2008.

Simulation of Compression-Resin Transfer-Molding Process for Manufacturing Net-Shape Structures

Principal Investigator: Suresh G. Advani
Department of Mechanical Engineering
University of Delaware
Newark, DE 19716
(302) 831-8975; fax: (302)-831-8525;
e-mail: advani@me.udel.edu

NSF Award ID: 0521789

All liquid composite molding (LCM) processes require one to place a fibrous preform inside the mold. The mold is sealed and a liquid resin is injected to saturate the preform. The fibers in the preform and the preform itself are usually stationary but in some variations they may undergo small (and slow) deformation during the injection process. Next, the resin is allowed to cure and the part is removed. Two commonly used techniques in this process are resin-transfer molding (RTM) and vacuum-assisted resin-transfer molding (VARTM).

The subject of this work, compression resin-transfer molding (CRTM) differs from the other LCM processes by injecting the resin before the mold is fully closed and preform compacted. The gap between preform and mold surface serves for uniform resin distribution over the part surface. Following mold closure and preform compaction then distributes the resin through the preform thickness.

This process offers the potential to manufacture moderately-sized structures in a few minutes while preserving the advantages of RTM, net-shape manufacturing of complex curvatures with Class A surface finish.

In all LCM variations, the flow of the resin through the preform is important. If particular sections of the preform remain dry after the injection is complete, the resulting void will seriously compromise the part properties. The cost of trial-and-error part design created a need for the simulation of the filling process using science-based process model. For conventional RTM processes, many reliable computer simulation tools have been established and validated with experiments. However, for the other LCM variations the modeling tools are scarce and RTM tools are usually adapted, though the results are sometimes not quite satisfactory.

The resin flow in CRTM process is more complex than in any other LCM variation. It exhibits three distinct stages. All of the phases can be modeled as flow through porous media under different boundary and initial conditions. The three stages are

1. Resin injection into the narrow gap between the mold platen and the fiber preform in the mold.

2. Closing of the gap while squeezing the resin into preform without direct contact between movable tool part and the preform.

3. Compaction of the preform by the mold platen along with continuing resin impregnation.

Research and Education Activities

No full report or summary submitted. A full report is expected in the annual progress report for fiscal year 2009.

L.   Hierarchical, Structure-Oriented Stochastic Approach to Model Liquid Molding Processes

Principal Investigator: Thanasis D. Papathanasiou
Department of Chemical Engineering
University of South Carolina
Columbia, SC 29208
(803) 777-7219; fax: (803) 777-6245; e-mail: papathan@engr.sc.edu

Department of Energy Technology Area Development Manager: Joseph A. Carpenter
(202) 586-1022; fax: (202) 586-1600; e-mail: joseph.carpenter@ee.doe.gov

National Science Foundation Monitor: Joycelyn S. Harrison
(703) 292-7088; fax: (703) 292-9056; email: j-harris@nsf.gov

Objective

- Our overall objective has been to develop models for the hydraulic permeability of fibrous media, taking explicit account of the underlying microstructure and its variability. A specific task for the preceding period was to investigate the effect of fiber clustering on the hydraulic permeability (K) of unidirectional random fiber arrays—this is covered in the first section of this report and the references identified therein. In addition, we computationally studied Stoke's flow at the interface between a fluid and a fiber bed. This was a collaborative study initiated by Prof. Pillai at the University of Wisconsin-Milwaukee and is covered in the second section. We also used the parallel boundary element method (BEM) to simulate solute transport across membranes filled with high aspect ratio platelets in order to elucidate the effect of microstructure on the anticipated barrier improvement factors (third section). Finally, experimental measurements of fluid velocities in the interstitial spaces within fiber arrays were carried out at Lulea University of Technology in Sweden (Prof. Lundstrom) using micro particle image velocimetry (PIV) in the fourth section.

Approach

- Our approach is computational. A large number of simulations have been carried out, using a parallel implementation of the BEM, in microstructures consisting of ~100s of fiber cross sections placed within a containing unit-cell by a Monte Carlo (MC) procedure. This allows a direct and unambiguous correlation between (K) and the microstructure of the fiber arrays.

Accomplishments

- The extent of fiber clustering is quantified using a new scalar metric, based on Ripley's K-function [1].

- The extent of fiber clustering is linked to the dimensionless temperature of the fiber assembly, as defined in the context of the Number-Volume-Temperature (NVT) Monte-Carlo process.

- Stokes flow simulations across such systems were carried out and the results, in terms of the principal permeabilities, were correlated with the above-mentioned microstructural metric.

- Analytical models for the transition of flow from an open channel into a fibrous medium have been evaluated by comparing their predictions to the results of first principles computation using the BEM.

- Analytical models for the effective transport coefficient of composite membranes have been evaluated by comparing their predictions to the results of first principles computation using the BEM.

- Obtained velocity profiles within fibrous media using the method of micro Particle Image Velocimetry.

Future Direction

- Not applicable since the project completed in September 2008.

Flow Through Clustered Systems [2]

This work has been published in [2] and relies on developments reported in our earlier work [3–5] to which interested readers are referred. Most previous studies of the permeability of fibrous media are based on periodic or random fiber arrays. There are relatively fewer studies that discuss the influence of the other commonly observed microstructural feature (i.e., fiber clustering, on the microscopic permeability). In fact, fiber clustering manifests in several ways. It is either naturally formed or purposely introduced. An example of the latter case can be found in a typical composite preform, where individual fiber strands are first bundled into tows and then the fiber tows are used to form a two dimensional or three dimensional woven mat. Direct numerical modeling studies of structured dual-scale fibrous medium, in which the arrangement of the fiber tows as well as the arrangement of fibers inside the fiber tow are periodic are limited. In this study we are concerned with the dependence of permeability on the microstructure that exhibits a random clustering feature. By the term "random clustering," we mean that the fiber cluster size distribution, the fiber cluster spatial distribution, and the fiber arrangement in a fiber cluster are not organized. Such clustering patterns may be induced by electrostatic forces or adhesive molecular forces, or by external forces that perturb an originally organized pattern. At this instance we are not interested in the physical mechanisms that underline the formation of such random clustering. Instead, we assume that a generic clustering model is suitable for us to establish the correlation between the permeability and a microstructural parameter that captures the key feature of clustering. For this purpose, we use the Monte Carlo method with the Lennard-Jones potential to generate different clustered fiber distributions, and determine the permeability of these distributions by solving the entire flow field

using the boundary element method (BEM). Our numerical results show that the permeability can be statistically correlated with several microstructural parameters.

Continuing from studies reported earlier, we consider the introduction of a clustering or aggregation mechanism for placing fibers. It is assumed that clustering of fibers can arise due to the presence of a short-range attractive force among fibers. Such clustered fiber distributions can be generated by the Metropolis Monte-Carlo method, a process during which the minimization of the system potential energy is being sought. In this process, fibers are moved from their initial location; the change in the system potential energy is calculated for each attempted move; any downhill move in energy will be accepted and any uphill move in energy will be accepted with a probability of $\exp(-\Delta E / k_B T)$ (T is temperature, ΔE is the energy change and k_B is the Boltzmann factor). To carry out this Monte-Carlo process, an explicit form of pair potential that describes the repulsive and attractive forces between a pair of particles must be provided in order to compute the system potential energy. For simplicity, we assume the hard-disk potential at distances $r \le r_\sigma$, accounting for the fact that fibers are not penetrable, and at $r > r_\sigma$ we take the Lennard-Jones potential to include the attractive force. This is given as

$$v(r) = \begin{cases} \infty & r \le r_\sigma \\ 4\varepsilon \left[\left(\dfrac{r_\sigma}{r} \right)^{12} - \left(\dfrac{r_\sigma}{r} \right)^6 \right] & r_\sigma < r < r_c \\ 0 & r > r_c \end{cases} , \quad (1)$$

where v is the pair potential, ε is the depth of the potential well, r_σ is the finite distance at which the potential becomes positive and r_c is the cutoff

distance after which the tail part of the potential is neglected. The fiber distributions thus generated are affected by T, ε and r_σ. In this study, we fixed ε (=1) and r_σ (=1.05D_f, where D_f is the fiber diameter), thus the resulting fiber distributions are dictated by T, as can be observed visually in Figure 1. In general, the extent of fiber clustering is inversely related to T.
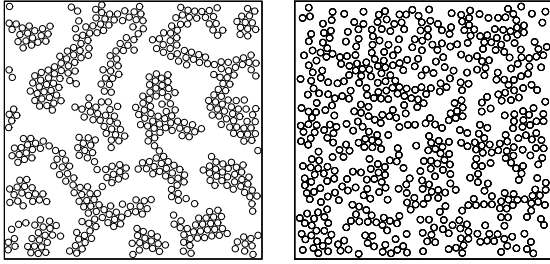
Figure 1. Sample distribution generated by the Metropolis MC method. The number of fibers in the assembly is N_f=576, the porosity ϕ=0.7, the minimum allowable inter-fiber distance is δ_{min}=0.05D_f and T^*=0.25 (left) and T*=1.0 (right). The extent of fiber aggregation decreases as the dimensionless temperature ($T^*=k_BT/\varepsilon$) is increased.

In principle, the Ripley's K function [1] is capable of discriminating between different fiber distributions. However, for quantification purposes, it is desirable to reduce $K(r)$ to some appropriate scalar value. In this direction we suggest the use of a microstructural parameter (χ), indicative of the deviation of a given pattern from complete randomness.

This is based on the averaging of the ratios between the $K(r)$ of a given microstructure and πr^2, the $K(r)$ of a Poisson distribution. The definition is

$$\chi = \frac{1}{b-a}\int_a^b \frac{K(r)}{\pi r^2}\,dr \approx \frac{1}{m}\sum_{i=1}^m \frac{K(r_i)}{\pi r_i^2} \quad , \qquad (2)$$

where [a, b] is the length scale range of interest. Usually, a is the fiber diameter, and b has to be larger than the largest fiber cluster size. In this study, we chose b to be one fourth of the computational domain. For fiber distributions generated by the Metropolis Monte Carlo method at different T^* values, the χ measures were obtained and the results are plotted versus T^*, as shown in Figure 2. An inverse relation between T^*

and χ is indicated for $0.25 \leq T \leq 1.0$. Outside this range, χ measure does not seem to vary much with T^*.
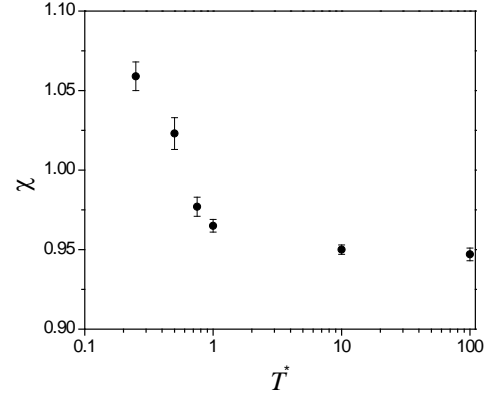
Figure 2. Plot of χ versus T^* for fiber distributions generated by the Metropolis method. At each T^*, ten distributions are generated. The microstructural parameter χ is evaluated for each distribution and the averages along with the $\pm\sigma$ error bars (based on the absolute values) are shown.

The Stokes equations are used to model saturated, slow viscous flow in the inter-fiber space, for the problems defined on the two-dimensional geometries shown in Figure 1. The governing equations are

$$\nabla \cdot \mathbf{u} = 0 \qquad \text{on } \Omega \quad \mu\nabla^2\mathbf{u} = \nabla p \qquad \text{on } \Omega \ , \quad (3)$$

in two dimensions, where $\mathbf{u}$, p, μ and Ω denote the velocity vector, pressure, viscosity and the flow domain, respectively. The boundary element method is used to convert Eq. (3) into boundary integral equations that involve boundary fluid velocities and tractions only. These are solved as presented in [3–5]. In this study, isoparametric quadratic boundary elements were used to discretize the governing equations. Typically, 36 nodes were used to discretize a fiber boundary. The resulting linear system of equations from the BEM is dense and asymmetric.

When hundreds of fibers (or $\geq 2 \times 10^4$ unknowns) are involved in a simulation, the solution task becomes computationally prohibitive on a single workstation. To overcome this difficulty, a parallel boundary element code that can use distributed-memory computing resources was developed. The

code was written in Fortran 90 and built on top of MPI, BLACS and ScaLAPACK libraries. The BEM solution yields the fluid velocities on the representative volume element (RVE) boundaries, from which the average velocity $\bar{u}$ can be obtained. The transverse permeability of the corresponding system can be computed by returning to Darcy's law, which gives $K = \bar{u}\mu L / \Delta p$, where (L) is the length of the RVE in the direction of the imposed pressure drop (ΔP), while (μ) is the fluid viscosity. One example velocity profile is shown in Figure 3.
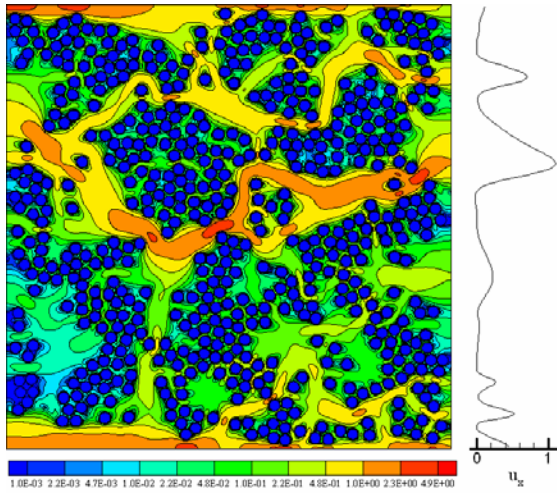
Figure 3. Plot of fluid speed contours and the resulting boundary velocity profile (u_x) from which the effective permeability is calculated, for a simulation containing 576 fibers at ϕ=0.7.

A correlation between the scalar metric (χ) and permeability has been obtained by carrying out a large number of simulations in geometries which exhibit various degrees of clustering. The results are summarized in Figure 4.

## **Flow at the Interface Between a Clear Fluid and a Fiber Bed [6]**

Problems involving fluid flow through a channel bound by porous surfaces are often encountered while modeling flow in liquid composite molding (LCM) processes. To conduct flow simulations inside a fiber preform unit-cell, proper boundary conditions need to be applied at the interface between the clear-fluid region and the fibrous porous medium. Our intention is to study computationally Stokes flow at such an interface

and compare the results with the predictions of existing models derived under certain assumptions concerning the boundary conditions at the clear-fluid/porous medium interface.
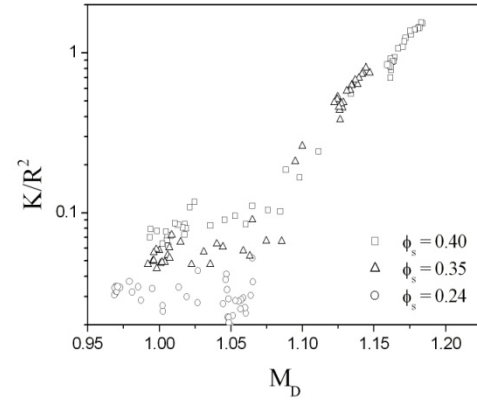

Figure 4. Correlation of the dimensionless permeability K_p/R_f^2, where R_f is the fiber radius, with the scalar metric ($M_D=\chi$) defined by Eq. (2), for fiber distributions showing various degrees of clustering. Moving to lower χ, as indicated by the arrow, results in less clustered microstructures.

With this objective in mind, we place a 2-D porous medium, made of a square arrays of cylinders of radii 10μm each, adjacent to a clear-fluid region in form of a channel (Figure 5). The depth *H* of clear fluid region is 720μm. The porosity ε of the porous medium region varies from 0.5 to 0.9 by changing the inter-cylinder space *e*. The boundary element method (BEM) is employed to solve the point-wise Stokes equation in such a domain.
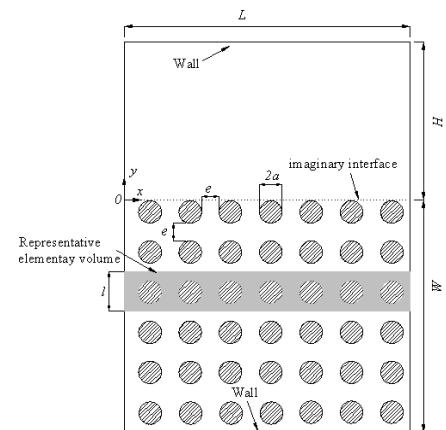
Figure 5. Simplified sketch of the model used in the point-wise simulation of Stokes equation using the BEM.

The Stokes and Brinkman equations are respectively used to model the steady-state creeping flow in the channel and porous medium shown in Figure 6.
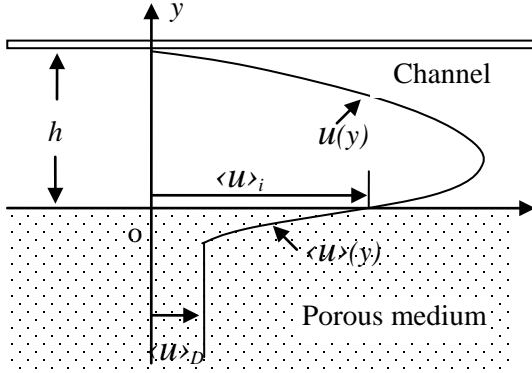
Figure 6. The geometrical model used in modeling a hybrid clear-fluid/porous-medium system.

If the velocity and stress are assumed to be continuous at the interface between the clear-fluid (channel) and porous-medium domains for the pressure-driven creeping flow, we can obtain the solution in terms of the velocity profiles in the clear-fluid and porous-medium domains as

$$u(y) = \langle u \rangle_i \left(1 + \sqrt{\frac{\mu'}{\mu}} \frac{y}{\sqrt{K}} \right) + \frac{K}{2\mu} \frac{dp}{dx} \left(2\sqrt{\frac{\mu'}{\mu}} \frac{y}{\sqrt{K}} + \frac{y^2}{K} \right) \quad (4)$$

for $0 \le y \le h$ and

$$\langle u \rangle (y) = \langle u \rangle_i + \left(\langle u \rangle_D - \langle u \rangle_i \right) \left[1 - \exp \left(\sqrt{\frac{\mu}{\mu'}} \frac{y}{\sqrt{K}} \right) \right] \quad (5)$$

for $-\infty \le y \le 0$,

where velocity at the interface $\langle u \rangle_i$ is given by

$$\langle u \rangle_i = \frac{-\dfrac{K}{2\mu} \dfrac{d\langle p \rangle^f}{dx} \left(2\sqrt{\dfrac{\mu'}{\mu}} \dfrac{h}{\sqrt{K}} + \dfrac{h^2}{K} \right)}{1 + \sqrt{\dfrac{\mu'}{\mu}} \dfrac{h}{\sqrt{K}}} \quad . \quad (6)$$

If a boundary-layer thickness δ_c can be defined as the width of the region inside the porous medium near the interface where $\langle u \rangle \big| \ge 1.01 \langle u \rangle_D$, then

$$\delta_c = \sqrt{K} \sqrt{\frac{\mu'}{\mu}} \ln \frac{50 \left(\dfrac{h^2}{K} - 2 \right)}{1 + \sqrt{\dfrac{\mu'}{\mu}} \dfrac{h}{\sqrt{K}}} \quad (7)$$

is obtained from $\langle u \rangle \big|_{y=-\delta} = 1.01 \langle u \rangle_D$.

We can find that the boundary-layer thickness is quite small and is of order $K^{0.5}$. When Darcy's law with the slip boundary condition is used, instead of the Brinkman equation with the stress-continuity condition, the velocity profile in the clear-fluid region is identical to Eq. (4), as long as the slip coefficient (α) is $\alpha = (\mu'/\mu)^{0.5}$. The difference between the two models is that there is no boundary layer inside the porous medium when using the Darcy's law, while a boundary-layer regime exists inside the porous medium when the Brinkman equation is used. Therefore, we can correlate the result from Brinkman equation with the stress-continuity condition to the solution from Darcy's law with the slip-velocity boundary condition.

Ochoa-Tapia and Whitaker [7] proposed that the governing equation for flow inside porous medium near the clear-fluid porous-medium interface is

$$-\nabla \langle p \rangle^f + \frac{\mu}{\varepsilon} \nabla^2 \langle \mathbf{u} \rangle - \frac{\mu}{K} \langle \mathbf{u} \rangle = 0 \quad , \quad (8)$$

where ε is the porosity of porous medium. Equation (8) (hereafter referred to as the *modified Brinkman equation*) is identical to the Brinkman equation (hereafter referred to as the *original Brinkman equation*) as long as $\mu' = \mu/\varepsilon$. Ochoa-Tapia and Whitaker found that the average velocity is continuous at the interface while the stress may not be. Using the rigorous volume averaging method, they derived a complex mathematical expression to describe a jump in the stress at the clear-fluid porous-medium interface. For 1-D parallel flow, the complex stress-jump interfacial condition reduces to

$$\frac{1}{\varepsilon} \frac{d \langle u \rangle}{dy} \bigg|_{y=0^-} - \frac{du}{dy} \bigg|_{y=0^+} = \frac{\beta}{\sqrt{K}} \langle u \rangle \ \text{at } y=0 \quad , \quad (9)$$

where β is a dimensionless coefficient on the order of one. Using the stress-jump boundary condition (9), solution to the Stokes and modified Brinkman equations can be expressed by the following:

$$u(y)=\langle u\rangle_i\left[1+\left(\frac{1}{\sqrt{\varepsilon}}-\beta\right)\frac{y}{\sqrt{K}}\right]+\frac{K}{2\mu}\frac{dp}{dx}\left(\frac{2}{\sqrt{\varepsilon}}\frac{y}{\sqrt{K}}+\frac{y^2}{K}\right)\quad(10)$$

for $0\leq y\leq h$

and

$$\langle u\rangle(y)=\langle u\rangle_i+\left(\langle u\rangle_D-\langle u\rangle_i\right)\left[1-\exp\left(\sqrt{\varepsilon}\frac{y}{\sqrt{K}}\right)\right]\qquad(11)$$

for $-\infty\leq y\leq 0$,

where velocity at the interface ‹*u*›ᵢ is given by

$$\langle u\rangle_i=\frac{-\dfrac{K}{2\mu}\dfrac{d\langle p\rangle^f}{dx}\left(\dfrac{2}{\sqrt{\varepsilon}}\dfrac{h}{\sqrt{K}}+\dfrac{h^2}{K}\right)}{1+\dfrac{h}{\sqrt{K}}\left(\dfrac{1}{\sqrt{\varepsilon}}-\beta\right)}\quad.\qquad(12)$$

Using the condition $\langle u\rangle\big|_{y=-\delta_j}=1.01\langle u\rangle_D$, the thickness of boundary-layer in the porous-medium flow can be defined as

$$\delta_j=\sqrt{\frac{K}{\varepsilon}}\ln\frac{50\left(\dfrac{h^2}{K}+\dfrac{2h\beta}{\sqrt{K}}-2\right)}{1+\dfrac{h}{\sqrt{K}}\left(\dfrac{1}{\sqrt{\varepsilon}}-\beta\right)}\quad.\qquad(13)$$

It is important to emphasize that the above solutions to the Brinkman equations are in terms of volume averaged quantities [i.e., the solutions are not on a point-wise scale but on the macro (RVE) scale]. More details on these analytical results for the stress-continuity and stress-jump conditions can be obtained in [6] and references therein.

The effective viscosity μ' must be determined in order to compare the Brinkman solution to the average velocity based on the point-wise solution. Similarly, the adjustable coefficient β in the stress jump condition needs to be determined as well. The parameter μ' is decided by adjusting μ' to

match the total flow rate in the channel calculated from Eqs. (4)–(6) with that from the BEM solution; this is conceptually equivalent to the experimental procedure used to calculate the slip coefficient by comparing an experimental velocity profile to the one predicted by theory. The coefficient β in the stress jump condition is determined by the same approach as well. If Darcy's law with the slip-velocity boundary condition is used for the porous medium instead of the Brinkman model with the stress continuity condition, the slip coefficient α is related to μ' by $\alpha=(\mu'/\mu)^{0.5}$. Values of μ'/μ, β and of the resulting slip coefficient α have been determined in this manner [6]. Figure 7 shows streamlines for the pressure-driven channel flow over square arrays of circular cylinders; only flow details near the top two rows of cylinders are shown. The streamlines above the top row of cylinders are smooth, and the streamline spacing indicates a slight perturbation in the channel flow due to the presence of cylinders below. However below the center-line of the top row of cylinders, the streamlines appear very wavy, indicating a rapidly diminishing x-direction velocity (as spacing increases downward) and a significant transverse velocity around the cylinders. In the second row of cylinders, the effect of the channel flow is almost negligible and the streamline pattern resembles that of the pressure-driven flow through an infinite square array of circular cylinders. In the low porosity (ε=0.5) case, the outermost recirculation eddies resembles those in the inner row of cylinders, which indicates that the flow field decays very rapidly with a reduction in the porosity.
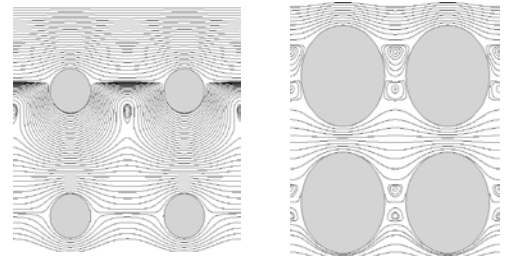
Figure 7. Streamlines for flow over an array of aligned fibers (left) ε=0.90, (right) ε=0.50.

It has frequently been assumed, in the context of the stress continuity condition, that the effective viscosity μ' is equal to the fluid viscosity μ. To

estimate the accuracy of this simplifying approach, we compare its solution with the volume averaged results obtained through the BEM. Figure 8 shows the comparison of the volume averaged velocity (essential detail on how this is calculated is omitted here for the sake of brevity; for more details see [6]) based on the point-wise BEM solution with the solution of the original Brinkman equation using the stress continuity condition with a suitable μ' or with $\mu'=\mu$, and with the solution of the modified Brinkman equation using the stress-jump condition.
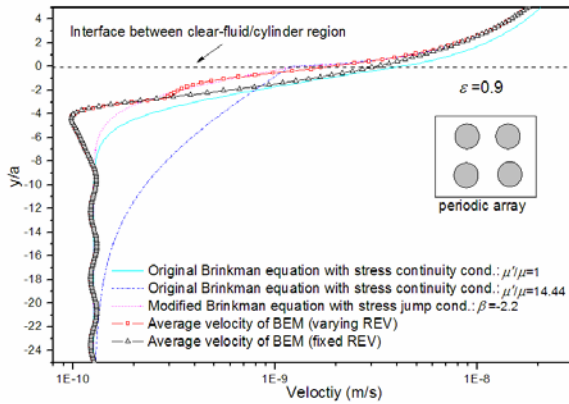
Figure 8. Comparison of average velocity based on the point-wise BEM solution with the Brinkman models using different interfacial conditions.

Overall, we have found that when the porosity (ε) is large, solution of the modified Brinkman equation using the stress-jump condition agrees well with the average-velocity profiles based on the point-wise BEM solutions, especially the varying RVE result. The slip velocity, the penetration depth of the boundary layer, and the velocity profile are well predicted through the use of the stress-jump condition. With a decrease in the porosity, the modified Brinkman equation with the stress-jump condition progressively fails to predict the volume averaged velocity near the interface; however it still predicts the penetration depth and slip velocity accurately. Our results also show that the original Brinkman equation with the stress-continuity equation cannot accurately predict the velocity profiles at the interfacial region for the full range of ε.

Transport Across Flake-Filled Membranes [8,9]

Flake-filled polymer membranes belong to an emerging class of composites that show promise as barrier materials in many industrial applications. Though the barrier property enhancement in flake-filled membranes is well known, its dependence on microstructural factors such as flake spatial distribution, size dispersion, and orientation is not well understood. In this study we carried out a micromechanics-based, direct numerical study to predict the Barrier Improvement Factors (BIF) of flake-filled membranes. Numerical calculations are conducted in two-dimensions for composite membranes containing aligned, impermeable flakes, using the fast multipole-accelerated boundary element method. The models that predict the barrier properties of flake-filled membranes are reviewed and evaluated by comparison with the boundary element calculations. Models evaluated in this study are two-dimensional, where flakes are aligned parallel to the membrane surface and diffusion is in the direction perpendicular to the membrane surface. The barrier improvement in the direction of diffusion is attributed to two phenomena: the increase in the diffusion path tortuosity and the reduction in the area available for diffusion. Therefore, the BIF can be approximated by

$$\frac{D_0}{D_f} = \left(\frac{A_0}{A_f} \right) \left(\frac{L'}{L} \right) , \qquad (14)$$

where

A_0	=	area available for diffusion in a pure membrane,
A_f	=	area available for diffusion in a flake-filled membrane,
L	=	membrane thickness,
L'		distance a solute must travel to cross a flake-filled membrane.

The path tortuosity factor is defined by L'/L. For a membrane containing uniformly spaced monodisperse rectangular flakes, Nielsen's model for the BIF is written as

$$\frac{D_0}{D_f} = \frac{1 + \frac{\alpha}{2}\phi}{1 - \phi} \quad , \qquad (15)$$

where D_0 and D_f are the diffusion coefficients of the virgin and the reinforced (filled) resin, respectively and

α	=	flake aspect ratio = l/t,
l	=	flake length,
t	=	flake thickness.

Using a conformal mapping method, Aris [10] developed an analytical expression for the BIF in a two-dimensional periodic array of obstacles. This is

$$\frac{D_0}{D_f} = 1 + \frac{\alpha^2\phi^2}{4(1-\phi)} + \frac{\alpha\phi}{2\lambda} + \frac{2}{\pi}\frac{\alpha\phi}{1-\phi}\ln\left[\frac{\pi\alpha^2\phi}{4\lambda(1-\phi)}\right] \quad , \qquad (16)$$

where $\lambda = 2s/t$ and (s) is the half-gap between two flakes.

For the same geometry, a slightly different model due to Wakeham and Mason [11] is

$$\frac{D_0}{D_f} = 1 + \frac{\alpha^2\phi^2}{4(1-\phi)} + \frac{\alpha\phi}{2\lambda} + 2(1-\phi)\ln\left(\frac{1-\phi}{2\lambda\phi}\right) . \qquad (17)$$

The difference between Eq. (16) and Eq. (17) lies in the fourth term on the right hand side. In Eq. (16), the fourth term is dependent on α, while in Eq. (17) it is not.

Cussler et al. [12] extended Aris' result [10] by considering the limit of a membrane having many layers of flakes, which leads to the following:

$$\frac{D_0}{D_f} = 1 + \frac{\alpha^2\phi^2}{4(1-\phi)} + \frac{\alpha\phi}{2\lambda} \quad . \qquad (18)$$

The second term on the right hand side of Eq. (18) becomes the leading term when $1/\lambda << \alpha\phi$.

Equation (18) was also extended by the same authors to the case where flakes of uniform size are randomly placed. The relevant expression is

$$\frac{D_0}{D_f} = 1 + \frac{\alpha^2\phi^2}{\beta(1-\phi)} \quad , \qquad (19)$$

where β is a geometric factor.

Recently, Lape et al. [13] developed models for the membranes containing randomly placed, monodisperse or polydisperse flakes, using an approach similar to Nielsen. For monodisperse flakes, the expression for BIF is

$$\frac{D_0}{D_f} = \frac{\left(1 + \frac{1}{3}\alpha\phi\right)^2}{1 - \phi} \quad . \qquad (20)$$

Implicit in the derivation of Eq. (20) is that the diffusion path around a flake is formed by straight lines. The BIF for polydisperse flakes was derived in a similar way. The expression for the BIF for flakes having a discrete size distribution is written as

$$\frac{D_0}{D_f} = \frac{1}{1 - \phi_{tot}}\left(1 + \frac{\phi_{tot}}{3}\frac{\sum_i m_i l_i^2}{t\sum_i m_i l_i}\right)^2 \quad , \qquad (21)$$

and the expression for flakes having a continuous size distribution is

$$\frac{D_0}{D_f} = \frac{1}{1 - \phi_{tot}}\left(1 + \frac{\phi_{tot}}{3}\frac{\int_0^\infty l^2 g(l)dl}{t\bar{l}}\right)^2 \quad . \qquad (22)$$

In Eq. (21), the subscript i is used to indicate different size classes; m_i and l_i are the number and the size of flakes in the i-th size class, respectively; ϕ_{tot} is the total flake volume fraction. In Eq. (22), $g(l)$ is the probability distribution function of sizes and $\bar{l}$ is defined as $\bar{l} = \int_0^\infty g(l)ldl$.

The flakes thickness (t) is assumed constant. It is not difficult to find that Eqs. (21) and (22) can be obtained by replacing α in Eq. (20) with a properly defined size-average, that is

$\bar{\alpha} = \sum_i m_i l_i^2 \Big/ t\sum_i m_i l_i$ and

$\bar{\alpha} = \int_0^\infty l^2 g(l)dl \Big/ t\int_0^\infty g(l)ldl$, respectively.

According to the above, the diffusivity of a membrane filled with monodisperse flakes is higher than that filled with polydisperse flakes. Hence, the barrier improvement caused by

polydisperse flakes is predicted to be superior to monodisperse flakes with the same average size. Experimental data on a 50-50% mixture of flakes indicates that this is qualitatively correct. However, extensive quantitative comparisons are still lacking.

The models reviewed above are based on intuitive assumptions rather than first principles. Their applicability in predicting the BIFs of real systems is therefore open to question. It is natural for us to ask which model is the most appropriate and how its use can be justified. In general, it is very difficult to obtain accurate experimental data for aligned flake-filled membranes. The reason is that preparing perfectly aligned flakes has not been proven possible. Hence any comparison between the BIF of experimental specimens and models predictions is always subject to (frequently unreported) experimental details. Comparing model predictions to results of direct simulation is free from this limitation.

Figure (9) shows typical models used in the numerical work: a random array of monodisperse flakes and a random array of polydisperse flakes. They are more realistic as random spatial distribution and size distribution of flakes are considered. However, because the microstructure is nonuniform, a Representative Volume Element (RVE) should be chosen such that a sufficient number of flakes are included in the analysis. This not only increases the model size but also creates new problems in selecting RVEs. In common practice, one can either choose a periodic RVE or choose a nonperiodic RVE. In a periodic RVE, fractioned flakes are allowed to reside at the RVE boundaries, and both geometry and boundary conditions are periodic. In a nonperiodic RVE, flakes are completely confined within a simulation box, and boundary conditions are of common types. A periodic RVE has several advantages in modeling, but is not applicable here due to the limitations of the numerical method we use. Thus, nonperiodic RVEs are chosen in this study. In a nonperiodic RVE, places near the RVE boundaries are free of flakes. In these places, local diffusion fluxes are high because there are no obstacles. It is of concern that BIF will be systematically underestimated if the fluxes in these easy diffusion areas are counted. To reduce the influence from

boundaries, a composite RVE is used, as illustrated in Figure 9(a), where the dashed lines divide the model into three regions. The middle region is a square of side length L, inside which the spatial distribution of flakes is random and periodic in the x direction. The flakes are separated by at least a distance of t from each other, and they are also apart from the horizontal boundaries by at least a distance of t.
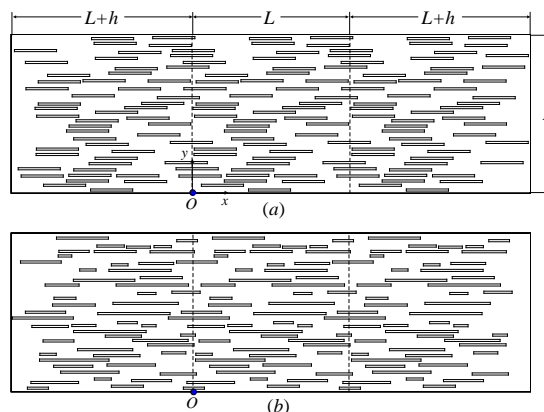

Figure 9. Computational models of random arrays of aligned flakes, (a) monodisperse flakes; (b) polydisperse flakes. The area of analysis is in the middle, separated from the rest by dashed lines.

Such random placement of nonoverlapping flakes at small volume fractions can be achieved without difficulty by using the random sequential addition algorithm. The flakes in the left and right regions are replicated from those in the middle by a translation of $-L$ and L, respectively. The x-dimensions of the left and right regions are increased by h so that the flakes are completely confined in the simulation box. The concentration field in the entire RVE will be solved, but the area of analysis is defined on the middle region, over which volume-average quantities are obtained and used to estimate effective properties. In this way, there is no artificially introduced easy diffusion path in the area of analysis except those naturally formed by randomly placed flakes. It is expected that the boundary influence will decay rapidly as it propagates inside, so its influence on the area of analysis should be insignificant provided that the sub-domain size is sufficiently large.

In general, the numerically predicted BIFs are higher than those predicted by theory (detailed

results are given in [8,9]. The deviations are more pronounced in the concentrated regime. To help explain this, Figure 10 shows a contour map of a concentration field in a nondilute geometry. Tortuous iso-concentration contour lines can be seen in Figure 10. As one would expect, if there were no flakes, the iso-concentration lines would be parallel to the *x*-axis and the diffusion paths, which are perpendicular to these iso-concentration lines, would be straight and vertical. In the presence of flakes, the iso-concentration lines are curved and so are the diffusion paths.
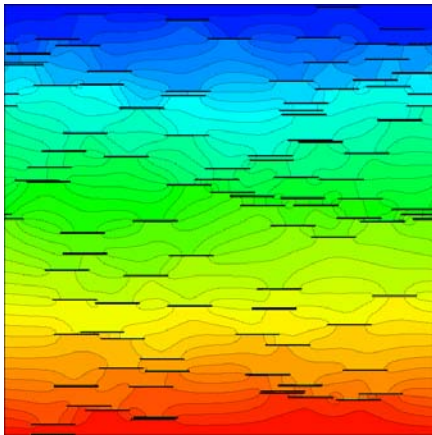
Figure 10. Contour map of concentration field in randomly placed monodisperse flakes,ϕ=0.01, α=100, N_f=100. The color scale is linearly distributed from 0 (blue) to 100 (red).

Because the flakes are impermeable, iso-concentration lines that end up on flake surfaces are normal to each flake surface. Therefore, in the vicinity of a flake, the diffusion path is parallel to the flake surface. This is commonly assumed by the analytical models to be the only contribution to the increase in the path tortuosity. According to these models, the concentration filed at a distance away from a flake is not perturbed; hence, the diffusion paths in these areas are still straight as if they were not influenced by nearby flakes. Such a simplification is only valid for dilute dispersions of flakes. It is evident in Figure 10 that in places where the local flake concentrations are high, the iso-concentration lines between nearby flakes are tilted with various angles to the *x*-axis rather than being straightly horizontal. This is an indicator of flake-flake interaction. As a result, the actual diffusion paths are more tortuous in these places

than assumed by the models. Such a nondilute effect can only be rigorously modeled by a numerical approach. Additional comparisons between theoretical models and computational results have been published in [8,9].

Experimental Measurement of Interstitial Fuid Velocities in Fiber Arrays Using Micro-Particle Image Velocimetry (μ-PIV) [14]
Experiments were conducted on the flow cell of Figure 11. The porous region of the channel consists of borosilicate glass fiber rods which can be arranged in different formations, perpendicular to the bulk flow direction – from left to right in Figure 11. The rod radius is *R*=150 µm.
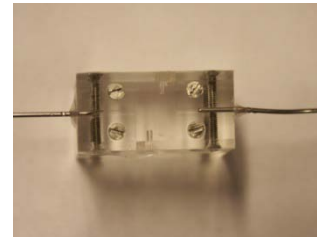
**Figure 11.** Flow cell, showing the inlet/outlet pipes.

The first investigation was made on a rectangular fiber array with relatively high porosity. The second investigation was made on a much denser hexagonally arranged fiber array with a fiber volume density of about 40 % (Figure 12).
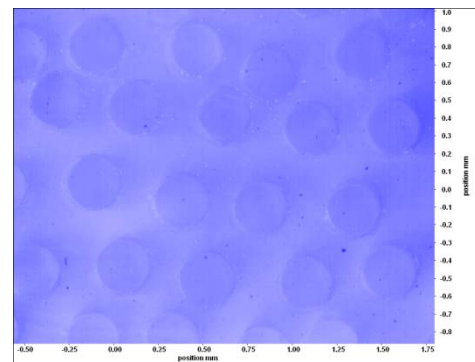
Figure 12. Image of a section of the fiber array obtained using 10x magnification. The bulk flow is in the direction perpendicular to the fiber axes.

In μ-PIV the flow is seeded with fluorescent particles and illuminated by a light source before it is imaged through a microscope into a CCD

camera. A schematic of the PIV setup is shown in Figure13.
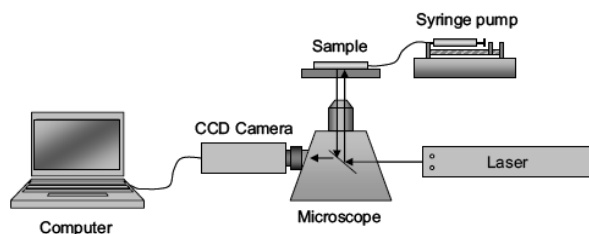

Figure 13. μPIV experimental setup.

A pulsed laser (Litron Lasers) emitting light with a wavelength of 532 nm was used as a light source in the experiments. The choice of fluid for the experiments was paraffin oil since it has a refraction index that is close to the refraction index of both, the glass walls of the channel and the fibers. The fluorescent particles used were 10.2 ± 0.17μm Rhodamine B particles from Microparticles GmbH. In order to get good results a homogenous distribution of particles in the fluid is needed. In order to get a constant velocity of the flow into the channel, a KDS Model 100 Series syringe pump was used with the volume flow rate set to 20 ml/h. A good signal-to-noise ratio was achieved by having as few particles as possible while still making it possible to obtain robust measurements.

The flow in the channel is three dimensional while the μ-PIV set-up used gives only the two planar components of the velocity field. It was therefore desired to measure the velocity field where the out-of-plane component of the flow had as little influence as possible, in other words in the centre of the channel. Since the permeability is much lower in the fiber bundle, the flow there is significantly slower. This implies that cross-correlation of the movement of the particle inside and outside of the porous domain at the same time is difficult. Either the flow is captured well around the fiber bundle and the fluid inside the bundle appears stationary, or the velocity field inside the bundle can be accurately described but the velocities obtained in the fast-moving fluid around the bundle are nonphysical. A typical velocity field obtained in the interstitial space is shown in Figure 14.
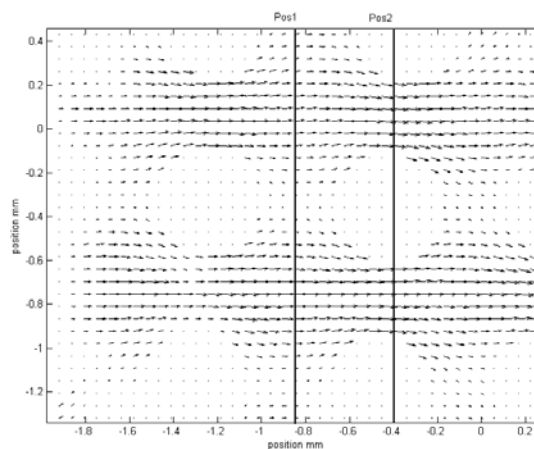
Figure 14. Velocity field in rectangular fiber array.

There is very limited movement between the rows of fiber and a converging-diverging flow can be observed. The periodic character of the flow in the interstitial spaces can also be visualised in Figure 15.
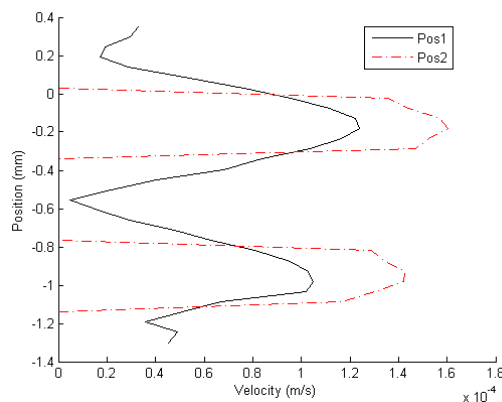
Figure 15. Velocity profiles for min and max cross-section area (reference figure 14 for positions 1 and 2).

References

1. B. Ripley, *Spatial Statistics*. Wiley: New York (1981).

2. X.-M. Chen, M. D. Woodward, and T. D. Papathanasiou, "Fiber clustering: Its quantification and influence on the permeability of unidirectional fibrous media," Proceedings SAMPE-2007, Baltimore, MD, USA, June 2007.

3. X. Chen and T. D. Papathanasiou, "Micro-scale modeling of axial flow through unidirectional disordered fiber arrays," *Composites Science and Technology*, 67, 1286–1293, 2007.

4. X. Chen and T. D. Papathanasiou, "The transverse permeability of disordered fiber arrays: A statistical correlation in terms of the mean nearest interfiber spacing," Transport in Porous Media," 71, 233–251, 2008.

5. X. Chen and T. D. Papathanasiou, "On the variability of the Kozeny constant for saturated flow across unidirectional, disordered fiber arrays," *Composites Part A: Manufacturing and Applied Science*, 37(6), 836–846, 2006.

6. Hua Tan, Xiao-Min Chen, Krishna M. Pillai, and T. D. Papathanasiou, "Evaluation of boundary conditions at the clear-fluid and porous medium interface using BEM," Proceedings to FPCM-9, 9th International Conference on Flow Processes in Composite Materials, Montreal, Canada, July 2008.

7. J. A. Ochoa-Tapia and S. Whitaker, *Int. J. Heat and Mass Transfer*, 38, 2635, 1995.

8. X. Chen and T. D. Papathanasiou, "Permeability of flake-filled membranes: review and Numerical Evaluation," Proceedings ANTEC-2007, Cincinnati, OH, USA, May 2007.

9. X. Chen and T. D. Papathanasiou, "Barrier properties of flake-filled membranes: Review and numerical evaluation," *Journal of Plastic Film and Sheeting,* 23(4), 319–346, 2007.

10. R. Aris, On a problem in hindered diffusion, *Arch. Rat. Mech. Anal.,* 95:83–91, 1986.

11. W. A. Wakeham and E. A. Mason, Diffusion through multiperforate laminae. *Ind. Eng. Chem. Fundam.*, 18(4): 301–06, 1979.

12. E. L. Cussler, S.E. Hughes, and W. J. Ward, Aris R. Barrier Membranes. *J. of Membrane Science*, 38:161–74, 1988.

13. N. K. Lape, E. E. Nuxoll, and E. L. Cussler, Polydisperse flakes in barrier films, 236:29–37, 2004.

14. A. G. Andersson, L. G. Westerberg, T. D. Papathanasiou, and T. S. Lundström, "Fluid flow through porous media with dual-scale porosity," Proceedings 19th International Symposium on Transport Phenomena, Reykjavik, Iceland, 17–20 August 2008.

M. Simulating Injection Molding of Thermoplastics Reinforced with Short and Long Fibers

Principal Investigator: Donald G. Baird
Virginia Polytechnic Institute and State University
Department of Chemical Engineering
Blacksburg, VA 24061
(540) 231-5998, fax: (540) 231-2732, email: dbaird@vt.edu

Co-Principal Investigator: Peter Wapperom
Virginia Polytechnic Institute and State University
Department of Mathematics
Blacksburg, VA 24061
(540) 231-7252, email: pwappero@vt.edu

Participants
Aaron P. R. Eberle, PhD. student, email: eberle@vt.edu
Gregorio M. Velez, PhD. student, email: gvelez@vt.edu
Kevin C. Ortman, PhD. student, email: kco3@vt.edu

Objective

- Improve the accuracy of the simulation of short (rigid) and long (flexible) fiber orientation in thermoplastics during injection molding by using a modified constitutive relation that incorporates non-affine motion and flexibility in combination with state-of-the-art numerical techniques.

- Establish a method (independent of the injection molding process) for determining a unique set of material parameters which is based on the transient shear rheological behavior of the composite fluid.

- Evaluate the accuracy of the simulation technique by comparing numerical predictions of glass fiber orientation to that first found in rheometrical flows and then in injection molded parts produced using basic mold geometries (end and center-gated parts).

Approach

- Determine an approach to conduct quantitative and reproducible rheological experiments on glass fiber-filled polymeric fluids.

- Conduct transient shear rheological studies on glass fiber-filled polypropylene (PP) and polybutylene terephthalate (PBT) systems in which fibers of various lengths (length: 0.2–11 mm, diameter: 12.5 microns) are used to assess the effects of both fiber length and the viscoelastic nature of the matrix on the transient rheology.

- Experimentally characterize the relationship between the rheological behavior and the associated fiber microstructure.

- Identify the limitations of current approaches to predict the evolution of fiber orientation by comparing model predictions to experimental observations.

- Use modified theory to address these limitations.

- Define and evaluate specific rheological tests to determine the material parameters in the constitutive equation which are unique and give consistent results when used in numerical simulations.

- Develop a finite element method simulation program capable of predicting fiber orientation during the mold filling stage of thermoplastic composite fluids containing short and long glass-fibers in an injection molding process.

- Modify the simulation to include the extensional flow kinematics of the advancing front region which may be critical to predicting fiber orientation at the mold wall.

- Assess the performance of the simulation by comparing predicted fiber orientation against values determined experimentally from injection molded samples.

Accomplishments

- Rheological Characterization Technique (short fibers): Developed a novel rheological technique that addresses problems associated with the nonhomogeneous shear field found in parallel-plate rotational rheometers and boundary interactions in cone-and-plate rheometers.

- Rheological Characterization Technique (long fibers): A fully functional sliding plate rheometer incorporating a shear stress transducer has been designed and fabricated primarily for the purpose of performing unbiased and reproducible steady shear rheological experiments on long glass fiber-filled polymeric fluids that are otherwise impossible to perform on rotational rheometers. Moreover, the device has been calibrated, and its behavior has been verified using two reference materials, a viscosity standard and a commercial low density polyethylene (LDPE). In addition to rheological studies, the rheometer will also be used in tracking the transient evolution of long fiber orientation upon startup and cessation of shear flow.

- Rheology: Rheological characterization of the short glass fiber composites was performed, including intermittent stress growth/relaxation tests to elucidate the stress contribution of the fiber, matrix, and flow field on the transient evolution of fiber orientation. A novel approach using donut shaped samples in a cone-and-plate rheometer was developed for tracking transient shear behavior of short-fiber composites.

- Model (short fibers): A constitutive relation has been developed that incorporates stress contributions from the fiber and the viscoelastic suspending medium and includes the ideas of non-affine motion. Model predictions show good agreement compared to rheological experiments and preliminary results for the experimentally determined fiber orientation.

- Fiber Orientation Measurements: We have determined an approach to characterizing the three-dimensional (3D) fiber orientation within composite parts using confocal laser microscopy. Additionally, an improved method that uses optical microscopy was also developed, and was shown to provide a more economical means for acquiring orientation measurements. This latter method is, therefore, expected to be the chosen method for future acquisition. With these techniques, we have initiated the characterization of fiber orientation in both rheometrical flows and complex flow geometries.

- Model (long fibers): Various approaches to modeling flexible fibers have been investigated. These approaches include modifying current theory for rigid fibers to include a "flexibility parameter," exploring constitutive equations resulting from bead-rod theory, track individual fibers using Hinch's infinitely flexible fiber theory, and extending Hinch's equations for concentrated polymer solutions through the concept of mobility. The choice of approach is still not determined but will be the emphasis of future research.

- Simulations (short): Developed a Galerkin/discontinuous Galerkin finite element simulation package to simulate the filling stage of injection molding. The features of this simulation package are: the use of multiple constitutive equations, the comparison with the Hele-Shaw approximation for an end-gated plaque and a center-gated disk, and a combined front tracking/ ALE technique for advancing front simulations.

- Simulations (long): Constructed a bead-rod orientation model for long fibers within the finite element simulation package. This model was used to gain preliminary results for long fiber orientation in injection molded center gated disks. Additionally, a program capable of utilizing an extension of Hinch's equation for concentrated polymer melts, through the use of a mobility tensor, was also written.

- Injection molding: A complete set of short and long glass fiber reinforced parts were molded, from which variables affecting fiber orientation and polymeric behavior (i.e., Newtonian-like/viscoelastic matrices, geometry, part thickness, and fiber length) are being studied.

Future Direction

- Compare model predictions of short glass fiber theory including non-affine motion to that of experimental results.

- Complete the analysis of orientation in center-gated disks and end-gated plaques using the alternate nonambiguous protocol for fiber orientation measurement in short glass fiber composites.

- Incorporate frontal flow in the simulation and compare to previous predictions using just Hele-Shaw approximation.

- Simulate fiber orientation in the runner of an injection mold cavity in order to establish the initial fiber orientation at the entrance to the cavity.

- Focus our attention on characterizing the transient rheological behavior of long glass fiber suspensions using the sliding plate rheometer.

- Use the sliding plate rheometer to gain an understanding of long fiber orientation development in simple shear experiments.

- Use the sliding plate rheometer to gain an understanding of fiber mobility in concentrated fiber suspensions and to assess the performance of Hinch's equation and its extensions.

- Assess the performance of the bead-rod model for various (long) fiber lengths by comparing model predictions to fiber orientation obtained in injection molded parts.

Introduction

The overall goal of our research is to be able to accurately predict the orientation of short and long fibers suspended in polymer melts generated during injection molding using a finite element analysis. To accomplish this goal we first have to establish a constitutive relation capable of predicting both the stress response to deformation of a composite fluid and the associated microstructure. As discussed, our approach to accomplish this goal begins with comparing model predictions to the rheological behavior and experimentally determined microstructure in the startup of simple shear flow experiments. Furthermore, unique material parameters for a specific composite fluid are established by fitting to these rheological measurements. Once established, the constitutive equation, using the unique model parameters, is then implemented into a finite element code for complex flow simulations typically found in injection molding, i.e., center-gated and end-gated flow.

We will highlight our advancements in the following order. First, we will discuss a unique method to accurately quantify the transient rheological behavior of short glass fiber-filled composite fluids and update the reader on the development of the sliding plate rheometer. After

this we will describe, in general, the transient rheological behavior of these fluids characterized using this technique. Then we will discuss the improvements/modifications made to the constitutive theory by incorporating the idea of non-affine motion and a parameter to control fiber flexibility. In addition, we will discuss current theories used for the dynamic simulation of long/flexible fibers. We then compare our experimental results and model predictions for short glass fiber suspensions and describe our approach at determining unique material parameters by fitting to the transient shear stress in start-up of flow. Following, we will describe our approach to characterizing the evolving microstructure of short glass fibers in simple flows and compare these results to model predictions. Finally we will outline our progress in the finite element simulation of a center-gated mold and describe our findings, i.e., the effect of initial conditions and non-affine motion.

Experimental Procedure

Rheological Characterization (Short Fiber Composite Fluids)

A key part of our research is to be able to *quantitatively* characterize the transient rheological behavior of glass fiber composite

fluids to assess our modeling approach and determine unique material parameters. Historically, researchers have used the parallel plate or disk geometry in rotational rheometers to characterize the transient rheological behavior of short glass fiber-filled fluids to minimize boundary-fiber interaction. To reduce the degree of boundary interaction, it has been suggested that the rheometer gap be at least three times the length of the longest dimension of the suspension particle. Experimental results using parallel plate geometry with various rheometer gaps confirmed that for the 30 wt% PBT there is a negligible effect on the sample rheological response when the gap is greater than twice the number average fiber length. The problem with this geometry (parallel plate) is the tangential velocity and, hence, shear rate varies with radial position from the center of the plates to the outside. Our experimental results have shown that this inhomogenous shear field causes unrealistic transient behavior and, therefore, cannot be used as a quantitative tool. As a result, we believe only a rheometer that imposes a homogeneous shear field should be used to quantitatively characterize suspensions of glass fibers.

The gap within the 50 mm cone and plate fixture varies linearly from 2.51 mm at the outer edge to 0.05 mm at the center. To remove the inevitable fiber-boundary interaction near the center, sample disks were pre-formed and a 25.4 mm diameter hole was drilled through the center creating a donut shaped sample. A schematic of the "donut" sample can be seen in Figure 1.
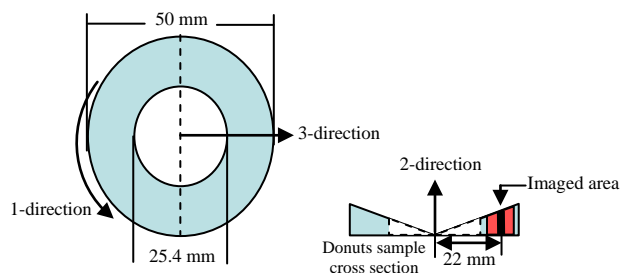

Figure 1. 50 mm cone and plate "donut sample" dimensions. The illustration defines the 1, 2, and 3 directions which are the direction of flow, velocity gradient, and radial directions, respectively. In the cross-sectional profile the black area is the area at which the confocal laser images were taken.

These samples combined with the cone and plate geometry ensure a homogeneous shear field and a gap that was always greater than two times the number average fiber length.

Sliding Plate Rheometer (Characterization of Long Fiber Composite Fluids)

After numerous attempts at characterizing suspensions containing long glass fibers using various techniques at our disposal, we concluded that the conventional melt rotational rheometers were inadequate. This was because of various difficulties posed by these rheometers, e.g., curvilinear streamlines and insufficient rheometer gap size. As a result, we initiated the design and fabrication of a sliding plate rheometer incorporating a wall shear stress transducer [shown in Figure 2(a–e)] with the primary purpose of being able to perform unbiased and reproducible steady shear rheological experiments on long glass fiber-filled polymeric fluids that are otherwise impossible to perform on rotational rheometers. After completion the device was calibrated and its behavior was verified. A viscosity standard and a commercial polymer Equistar PETROTHENE NA 952, a LDPE with no processing aids or antiblock agents, were used as reference materials in verification.

Localized shear stress measurement and a homogenous shear field with rectilinear streamlines are two key improvements the sliding plate rheometer offers over rotational rheometers. While localized stress measurement eliminates the problems arising due to edge effect, the homogenous shear field insures removal of unrealistic transient behavior. Moreover, theoretically it has no restriction on the gap size. Though the main purpose of sliding plate rheometer is to perform rheological measurements on long glass fiber composites but in future it will also be used in tracking the transient evolution of long fiber orientation upon startup and cessation of shear flow.
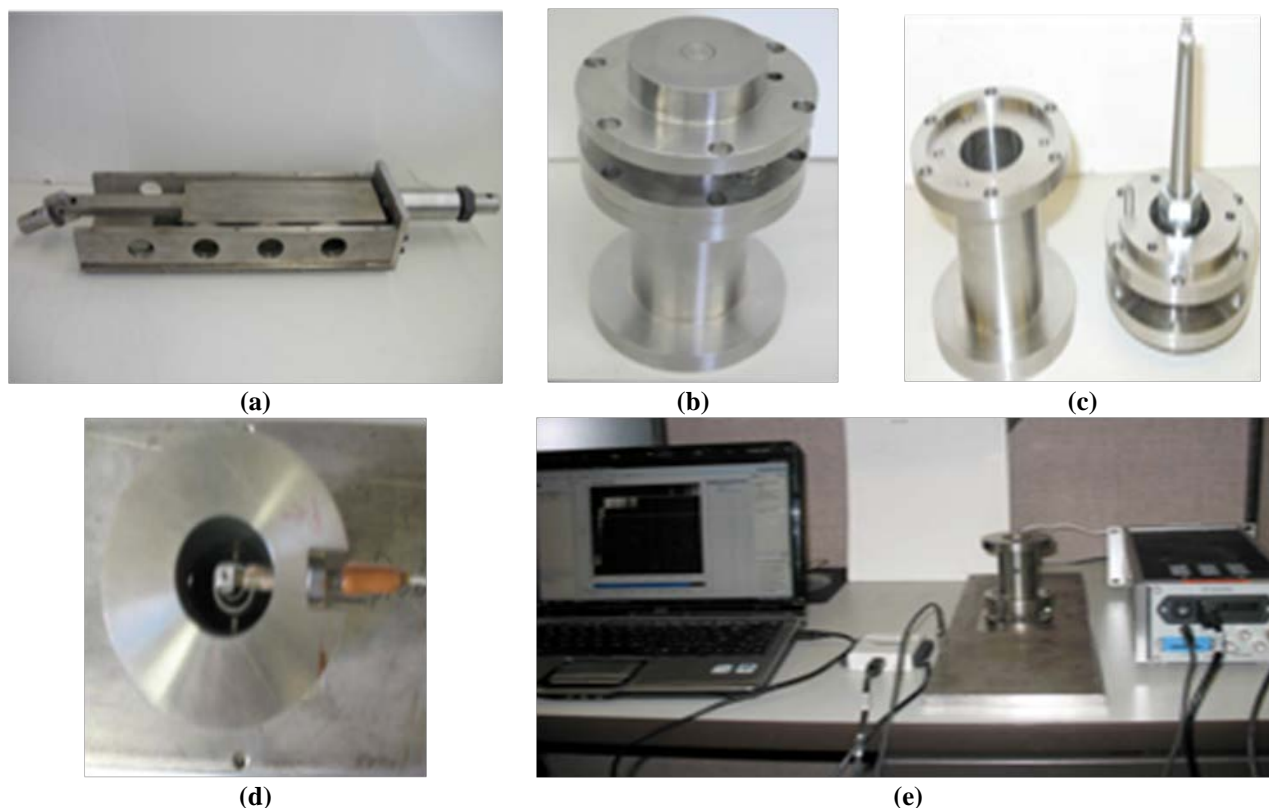
Figure 2. Sliding plate rheometer. (a) Sliding plate, (b) wall shear stress transducer, (c) disassembled shear stress transducer showing rigid beam, (d) shear stress transducer with capacitance probe, (e) complete assembly with all electrical components.

Rheological Behavior

Subsequently, we outlined the pertinent shear rheological behavior exhibited by the short glass fiber composite fluids as it will aid in the discussion on model development. When an undeformed sample is subjected to a start-up of flow experiment, the sample exhibits a relatively large stress overshoot in both the shear stress and the first normal stress difference. This behavior can be seen in Figure 3 (a) and (b) (τ^+ and N_1^+ vs. time, respectively) for the 30 wt% PBT. The relatively large overshoot is believed to be a result of the fibers rotating as a result of the flow field to align in the flow direction. Once the fibers reach a steady-state, the stresses reach a steady-state. An interesting observation is that when the flow is removed and then reapplied, after some period of time, the stresses return to their previous value. From this behavior we believe that during stress relaxation the fibers maintain their orientation so that when the flow is turned back on the stresses immediately grow to their previous value. Hence,

the transient rheological behavior is coupled with the fiber orientation and being able to model the evolution of orientation is imperative to correctly predicting the rheological behavior and fiber orientation in complex flow simulations.

## Theory: Model Development (Short Fibers)

Evolution of Fiber Orientation

The most common approach to represent the orientation state of a fiber is by defining a unit vector, **u**, parallel to the fiber backbone. In the case of an ideal suspension which consists of a large number of fibers that are identical in size and shape and whose concentration is spatially uniform the average orientation state of the fibers can be described with an orientation distribution function, $\psi(\mathbf{u},t)$. However, using the distribution function is numerically cumbersome. Another way to describe the average orientation state of the suspensions is with the second order orientation

tensor, **A**, and it is defined as the second moment of the orientation distribution function[1]:

$$\mathbf{A}(t) = A_{ij}(t) = \int \mathbf{uu}\,\psi(\mathbf{u},t)\,d\mathbf{u} \quad , \qquad (1)$$

where A_{ij} denotes the components of the second order orientation tensor. The trace of **A** is always equal to 1 and for a completely random orientation **A** = 1/3 **I**, where **I** is the identity tensor. In the limit where all the fibers are perfectly aligned in the 1-direction the only nonzero component is A_{11} = 1. In flow problems, in addition to the **A**, the fourth order orientation tensor (**A₄**) is commonly used. For a more complete description of orientation tensors and their use in representing fiber suspension the reader is referred to Advani and Tucker [1].

(a)

(b)
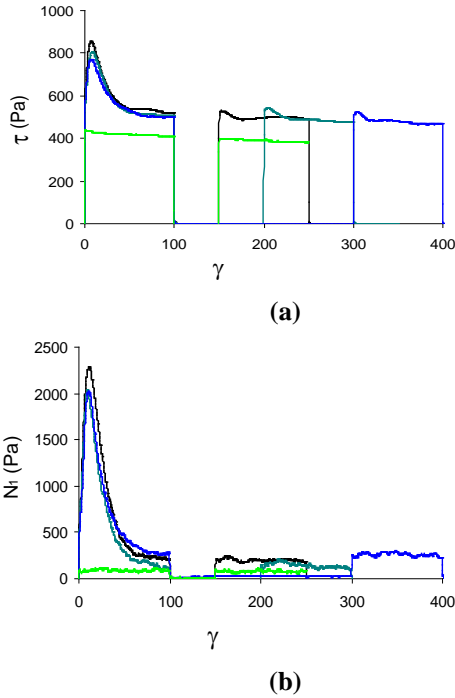
Figure 3. Stress vs strain for intermittent stress growth/relaxation tests performed on the 30 wt % short glass fiber filled PBT. (a) Shear stress, (b) first normal stress difference. The light green line is the suspending medium. All tests were performed using cone and plate geometry combined.

For suspensions containing rigid fibers the most common approach to modeling the evolution of fiber orientation is the Folgar-Tucker (F-T) model [2]. This model uses the generalized Jeffery equation [3] and adds an isotropic rotary

diffusivity term, to represents the inter-particle interactions. For simple flows the Folgar-Tucker model can be written in terms of **A** as follows:

$$\frac{D\mathbf{A}}{Dt} = (A \cdot W - W \cdot A) + \lambda(D \cdot A + A \cdot D - D : A_4)$$
$$+ 2C_1 |D|(\delta - 3A) \qquad , \qquad (2)$$

where $\mathbf{W} = [(\nabla v) - (\nabla v)^t]/2$, $\mathbf{D} = [(\nabla v) + (\nabla v)^t]/2$, ∇v is the velocity gradient, λ is a constant defining the ellipticity of the particle and C_1 is a constant named the interaction coefficient which is related to the magnitude of the inter-particle interactions. The first two terms in Eq. (2) correspond to the generalized Jeffery equation. For fibers it is common to assume the particle's aspect ratio approaches infinity and to use $\lambda = 1$.

As discussed later (Results and Discussion), the predictions using the generalized Jeffery equation will be compared to our experimental results. From this comparison our research shows that the generalized Jeffery equation overpredicts the rate of fiber reorientation. As a result, we are unable to predict the transient rheological behavior of these composite fluids. It is our hypothesis that this is a direct result of the fibers moving non-affinely with the suspending medium. To account for this behavior we add a term to the generalized Jeffery equation part in Eq. (2) referred to as the non-affine motion parameter, α. The resulting equation has the form

$$\frac{D\mathbf{A}}{Dt} = \alpha[A \cdot W - W \cdot A + D \cdot A + A \cdot D - D : A_4] \quad . \qquad (3)$$

The non-affine motion parameter effectively retards the rate of fiber reorientation predicted by the generalized Jeffery equation. Its values range between 0–1 and is thought to be function of fiber concentration, aspect ratio and the velocity gradient. Additionally, the non-affine parameter was used in the F-T model. Comparison between experimental data and model predictions for Jeffery and F-T model with and without the non-affine parameter can be found in the results and discussion section of this report.

Stress Contribution

With knowledge of the fiber orientation and deformation gradient the stresses can then be calculated from the following equation[4]:

$$\sigma = -P\boldsymbol{I} + 2\eta_s\boldsymbol{D} + 2\eta_s N_p \boldsymbol{D}:\boldsymbol{A}_4 \quad , \qquad (4)$$

where P is the isotropic pressure, η_s is the suspending medium viscosity, and N_p is a dimensionless parameter that describes the magnitude of the total hydrodynamic drag in the system. The terms on the right hand side of the equals sign are the contributions from the isotropic pressure, suspending medium, and hydrodynamic drag of the fluid on the fiber, respectively. The suspending medium viscosity, η_s, in Eq. (4) can be taken to be a constant for a Newtonian fluid, a generalized Newtonian fluid in which the viscosity depends on shear rate only and represented with an empiricism such as the Carreau-Yasuda model or predicted using a viscoelastic constitutive equation for fluids that exhibit both viscous and elastic responses. There are various theories for calculating N_p for dilute and semi-dilute systems (i.e., Dinh-Armstrong [4] and Shaqfeh-Fredrickson [5]), but none for concentrated systems. For our model predictions we fit N_p to the peak of the shear stress overshoot. This will be discussed in detail in the results and discussion section.

Theory: Model Development (Long Fibers)

It is of primary interest to try and extend the existing simulation approach for short glass fiber systems to long glass fiber systems. This has proven to be a difficult task, but we have come up with a possible approach by incorporating what we term a *flexibility parameter*, β, into the generalized Jeffery equation as follows:

$$\frac{D\boldsymbol{A}}{Dt} = \alpha\left[\boldsymbol{A}\cdot\boldsymbol{W} - \boldsymbol{W}\cdot\boldsymbol{A} + \boldsymbol{D}\cdot\boldsymbol{A} + \boldsymbol{A}\cdot\boldsymbol{D} - \beta\boldsymbol{D}:\boldsymbol{A}_4\right] \quad . \qquad (5)$$

In the generalized Jeffery equation the term $\boldsymbol{D:A_4}$ is the term associated with stretch along the backbone of the fiber. If we take that same theory but treat the unit vector not as a unit vector along the backbone of the particle, as in Figure 4(a), but as a unit vector describing the end-to-end distance

and average orientation state of the system, then we can control the amount of fiber flexibility by multiplying the term $\boldsymbol{D:A_4}$ by some constant, β.
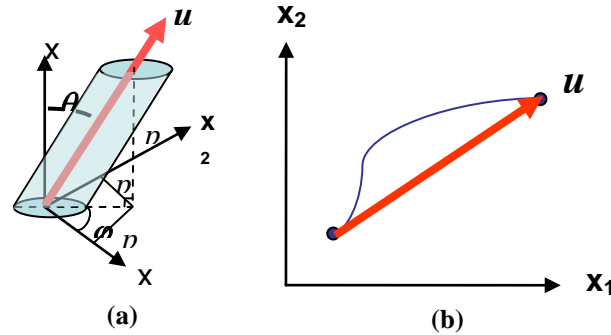
Figure 4. Unit vector **u**: (a) along the backbone of a rigid fiber, (b) an end-to-end vector representing the average position of a bent fiber.

The addition of this parameter β, has an interesting effect on the transient fiber orientation in start-up of flow. This can be seen in Figure 5 which is the A_{12}-component of the tensor **A** vs. strain. The magnitude of the shear stress is directly proportional to the magnitude of the A_{12}-component. From this figure one can see that an increase in β results in a decrease in the A_{12} component. Unfortunately, we currently do not have any rheological behavior of a long glass fiber system to compare to at this point (It is the emphasis of the continued research effort).
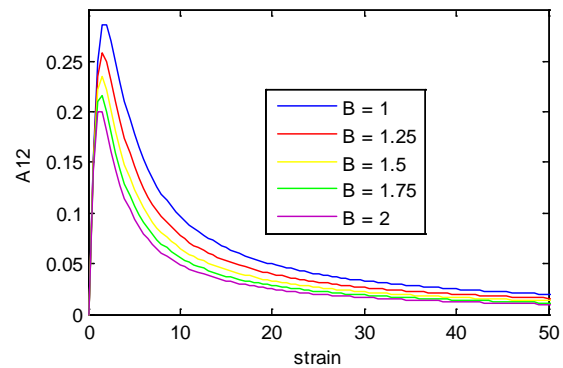
Figure 5. A_{12} component vs. strain for various β values in start-up of flow simulation.

Another approach to modeling long/flexible fiber systems is by simulating the dynamic behavior of individual fibers. This can be done in various ways but the most "straight forward" approach is to

begin with the theoretical work of Hinch [6] for an infinitely flexible fiber. In this theoretical development, the tension forces within the thread, *T*, are set equal to the viscous forces acting on the thread. As a result, two equations are formed, one describing *T* at discretized points along the thread, Eq. (6), and one defining the time rate of change of the nodal points as a function of *T*, Eq. (7).

$$\frac{\partial^2 T}{\partial s^2} - \frac{1}{2}\left(\frac{\partial^2 \vec{x}}{\partial s^2}\right)T = -\frac{\partial \vec{x}}{\partial s} \bullet \underline{\underline{D}} \bullet \frac{\partial \vec{x}}{\partial s} \quad . \tag{6}$$

$$\frac{\partial \vec{x}}{\partial t} = \underline{\underline{\nabla v}} \bullet \vec{x} + \frac{\partial T}{\partial s}\frac{\partial \vec{x}}{\partial s} + \frac{1}{2}T\frac{\partial^2 \vec{x}}{\partial s^2} \quad . \tag{7}$$

In Eqs. (6) and (7), *s* is the arc length, and *x* is the position vector. Given an initial fiber orientation, one can solve Eqs. (6) and (7) for the time rate of change of the fiber configuration. Model predictions for simple shear flow can be seen in Figure 6. Strain 0 relates to the initial fiber orientation and strains 1–4 show the evolution of orientation with a localized center of mass. This model predicts that, in simple flow, the fiber straightens and aligns itself with the flow direction.

In addition to Hinch's equation, Goddard and Huang [7] extended the work for a perfectly flexible fiber by encompassing the concept of mobility into the evolution equation. The Goddard and Huang model is described by

$$\frac{\partial \vec{x}}{\partial t} - K_L \frac{\partial T}{\partial s}\frac{\partial \vec{x}}{\partial s} = T\underline{\underline{K}}_T \bullet \frac{\partial^2 \vec{x}}{\partial s^2} + \vec{v}(\vec{x},t) \tag{8}$$

and

$$-\frac{\partial \vec{x}}{\partial s} \bullet \frac{\partial \vec{v}(\vec{x},t)}{\partial s} = \frac{\partial}{\partial s}\left(K_L \frac{\partial T}{\partial s}\right)$$
$$-\left(\frac{\partial^2 \vec{x}}{\partial s^2}\right)\bullet\left(K_L\underline{\delta}+\underline{\underline{K}}_T\right)\bullet\left(\frac{\partial^2 \vec{x}}{\partial s^2}\right)T \tag{9}$$

X axis labeled X from -4 to 6; Y axis labeled Y from 0 to 10. Legend: γ = 0, γ = 1, γ = 2, γ = 3, γ = 4.
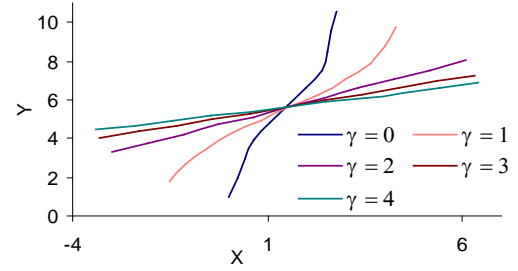
Figure 6. Model predictions for the Hinch infinitely flexible fiber in simple shear flow. Strain 0 relates to the initial orientation and strains 1–4 show the evolution of orientation with a common center of mass.

where the mobility tensor components K_L, K_n, and $\underline{\underline{K}}_T$ are denoted by the lateral mobility, the normal mobility, and the transverse mobility tensor, respectively. Again, T is the tension. This model suggests that in concentrated fiber suspensions there exists a preferred direction for the motion of a single fiber. The mobility tensor provides insight into the kinematic restrictions of a fiber caused by the presence of its neighbors. This restricted motion affects the orientation development of the fibers. Therefore, our future work will be to assess this model by studying the mobility tensor in simple shear flow, with the use of the sliding plate rheometer.

Lastly, a relatively recent model was published for semi-flexible fibers in dilute solutions by Strautins and Latz [8]. The authors construct a continuum model that provides a first approximation to flexibility. This is accomplished by modeling a fiber as two rods connected by a pivot allowing bead (Figure 7).

Bead-Rod (BR2)

$l_B \vec{q}$ θ $l_B \vec{p}$

$\vec{q} \cong -\vec{p}$
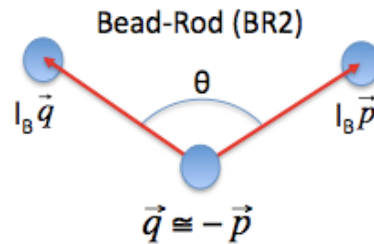
Figure 7. Fiber model, with segment length l_B, allowing semi-flexibility. The segment orientations are denoted by unit vectors $\vec{p}$ and $\vec{q}$, and are separated by an angle θ with some given bending rigidity.

The model considers the flexible fiber to consist of two rigid segments with length l_B that are allowed to slightly pivot about the connecting bead with some restorative bending rigidity, k. Both $\vec{p}$ and $\vec{q}$ are unit vectors that represent the orientation of the corresponding fiber segments with respect to the center bead. The tensor $\underline{\kappa}$ is the velocity gradient. The model equations are developed and are given as

$$\frac{D\underline{\underline{A}}}{Dt} = \underline{\underline{A}} \cdot \underline{\kappa}^T + \underline{\kappa} \cdot \underline{\underline{A}} - [(\underline{\kappa} + \underline{\kappa}^T):\underline{\underline{A}}]\underline{\underline{A}}$$
$$+ \frac{l_B}{2}[\vec{C}\vec{\mu} + \vec{\mu}\vec{C} - 2(\vec{\mu}\cdot\vec{C})\underline{\underline{A}}] - 2k[\underline{\underline{B}} - \underline{\underline{A}}\ tr(\underline{\underline{B}})] \quad , \quad (10)$$

$$\frac{D\underline{\underline{B}}}{Dt} = \underline{\underline{B}} \cdot \underline{\kappa}^T + \underline{\kappa} \cdot \underline{\underline{B}} - [(\underline{\kappa} + \underline{\kappa}^T):\underline{\underline{A}}]\underline{\underline{B}}$$
$$+ \frac{l_B}{2}[\vec{C}\vec{\mu} + \vec{\mu}\vec{C} - 2(\vec{\mu}\cdot\vec{C})\underline{\underline{B}}] - 2k[\underline{\underline{A}} - \underline{\underline{B}}\ tr(\underline{\underline{B}})] \quad , \quad (11)$$

$$\frac{D\vec{C}}{Dt} = \underline{\kappa} \cdot \vec{C} - (\underline{\underline{A}}:\underline{\kappa})\vec{C} + \frac{l_B}{2}[\vec{\mu} - \vec{C}(\vec{\mu}\cdot\vec{C})]$$
$$- k\vec{C}[1 - (tr(\underline{\underline{B}}))] \quad , \quad (12)$$

and

$$\vec{\mu} = \sum_{i=1}^{3}\left(\sum_{j=1}^{3}\sum_{k=1}^{3}\frac{\partial^2 v_i}{\partial x_i \partial x_k}A_{jk}\right)\vec{e}_i \quad , \quad (13)$$

where the two orientation tensors represent the second moment of the distribution function of the unit vectors, $\vec{p}$ and $\vec{q}$, in the following manner:

$$\underline{\underline{A}} = \int \vec{p}\vec{p}\ \psi(\vec{p},\vec{q})d\vec{p}\ d\vec{q} \quad , \quad (14)$$

$$\underline{\underline{B}} = \int \vec{p}\vec{q}\ \psi(\vec{p},\vec{q})d\vec{p}\ d\vec{q} \quad . \quad (15)$$

As a direct consequence to the bending rigidity, encompassed within the model parameter k, the expectancy of a segment orientation (with respect to the orientation distribution function) may be nonzero in general and is accounted for in Eq. (12) by the following definition:

$$\vec{C} = \int \vec{p}\ \psi(\vec{p},\vec{q})d\vec{p}\ d\vec{q} \quad . \quad (16)$$

Lastly, Eq. (13) contributes second order derivatives of the velocity field that originate from a Taylor series approximation applied to the bead kinematics. In simple shear flow, for example, all components are *0*. This vector, in Eq. (13), is formed by the unit dyads $\vec{e}_i$.

Our future work will center on determining how well this model describes long fiber orientation. Currently, the bead-rod model is being explored for the case of a center gated disk, for which preliminary results have been obtained. It is also within our interest to understand what length scales this model best describes. It is believed that these efforts will greatly enhance our understanding of long fiber evolution.

Experimental Results vs. Model Predictions

Subsequently, we compared model predictions of startup of flow to that of experimental results obtained using the 30 wt% short glass fiber-filled PBT. First, we consider predictions using the generalized Jeffery equation, Eq. (2), in combination with Eq. (4) defining the stress contribution. Figure 8(a) depicts the model predictions for both the shear stress and first normal stress difference vs. strain in which the material parameters C_1 (from Bay and Tucker [9]) and N_p (from Dinh-Armstrong [4]) are calculated directly from current theory. These predictions are plotted in combination with the experimental rheological behavior. First, the model does predict an overshoot in both the shear and first normal stress difference. However, the model is incapable of predicting the magnitude or the width of either overshoot. It is our hypothesis that being able to predict this transient overshoot behavior is the key to then being able to predict the fiber orientation in the complex flow simulations.

To improve on the model predictions, we incorporated the non-affine motion term, Eq. (3), and fit the material parameters instead of calculate them based on theory. N_p we fit to the peak of the shear stress overshoot and α we fit to the width of the shear stress overshoot. Model predictions using this approach compared to the experimental results can be seen in Figure 8(b). Now we come much closer to predicting the transient behavior of both the shear and first normal stress difference.

(a)

(b)

Figure 8. Experimental results compared to model predictions for the transient stresses in start-up of flow at a shear rate of $1s^{-1}$. (a) Model predictions using current theory to calculate C_1 and N_p. (b) Model predictions incorporating non-affine motion and parameters fit to transient shear overshoot.

Measurement of Fiber Orientation

To characterize the evolving fiber orientation under dynamic conditions, donut samples composed of PBT-30 were deformed using the RMS-800 with the cone and plate geometry at a shear rate of $1 \ s^{-1}$ for a specified amount of time at 260°C in a nitrogen environment. Directly after the applied deformation, the sample temperature was lowered below the suspension melt temperature. The samples were then bisected at the center of the sample creating a plane perpendicular to the flow direction, encapsulated in epoxy and sanded/polished to a final abrasive particle size of 0.3 μm Al_2O_3 following standardized techniques. Images of the polished surface were taken using a Zeiss LSM510

confocal laser scanning microscope fitted with a 40× water immersion objective lens and a laser excitation wavelength of 543 nm. The confocal laser is able to focus on the sample surface and penetrate the sample to a depth of 10 μm. This allows us to construct a 3-D image of the fiber orientation. For each sample, ten sequential images were taken from the bottom of the donut sample to the top at a position of 22 mm from the center. An illustration depicting the position at which the pictures were taken can be seen in Figure 1. The cross-section of each fiber appears as a circle or an ellipse. To process the image, the circumference of each ellipse was traced by hand in Power Point to improve the contrast between the fibers and the matrix. A simple computer program was written combined with image analysis software in MATLAB that measured the position of the center of mass, the major and minor axis and θ angle of each ellipse. For each sample, the total number of ellipses analyzed varied from 321 for strain = 4 to roughly 456 for strain = 200.

Figure 9(a) shows experimental results (points) and model predictions using the generalized Jeffery equation (Jeff_A_{ii}) for the diagonal components of the tensor **A**. From this figure it is easy to see that the generalized Jeffery equation overpredicts the rate of fiber reorientation. We believe this is a result of direct fiber contact. Figure 9(b) depicts the experimentally determined A_{11}-component with various model predictions using the generalized Jeffery combined with the calculated F-T constant, Jeff+F-T(calc.)_A_{11}, and the generalized Jeffery combined with slip parameter fit to the transient rheology and the F-T constant fit to the steady state orientation value, Jeff(w/slip)+F-T(fit)_A_{11}. With the addition of the non-affine motion parameter and by fitting C_1 to the steady state orientation, we come much closer to predicting the dynamic behavior of the fiber.

(a)

(b)
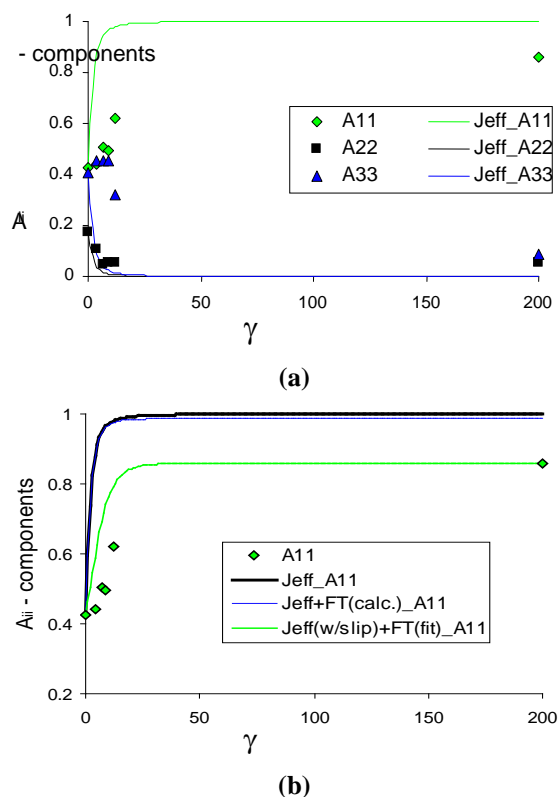
Figure 9. Experimental results from confocal laser microscopy compared to model predictions for start-up of flow vs. strain at a shear rate of 1 s^{-1}. (a) Experimental results (points) and model predictions using the generalized Jeffery equation (Jeff_A_{ii}) for the diagonal components of the tensor **A**. (b) Experimental results of the A_{11}-component (points), model predictions with the generalized Jeffery equation plus theoretically calculated F-T constant [Jeff+F-T(calc.)-A_{11}], model predictions with the generalized Jeffery equation plus the fit non-affine motion term α F-T constant fit to the steady state orientation [Jeff(w/slip)+F-T(fit)-A_{11}].

Injection Molded Samples/Fiber Orientation Analysis

The experimental program dealing with the injection molding of parts was finished last year. It consisted of a study including four factors (i.e., matrix material, geometry, fiber length, and part thickness of cavity, in 12 combinations). The fiber concentration was chosen to be a constant parameter and selected to be in the concentration range of 30 wt%, typically found in commercially used composites. Figure 10 depicts the factors and combinations involved in the experimental program. The parts were molded to obtain short

shots of 75% of the dimension of the full part. A center-gated disk of 1.3 mm in thickness, PBT matrix and fibers 500 μm have been analyzed. For this part, the short shot size (R) was determined as the difference of the outer minus inner radius. The evaluation of the orientation was performed using the method of ellipses with images taken from confocal laser microscopy following several publications of Clarke's group [10]. Figure 12 depicts the experimental profile of orientation component A_{11} along the height of the cavity (z-dir) in the gate 0R, 0.4R, and 0.9R. An asymmetric orientation profile can be seen at the gate region, which corroborates predictions indicated in the literature but never validated e.g., VerWeyst and Tucker [11] and Chung and Kwon [12]. This experimental result is important for assessing our simulations because the orientation needs to be prescribed at the gate. In the literature, the gate orientation has typically been assumed constant (random or averaged), especially for a center-gated disk. Figure 11 shows that the fibers aligned in the flow direction close to the walls, far away from the gate. However, A_{11} profiles are still asymmetric.

The confocal laser microscopy (CLM) technique used to determine the experimental orientation has similar ambiguity problems that are inherent to reflection microscopy techniques for the complex flow experiments. The penetration of the laser beam is limited to 5 μm due to the opacity of the matrix. The differences in the ellipses between images at the surface and at 5 μm below the surface are only perceptible for fibers with a large zenith angle. Therefore, there is an ambiguity for fibers almost perpendicular to the surface plane. A weakness in the CLM technique is the inability to detect fibers parallel to the surface plane inspected. This problem is evident in the regions close to the wall when the r,z-plane is analyzed. Figure 11 shows this limitation for the positions 0.0R and 0.4R. An alternative method is under development using the recommendations of Bay and Tucker consisting of images taken from two mutually perpendicular planes. A medical grade X-ray computed tomography was used to determine the orientation of fibers below the polished plane, but the resolution of the instrument was not good enough to obtain clear images of the fibers.
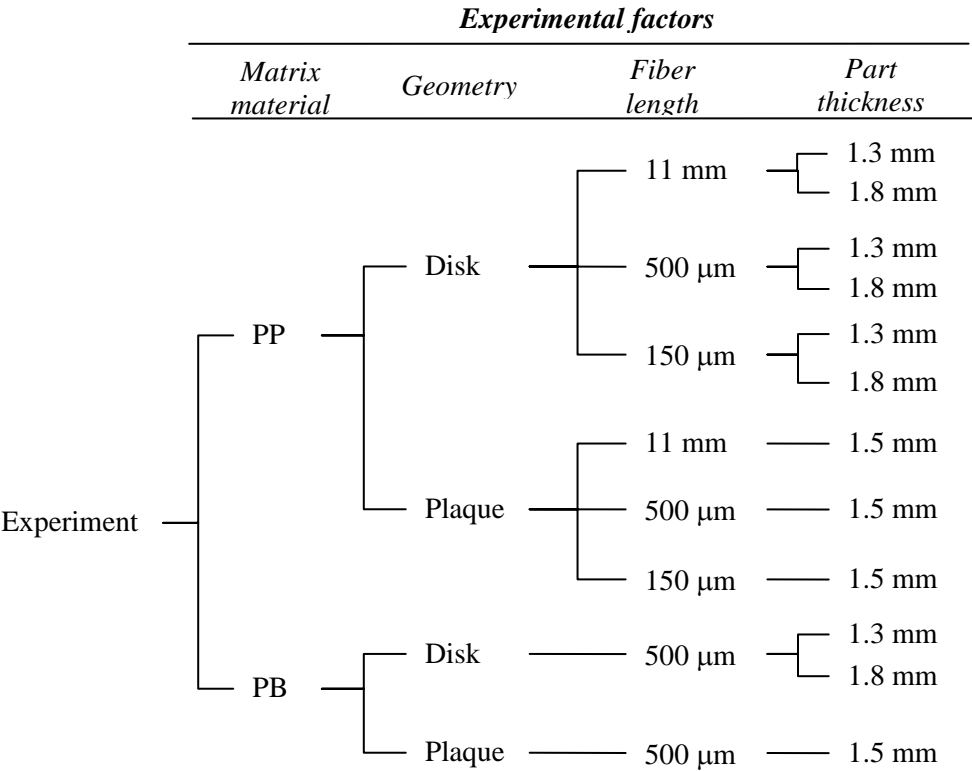
		Experimental factors	
Matrix material	*Geometry*	*Fiber length*	*Part thickness*

Figure 10. Experimental design.
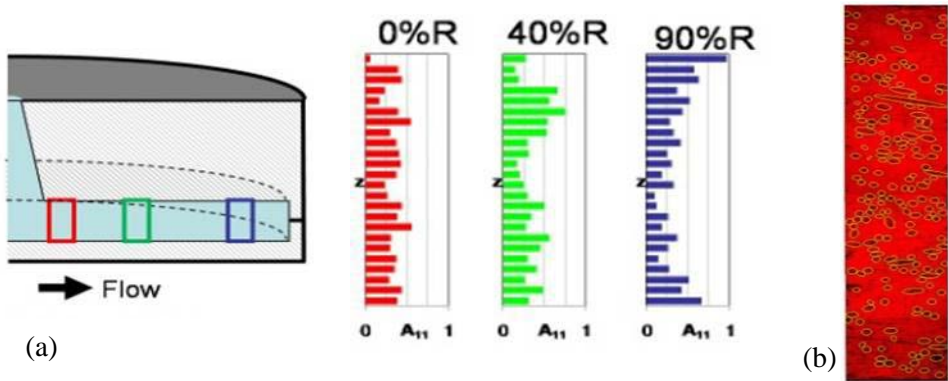

(a)   (b)

Figure 11. (a) Distribution of orientation component A_{11} along the gapwise direction in a center gated disk at 0%R, 40%R, and 90%R. (b) The typical images obtained by using confocal laser microscopy for the 30 wt% glass fiber-filled PBT.

A method for orientation and image analysis script has been developed to compute unambiguous values of the orientation tensor. This method consists of plasma etching of a polished plane with

the purpose of excavating the surface surrounding the fibers. With this process, the fiber borders become exposed, allowing the fiber's unambiguous orientation to be detected and measured with the use of microscopy and digital imaging. The contribution of Vlastimil Kunc form Oak Ridge National Laboratory in the development of the modified method and the image-analysis tool should be noted.

Simulation

Short Glass Fibers

The generalized Jeffery equation containing the non-affine motion parameter, Eq. (5), and the Folgar-Tucker term, last term in Eq. (2), was implemented in the simulation package. In addition various closure approximations have been implemented which include the quadratic, hybrid, linear and Invariant Based Optimal Fitting (IBOF).

Decoupled Simulations Using Delayed Generalized Jeffery Model

Figure 12(a) shows the measured orientation at the top half of the gate (-x- symbol) and 0.9R

(-•- symbol) for PBT filled with short glass fiber and the prediction at 0.9R using only Jeffery's model with measured orientation values at the gate (continuous line). The prediction using measured gate orientation shows several peaks and valleys that can be related to the layered structure formed at the gate which evolves locally as the flow progresses. The predicted profile at 0.9R can reproduce, at least qualitatively and in some regions quantitatively, the experimental profile. This is in sharp contrast with predictions using a random orientation at the gate (dashed line) or a prescribed constant orientation at the gate (not shown) which fail to show the layered structure.
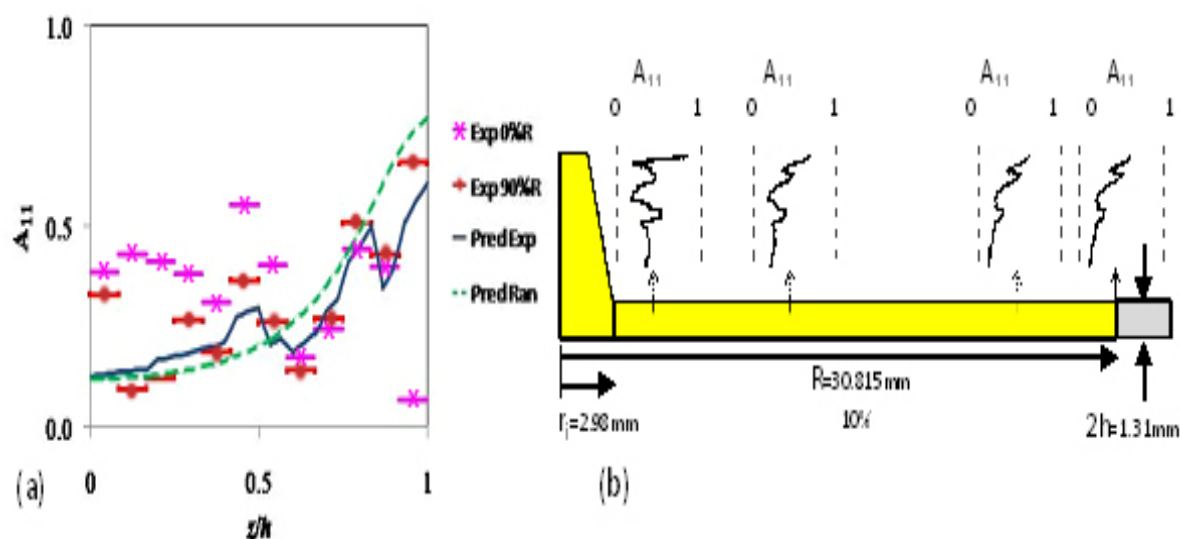
Figure 12. (a) Experimental values of A_{11} at the gate and close to the end of the mold (90% of radial flow length) with the predicted values of A_{11} orientation component close to the end of fill using random or measured orientation at the gate. (b) Evolution of orientation in a 75% short shot showing a layered structure expressed through the predicted A_{11} profiles at several locations in the top half of the disk.

These two gate orientations are always used in injection molding simulations and result in similar orientation profiles. All simulations fail to predict the measured orientation for the segment next to the axis of symmetry, the reason for this needs further investigation. Results for the orientation component A_{11} using piecewise gate orientation suggest a fading effect of the initial multilayered structure forming at least a shell-transition-core layer structure at long radial distances from the gate, as illustrated in Figure 12(b). A similar effect has been observed for the other dominant orientation component, A_{33}. The inter-particle

interactions through the Folgar-Tucker term (C_I=0.001) were considered in the model to try to improve the predictions obtained with the Jeffery model. However, the predictions using the additional terms with experimental piecewise initial orientation produced only slight changes in the predicted orientation, almost overlapping the predictions obtained using the Jeffery's model. Increasing the value of C_I to values in the range of 0.016 to 0.003, commonly found in the literature (e.g., Larson [13] and Folgar and Tucker [2]), also did not significantly change the orientation predictions.

Decoupled Simulations Using the Delayed Folgar-Tucker Model

Figures 13(a) and (b) show decoupled simulation results for the radial locations of 40% and 90% (R-r_i), respectively, focused on the upper half cavity at a dimensionless simulation time of 290. These predictions (lines) overestimate the A_{rr} orientation components while they underestimate the $A_{\theta\theta}$ and A_{rz} orientation components, when compared to experimental results (symbols). The smooth predicted profile could not reproduce a series of peaks and valleys observed in the experimental profile of orientation. These features

in the orientation profile can be related to the layered structure formed at the gate, which evolves locally as the flow progresses as indicated in the previous paragraph. However, when the experimental orientation profile is compared with simulation results at a dimensionless simulation time of 2.90 (1% of the simulation time), the values and features of orientation are successfully reproduced. This implies that the decoupled simulation using the delayed Folgar-Tucker model is evolving faster than the experimental evolution of orientation.
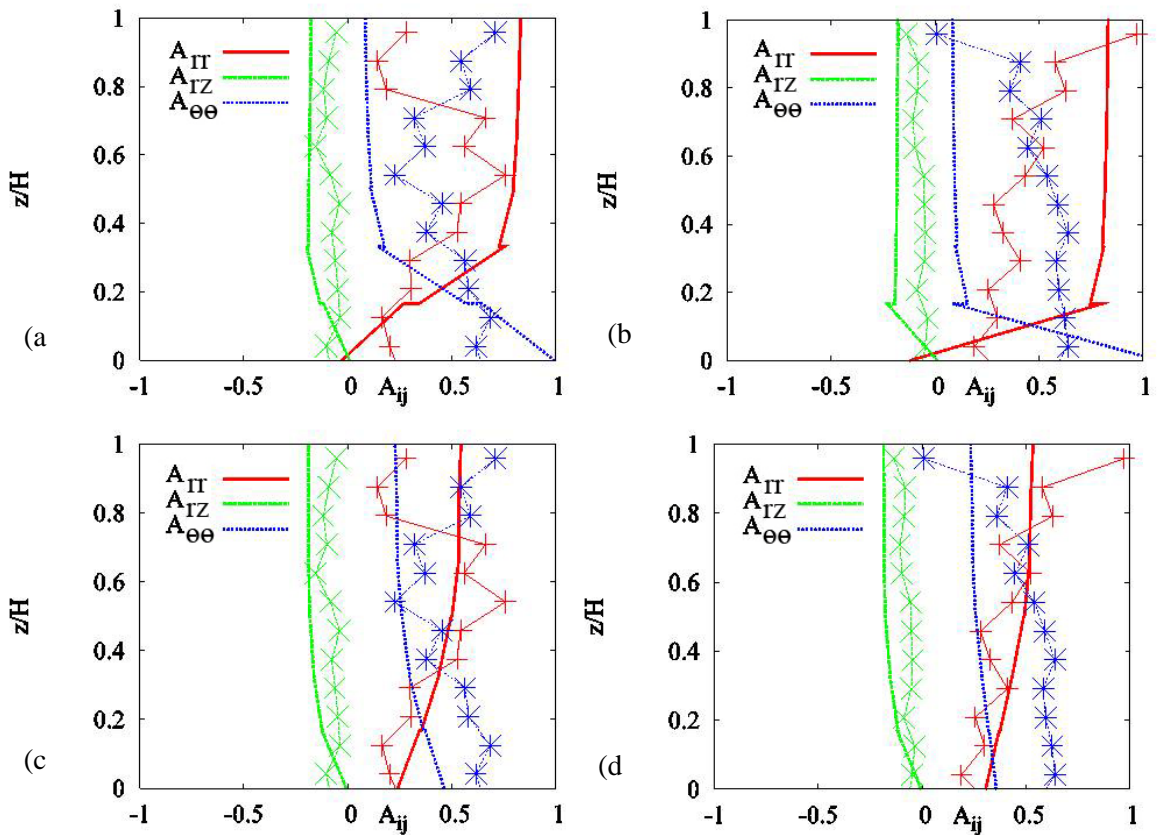
Figure 13. Experimental and predicted orientations from decoupled simulation at (a) 40% (R-r_i), and (b) 90% (R-r_i) and coupled simulation at (c) 40% (R-r_i) and (d) 90% (R-r_i). These simulations were run at a dimensionless time of 290. The lines denote the predictions, while the symbols are used to indicate the experimental results.

Coupled Simulations Using Delayed Folgar-Tucker Model

The results of the coupled simulation show improvement in the prediction of the orientation profile. Figure 13 depicts the upper half of the

orientation profile at a dimensionless time of 290 for (c) 40% (R-r_i), and (d) 90% (R-r_i). The results are sensitive to the use of the delayed Folgar-Tucker model because the retardation of evolution considerably improves the prediction of A_{rr}, but the profile of the predicted orientation is smooth.

In general the $A_{\theta\theta}$ is under estimated, but not as severely as in the decoupled approach. An interesting observation in coupled simulations is that the difference between experimental and predicted $A_{\theta\theta}$ is greater at 90% (R-r_i) than at 40% (R-r_i). This can be an effect of using the Hele-Shaw approximation, because this simplification ignores the existence of the flow front. It is well known that the front is a region dominated by extensional flow that is the driving mechanism for $A_{\theta\theta}$. Therefore, these coupled results suggest the need for full simulations, which are especially important in small geometries where the evolution of orientation never reaches the stable structure of orientation.

Long Glass Fibers

The generalized Jeffery equation containing the flexibility parameter, Eq. (5), was implemented in the simulation package. The flexibility parameter accounts for the flexibility of the fibers in a simplified manner. The idea was to evaluate the flexibility as a shrinkage occurring in the end-to-end vector of long glass fibers. To evaluate the model, simulations for short glass fiber PBT composites were performed. Long glass fiber 3-D orientation determination was attempted using a micro X-Ray tomography instrument at Virginia Tech, but the resolution of the instrument was not enough to obtain reliable orientation results. Figure 14 illustrates the experimental and predicted orientation profile for the A_{11} components at 0.4R (a) and 0.9R (b) when the flexibility of the fibers is considered. The continuous line indicates the predictions for the Jeffery's model (β=1) while the dashed line the predictions for Jeffery's model with flexibility parameter β=0.80. The results indicate that the model does not change significantly in the core region with the addition of the β parameter but causes a slight increase in the predictions for A_{11} close to the wall. In order to predict the orientation in a more robust way, the approach of the approach of the bead-rod model in a flow-driven system recently introduced by Strautins and Latz[8] was written into the simulation package.

(a)

(b)
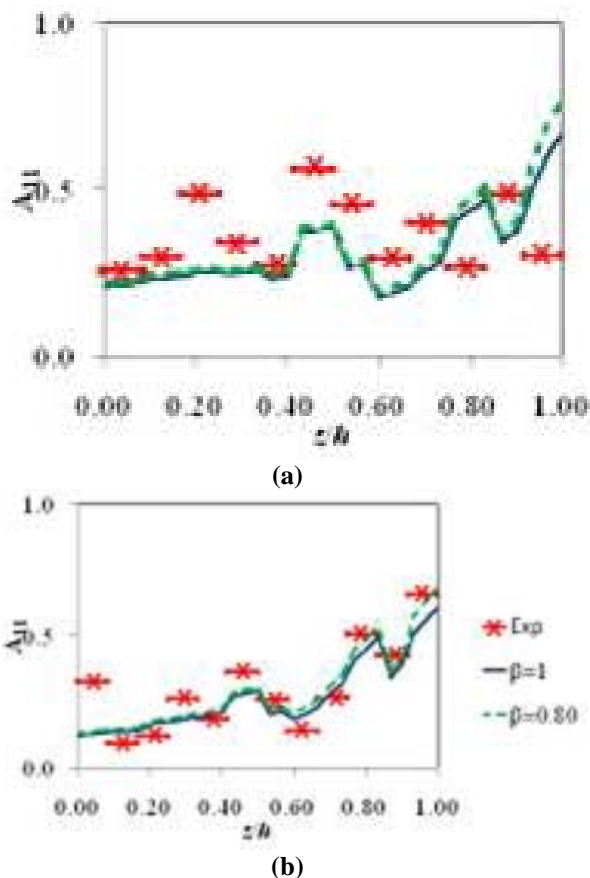
Figure 14. Predicted and experimental values of A_{11} at 0.40R (a) and 90R% (b) of a center-gated disk for the Jeffery model with β=1 and β=0.80 for the 30 wt% glass fiber-filled PBT.

In an effort to obtain preliminary results, the bead-rod model was used to simulate the case of a center-gated disk with random initial orientation at the gate. The simulation was performed with a velocity field obtained from parallel disk flow. The simulation results for the fiber orientation were then compared to experimentally determined orientations analyzed at 40% of the short shot length. Similar to the simulations conducted by the model's author (Strautins and Latz [8]), the parameter k is presently set equal to a dimensionless value of *0.5*. An analysis of this parameter's value will be conducted in the future to ensure its legitimacy. Additionally, the segment length l_B was given a dimensionless value that approximately corresponds to 0.5 mm; however, long fiber attrition data is currently being obtained for model length accuracy. The numerical results and experimental data are depicted in Figure 15. For comparison, a simulation using the Folgar-

Tucker model (with CI = 0.01) is also presented in this figure.
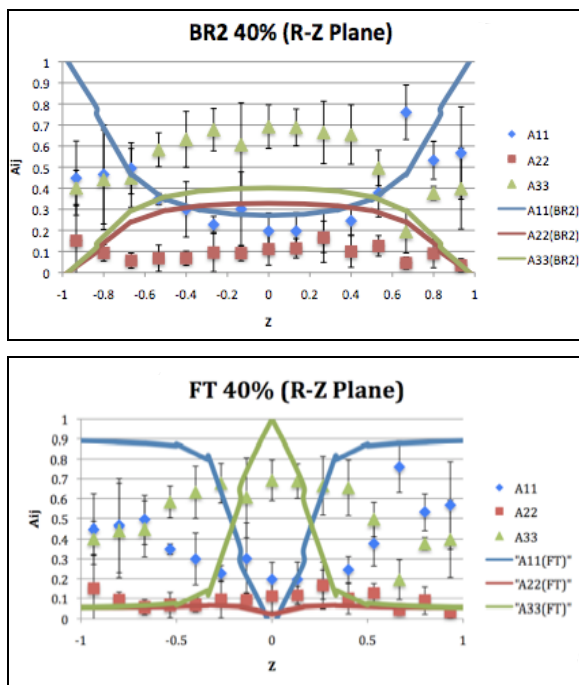
Figure 15. (top) Bead-Rod (BR2) and (bottom) Folgar-Tucker (F-T) simulation and experimentally measured results, for the trace components of the orientation tensor, versus the dimensionless mold thickness at 40% of the center gated disk length. The components are given by "r = 1," "z = 2," "θ = 3."

Preliminary results for the bead-rod simulation predict a much broader orientation distribution compared to what was obtained using the Folgar-Tucker model, which appears to more correctly describe the qualitative shape of the experimentally measured orientations. Additionally, an improvement in the A_{11} component is noticeable, but the A_{33} component is still underpredicted. More experimentation, however, is still in need before a complete opinion of this model's validity can be made. Future experiments will focus on fiber length and model parameter effects. Model predictions will then be compared to experiments for validation.

Conclusions

Short Glass Fiber Suspensions

We have determined a constitutive equation capable of predicting the transient rheological behavior of short glass fiber-filled polymeric

fluids. In addition we have developed a method to determine unique material parameters that are independent of shear rate. In general, we have developed a scheme which allows us to obtain the fundamental parameters from simple shear flow and then incorporate these into the simulation package. This is an improvement over the existing approach which using injection molding data (which is what one is trying to simulate). We have also developed a coupled approach in which the velocity field and orientation are calculated simultaneously. The simulations indicate that the orientation measured at the gate is crucial in obtaining the correct orientation pattern inside the cavity. (It has been assumed to be random to date.)

Long Glass Fiber Suspensions

We have designed and fabricated a sliding plate rheometer primarily for the purpose of performing unbiased and reproducible rheological experiments on long glass fiber-filled polymeric fluids that are otherwise impossible to perform on rotational rheometers. In addition, we have developed a simple approach to incorporate fiber flexibility into existing simulation structures for short glass fiber suspensions by incorporating a flexibility parameter β. Also, the bead-rod model presented within this research was shown to produce broad orientation distributions, a characteristic that preliminary results show to be consistent with long fiber flexibility. The bead-rod model is currently being assessed to see if it can correctly explain the dynamics of long fibers in complex flow. Lastly, an extension of Hinch's equation was written for tracking single fibers in concentrated polymer solutions. The use of this model in cooperation with parallel plate experiments will be used to gain further knowledge of long fiber dynamics through the use of mobility. The thrust of the future efforts will be on predicting orientation and configuration of long fibers during molding (compression and injection molding).

Publications as a Result of this Work

1. G. M. Velez, K. Ortman, A. P. R. Eberle, P. Wapperom, and D. G. Baird, "Simulation of Orientation in Injection Molding of a Highly Concentrated, Short Glass Fiber

Thermoplastic Composites," *SPE ANTEC Technical Paper*, accepted on Jan 2009.

2. K. Ortman, P. Wapperom, and D. G. Baird, "Long Glass Fiber Orientation in Thermoplastic Composites Using a Model that Accounts for the Flexibility of the Fibers," *SPE ANTEC Technical Paper*, accepted on Jan 2009.

3. P. R. Eberle, D. G. Baird, P. Wapperom, and G. M. Velez-Garcia, "Obtaining Reliable Transient Rheological Data on Concentrated Short Fiber Suspensions Using a Rotational Rheometer," J. Rheol., Accepted.

4. P. R. Eberle, G. M. Velez-Garcia, D. G. Baird, and P. Wapperom, "Fiber Orientation Kinetics of a Concentrated Short Glass Fiber Suspension in Startup of Simple Shear Flow," J. Non-Newt. Fl. Mech., submitted.

5. P. R. Eberle, D. G. Baird, P. Wapperom, and G. M. Velez-Garcia, "Using Transient Rheology to Determine Material Parameters in Fiber Suspension Theory," J. Rheol., accepted.

6. G. M. Velez, K. Ortman, A. P. R. Eberle, P. Wapperom, and D. G. Baird, "2-D Simulations of Orientation in Highly Concentrated Short Glass Fiber Thermoplastic Composites Made by Injection Molding," *Proceedings of the PPS Americas Regional Meeting*, Charleston, South Carolina, 26–29 October 2008.

7. K. Ortman, D. G. Baird, and P. Wapperom, "Long Glass Fiber Orientation in Thermoplastic Composites Using a Model that Accounts for Flexibility of the Fibers," *Proceedings of the PPS Americas Regional Meeting*, Charleston, South Carolina, 26–29 October 2008.

8. A. P. R. Eberle, G. M. Velez, P. Wapperom, and D. G. Baird, "Fiber Orientation Kinetics of a Concentrated Short Glass Fiber Suspension in Start Up of Shear Flow," *Proceedings of the PPS Americas Regional Meeting*, Charleston, South Carolina, 26–29 October 2008.

9. G. M. Velez, K. Ortman, A. P. R. Eberle, P. Wapperom, and D.G. Baird, "Simulation of Orientation in Injection Molding of High Aspect Ratio Particle Thermoplastic Composites," *Proceedings of the XVth International Congress of Rheology*, Monterey, California, 3–8 August 2008.

10. A. P. R. Eberle, G. M. Velez, D. G. Baird, and P. Wapperom, "The Dynamic Behavior of a Concentrated Non-Brownian Glass Fiber Suspension in Simple Shear Flow," *Proceedings of the XVth International Congress of Rheology*, Monterey, California, 3–8 August 2008.

11. A. P. R. Eberle, D. G. Baird, and P. Wapperom, "The rheology of non-Newtonian fluids containing glass fibers: A review of experimental literature," Ind. Eng. Chem. Res., 47:9, 2849–2872 (2008).

12. A. P. R. Eberle, G. M. Velez, D. G. Baird, and P. Wapperom, "The Dynamic Behavior of a Concentrated Polymeric Suspension Containing Non-Brownian Glass Fibers in Simple Shear Flow," *SPE ANTEC Technical Paper*, **2008**, 868–872.

Presentations Directly Related to this Work (underline denotes presenting author)

1. <u>G. M. Velez</u>, K. Ortman, A. P. R. Eberle, P. Wapperom, and D. G. Baird, "Frontal Flow Effects in 2D Simulations of Orientation in High Aspect ratio Particles Composites Made by Injection Molding," *AIChe Annual Meeting*, Philadelphia, PA, USA, November 2008.

2. K. Ortman, <u>G. M. Velez</u>, A. P. R. Eberle, D. G. Baird, and P. Wapperom, "Long Glass Fiber Orientation in Thermoplastic Composites Using a Model that Accounts for the Flexibility of Fibers," *AIChe Annual Meeting*, Philadelphia, PA, USA, November 2008.

3. A. P. R. Eberle, G. M. Velez, <u>D. G. Baird, and P.</u> Wapperom, "Shear Rheology and Microstructure of a Concentrated Short Glass Fiber-Filled Polybutylene Terephtalate (PBT)," *AIChe Annual Meeting*, Philadelphia, PA, USA, November 2008.

4. <u>G. M. Velez</u>, A. P. R. Eberle, K. Ortman, P. Wapperom, and D. G. Baird, "2-D Simulations of orientation in Highly Concentrated Short Glass Fiber Thermoplastic Composites Made by Injection Molding," *PPS Regional Meeting*, Charleston, SC, USA, October 2008.

5. <u>K. Ortman</u>, G. M. Velez, A. P. R. Eberle, P. Wapperom, and D. G. Baird, "Long Glass

Fiber Orientation in Thermoplastic Composites Using a Model that Accounts for Flexibility of the Fibers," *PPS Regional Meeting*, Charleston, SC, USA, October 2008.

6. A. P. R. Eberle, D. G. Baird, <u>P. Wapperom</u>, and G. M. Velez, "Fiber Orientation Kinetics of a Concentrated Short Glass Fiber Suspension in Start Up of Shear Flow," *PPS Regional Meeting*, Charleston, SC, USA, October 2008.

7. G. M. Velez, A. P. R. Eberle, K. Ortman, <u>P. Wapperom</u>, and D. G. Baird, "Simulation of Orientation in Injection Molding of High Aspect Ratio Particle Thermoplastic Composites," *XVth International Congress of Rheology*, Monterey, CA, August 2008.

8. A. P. R. Eberle, G. M. Velez, <u>D. G. Baird</u>, and P. Wapperom, "The Dynamic Behavior of a Concentrated Non-Brownian Glass Fiber Suspension in Simple Shear Flow," *XVth International Congress of Rheology*, Monterey, CA, August 2008.

9. D. G. Baird, "Rheology and Simulation of Flows of Polymeric Fluids Containing Rigid and Flexible Fibers," University of Naples, June 13, 2008.

10. A. P. R. Eberle, <u>G. M. Velez</u>, D. G. Baird, and P. Wapperom, "The Dynamic Behavior of Concentrated Polymeric Suspension Containing Non-Brownian Glass Fibers," *SPE ANTEC Annual Technical Conference*, Milwaukee, WI, USA, May 2008.

11. <u>A. P. R. Eberle</u>, G. M. Velez, D. G. Baird, and P. Wapperom, "The Dynamic Behavior of Concentrated Non-Brownian Glass Fiber Suspensions," *Invited lecture: Virginia Tech*, Blacksburg, VA, March 2008.

12. <u>A. P. R. Eberle</u>, G. M. Velez, D. G. Baird, and P. Wapperom, "The Dynamic Behavior of Non-Brownian Glass Fiber Suspensions," *Invited lecture: University of Delaware*, Newark, DE, January 2008.

References

1. S. G. Advani and C. L. Tucker, "The use of tensors to describe and predict fiber orientation in short fiber composites," J Rheol **31** (8), 751–784 (1987).

2. F.P. Folgar and C. L. Tucker, "Orientation behavior of fibers in concentrated suspensions," J Reinf Plast Comp **3**, 98–119 (1984).

3. G. B. Jeffery, "The motion of ellipsoidal particles immersed in a viscous fluid," Proc. R. Soc. A **102**, 161–179 (1922).

4. S. M. Dinh and R. C. Armstrong, "A rheological equation of state for semi-concentrated fiber suspensions," Journal of Rheology **28** (3), 207–227 (1984).

5. E.S.G. Shaqfeh and G. H. Fredrickson, "The hydrodynamic stress in a suspension of rods," Phys Fluids A-Fluid **2** (1), 7–24 (1990).

6. E. J. Hinch, "The distortion of a flexible inextensible thread in a shearing flow," *J Fluid Mech* **74**, 317–333 (1976).

7. J. D. Goddard and Y. H. Hung, "On the motion of flexible threads in a Stoke's shear field," J Non-Newton Fluid Mech **13**, 47–62 (1983).

8. U. Strautins and A. Latz, "Flow-driven orientation dynamics of semi-flexible fiber systems," *Rheol Acta* **46**, 1057–1064 (2007).

9. R. S. Bay and C. L. Tucker, "Stereological measurement and error estimates for three-dimensional fiber orientation," Polym Eng Sci **32** (4), 240–253 (1992).

10. C. Eberhardt and A. Clarke, "Fibre-orientation measurements in short-glass-fibre composites. Part I: automated, high-angular-resolution measurement by confocal microscopy," Composites Science and Technology **61**, 1389–1400 (2001); A.R. Clarke, Eberhardt, C.N., *Microscopy techniques for materials science* (CRC Press Boca Raton, FL, 2002).

11. B. E. VerWeyst and C. L. Tucker, "Fiber suspensions in complex geometries flow/orientation coupling," Can J Chem Eng **80**, 1093–1106 (2002).

12. D. H. Chung and T. H. Kwon, "Numerical studies of fiber suspensions in an axisymmetric radial diverging flow: the effects of modeling and numerical assumptions," J. Non-Newtonian Fluid Mech. **107**, 67–96 (2002).

13. R. G. Larson, *The structure and rheology of complex fluids*. (Oxford University Press, New York, 1999).

N. Incorporating Higher-Order Tensors in the Computation of Polymer Composite Mechanical Properties

Principal Investigator: Douglas E. Smith
University of Missouri
E2411 Lafferre Hall/MAE Dept., Columbia, MO 65211
(573) 884-6552; fax: (573) 884-5090; e-mail: smithdoug@missouri.edu

Technology Area Development Manager: Joseph A. Carpenter
(202) 586-1022; fax: (202) 586-1600; e-mail: joseph.carpenter@ee.doe.gov

Participants: David A. Jack, Elijah C. Caselman and Joseph Middleton, University of Missouri

Objective

- Develop a predictive capability that incorporates higher-order orientation tensors to evaluate mechanical properties of short- and long-fiber reinforced polymer composites.

Approach

- Develop a model for predicting mechanical properties from higher-order orientation tensors derived from flow simulations or measurements that are not limited by the material symmetry requirements imposed by current models.

- Develop an automated three-dimensional (3D) voxel-based finite element modeling technique that may be used to predict the effective mechanical properties of short- and long-fiber suspensions.

- Integrate Micro-CT derived fiber reconstructions (obtained from industry or DOE) to illustrate the applicability of the proposed approach on production hardware.

- Perform a statistical assessment of mechanical property calculations to address sampling issues associated with using the proposed averaging techniques.

- Demonstrate the proposed methodology on an industrially-relevant polymer composite product where flow simulation software is to be provided by Moldflow Corporation.

Accomplishments

- Derived an analytical relationship between elastic mechanical properties and fiber orientation tensors for statistically independent short fibers, including both the property's mean and variance.

- Evaluated mechanical properties using existing property models from simple melt flow simulations that employ 4th and 6th order tensor closures.

- Developed a Monte Carlo method for computing mean and variance of elastic properties of short fiber composites from fiber orientation distribution functions.

- Evaluated mechanical properties of short fiber composites via Monte Carlo sampling procedures, validating analytical approach developed as part of this project.

- Developed a 3D voxel-based finite element model using a Representative Volume Element (RVE) and related periodic boundary conditions for predicting elastic material properties of short and long fiber polymer composites.

- Computed elastic properties for continuous, short aligned, and short random fiber composites and compared results with existing analytical models using the 3D voxel-based finite element modeling approach.

- Computed elastic properties for a long random fiber composite sample using the 3D voxel-based finite element modeling approach where fiber locations were determined from Micro-CT scans provided by Oak Ridge National Laboratory.

Future Direction

- Continue verification work for the 3D voxel-based finite element procedure for fiber reinforced polymer composites.

- Integrate 3D voxel-based finite element approach with loaded CT testing to better understand the local and global structural behavior of long fiber composites.

- Apply 3D voxel-based finite element approach to predict the structural response of actual products made of long fiber composite materials.

- Continue to develop an automated procedure for defining three-dimensional finite element models of a representative cell that may be used with analytically derived fiber orientation distribution functions, or fiber orientation states obtained from Micro-CT measurements.

- Develop computational approach to evaluate 3D long fiber locations and orientations from polymer flow simulations.

- Develop fracture analysis capability for 3D voxel-based finite element procedure.

Introduction

The purpose of this project is to develop a predictive capability that incorporates higher-order orientation tensors to evaluate mechanical properties of short- and long-fiber reinforced polymer composites. To realize this goal, the project will develop a computational methodology to predict elastic mechanical properties from orientation tensors of second- and fourth-order which are computed during melt flow simulations. The micromechanics of both short- and long-fiber suspension will be simulated with a three-dimensional (3D) voxel-based finite element modeling approach, so that the mechanical properties of randomly oriented fiber samples can be computed. Simulated fiber orientation states, as well as those obtained from Micro-CT scans will serve as input. Finally, fiber orientation states from industrially-relevant products will be evaluated with the new methodology to assess its applicability with complex geometries.

This report provides a brief description of the three year project, a predictive method for mean and variance of elastic properties using higher-order tensors, Monte Carlo Validation, and results from our 3D voxel-based finite element approach

applied to continuous, short- and long-fiber composites.

Project Deliverables

The primary deliverable of this research is a relationship between higher-order (i.e., fourth-order) orientation tensors, fiber orientation distribution functions, and/or long fiber geometry and the elastic mechanical properties of the composite structure. An assessment of the variability of mechanical properties among fiber orientation states will be provided, along with a computational procedure for evaluating the same properties for a specific orientation state. This document serves as a final report generated to communicate the functional form of the mechanical properties and the relevant model parameters for the specific examples studied.

Background

Orientation tensors are used extensively to represent the stochastic nature of polymer composite fiber suspensions in a form that is suitable for large-scale melt flow simulations. Orientation tensor research over the past two decades has advanced the state-of-the-art related to polymer composites; however, the use of

tensors today is still basically the same as it was when these methods were first developed nearly twenty years ago. In addition, the application of orientation tensors to long-fiber composites is nearly non-existent.

The continued advancement of our basic understanding of short- and long-fiber reinforced polymer composites is critical in numerous industries including consumer products and automotive which rely heavily on the low cost, design flexibility, and superior performance offered by these materials. A major focus of the National Science Foundation/US Department of Energy/American Plastics Council sponsored workshop [1] co-organized by the PI in June, 2004 was the need for the US automotive industry to incorporate more fiber reinforced polymer composites in the design of future vehicles to reduce the weight, emissions, and fuel consumption.

For example, a specific goal of the 2010 FreedomCAR is to reduce the weight of an automotive structure by 50% for the same cost and durability as seen in today's products. The key to meeting these objectives is a comprehensive predictive engineering approach that is capable of accurately simulating critical attributes associated with the design of both the product and its manufacturing process. In this approach, a critical link that connects the computation of materials processing attributes with the prediction of a composite product's performance is the evaluation of structural mechanical properties from melt flow predictions.

Given the dramatic increases in affordable computing over the past decade and the anticipated demands on our predictive capabilities for composite materials over the next decade, it is now time to reconsider assumptions that compose today's fiber orientation models. For example, limiting fiber orientation predictions to solving for only the second-order orientation tensor components in an effort to reduce computational effort may not be necessary.

Evaluating Elastic Properties from Orientation Tensors

One task of this research is to develop a formulation for computing short- and long-fiber composite elastic properties from orientation tensors. Here we consider the expected value of the elasticity tensor $\langle C_{ijkl} \rangle$ defined in terms of the orientation distribution function $\psi(\mathbf{p})$ as

$$\langle C_{ijkl} \rangle = \int_S Q_{pi}(\mathbf{p})Q_{qj}(\mathbf{p})Q_{rk}(\mathbf{p})Q_{sl}(\mathbf{p})\overline{C}_{pqrs}\,\psi(\mathbf{p})d\mathbf{p}$$

where $\mathbf{p}$ is a unit vector in the fiber direction as shown in Figure 1. In this calculation, $\overline{C}_{pqrs}$ is the
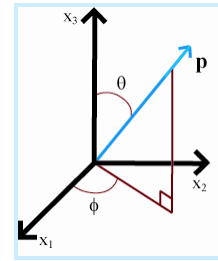
Figure 1. Coordinate system defining fiber direction with the unit vector p(θ,ϕ).

underlying unidirectional compliance tensor for a single fiber (computed using the Mori-Tanaka, Halpin-Tsai, or similar inclusion model) and $Q_{ij}(\mathbf{p})$ is a rotation tensor that rotates the unidirectional components into a selected coordinate system. Elasticity tensor components may be computed in this manner for various orientation distribution functions. However, when $\psi(\mathbf{p})$ is written in terms of the Fourier basis functions such as those given in Advani and Tucker [2], it can be shown that $\langle C_{ijkl} \rangle$ reduces to the well-known result

$$\begin{aligned}
\langle C_{ijkl} \rangle = &\, B_1\left(a_{ijkl}\right) + B_2\left(a_{ij}\delta_{kl} + a_{kl}\delta_{ij}\right) \\
&+ B_3\left(a_{ik}\delta_{jl} + a_{il}\delta_{jk} + a_{jl}\delta_{ik} + a_{jk}\delta_{il}\right) \\
&+ B_4\left(\delta_{ij}\delta_{kl}\right) + B_5\left(\delta_{ik}\delta_{jl} + \delta_{il}\delta_{jk}\right)
\end{aligned}$$

where a_{ij} and a_{ijkl} are the 2nd and 4th order fiber orientation tensors, δ_{ij} is the identity tensor, and the constants B_1–B_5 are computed from $\overline{C}_{pqrs}$.

This derivation shows that when the elastic properties are computed as the volume-averaged result of unidirectional fibers weighted by the orientation distribution function, the highest-order orientation tensor that contributes is the fourth. In this case, sixth- and higher-ordered orientation tensors do not define to the composite's elasticity tensor. What is important to note about this result is that the equations above implicitly assume that the fibers composing aij and aijkl do not interact when stresses are imposed on the fiber-matrix structure. While the effect of fiber interaction has received much attention in melt flow analyses, little effort has been devoted to understanding its role on elastic response of these composites. The elastic response of a high volume-fraction short-fiber composite, as well as long-fiber composites, is expected to be influenced by structural fiber-fiber interaction.

The variance σ^2_{ijkl} of the elastic properties may be computed in a similar manner by taking the second moment of the rotated unidirectional compliance tensor about the mean given as

$$\sigma^2_{ijkl} = \oint_{S^2} \left(Q_{qi}(\mathbf{p})Q_{rj}(\mathbf{p})Q_{sk}(\mathbf{p})Q_{tl}(\mathbf{p})\overline{C}_{qrst} - \langle C_{ijkl} \rangle \right)^2 \psi(\mathbf{p})d\mathbf{S}$$

For relatively simple $\psi(\mathbf{p})$, an analytical result for variance may be obtained by integrating the above equation. This has been performed here for several fiber orientation distribution functions $\psi(\mathbf{p})$. These results are beyond the scope of this report but may be found elsewhere [3]. It is important to note here that while the mean value of the elasticity tensor $\langle C_{ijkl} \rangle$ contains orientation tensors through 4th order, the variance σ^2_{ijkl} is a function of orientation tensors through 8th order. Therefore, to use the result described here, analytical or approximate values of the 2nd, 4th, 6th, and 8th order orientation tensors are required.

Monte Carlo Simulation

A Monte Carlo simulation method was developed to validate analytical results for the mean and variance obtained above for the elastic properties of a short fiber composite. The Monte Carlo calculations included an Accept-Reject algorithm to obtain a set of fiber orientation angles for any given orientation distribution that is described by an orientation distribution function or set of orientation tensors. The mean and variance of the compliance matrix are computed in these Monte Carlo simulations using a discrete form of the continuous equations given above for $\langle C_{ijkl} \rangle$ and σ^2_{ijkl}.

Several example Monte Carlo calculations were performed that validate the analytical forms described above. Here we consider the fiber orientation distribution function

$$\psi(\theta, \phi) = c \sin^{2n} \theta \cos^{2n} \phi$$

where θ and ϕ describe fiber angles shown in Figure 1. Figure 2 illustrates the form of this distribution function (with n = 4, and c = 9/4π) which is highly aligned in the x1 direction. Figure 2 also shows a representative volume of fibers with a volume fraction of 10% that has generated for the Monte Carlo simulations. Computed results for C1111 are shown in Figure 3 for 108 Monte Carlo simulations where matrix and fiber properties are taken from Tucker and Lang [4] and the volume fraction is 10%. As shown in the figure, this component of the compliance tensor varies between a predictable lower and upper bound with a nearly linear probability distribution.

(a)   (b)
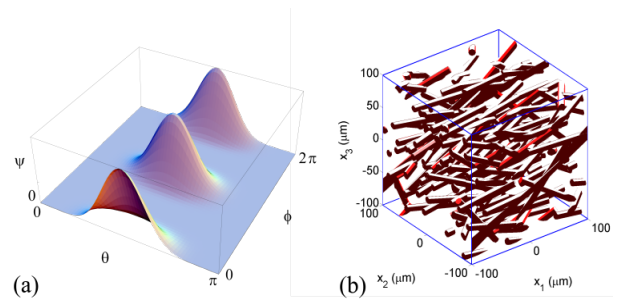
Figure 2. Fiber orientation distribution function used in example calculations (a) and a representative sample set of fibers (b).
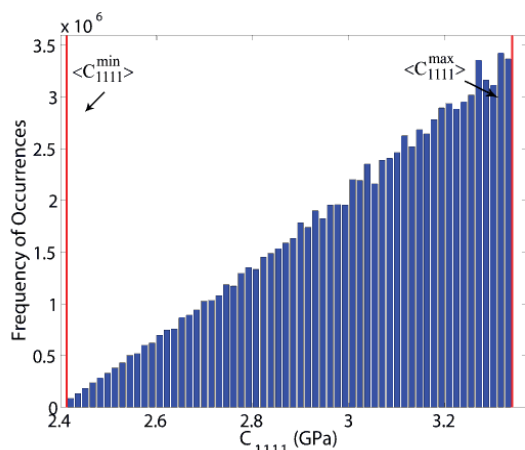
Figure 3. Histogram from Monte Carlo calculations for C_{1111} using 10^8 fiber occurrences.

Of more practical use is the predicted distribution and related statistical properties for multiple sets of fibers since we are typically interested in the elastic properties of a material point which can vary from part to part. To this end, we apply the Central Limit Theorem to compute the statistical nature of multiple sets of fibers such as that shown in Figure 2(b). Figure 4 shows the results of 10^6 sets of fibers where each set contains 101 fibers. As predicted by the Central Limit Theorem, the results become normally distributed. Also shown is the analytically evaluated normal distribution function obtained by applying the Central Limit Theorem to the analytical mean and variance equations given above. The figure clearly shows that the analytical form that we have derived for the statistical properties of fiber suspensions is verified through our Monte Carlo simulations.
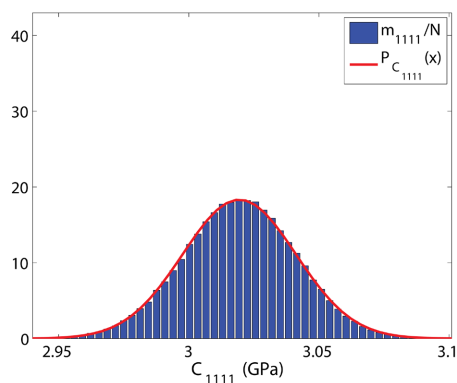
Figure 4. Histogram and normal probability distribution function for C_{1111} using 10^6 fiber sets of 101 fibers each.

Monte Carlo simulations have also been performed to predict the statistical behavior of the compliance tensor for composites that result from center-gated disk flow. Results are computed from the expression given above for the mean and standard deviation (Pc_{1111}) in addition to those obtained via Monte Carlo simulation (m_{1111}/N for 10^6 sets of N=203 fibers) for C_{1111} appear in Figure 5.
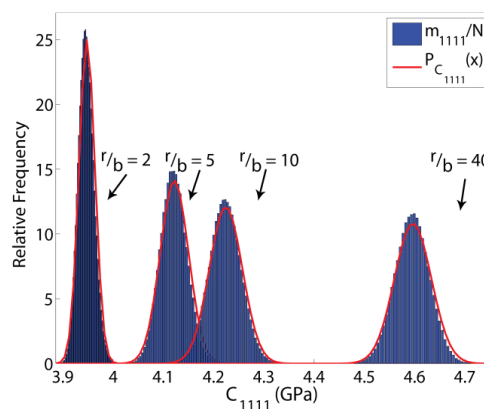
Figure 5. Center-gated disk elastic properties at various distances from gate (r = radius, b = disk thickness).

Three-dimensional Finite Element Analysis for Evaluating Mechanical Properties

All of the calculations described above are restricted to short fiber composites, and explicitly assume that the stress state around each fiber is not influenced by its neighbors. To address these shortfalls, a voxel-based 3D finite element modeling technique was developed that can be used to gain a better understanding of the effect of fiber-fiber interaction in the elastic solid. Our approach is to use a voxel-based finite element model to define a Representative Volume Element (RVE) within the composite structure. Properties of each point within the model are based on fiber distributions obtained analytically, or through experimentally derived procedures, making it possible to include short- and long-fiber composites in the analysis.

To reduce the number of degrees-of-freedom in these 3D finite element simulations, a custom element computed from

$$K^e = \int_{V_e} \hat{B}^T C \hat{B} J dV$$

which is evaluated numerically in the usual manner. Material properties at each sampling (or Gauss) point within the elements are defined based on their position within the composite structure. This allows for a more refined spatial definition without increasing the number of degrees of freedom in the system matrices. In the above, $\hat{B}$ is based on unique elemental shape functions that have been created to increase the complexity of the displacement field in each element. Using our modified shape functions, elements which contain both matrix and fiber are not over-constrained by the more traditional bi-linear response.

This modeling approach was implemented in the general purpose finite element program ABAQUS with a user defined element. RVEs [see e.g., Figure 2(b)] are defined by a uniform grid of 3D elements where the elastic properties of each Gauss point are defined by its spatial location in relationship to the position of the fibers. The number of Gauss points is increased within each element to provide the required spatial refinement. In addition, periodic boundary conditions are implemented so that both axial and shear loads may be accurately applied to the RVE. A fitting procedure has also been developed to compute the compliance tensor and elastic properties from multiple RVE runs where constraints are imposed to enforce a desired material symmetry.

Figure 6(a) shows a finite element model of a continuous boron ($E = 379.3$ GPa, $\nu = 0.1$, volume fraction = 0.47) fiber embedded in an aluminum ($E = 68.3$ GPa, $\nu = 0.3$) matrix that has been used to validate our calculation procedure. The dimensions and properties for this model are taken from Xia et al. [5], who provide analytical, numerical, and experimental results for comparison. Figure 6b shows a voxel-based finite element model of the same geometry where contours are provided to indicate the fiber's location. Note that this plot simply shows element by element values, and thus does not provide insight into the spatial refinement within each element that is included with our multiple-Gauss point approach. Both of these models were loaded in tension and shear to generate the response data

(a)   (b)
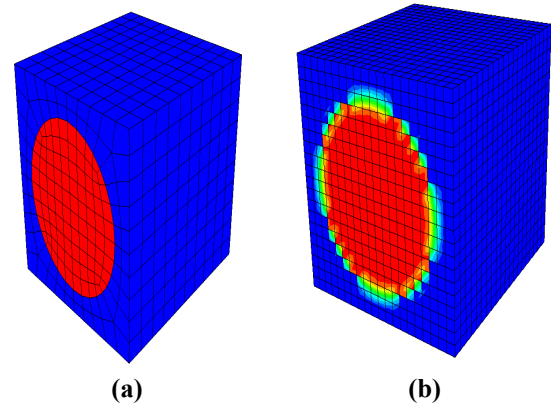
Figure 6. (a) Two material RVE finite element model as defined by Xia et al., and (b) contours illustrating elements that contain fiber, matrix, or both.

required for our elastic property curve fitting procedure.

Table 1 compares engineering elastic constants obtained from the models in Figure 6 with values provided by Xia et al. It can be seen that our two-material model [Figure 6(a)] provides results that are nearly identical to Xia's results (as expected) which compare well with experimental data as reported in their paper. Table 1 also shows that results obtained with our 3D voxel-based FE [see Figure 6(b)] model agree quite well with the two material models. These latter results are computed with 10 elements in each of the *x*, *y*, and *z* directions where the elements have 6 Gauss points in each direction.

Table 1. Elastic properties computed from two material and voxel-based finite element models (Moduli in GPa).

| Elastic Constants	Xia et al.	Two mat model Figure 6(a)	Voxel-based model Figure 6(b)
E_{11}	214	214.4	216.1
E_{22}	143	143.7	147
E_{33}	143	143.7	147
G_{12}	54.2	53.9	56.4
G_{23}	45.7	45.4	45.6
G_{13}	54.2	53.9	56.4
ν_{12}	0.195	0.195	0.194
ν_{23}	0.253	0.253	0.244
ν_{13}	0.195	0.195	0.194

Aligned Short Fiber Models

The voxel-based multi-Gauss point FEA method described above was also applied to aligned short fiber models. The composite structure evaluated in Tucker and Liang[4] is studied here to validate our computational procedure. Fibers in both a regular and staggered array have been modeled with a fiber volume fraction and aspect ratio of 0.2 and 8, respectively. Elastic properties of the fiber and polymer matrix appear in Table 2.

Table 2. Aligned short fiber polymer composite model elastic properties.

Material	E (GPa)	ν
fiber	30	0.2
matrix	1	0.38

Figure 7 shows a conventional finite element model (i.e., one with element boundaries that separate fiber and matrix) of a regular array short fiber composite. The uniform mesh model of the same composite (not shown) is a rectangular solid FE model of the same size with cubic finite elements with similar edge lengths as the model in Figure 7.
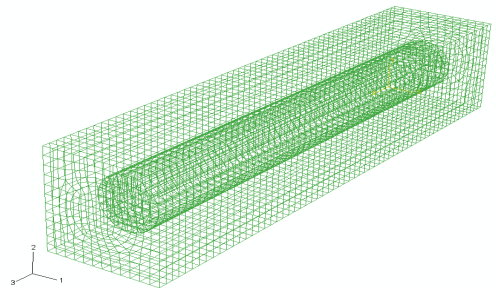
Figure 7. Conventional FE model of regular array aligned short fiber composite.

Figure 8 illustrates stresses in the conventional and uniform mesh FE models under axial loading along the fiber axis. The boundary of the fiber is clearly seen in the conventional model, while elements along the fiber's boundary in the uniform mesh model have average values between those in the fiber and matrix. The shear stress along the length of the fiber is shown in Figure 9 for the same two models. The shape of the boundary in both deformed models illustrate that the periodic boundary conditions are correct.
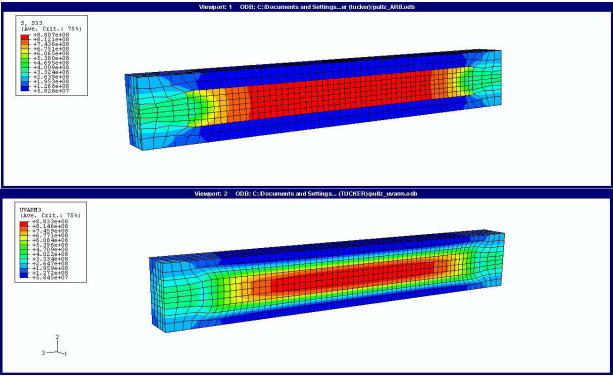
Figure 8. Axial stresses for the regular array aligned short fiber models under tension along the fiber's axis. Top: conventional model. Bottom: uniform mesh model.
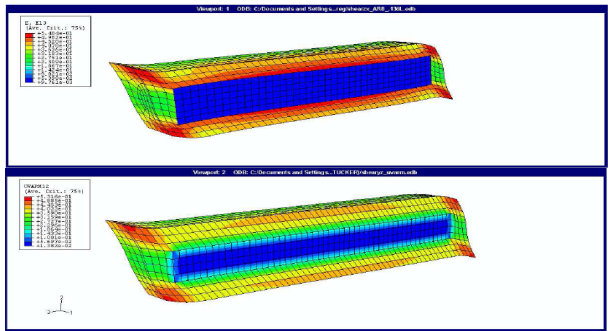
Figure 9. Shear strains for the regular array aligned short fiber models under shear along the fiber's axis. Top: conventional model. Bottom: uniform mesh model.

Table 3 summarizes calculated effective elastic properties for the aligned short fiber composite models studied here. Our results are compared with those given in Tucker and Liang[4] and the classical theory of Tandon-Weng. Results are in good agreement with minor deviations for some values. Note that the uniform mesh results were computed with 8 Gauss points in each of the three coordinate directions.

Random Fiber Orientations

The multi-Gauss point FE method described above was applied to random short fiber composites where individual fibers having a diameter of 10 microns and an aspect of 10 were generated in 200×200×200 micron cube following the analytical fiber orientation distribution function given above with $n = 4$ and $c = 9/4\pi$ and shown in Figure 2. Volume fractions considered ranged

Table 3. Effective elastic properties for aligned short fiber composite.

Elastic constant	Tucker-Liang[4]	Tandon-Weng	Conv. mesh	Uniform mesh
E_{11}/E_m	4.2	3.37	3.97	4.06
E_{22}/E_m	1.55	1.51	1.62	1.67
G_{12}/E_m	na	0.54	0.53	0.54
G_{23}/E_m	na	0.51	0.49	0.48
v_{12}	0.335	0.362	0.338	0.338
v_{23}	0.48	0.49	0.487	0.471

from 2% to 30% and a Monte Carlo simulation method was used to define the orientation vector **p** for each fiber in the cube. All results are compared with analytical results using both the Halpin-Tsai and Tandon-Weng procedures.

All calculations are based on 10 cubes of fibers where each cube includes fibers from the same distribution function and volume fraction. A convergence analysis was performed using a volume fraction of 0.1 with 8,000–64,000 elements and 6–10 Gauss points in each of the three coordinate directions. It was found that over this broad range of model parameters, elastic constants varied by less than 1.5%. All results reported below include 27,000 elements with 6 Gauss points in each direction.

Figure 10 shows average values of E_{11} and E_{22} for random short fiber composite samples over a range of volume fractions. Results agree well with similar results computed with the Halpin-Tsai and Tandon-Weng equations at low volume fractions. Stiffer results are computed using our FEA approach as the volume fraction increases. Fiber interactions in the structural model are expected to have increased the stiffness prediction in the uniform mesh FEA model when compared to the analytical methods which treat fibers as statistically independent. Poisson's ratios (not shown) tend to have larger deviations between our numerical results and those computed using the classical analytical procedures. Overall, the 3D voxel-based, multi-Gauss point approach provides elastic constants over a range of volume fraction that are potentially more accurate than those provided by prior methods.
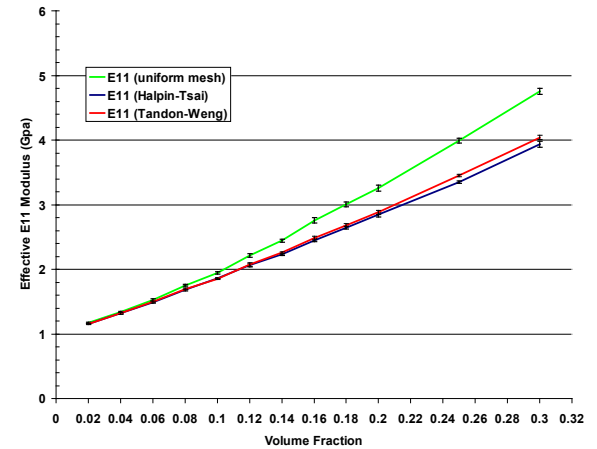
(a)
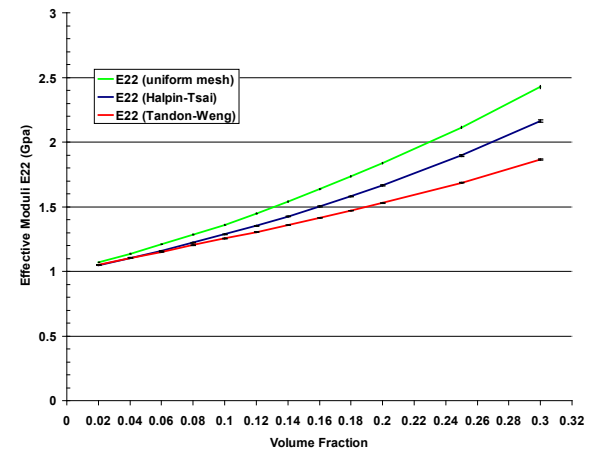
(b)

Figure 10. Elastic properties of a short fiber composite sample as a function of volume fraction: (a) E_{11} and (b) E_{22}
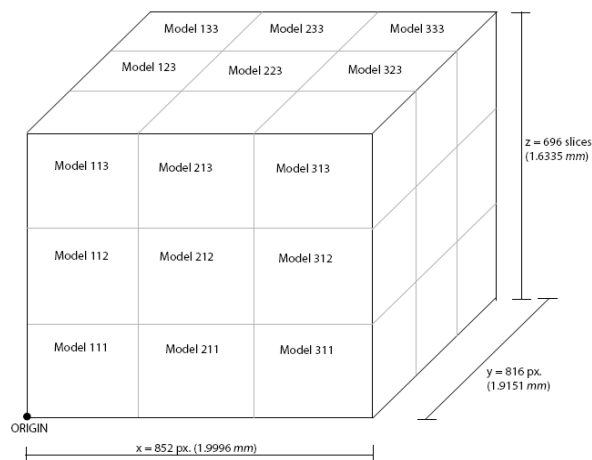
Long Fiber Composite Analyses

A long fiber composite material was evaluated using the uniform mesh, multi-Gauss point method described above. The long fiber geometry was evaluated from micro CT images obtained from Vlastimil Kunc at Oak Ridge National Laboratory. One thousand, two hundred slices of data were analyzed for the approximately 2×2×1.63 mm long fiber sample. A rendering of a sub region of the 3D sample appears in Figure 11. Raw data are shown here, however, calculations described below were performed after several image processing steps that filtered and smoothed the voxel values to better serve the needs of the present study.
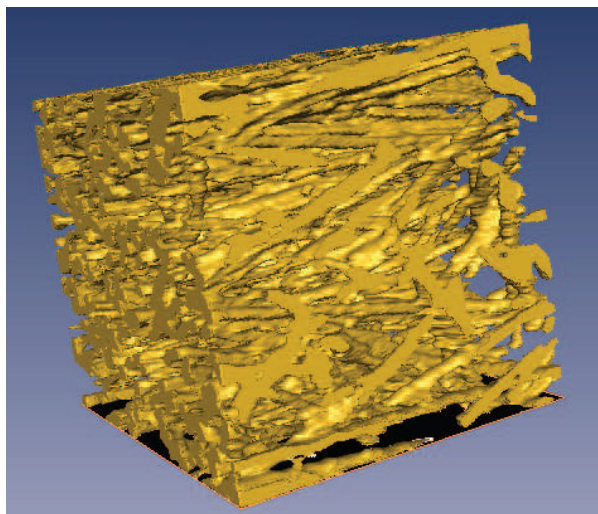
Figure 11. 3D rendering of sub region of long fiber composite model generated from micro CT slice data.

Data from the long fiber composite sample were split into 27 sub regions in a 3D grid of 3×3×3 along each edge of the original rectangular solid of material as shown in Figure 12. Then, FE models of each sub region were defined and analyzed to predict the elastic mechanical properties for the composite. Each sub region model contained 36×34×29 elements for a total of 35,496 elements. The spatial location of the mirco-CT data of each sub region was collocated with the finite element model for each analysis. Then, each Gauss point in all of the elements of the FE model were mapped onto the micro-CT data to determine if it is positioned within a fiber or the matrix. The appropriate material properties were then applied. Each sub region model was treated as a repeating volumetric unit with the appropriate periodic boundary conditions to accommodate axial and shear loading. Elastic properties were evaluated through the fitting procedure developed as part of this research project.

Figure 13 shows the computed results for E_{11} throughout the long fiber composite sample. Each bar chart shows nine values in each of the 3 model layers in the z-direction of Figure 12. The fiber and matrix material properties in the actual sample where not available, so the values in Table 2 where used in the current calculations. It is apparent from Figure 13 that there is a more compliant core in the sample that extends throughout the sample in the z-direction. Other

Figure 12. 3×3×3 array of sub regions used in the long fiber composite elastic property evaluations.

properties such as E_{22} (not shown) are also reduced through the core. Our calculation of volume fraction is also lower throughout the center of the sample, providing a possible cause for the reduced material properties.

The mean and standard deviation for all of elastic properties were computed based on the 27 values of each that were evaluated with the multi-Gauss point FE model as described above. Table 4 summarizes these results using elements with 6 Gauss points in each direction.

Conclusions

This research project focuses on the prediction of elastic mechanical properties from higher-order fiber orientation tensors, fiber orientation distribution functions, and/or micro CT data of actual composite samples. As part of this work, the expression for computing elastic properties form fiber orientation tensors is verified and shown to ignore fiber-fiber interaction. In addition, the role of higher-order tensors on mechanical property prediction when using this approach is explored. A 3D voxel-based finite element modeling procedure has been developed which has been found to be in good agreement with more conventional FE approaches for continuous fiber and aligned short fiber composites.
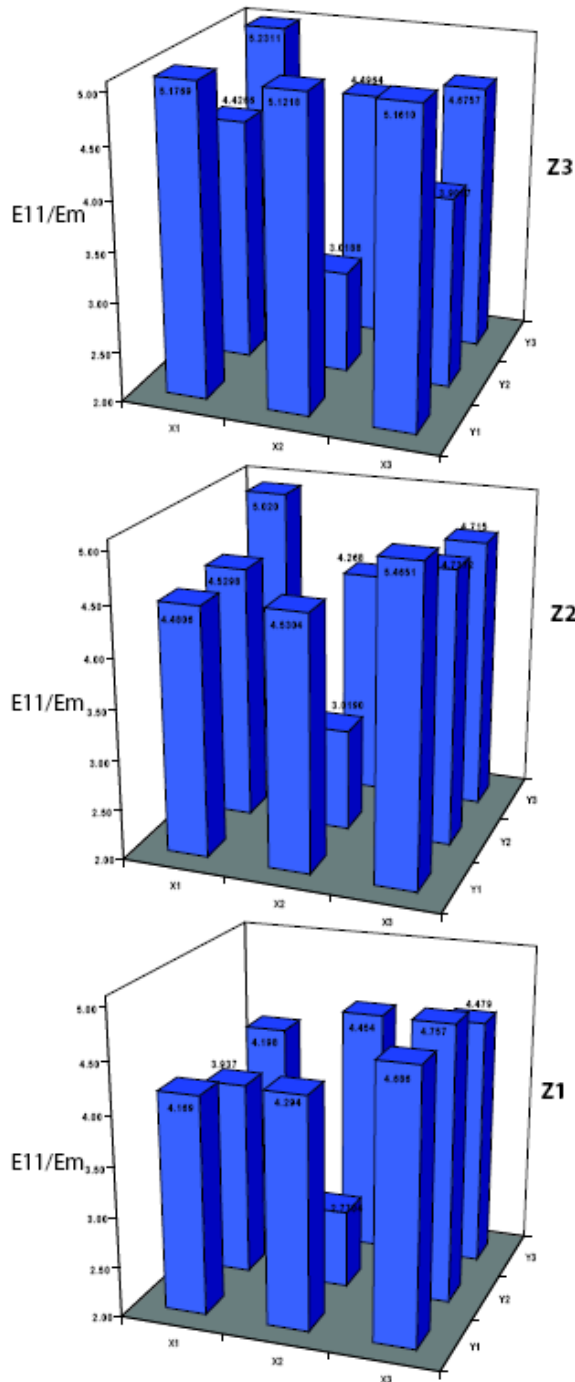
Figure 13. Computed results for E_{11} for each of the 27 sub regions in the long fiber composite sample.

Future Work

The work completed here provides tools and insight for future research in the understanding of short and long random fiber composites. A partial list follows:

Table 4: Computed elastic properties for a long fiber composite sample from 27 sub regions distributed as shown in Figure 12 (mean and standard deviation in GPa),

Material property	Mean	Standard deviation
vol. frac.	0.435	0.046
E_{11}/E_m	4.43	0.665
E_{22}/E_m	8.05	1.107
E_{33}/E_m	4.09	0.746
v_{12}	0.09	0.008
v_{21}	0.17	0.016
v_{13}	0.20	0.027
v_{31}	0.19	0.021
v_{23}	0.19	0.019
v_{32}	0.09	0.010
G_{12}/E_m	1.93	0.240
G_{23}/E_m	1.92	0.293
G_{31}/E_m	1.41	0.212

1. Perform additional detailed verification studies on long fiber composite samples.

2. Integration of the developed 3D voxel-based FE method with stress-strain testing of short and long fiber composites.

3. Application of FE approach developed here to actual long fiber composite products produced via molding processes.

4. Further integration of elastic property prediction method with polymer manufacturing process simulation.

5. Develop image processing methods to better extract long fiber geometry data from micro CT scans.

6. Development of a material fracture model within the 3D long fiber composites model.

7. Include elastic-plastic behavior to better represent the polymer matrix under load.

8. Further development of a packing algorithm for random short fibers at increasing volume fractions.

9. Addition of a flexible fiber model into the packing algorithm.

10. Include non-isotropic fiber constitutive models into the 3D voxel-based FE method.

11. Use 3D voxel-based FE results to develop a long fiber composite constitutive model.

References

1. http://web.missouri.edu/~smithdoug/nsf/index.htm.

2. S. Advani and C. L. Tucker, *J. of Rheology*, vol. 31, no. 8, pp. 751–784, 1987.

3. D. A. Jack and D. E. Smith, *J. of Composite Materials*, vol. 42, no. 3, pp. 277–308, 2008.

4. C. L. Tucker and E. Liang, *Comp. Science and Technology*, vol. 59, pp.655–671, 1999.

5. Z. Xia, Y. Zhang, and F. Ellyin, *Solids and Structures*, vol. 40, pp. 1907–1921, 2003.

Presentations/Publications/Patents

1. D. A. Jack and D. E. Smith, "Elastic properties of short-fiber polymer composites, derivation and demonstration of analytical forms for expectation and variance from orientation tensors," *J. of Composite Materials*, **42**:3, pp. 277–308, 2008.

2. J. E. Middleton, *Elastic property prediction of long fiber composites using a uniform mesh finite element method*, MS Thesis, University of Missouri, August, 2008.

3. E. C. Caselman and D. E. Smith, "A Multi-Gauss point finite element approach for the predicting elastic properties of short fiber composites," The Annual Meeting of the Polymer Processing Society, PPS-24, Salerno (Italy), 15–19 June 2008.

4. D. E. Smith and D. A. Jack, "Computing elastic material properties of short fiber composites via Monte-Carlo simulation," Poster presentation at the *2008 NSF Engineering Research and Innovation Conference*, Knoxville, Tennessee, January, 2008.

5. E. Caselman, *Elastic property prediction of short fiber composites using a uniform mesh finite element method*, MS Thesis, University of Missouri—Columbia, December, 2007.

6. D. A. Jack and D. E. Smith, "Mechanical Properties from the INV6 Closure for Short-Fiber Suspensions," SPE ANTEC 2006, Charlotte, North Carolina, May 7–11, 2006.

7. D. A. Jack, *Advanced analysis of short-fiber polymer composite material behavior with higher-order orientation tensor closure methods*. PhD thesis, University of Missouri—Columbia, December 2006.

8. D. E. Smith, M. T. Grimshaw, and D. A. Jack, "Incorporating higher order tensors in the computation of polymer composite mechanical properties," Poster presentation at the *2006 NSF Design, Service and Manufacturing Grantees and Research Conference*, St. Louis, Missouri, July 24–27, 2006.

9. D. A. Jack and D. E. Smith, "A statistical method to obtain material properties from the orientation distribution function for short-fiber polymer composites," IMECE2005-81263, Proceedings of ASME IMECE'05, Orlando, Florida, Nov. 5–11, 2005.

10. D. E. Smith and E. Caselman, "A 3D multi-Gauss point finite element method for computing elastic properties of composite materials," in preparation.

11. D. E. Smith, J. Middelton, V. Kunc, and B. N. Nguyen, "Computing elastic properties of random long fiber composite materials," in preparation.

O. Linking Process-Induced Properties to Thermoplastic-Matrix Woven-Fabric Composites Performance

Principal Investigator: James A. Sherwood
Department of Mechanical Engineering
University of Massachusetts Lowell
One University Avenue
Lowell, MA 01854
(978) 934-3313; fax: (978) 934-3048; e-mail: James_Sherwood@uml.edu

Co-Principal Investigators: Julie Chen, Larissa Gorbatikh
Department of Mechanical Engineering
University of Massachusetts Lowell
Lowell, MA 01854
(978) 934-2992; fax : (978) 934-3048; e-mail: Julie_Chen@uml.edu

Technology Area Development Manager: Joseph A. Carpenter
(202) 586-1022; fax: (202) 586-1600; e-mail: joseph.carpenter@ee.doe.gov

Objectives

- Provide a direct link among part geometry, material selection, process conditions, process-induced local properties, and part performance, allowing for informed feedback to the design process.

- Model the in-service performance of thermoplastic-matrix woven-fabric-reinforced structural composites – e.g., damage tolerance, crashworthiness, vibration.

- Attain a fundamental understanding of two governing physical phenomena – interlayer (fabric-fabric) friction.

- Validate and demonstrate the capabilities of the integrated structure-process-performance design tool to identify critical process and material parameters for one particular performance condition – vibration.

- Apply the proposed methodology to the thermostamping of woven-fabric composites to show how quality lightweight composite parts can be made at a rate and cost that is competitive with the currently used manufacturing process for stamping metal parts.

Approach

- Utilize an integrated analytical, experimental, and numerical effort to attain a fundamental understanding of two governing physical phenomena—interlayer (fabric-fabric) friction and interconnected through-thickness and in-plane compaction.

- Extend a combined inter-tow friction model, developed in a previous NSF-funded research program (DMII-0331267), based on the equilibrium equations of the unit cell of a balanced plain-weave glass/polypropylene woven fabric to account for fiber compaction.

- Design and build a friction-testing apparatus that is capable of examining tool/fabric and fabric/fabric friction for controlled load, speed and temperature conditions.

- Implement the methodology in commercially available finite element programs to simulate the composite forming process and have the result of the simulation of the manufacturing process be a finite

- element model of the formed composite part for use in structural analysis—thereby linking the manufacturing process to the resulting part performance.

Accomplishments

- Developed an analytical model that accounts for fiber compaction and can predict the shear behavior for woven fabrics and demonstrated the capabilities of the analytical shear model.

- Designed, built and implemented a self-contained friction testing apparatus that can replicate the tool/fabric and fabric/fabric interaction that occurs during the thermostamping process. The apparatus can be run under either load control or displacement control to characterize the static and dynamic friction coefficients as a function of speed, pressure and temperature.

- Confirmed that the friction behavior during the thermostamping for a Twintex® woven fabric, which is made from yarns of commingled fiberglass and polypropylene fibers, can be related to the Hersey number using Stribeck theory. When the polypropylene fibers melt and infuse the fiberglass fibers, the friction can be classified as hydrodynamic. The friction coefficient increases with increasing speed and decreases with increasing pressure for a given temperature. Such dependencies have been implemented in ABAQUS/Standard, ABAQUS/Explicit, and LS-DYNA (explicit version) through user-defined friction subroutines for finite element modeling of the thermostamping process.

- Characterized the mechanical behavior of three different Twintex® woven fabrics using experimental data from a series of shear frame and uniaxial tests.

- Developed constitutive models to describe the nonlinear shear behavior of woven fabrics and the nonlinear tensile behavior of crimped yarns in a woven fabric for large deformations. These constitutive models have been implemented in ABAQUS/Standard, ABAQUS/Explicit, and LS-DYNA (explicit version) through user-defined material subroutines for finite element modeling of the thermostamping process.

- Demonstrated a design tool to link part geometry, material behavior, and process conditions to the resulting process-induced local properties and overall structural performance from the thermostamping of woven-fabric composites for a simple hemisphere geometry and for a complex tub geometry.

Future Work and Direction

- Conduct parametric studies of the thermostamping process using the Hersey number friction model and different binder forces in the finite element simulations to enhance the understanding of the effect of the in-plane tension on the wrinkling and tearing of the fabric.

- Investigate the effect of fiber orientation on the friction coefficient to conclude the importance of yarn orientation and the state-of-shear on the friction behavior.

- Perform modal testing of a stamped part using a three-dimensional laser vibrometer and compare the experimentally found mode shapes and frequencies with finite element modal analysis results using the final shapes and fiber orientations predicted by the forming simulation. These comparisons will show the ability of the design tool to provide useful data for subsequent structural analyses.

- Extend the design tool to model the composite forming processes for composite wind turbine blades.

Introduction

Modeling of the in-service performance of thermoplastic-matrix woven-fabric-reinforced structural composites (e.g., damage tolerance, crashworthiness, vibration) is currently inadequate for parts of any geometric complexity because of the inability of existing performance models to capture the true deformed material properties. As a result, lightweight composite materials are utilized inefficiently or not at all; alternatively, extensive experimental trial and error or design of experiments must be conducted to develop a satisfactory product. The key to addressing this barrier is to provide a direct link among part geometry, material selection, process conditions, process-induced local properties, and part

performance, allowing informed feedback to the design process.

Fiber-reinforced thermoplastic composites have a variety of applications including structural components in the automotive, aerospace, marine, infrastructure and recreation industries. The main advantage of these composites over metals is their high specific strength. They also have other beneficial properties including low thermal expansion and good corrosion resistance when compared to metals. Woven fabrics offer many other advantages when compared to metals in terms of deformation capabilities, including dimensional stability, good conformability, and deep-draw shapability. Compared to nonwoven-fabric composites, the woven-fabric composites provide more balanced properties, higher impact resistance, easier handling and lower fabrication cost, particularly for parts with complex shapes. The objective of this research was to utilize an integrated analytical, experimental, and numerical effort to attain a fundamental understanding of two governing physical phenomena—interlayer (fabric-fabric) friction and interconnected through-thickness and in-plane compaction. The former is important in multiple-layer and multiple-step forming, both needed for industrial processes. The latter is a critical factor affecting the final part thickness, void content, fiber orientation, and fiber distribution—all are important for structural stiffness and damage tolerance. To validate and demonstrate the capabilities of the integrated structure-process-performance design tool, the model will be used to identify critical process and material parameters for one particular performance condition—vibration.

A combined inter-tow friction model, developed in a previous NSF-funded research program (DMII-0331267), based on the equilibrium equations of the unit cell of a balanced plain-weave glass/polypropylene woven fabric is extended to account for fiber compaction. To accomplish this extension of the model, fiber-compaction experiments were completed and the results are reported.

The design and use of a 3rd-generation friction-testing apparatus is presented. Previous research efforts used a constant-displacement control device to load the undeformed fabrics during the friction testing. While the information learned in these tests was valuable in developing a fundamental understanding of the tool-fabric behavior, the 3rd-generation friction-testing apparatus is a load-control device and yields a very complete fundamental understanding of the friction mechanisms by being able to study inter-layer friction between fabrics and tool/fabric friction on undeformed and deformed fabrics and to capture the static and dynamic friction behaviors of a woven-fabric system. Results are reported for two material systems—one has a thermoplastic matrix and the other has a thermoset matrix.

The methodology is implemented in the commercially available finite-element programs ABAQUS and LS-DYNA. The elements for the fabric models are inherent to these finite-element programs, so no special coding of elements is required. The material and friction behaviors are incorporated in the finite-element modeling by user-defined subroutines with simple input cards for specifying material and friction properties. Thus, the design tool is packaged in a form that should make the transition to industry relatively seamless and easily used by composite design engineers in industry.

The Thermostamping Manufacturing Process

Thermostamping is a manufacturing process that can produce quality composite parts with processing costs and time margins that are comparable to the fabrication of the currently stamped metal parts. The thermostamping process deforms a flat sheet of machine-woven continuous fibers (glass and/or carbon) commingled with thermoplastic fibers into a particular geometry using a pair of dies.

The thermostamping process (Figure 1) starts with the alignment of a sheet of fabric in a rigid steel frame. Multiple layers of fabric are stamped into one part to achieve the desired part thickness and mechanical properties. For a thermoplastic-matrix woven fabric, the frame and fabric are placed in an oven and are soaked until the fabric reaches a desired temperature for the thermoplastic
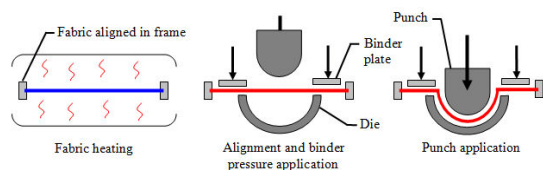
Figure 1. Schematic example of the thermo-stamping process.

polypropylene fibers, which are commingled with fiberglass fibers, to melt. The melting of the thermoplastic fibers infuses the fiberglass fibers with the resin. The frame is then aligned with a punch and die, and pressure is applied around the circumference of the punch area by binder plates. The application of force by the binder plate provides the in-plane forces that are necessary to reduce wrinkling of the fabric as the woven material is drawn into the die by the punch. The finished piece assumes the geometry of the die and punch and hardens into a firm part after the thermoplastic has cooled.

For the thermoset material, the woven fabric is compounded with a pliable thermoset resin. The frame holding the woven fabric is stamped into shape using the punch and die and then held at elevated temperature to harden the thermoset resin matrix.

A hemisphere formed from a commingled glass-polypropylene fabric using this thermostamping process is shown in Figure 2. The primary mode of deformation for the fabric is rotation (shearing) of the yarns, also known as 'trellis deformation'.

Figure 2. Formed hemisphere using the thermo-stamping process.

The processing parameters associated with the thermostamping operation can have a significant effect on part quality. Figure 3 shows the resulting part quality in a section under the binder plate from the stamping process of a commingled glass-polypropylene woven-fabric as studied by Wilks [1]. The resulting part quality is shown for cases of different pressure-and-temperature combinations. For this test, the pressure applied by the binder plate was controlled by springs and the binder plate was either unheated or heated during the process. With the binder plate unheated, fiber separation and tow breakage occurred sooner than when the binder plate was heated as pressure was increased [Figure 3(d–f)]. The presence of fiber wrinkling was reduced as pressure increased [Figure 3(e)]. Thus, it can be observed that part quality is a function of temperature and applied force, and in turn friction between the fabric and the tool.
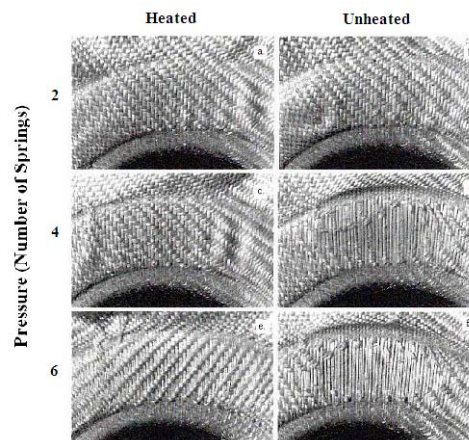
Figure 3. Effect of temperature and pressure on part quality during the thermostamping process [1].

The mechanical behavior of the woven fabric during the forming process is dominated by the evolution of the in-plane shear stiffness as the yarns rotate and the uncrimping of the yarns due to in-plane tensile forces. By using a series of simple tests to characterize the mechanical behavior of a woven fabric, material parameters can be found. As an alternative to experimental characterization, there has been some limited success to develop purely analytical models of woven fabrics to estimate the mechanical behavior of a woven fabric. These analytically and/or experimentally

determined material properties can be used in a finite-element program to simulate the manufacturing process of a composite structure.

The inextensible characteristic of the yarns (fiberglass and/or carbon) requires draw-in and shearing of the fabric to occur for the material to conform to the tool geometry in forming the part. During fabric draw-in, the fabric slides under the metal binder plate and over the surfaces of the punch and die. For multilayer parts, there is possibly going to be some sliding between adjacent layers of fabric. Considering the interactions that take place between the fabric and tool and between adjacent layers of fabric during the manufacturing process and the effect of the process parameters (e.g., pressure, temperature and rate, on part quality), it is clear that characterizing the friction between the tool and the fabric and the friction between adjacent layers of fabric is critical to modeling the manufacturing process accurately.

Analytical Modeling of the Shear Behavior of Woven-Fabric Composites

Trellis shear, as shown in Figure 4, is the main deformation mode during the stamping process of woven-fabric composites [2]. Thus, the formability of woven-fabric composites is primarily a function of the shear properties of the woven fabric. Therefore, analytical models to obtain the shear properties of woven-fabric
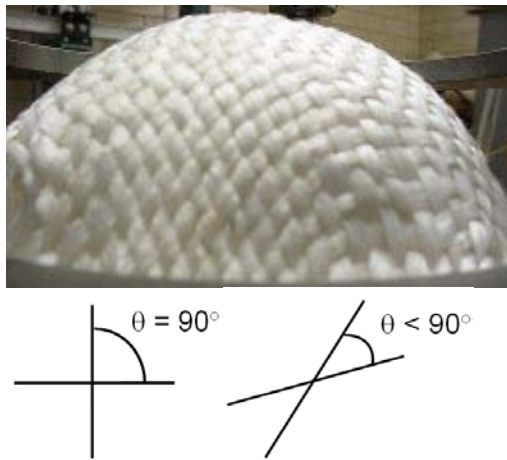
Figure 4. Trellis deformation of a stamped hemisphere.

composites would be very useful to characterize the mechanical behavior of an existing fabric without doing time-consuming experiments or for characterizing a yet to be made fabric for which experimentation is not an option.

An analytical unit-cell model, which includes (1) the key shear-deformation-resistant mechanisms, (2) the friction between the warp and weft yarns at every crossover, and (3) the lateral compaction between adjacent yarns, was developed by Liu et al. [3,4] to predict the shear properties of woven fabrics for the thermostamping process. In the model, some yarn parameters such as the yarn-to-yarn coefficient of friction μ, the fiber contact frequency ratio β, and the ideal maximum fiber volume fraction V_a, were chosen to develop an empirical model to fit the experimental data. Validation of those parameters is necessary to complete the unit-cell model.

The maximum yarn-fiber volume fraction V_a is an ideal limit to which fibers in a yarn can be compacted. As the yarn-fiber volume fraction approaches this maximum value, the stiffness in the transverse direction increases dramatically to approach the stiffness of the solid fiber material. According to the packing theory of uniform sizes of fibers, square packing corresponds to V_a of $\pi/4$ (or 0.785), and hexagonal packing results in a value of $\sqrt{3}\pi/6$ (or 0.907). Because the diameters of the polypropylene and glass fibers are different in the commingled polypropylene/glass yarn, the square packing theory is modified for the commingled fibers, and the obtained V_a equals 0.813 [5].

The compaction was studied using plane-strain compression tests, where 50-mm-long fiber bundles were placed in a channel fixture as shown in Figure 5. A compressive force was applied perpendicular to the axial direction of the fibers (Z direction) using an Instron machine at a rate of 0.042 meters (m)/second (sec). Load and extension data were logged so that stress and strain in the Z direction could be calculated. Because the transverse compliance can also be calculated in the fiber bundle model as a function of β, regression of the experimental data will give the mean value of β. In Figure 6, the predicted and
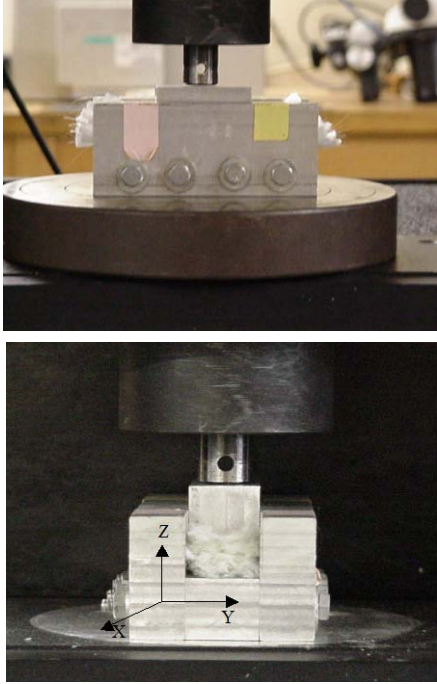
**Figure 5.** Plane-strain compression test fixture [5].
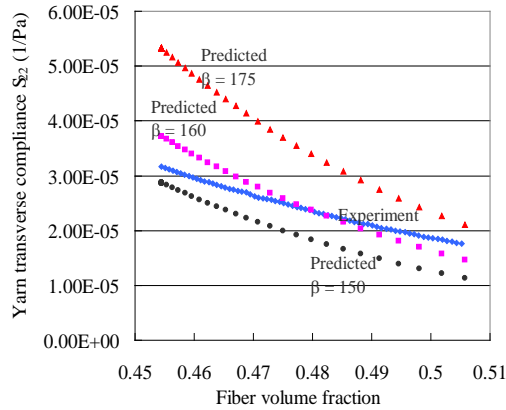
Figure 6. Comparison of the values of S_{22} obtained from the plane-strain compression tests and the fiber bundle modeling [6].

experimental values of the yarn transverse compliance S_{22} are compared for various values of β. The experimental results were obtained from the plane-strain compression tests for five layers of yarns as described in [6]. From Figure 6, it can be seen that the values of β are in the range from 150 to 175 for the commingled polypropylene and glass yarns explored in this research.

To investigate the sensitivity of the model to the yarn input parameters such as the maximum fiber volume fraction V_a, the fiber contact ratio β and the yarn-to-yarn coefficient of friction μ, a parametric study was conducted. To separate the individual contributions from friction and lateral compaction, intermediate models were studied separately (i.e., the lateral compaction resistant moment was set to be zero to study the coefficient of friction), while in the study of β and V_a, the friction resistant moment was set to be zero in the equilibrium equation.

Figure 7 shows the results of the simulation of β varying from 150 to 175. In the figure, it can be seen that as the value of β decreases, the shear load increases. The loads increase because at relatively low values of β, the yarn stiffness in the
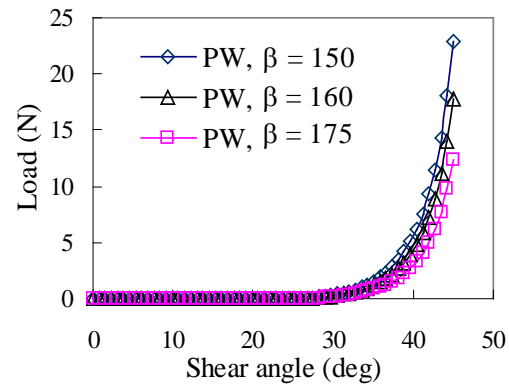
Figure 7. Simulation of the fiber contact frequency ratio.

transverse direction increases due to increased fiber bending. As shown in Figure 8, decreasing the value of V_a has a similar effect because, with relatively low values of V_a, yarn stiffness in the transverse direction increases due to decreased space for compaction.

Thus, with the main parameters all validated, the developed analytical model can be used to predict the shear properties of woven-fabric composites and reduce or eliminate the need for curve fitting of fabric-level experimental data.
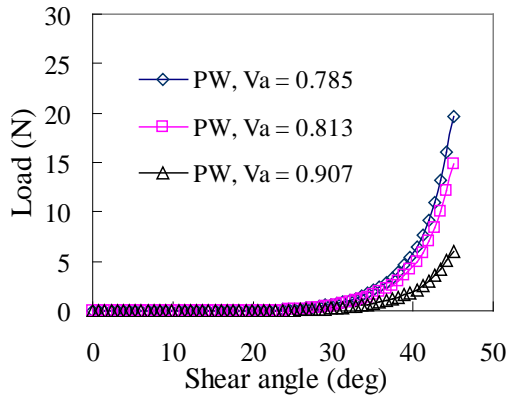
Figure 8. Simulation of the maximum fiber volume fraction.

Friction Behavior for Woven Fabrics

Past research led to advances in a user-defined friction subroutine for use in finite-element applications. The notations PW, TWI and TWII refer to the plain-weave; the thin-twill-weave and the thick-twill-weave fabrics, respectively. The Stribeck curve (Figure 9 [7]) and the Hersey number, *H*, (Eq. 1) were used to find the friction coefficient for the ranges of velocities and normal forces studied.

$$H = \frac{\eta \cdot U}{N} \qquad (1)$$

where η is the viscosity, *U* is the fabric velocity and *N* is the normal force.

The results of parametric studies conducted by Gorczyca [8,9] showed that the velocity of the fabric, tool temperature, and applied normal force had the greatest effects on the friction coefficient. From these results, she developed a model that related the friction coefficient μ to the Hersey number,

$$\mu = (6.1191 \cdot H + 0.2718) — \mu_\upsilon \qquad (2)$$

where μ_υ is a scaling term included for the effects of the tool temperature. Because the method of normal force application used in her research was displacement controlled, her results were limited to measuring only the static coefficient of friction [8,10,11].
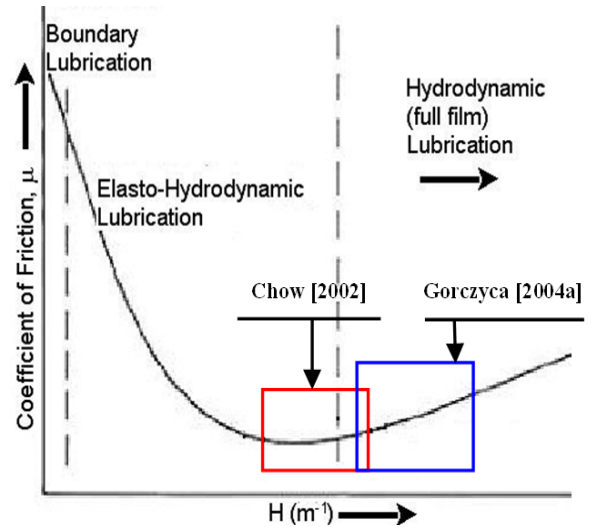
Figure 9. The Stribeck Curve and areas of interest pertaining to current research. Adapted from [7].

It was found that during a typical friction test the normal force applied to the fabric surface decreased, as shown in Figure 10 where the initial applied load was approximately 1500 N and dropped by ~400 N over the duration of the test. The mechanisms behind this decrease in normal force are fabric nesting and tow compaction. The fabric tows adjust their position as the adjacent layers of fabric nest, tow undulation decreases and fibers compact due to the combination of heat and pressure. Any one or more of these mechanisms causes a slight change in the displacement necessary to maintain the targeted normal force.
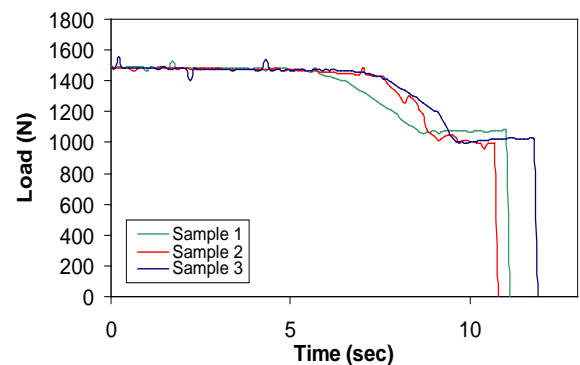
Figure 10. Normal force decrease over time for displacement controlled test of commingled glass-polypropylene plain-weave fabric.

Due to the drop in normal force, only the static coefficient of friction, which is the value obtained

at the first instant of fabric movement, could be reliably quantified by Gorczyca using the 2nd-generation displacement-control friction test apparatus. Being able to capture the dynamic coefficient of friction would give a friction model that accurately represents the frictional behavior over the entire duration of the thermostamping process where the friction is both static and dynamic.

To gain the ability to determine the dynamic coefficient of friction, a load-controlled application mechanism was designed and built as one component of the current research [12]. The force-controlled mechanism consists of a pneumatic air-spring actuator and a closed-loop control algorithm to continuously monitor and regulate the magnitude of force applied to the fabric throughout the duration of the friction test. The temperature of the tool and the pullout speed can be prescribed over a range of values that are observed to be present in the thermostamping process.

For the stamping of a hemisphere with a plain-weave fabric (as shown in Figures 1 and 2), the tows are initially oriented ~90° with respect to one another, and this angle decreases as the fabric conforms to the dual-curvature surface of the hemisphere as shown in Figure 4. The significance of the effect of tow orientation on the friction response is currently being investigated.

Test Fixture

The 3rd-generation friction-testing apparatus is a stand-alone test machine. The limiting factor for the previous test apparatus was its dependence on the Instron testing machine. By integrating all fabric movement into one test apparatus, the travel time from the oven to the press can be reduced from ~20 seconds to be less than 3 seconds, thereby reducing the influence of any cooling effects as the fabric is transferred from the oven to the press. Figure 11 shows a schematic of the overall 3rd-generation friction-testing system, and Figure 12 is a photograph of the press portion of the system.
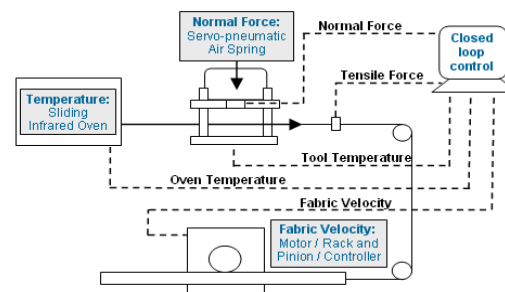
Figure 11. Schematic representation of the 3rd-generation friction test apparatus.
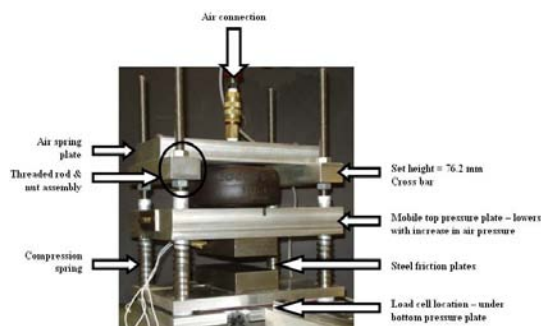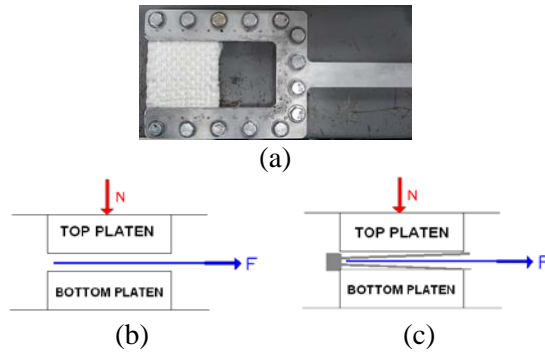

Figure 12. The friction press.

Experiments

The load-control friction test apparatus [13] was used to capture the static and dynamic coefficients of friction. The objective of the friction-test apparatus is to accurately simulate the combinations of pressure, temperature and speed observed in the actual thermostamping process.

In a friction test, the fabric is clamped in a holder [Figure 13(a)], heated in an infrared oven and subsequently shuttled to the press (similar to what is shown in Figure 1 for the thermostamping process), which features two heated platens. A direct current (DC) motor drives a rack and pinion to pull the sample through the press. The transfer from the oven to the press is done manually, and the fabric sample typically sits pressurized between the platens for about one second before the motor begins to pull. Experiments have shown that this one-second time is sufficient to keep the thermoplastic melted.

For the fabric/fabric friction characterization, one fabric layer is placed between two "outside" layers of fabric. The two outer layers are clamped

(a)

(b)   (c)

Figure 13. Fabric holder and schematics of the friction test setups for tool/fabric and fabric/fabric interfaces.

together on one end, and the inner layer is pulled between these two outer layers. The fully compressed platens prohibit the clamp which holds the two outer layers from moving. The fabric holder which is used to pull the fabric through the press is shown in Figure 13(a) and schematics of the friction test setup for the fabric/tool and fabric/fabric conditions are shown in Figures 13(b) and (c), respectively.

The effective coefficient of friction is calculated by

$$\mu_{eff} = \frac{F}{2N} \qquad (3)$$

where the normal force, N, is multiplied by a factor of two to account for the two contacting surfaces on either side of the fabric sample.

The test conditions were also based on simulating a range of thermostamping process conditions. Experiments were performed on a Twintex[®] balanced plain-weave fabric. All samples were cut to be 51×76 mm^2, and tests were performed in triplicate to account for any variation among fabric samples.

The coefficient of friction was plotted against the pullout displacement. These curves can result in an initial peak, followed by a drop and then a relatively flat response for the Twintex[®] woven fabric used in this research. The peak and "flat" portions of the curves correspond to the static and dynamic coefficients of friction, respectively. The magnitude of the peak is a function of the pulling speed and pressure. Figure 14 shows typical
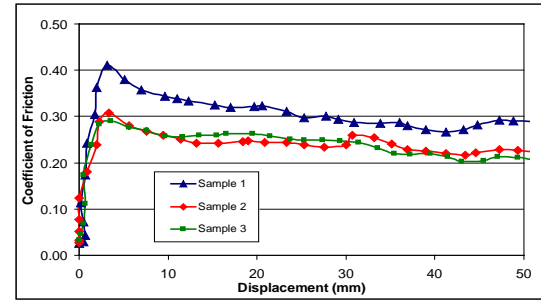
Figure 14. Coefficient of friction as a function of pullout length for three tests at a pressure of 110 kPa, pullout velocity of 16.7 mm/s, and tool temperature of 85°C.

coefficients of friction vs. displacement curves for three tests at a pressure of 110 kPa, pullout velocity of 16.7 mm/s, and tool temperature of 85°C.

A constant fabric area remains between the platens for approximately 50 mm of displacement. A drop in the fabric temperature after the fabric is in contact with the platens explains why small variations in the pullout force in the displacement range associated with the dynamic coefficient of friction are observed.
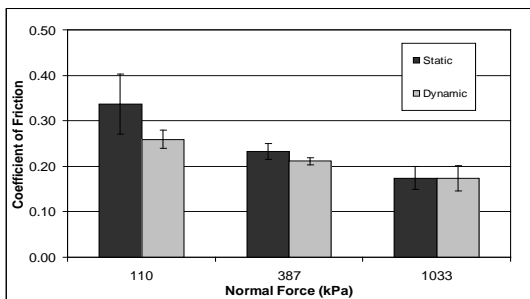
Friction Test Results

Figure 15 shows the static and dynamic coefficients of friction at the fabric/tool interface for the Twintex[®] balanced plain-weave fabric as a function of pullout velocity [14]. All tests were run with the baseline pressure of 387 kPa and a tool temperature of 85°C. The baseline values were determined from the typical processing conditions for the Twintex[®] fabric being considered in this research. In Stribeck theory, an increase in velocity causes an increase in the Hersey number. Similarly, an increasing velocity causes viscosity to increase, which also increases the Hersey number. In the hydrodynamic range of the Stribeck curve, an increasing Hersey number corresponds to an increasing coefficient of friction. Figure 15 implies that the friction response is in the hydrodynamic behavior region of the Stribeck curve (Figure 9) because the coefficient of friction increases with increasing velocity and likewise increasing Hersey number.
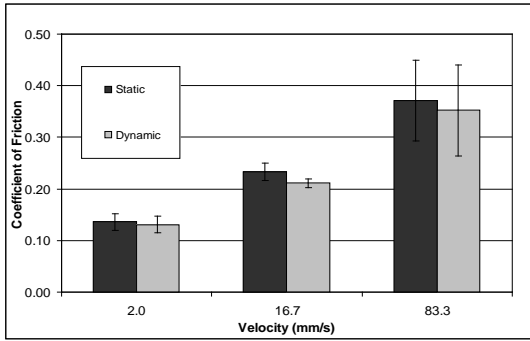
Figure 15. Experimental results (fabric/tool) at different pullout velocities with the baseline pressure of 387 kPa and the baseline tool temperature 85°C [14].

Quantifying the variation of the friction coefficient as a function of velocity is important because during the forming process, the fabric does not necessarily move at a constant velocity along the tooling. In addition, as the fabric conforms to the shape of the die, the tows of the fabric are sheared and reoriented, affecting the rate at which the fabric slides over the surfaces that it is contacting.

Figure 16 shows the variation of the static and dynamic coefficients of friction with changes in normal force (or pressure). The pullout speed was the baseline value of 16.7 mm/s. In Eq. (1), it can be seen that normal force is inversely related to the Hersey number. Therefore, the decrease in the friction coefficient with an increase in normal load shown in Figure 16 also implies the friction behavior to be in the hydrodynamic-friction region of the Stribeck curve (Figure 9).

Figure 16. Experimental results (fabric/tool) at different normal loads with the baseline pullout velocity of 16.7 mm/s and the baseline tool temperature of 85°C [14].

Figure 17 shows the static and dynamic coefficients of friction for the balanced plain-weave fabric at the fabric/fabric interface as a function of pullout velocity. Similar to the fabric/tool interface, the coefficient of friction was observed to increase with increasing velocity at the fabric/fabric interface.
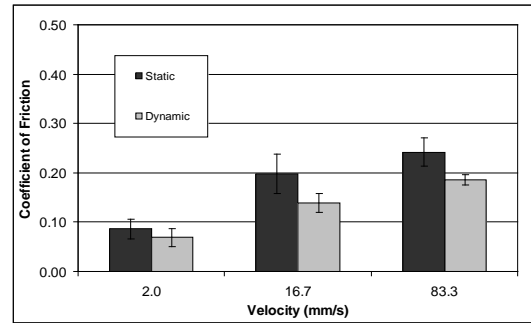
Figure 17. Experimental results (fabric/fabric) at different pullout velocities with the baseline pressure of 387 kPa and the baseline tool temperature of 85°C [14].

Figure 18 displays the effect of normal force on the friction coefficient at the fabric/fabric interface. The decrease in the coefficient of friction with increasing normal force follows the same trend as the results from the fabric/tool interface. Similar trends for the coefficients of friction as a function of normal force and velocity were observed at both the fabric/tool and fabric/fabric interfaces, where only the magnitude of the friction coefficients differed. These trends support that the Stribeck curve can explain the observed friction behaviors.
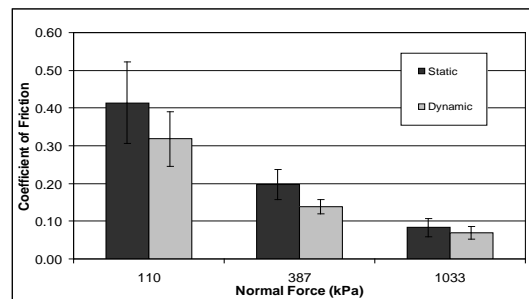
Figure 18. Experimental results (fabric/fabric) at different normal loads with the baseline pullout velocity of 16.7 mm/s [14].

Due to significant differences in friction coefficients under different processing conditions,

any finite-element simulation of the manufacturing process must be able to capture the coefficient of friction as a function of pressure, velocity and temperature. Such dependencies have been implemented in ABAQUS/Standard [**Error! Bookmark not defined.**] ABAQUS/Explicit, and LS-DYNA (explicit version) [15,16] through user-defined friction subroutines for finite-element modeling of the thermostamping process. The effect of fiber orientation on the friction coefficient is currently under further investigation to conclude the importance of yarn orientation on the friction behavior. If orientation is found to be important, then a yarn-orientation parameter will be incorporated in the user-defined friction subroutine.

Characterization of the Mechanical Behavior of the Woven Fabrics Using Experimental Methods

Experimental data were used to derive the material parameters for the constitutive models used in the simulation of the mechanical behavior of the fabrics studied in the forming simulations of the current research. For the forming of composite parts using woven fabrics, these material parameters were needed to describe the nonlinear tensile behavior of the yarns and the nonlinear shear behavior of the fabric.

A yarn behaves differently when incorporated within a crimped fabric than alone because of the undulations of the yarns and the influence of the perpendicular yarns in the fabric. A biaxial tensile test allows the stretching of the fabric in the two yarn directions at the same time, and hence, the determination of the tensile properties of the fabric due to a variety of in-plane-force combinations. In a first approximation, models generally do not account for the effect of the tension in the lateral direction, and that is why the simpler uniaxial testing of single yarns was chosen for the material characterization in this research.

The nonlinear tensile behavior of the fabric due to the decrimping is essential to perform reliable simulations [17]. If the crimp ratio (difference between the length of the yarn and the length of the fabric) is known, then the decrimping part of

the stress-strain curve can be extrapolated from the experimental data.

The in-plane shear properties were obtained by a shear-frame test. In the speed range attainable with a conventional tensile machine, the fabric load-deformation response in the shear-frame test was not found to be rate dependent [3].

Experimental Results of the Mechanical Behavior

Three Twintex® woven fabrics composed of commingled polypropylene and glass fibers designed for thermostamping were tested [18]. The fabric characteristics can be found in [19].

Uniaxial tensile testing was performed on an Instron 4464 machine with a 2-kN load cell. Pneumatic cord and yarn grips were used, and the gauge length was set to approximately 1 m to minimize the effect of the deformation in the grips. The displacement rate was 5 mm/s. The stiffness of the yarns was determined from the slope of the load/true-strain curves. In addition, measurements of the crimp ratio were performed. The results, presented in Table 1, were used to assess the tensile behavior of the yarn within the fabric via an extrapolation of the decrimping (Figure 19).

Table 1. Yarn tensile stiffness [18]

Pattern	Tensile stiffness (kN)	Crimp ratio (%)
PW	24.6 ± 0.7	2.0
TWI (warp/weft)	$25.1 \pm 0.6/$ 50.3 ± 0.4	4.4/0.8
TWII (warp/weft)	56.0 ± 0.6	3.0/0.0

Shear-frame tests were performed on the Instron 4464 machine. The geometry chosen for the specimen is shown in Figure 20. Note that to avoid the shearing contribution of the arms, the cross yarns were removed from this part of the sample. The length of the frame L_F was 216 mm, and the length of the fabric L_f was 120 mm.

The specimen was sheared at the rate of 2 mm/s. A mechanical conditioning of five pre-test shearing runs was applied. The mechanical conditioning
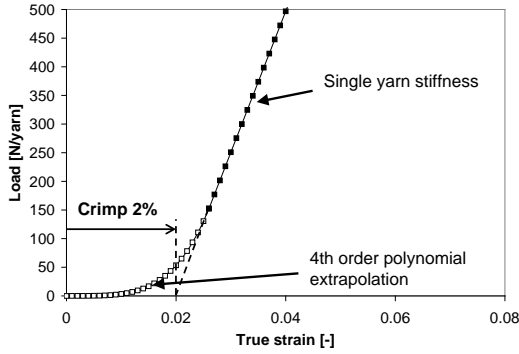
Figure 19. Extrapolation of the fabric tensile behavior from the single yarn stiffness and the crimp ratio for the plain-weave fabric.
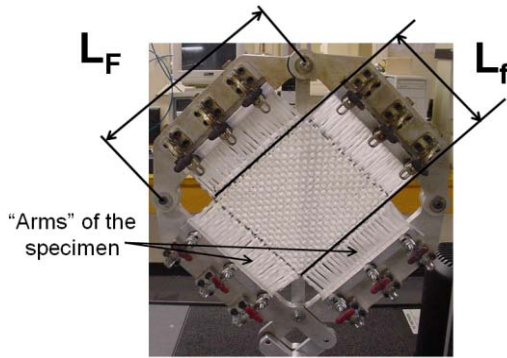
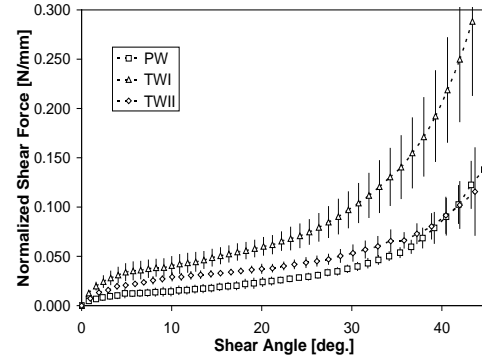**Figure 20.** Geometry of the shear frame. Free yarns have been removed in the "arms" of the specimen.

Figure 21. In-plane shear behavior at room temperature [18].
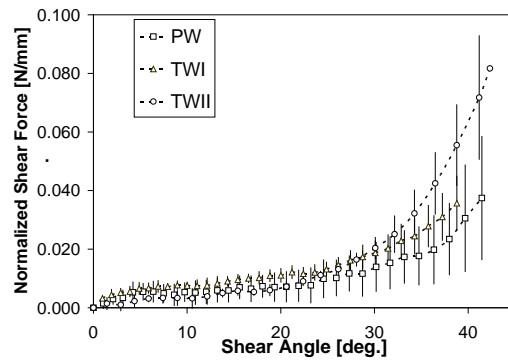
Figure 22. In-plane shear behavior at 175°C [18].

ensured a uniform distribution of the yarns across the sample. The normalized shear force F_{sh} and the shear angle γ were determined from the crosshead displacement δ and the total load on the frame F by the following equations [19]:

$$\gamma = \frac{\pi}{2} - 2.\arccos(\frac{\delta}{2.L_F} + \frac{\sqrt{2}}{2}) \tag{4}$$

$$F_{sh} = \frac{L_F}{L_f^2} \frac{F}{2\cos(\pi/4 - \gamma/2)} \tag{5}$$

Tests were performed at room temperature and at 175°C, which is the recommended processing temperature for forming of these fabrics. The results are presented in Figures 21 and 22.

The TWI fabric has a very tight weave and exhibits logically higher shear stiffness than the two other Twintex® fabrics. It is worth noting that

the repeatability (represented by the error bars) is good up to the locking angle (~30° for TWI, ~40° for PW and TWII). At least five tests were used to obtain a reliable average.
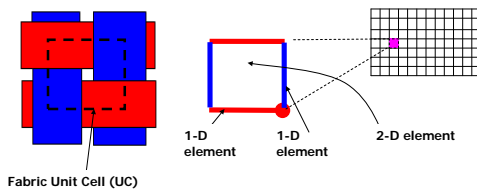
Finite-Element Modeling [20,21]

Several modeling approaches have been developed to account for the evolution of the orthotropic directions during high shearing, and these approaches include the continuous approach, the semi-discrete finite element approach and the mesoscopic approach [22]. The first two approaches, while giving good results and being efficient in terms of computing time are generally somewhat complex and sometimes very challenging to implement into commercially available finite element packages. In this research, a discrete mesoscopic approach, based on built-in elements and user-defined material and friction subroutines in commercially-available finite element codes was used. The explicit codes used are ABAQUS and LS-DYNA, and the material

parameters were derived from conventional tensile and shear-frame experimental data as previously discussed in this report.

The method was also implemented into ABAQUS/Standard (implicit solver) [23]. However, problems with convergence in ABAQUS/Standard due to the contact of the fabric with binders other than binder plates that covered all of the fabric could not be overcome. The elements needed for the methodology are not currently available in LS-DYNA's implicit solver, so using the LS-DYNA implicit solver for the process simulation was not an option for this research.

Model Description

The unit cell of the mesoscopic model used in this research for a plain-weave fabric consists of four one-dimensional (1-D) elements and one two-dimensional (2-D) element as shown in Figure 23 for a plain-weave fabric. The 1-D elements carry the tensile loads through the fabric and are able to rotate freely as the fabric is sheared. This rotation of the 1-D elements is a simple and automatic way of accounting for the local changes in orientation of the principal load directions through the fabric. The 2-D element is included in the model to capture the in-plane shear stiffness of the fabric and has no tensile stiffness. The respective material models for the 1-D and 2-D elements were implemented in the finite- element codes by user-defined subroutines. These material models capture the nonlinear load-displacement behavior of the fabric for in-plane tensile and shearing deformations. Unit cells can likewise be defined by a combination of 1-D and 2-D elements for other weave patterns, such as satin and twill weaves [20,23].

Figure 23. Representative unit cell of the hybrid mesoscopic modeling of a plain-weave fabric [23].

Constitutive Equation for 1-D Elements

The explicit finite-element codes ABAQUS and LS-DYNA allow for customized stress-strain relationships at each time step via a user-defined material subroutine [24]:

$$\Delta \sigma_{ij}^{t+1} = C_{ijkl}.\Delta \varepsilon_{kl}^{t+\frac{1}{2}} \tag{6}$$

where $\Delta \sigma_{ij}^{t+1}$ is the stress increment at time step $t+1$, C_{ijkl} is the constitutive matrix defined by the user-supplied material parameters at time step t, and $\Delta \varepsilon_{kl}^{t+\frac{1}{2}}$ is the midpoint strain increment from the solver. For 1-D elements, Eq. (6) becomes:

$$\Delta \sigma_{11}^{t+1} = C_{11}(\varepsilon_{11}).\Delta \varepsilon_{11}^{t+\frac{1}{2}} \tag{7}$$

where C_{11} is the tangent tensile modulus and is a function of ε_{11}. This tangent modulus is easily deduced from experimental tensile stress-true strain data of the fabric.

Constitutive Equation for 2-D Elements

The incorporation of the in-plane shear behavior in a shell/membrane element for finite-strain analysis is more challenging than the tensile behavior of the 1-D elements. Two reference frames as depicted in Figure 24 have to be considered as the
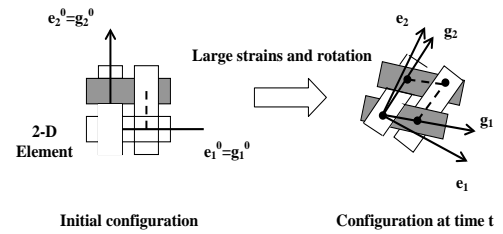
Figure 24. Schematic representation of the reference frames used.

fabric shears from its initial orthogonal configuration to a nonorthogonal configuration. The e_i unit vectors define the local orthogonal reference frame that rotates with the material, and the g_i basis vectors form a nonorthogonal frame that follows the fiber directions:

$$\vec{g}_i = \underline{\underline{F}}.\vec{g}_i^0 = \underline{\underline{F}}.\vec{e}_i^0 \tag{8}$$

where $\underline{\underline{F}}$ is the deformation gradient tensor known at each increment in the deformation process.

The in-plane shear-stress/shear-strain behavior of the woven fabric is captured by:

$$\Delta \tilde{\sigma}_{12}^{t+1} = \tilde{C}_{33}(\gamma_{12}).\Delta \gamma_{12}^{t+\frac{1}{2}}$$

$$\text{with } \Delta \gamma_{12}^{t+\frac{1}{2}} = 2.\Delta \varepsilon_{12}^{t+\frac{1}{2}} \qquad (9)$$

where $\Delta \tilde{\sigma}_{12}^{t+1}$ is the shear-stress increment expressed in $\boldsymbol{g}_i$ and $\tilde{C}_{33}(\gamma_{12})$ is the tangent shear modulus that can be determined from experimental data or by using the analytical method described earlier in this paper. This constitutive equation uses the tensorial shear-strain increment $\Delta \varepsilon_{12}^{t+\frac{1}{2}}$ expressed in the $\boldsymbol{e}_i$ reference frame as it is given by the finite element solver to the user-defined material subroutine. However, the obtained stress increment is expressed in terms of the $\boldsymbol{g}_i$ basis and needs to be returned to the finite-element solver in the $\boldsymbol{e}_i$ basis at the end of the user-defined subroutine. The rotation matrix relating the two reference frames can be obtained from a geometric analysis [25]. The 1-D elements carry the stresses in the $\boldsymbol{g}_1$ and $\boldsymbol{g}_2$ directions, and consequently $\Delta \tilde{\sigma}_{11} = \Delta \tilde{\sigma}_{22} = 0$ in the $\boldsymbol{g}_i$ reference frame within the 2-D element. Therefore, the stress increments are returned to the finite-element solver in the $\boldsymbol{e}_i$ basis using:

$$\Delta \sigma_{11} = 2.\cos \alpha \cos(\alpha + \theta).\Delta \tilde{\sigma}_{12}$$

$$\Delta \sigma_{22} = 2.\sin \alpha \sin(\alpha + \theta).\Delta \tilde{\sigma}_{12} \qquad (10)$$

$$\Delta \sigma_{12} = \sin(2\alpha + \theta).\Delta \tilde{\sigma}_{12}$$

where the $\Delta \sigma_{ij}$ are the stress increments in the $\boldsymbol{e}_i$ reference frame and the $\Delta \tilde{\sigma}_{ij}$ are the stresses in the $\boldsymbol{g}_i$ reference frame. The angle between $\boldsymbol{e}_1$ and $\boldsymbol{g}_1$ is α, and the angle between $\boldsymbol{g}_1$ and $\boldsymbol{g}_2$ is θ.
To be consistent with finite-element codes that use the logarithmic strains for the summation of the strains increments, the logarithmic definition of strains should be used to determine $\tilde{C}_{33}(\gamma_{12})$ from the experimental data or analytical shear-frame model of the fabric. The true or "logarithmic" shear angle γ^L can be obtained from the logarithmic strains in the principal stretch directions ε_I^L and ε_{II}^L by a 45° Mohr's circle transformation. In the case of a shear frame test, a

geometrical analysis leads to the expression of γ^L as a function of the geometric shear angle γ:

$$\gamma^L = \varepsilon_I^L - \varepsilon_{II}^L = -\ln(\tan(\pi/4 - \gamma/2)) \qquad (11)$$

The shear stress $\tilde{\sigma}_{12}$ is equal to the normalized shear force F_{sh} [18] divided by the thickness of the fabric. Finally, $\tilde{C}_{33}(\gamma^L)$ is obtained from a derivation of $\tilde{\sigma}_{12}$ versus γ^L of the experimental shear frame test data or using the analytical shear-frame model.

Implementation via the User-Defined Material Subroutines

The method has been implemented via user-defined material subroutines in the explicit finite element codes ABAQUS and LS-DYNA. For ABAQUS, B31 beam elements and S4R shell elements were used, and for LS-DYNA seatbelt elements and Hughs-Liu reduced integration shells (Shell 6) were used. Truss elements can also be used in either ABAQUS or LS-DYNA for modeling of the yarns. However, for large and complex deformations, the convergence of the analysis was found to be difficult to achieve when using truss elements. The LS-DYNA seatbelt element is very efficient in terms of computational time and has the added benefit of having zero compressive stiffness. The modeling of the shear contribution to the material stiffness could potentially be captured using either shell or membrane elements with careful attention being given to the accuracy of the element response at high shear strains.

To demonstrate the capabilities of the methodology to simulate the manufacturing process for Twintex® woven fabrics, plain-weave experimental data at room and elevated temperatures were used to conclude the material parameters for the user-defined material subroutines used in the finite element simulations. The shear stress versus γ^L curve was first developed from normalized experimental data:

- shear stress was assessed from normalized shear force F_{sh} assuming a fabric thickness of 0.5 mm, and
- γ^L was obtained from the geometrical shear angle γ using Eq. (11).

The tangent shear modulus $\tilde{C}_{33}(\gamma^L)$ was then obtained by fitting a 4th-order polynomial to the shear stress vs. γ^L experimental data.

Similarly the tangent tensile modulus was obtained from the tensile load vs. true strain experimental data. The "effective" section of the yarn A_{yarn}, with the assumption of no voids among the fibers was used. It was determined from the known data using the following equation [23]:

$$A_{yarn} = \frac{\rho_{yarn}}{VF_{glass} \cdot \rho_{glass} + (1 - VF_{glass}) \cdot \rho_{PP}} \quad (12)$$

where VF_{glass} is the glass volume fraction, ρ_{yarn} is the yarn linear density, and ρ_{glass} and ρ_{PP} are the glass and polypropylene densities, respectively. The resulting A_{yarn} is for the fabric being considered in the study. A square beam section was chosen for ABAQUS beams. However, other cross-section geometries (e.g., circle or oval) can be implemented should they be deemed more representative of the fabric. Because of the specific formulation of LS-DYNA seatbelt elements, only the section area could be defined and no cross-section type could be described.

Validation

To validate the modeling approach, a shear frame test and a bias extension test were simulated at room temperature, and the results were compared to experimental data. A finite element model of the shear-frame test used at UMass Lowell was built, including the "arms" of the specimens [18]. The procedure used for completing the shear-frame testing required the removal of the free yarns in the arms of the specimens, so only 1-D elements were used in the model in the area of the arms [Figure 25(a)]. A bias-extension test was also simulated. The characteristic shear-strain field of this test [26] was obtained as shown in Figure 25.

Figures 26 and 27 show a comparison among finite-element results from ABAQUS and LS-DYNA and experimental data to previous experimental work at UMass-Lowell (Shear frame data [18]) and to experimental data from Peng and Cao (Bias extension data [25]) for the Twintex® woven-fabric thermoplastic composite. Very good
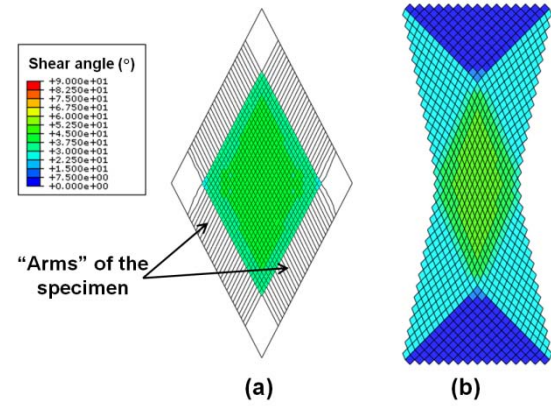
Figure 25. Shear angle contour of (a) the shear frame and (b) the bias extension models (ABAQUS).
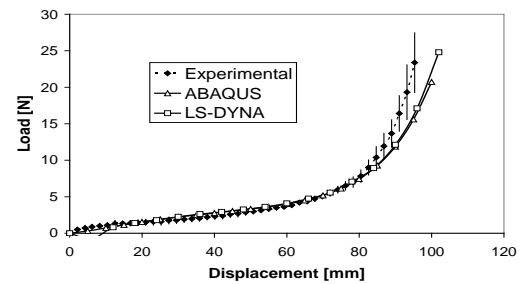
Figure 26. Comparison of the load-displacement curves for the experimental and finite-element simulations of the shear-frame test.
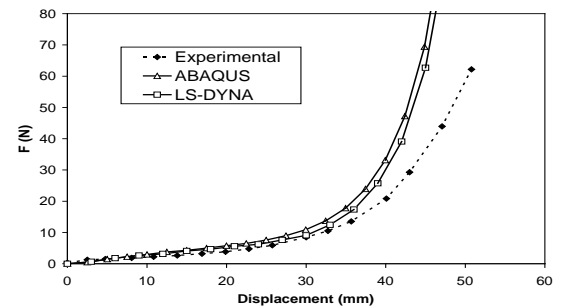

Figure 27. Comparison of the load-displacement curves for the experimental and finite-element simulations of the bias-extension test.

correlation was obtained between the ABAQUS and LS-DYNA results for both test conditions. The error bars in Figure 26 denote one standard deviation. The simulations correlate well with the experimental data for the shear frame test, which validates the approach used, in particular the way the in-plane shear behavior is implemented.

Concerning the bias-extension test, experimental and simulation curves tend to diverge after 35 mm of displacement. This divergence could be a consequence of yarn sliding during the experiment [27], that is not considered in the simulation. This fact has been recently confirmed by experimental data obtained with a Digital Correlation Image technique used to track the shear deformation during the bias-extension test [21]. However, this sliding occurs at very large shear angles that may not be practical in the manufacture of quality parts using this composite forming process.

Thermostamping Modeling

The stamping of a hemisphere was simulated to demonstrate the capability of the approach for compound curvatures. A binder was used to induce in-plane tensile forces within the fabric to eliminate wrinkling. The two finite-element codes give very similar results in terms of shear angle contours (Figure 28). Although an actual thermo-stamped part is not shown here, these finite-element results agree with what is observed in an actual part. For these simulations, the coefficient of friction was 0.3. Future work will use the varying friction coefficient as determined by the 3rd-generation friction testing apparatus.
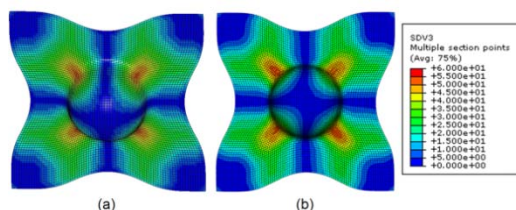
Figure 28. Shear angle contour comparison between (a) LS-DYNA and (b) ABAQUS simulations.

The proposed simulation methodology was also applied to the forming of a composite tub for the automotive industry [28]. The fabric used for these simulations was a plain-weave fabric compounded with a thermoset resin which is pliable at room temperature. This fabric was characterized experimentally using tensile, shear-frame and friction tests. The friction was determined by the 3rd-generation friction testing apparatus to be essentially zero due to the lubrication effect resulting from the compounding material. The woven-fabric material properties were

incorporated in the finite element model to simulate the forming process. The resulting parts are shown in Figure 29.
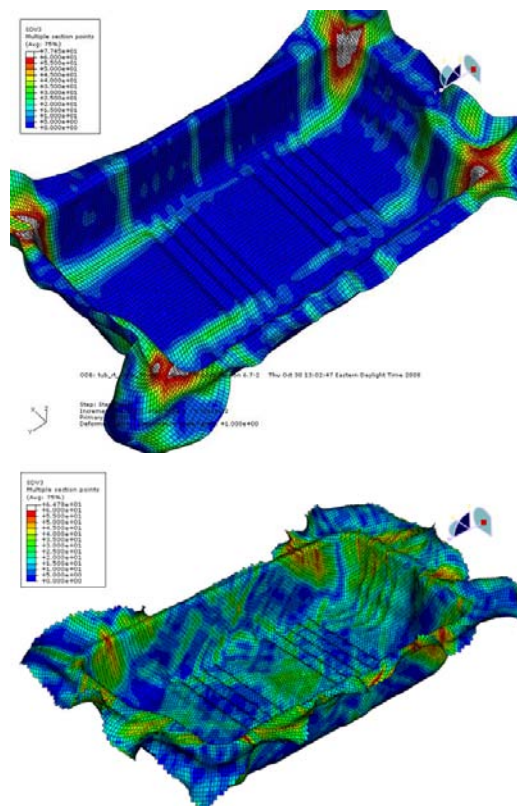
Figure 29. Forming simulation of the Tub for a 0°/90° ply orientation (left) and a ±45° (right). Shear angle contour (blue to red = 0° to 60°, white above 60°).

For the tub shown in Figure 29, the top contour plot shows the resulting shear-strain distribution across the part for a 0°/90° ply orientation, and the bottom is for a ±45° ply orientation. The shear contours range from 0° to 60° as the color contours span from blue to red, respectively. Any shear angles above 60° are shown in white. Note how the 0°/90° ply is blue over a majority of the part. As a result, there is very high shearing in the corners to allow the fabric to assume the shape of the tub. This high shearing of greater than 60° is associated with localized wrinkling. By rotating the fabric 45° as shown in the bottom contour plot, the shearing can be distributed across the part and thereby avoid locally high shearing which can result in wrinkling.

Future Work

Parametric studies of the thermostamping process using the Hersey number friction model and different binder forces will be done to achieve a better understanding of the effect of the in-plane tension on the wrinkling and tearing of the fabric. These studies will demonstrate the usefulness of the model to determine the most appropriate binder force to avoid wrinkling and tearing.

The effect of fiber orientation on the friction coefficient is currently under further investigation to conclude the importance of yarn orientation on the friction behavior. In addition, the importance of the state-of-shear is being investigated.

The modal testing of a stamped part will be performed using a three-dimensional laser vibrometer. Then, comparisons with finite element modal analyses using the final shapes and fiber orientations predicted by the forming simulations will be conducted. This final exercise will show the ability of the approach to provide useful data for subsequent structural analysis in addition to the information on the drapability.

A proposal has been submitted to DOE to use the design tool to simulate the composite forming process of wind turbine blades. The proposed research will investigate the root cause of wrinkling in large composite wind turbine blades which can lead to discarding the part completely or seriously comprising the maximum load capatity of the blade and useful life.

Conclusions

Yarn and fiber parameters were investigated and their ability to model the compaction behavior of commingled fibers has been demonstrated by their influence on the resulting shear load-deformation curve. A 3rd-generation friction-test apparatus using load-control to apply the normal force to the surface of the fabric has been designed, built and validated allowing for the static and dynamic coefficients of friction to be quantified for tool-fabric and fabric-fabric friction. A set of experiments has been developed to quantify the mechanical behavior of woven fabrics for the forming process. A set of constitutive models has been implemented in the ABAQUS and LS-DYNA explicit finite element codes. The ability of the numerical design tool to simulate the forming of composite parts for woven fabric composites has been demonstrated. The design tool is now being used to validate its ability to link the manufacturing process to the structural response of the formed part. This validation will be done by comparing experimental and finite element results for structural stiffness and vibration response of a relatively complex part.

Publications

1. L. Gamache, J. A. Sherwood, J. Chen, and J. Cao. Characterization of the Fabric/Tool and Fabric/Fabric Friction during the Thermostamping Process. Proceedings of the 10th International ESAFORM Conference on Material Forming. Zaragoza, Spain, 2007.

2. L. Gamache. The Design and Implementation of a Friction Test Apparatus Based on the Thermostamping Process of Woven-Fabric Composites, MS Thesis, Department of Mechanical Engineering. Lowell, MA: University of Massachusetts Lowell, 2007.

3. J. Cao, R. Akkerman, P. Boisse, J. Chen, H. S. Cheng, E. F. DeGraaf, J. Gorczyca, P. Harrison, G. Hivet, J. Launay, W. Lee, L. Liu, S. Lomov, A. Long, E. Deluycker, F. Morestin, J. Padvoiskis, X. Q. Peng, J. Sherwood, T. Stoilova, X. M. Tao, I. Verpoest, A. Willems, J. Wiggers, T. X. Yu, and B. Zhu. Characterization of mechanical behavior of woven fabrics: experimental methods and benchmark results. Composites: Part A, 39:1037–1053, 2008.

4. K. A. Fetfatsidis, J. A. Sherwood, J. Chen, and D. Jauffres. Characterization of the fabric/tool and fabric/fabric friction during the thermostamping process. Proceedings of the 12th International Conference. Twente, Nederlands, 2009.

5. D. Jauffres, C. D. Morris, J. Sherwood, and J. Chen. Simulation of the thermostamping of woven composites: determination of the tensile and in-plane shearing behaviors. Proceedings of the 12th International ESAFORM Conference. Twente, Nederlands, 2009.

6. D. Jauffres, C. D. Morris, J. Kremer, J. Sherwood, and J. Chen. Simulation of the thermostamping of woven composites: mesoscopic modeling using FEA explicit codes. Proceedings of the 12th International ESAFORM Conference. Twente, Nederlands, 2009.

7. D. Jauffres, C. D. Morris, J. Sherwood, and J. Chen. Discrete mesoscopic modeling for woven fabric reinforcement forming simulation. International Journal of Material Forming: (in preparation), 2009.

8. D. Jauffres, J. A. Sherwood, J. Chen, C. D. Morris, and J. Kremer. Mesosocopic finite element modeling of woven reinforcements applied to sheet molding compound forming simulation. Proceedings of the 17th International Conference on Composite Materials. Edinburgh, UK, 2009.

9. K. A. Fetfatsidis. Characterization of the Tool/Fabric and Fabric/Fabric Friction for Woven Fabrics: Static and Dynamic, MS Thesis, Department of Mechanical Engineering. Lowell, MA: University of Massachusetts Lowell, 2009.

10. C. D. Morris. Simulation of the Thermostamping Process for Woven Fabric Composites using LS-DYNA, MS Thesis, Department of Mechanical Engineering. Lowell, MA: University of Massachusetts Lowell, 2009.

Acknowledgements

References

1. C. E. Wilks. Characterization of the tool/ply interface during forming. PhD Thesis, School of Mechanical, Materials, Manufacturing and Management. Nottingham, UK: University of Nottingham, 1999.

2. A. E. Long, C. D. Rudd, M. Blagdon, and P. Smith. Characterizing the processing and performance of aligned reinforcements during preform manufacture. Composites: Part A, 27:247–253, 1996.

3. L. Liu, J. Chen, J. Gorczyca, and J. Sherwood. Modeling of friction and shear in thermostamping of composites - Part II. Journal of Composite Materials, 38:1931–1947, 2004.

4. L. Liu, J. Chen, X. Li, and J. Sherwood. Two-dimensional macro-mechanics shear models of woven fabrics. Composites: Part A, 36:105–114, 2005.

5. L. Liu, J. Chen, and J. Sherwood. Analytical model of shear of 4-harness satin weave fabrics. American Institute of Physics Proceedings 712, 8th NUMIFORM Technical Conference, June 13–17. Columbus, OH, 2004.

6. A. Bulusu. Modeling of Architecture and Deformation of Dry Woven Fabrics during Shear. MS Thesis, Department of Mechanical Engineering. Lowell, MA: University of Massachusetts Lowell, 2001.

7. I. M. Hutchings. Tribology: Friction and Wear of Engineering Materials. Ann Arbor, MI: CRC Press, 2002.

8. J. Gorczyca. A Study of the Frictional Behavior of a Plain-Weave Fabric during the Thermostamping Process. DEng Dissertation, Department of Mechanical Engineering. Lowell, MA: University of Massachusetts Lowell, 2004.

9. J. Gorczyca-Cole, J. A. Sherwood, and J. Chen. A friction model for thermostamping commingled glass–polypropylene woven fabrics. Composites: Part A, 38:393–406, 2007.

10. J. Gorczyca, J. Sherwood, L. Liu, and J. Chen. Modeling of friction and shear in

Thermostamping process - Part I. Journal of Composite Materials, 38:1911–1929, 2004.

11. S. Chow. Frictional Interaction between Blank Holder and Fabric in Stamping of Woven Thermoplastic Composites. MS Thesis, Department of Mechanical Engineering. Lowell, MA: University of Massachusetts Lowell, 2002.

12. L. Gamache. The Design and Implementation of a Friction Test Apparatus Based on the Thermostamping Process of Woven-Fabric Composites, MS Thesis, Department of Mechanical Engineering. Lowell, MA: University of Massachusetts Lowell, 2007.

13. L. Gamache. J. A. Sherwood. J. Chen, and J. Cao. Characterization of the Fabric/Tool and Fabric/Fabric Friction during the Thermostamping Process. Proceedings of the 10th International ESAFORM Conference on Material Forming. Zaragoza, Spain, 2007.

14. K. A. Fetfatsidis, J. A. Sherwood, J. Chen, and D. Jauffres. Characterization of the fabric/tool and fabric/fabric friction during the thermostamping process. Proceedings of the 12th International Conference on Material Forming. Twente, Nederlands, 2009.

15. K. A. Fetfatsidis. Characterization of the Tool/Fabric and Fabric/Fabric Friction for Woven Fabrics: Static and Dynamic, MS Thesis, Department of Mechanical Engineering. Lowell, MA: University of Massachusetts Lowell, 2009.

16. C. D. Morris. Simulation of the Thermostamping Process for Woven Fabric Composites using LS-DYNA, MS Thesis, Department of Mechanical Engineering. Lowell, MA: University of Massachusetts Lowell, 2009.

17. A. Willems, S. Lomov, D. Vandepitte, and I. Verpoest. Double dome forming of woven textile composites. Proceedings of the 9th International ESAFORM Conference on Material Forming. Glasgow, UK, 2006.

18. D. Jauffres, C. D. Morris, J. Sherwood, and J. Chen. Simulation of the thermostamping of woven composites: determination of the tensile and in-plane shearing behaviors.

Proceedings of the 12th International ESAFORM Conference on Material Forming. Twente, Nederlands, 2009.

19. J. Cao, R. Akkerman, B. Boisse, J. Chen, H. S. Cheng, E. F. DeGraaf, J. Gorczyca, P. Harrison, G. Hivet, J. Launay, W. Lee, L. Liu, S. Lomov, A. Long, E. Deluycker, F. Morestin, J. Padvoiskis, X. Q. Peng, J. Sherwood, T. Stoilova, X. M. Tao, I. Verpoest, A. Willems, J. Wiggers, T. X. Yu, and B. Zhu. Characterization of mechanical behavior of woven fabrics: experimental methods and benchmark results. Composites: Part A, 39:1037–1053, 2008.

20. D. Jauffres, C. D. Morris, J. Kremer, J. Sherwood, and J. Chen. Simulation of the thermostamping of woven composites: mesoscopic modeling using FEA explicit codes. Proceedings of the 12th International ESAFORM Conference on Material Forming. Twente, Nederlands, 2009.

21. D. Jauffres, C. D. Morris, J. Sherwood, and J. Chen. Discrete mesoscopic modeling for woven fabric reinforcement forming simulation. International Journal of Material Forming: (in preparation), 2009.

22. P. Boisse, N. Hamila, F. Helenon, B. Hagege, and J. Cao. Different approaches for woven composite reinforcement forming simulation. International Journal of Material Forming, 1:21–29, 2008.

23. X. Li. Material characterization of woven-fabric composites and finite element analysis of the thermostamping process. DEng Dissertation, Department of Mechanical Engineering. Lowell, MA: University of Massachusetts Lowell, 2005.

24. K. J. Bathe. Finite Element Procedures. Englewood Cliffs: New Jersey: Prentice Hall, 1996.

25. X. Q. Peng and J. Cao. A continuum mechanics-based non-orthogonal constitutive model for woven composite fabrics. Composites: Part A, 36:859–874, 2005.

26. S. Lomov, P. Boisse, E. Deluycker, F. Morestin, K. Vanclooster, D. Vandepitte, I. Verpoest, and A. Willems. Full-field strain

measurements in textile deformability studies. Composites: Part A, 39:1232-1244, 2008.

27. P. Harrison, M. J. Clifford, and A. Long. Shear characterization of viscous woven textile composites: a comparison between picture frame and bias extension experiments. Composites Science and Technology, 64:1453–1465, 2004.

28. D. Jauffres, J. A. Sherwood, J. Chen, C. Morris, and J. Kremer. Mesosocopic finite element modeling of woven reinforcements applied to sheet molding compound forming simulation. Proceedings of the 17th International Conference on Composite Materials. Edinburgh, UK, 2009.

P. Structural Nanocomposite Design

Principal Investigator: Thomas E. Lacy
Associate Professor, Aerospace Engineering
Mississippi State University
316c Walker Bldg., P.O. Box A
Mississippi State, MS 39762
(662) 325-2754; fax: (662) 325-7730; e-mail: Lacy@AE.MsState.edu

Co-Principal Investigator: Chuck Pittman
Lecturer, Chemistry
Mississippi State University,
Hand Land, Rm 3337
Mississippi State, MS 39762
(662) 325-7616; e-mail: cpittman@chemistry.msstate.edu

Co-Principal Investigator: Hossein Toghiani
Associate Professor, Chemical Engineering
Mississippi State University,
Swalm Engineering Bldg.
Mississippi State, MS 39762
(662) 325-8607; e-mail: hossein@che.msstate.edu

Co-Principal Investigator: Yuanxin Zhou
Assistant Professor, Tuskegee Center for Advanced Materials (T-CAM), Department of Mechanical Engineering
Tuskegee University
Tuskegee AL 36088
(334) 724-4222; fax: (334) 727-8801; e-mail: yzhou@tuskegee.edu

Co-Principal Investigator: Shaik Jeelani
Director, Tuskegee Center for Advanced Materials (T-CAM)
Vice President, Research and Sponsored Programs
Tuskegee University
Tuskegee, AL 36088
(334) 727-8970; fax: (334) 724-4224; e-mail: jeelanis@tuskegee.edu

Technology Area Development Manager: Joseph A. Carpenter
(202) 586-1022; fax: (202) 586-1600; e-mail: joseph.carpenter@ee.doe.gov

Field Project Officer: Aaron D. Yocum
(304) 285-4852; fax: (304) 285-4403; e-mail: aaron.yocum@netl.doe.gov

---

Objective

- Design low-cost nanoreinforced composite systems for automotive structural applications.

- Approach

- A multiscale design methodology is being employed to investigate the effects of nanoreinforcements on the mechanical properties of fiber-reinforced composites for automotive structural applications. Critical issues being addressed include: selection of key combinations of fibers (glass, carbon, natural, *etc.*), matrix materials (thermoset, thermoplastic), and relatively cost-effective nanoreinforcements (vapor grown carbon nanofibers, nanoclay particles, *etc.*); fabrication of fine-scale and coupon-scale material samples for static and dynamic testing; and development of a multiscale materials modeling strategy for assessing high-performance nanocomposites that accounts for the influence of material processing parameters on mechanical properties of the material under static and dynamic loads. This effort involves completion of five primary objectives.

- Determine appropriate composite fiber-matrix systems and identify and prioritize candidate nanoreinforcements for evaluation.

- Investigate the effects of different mixtures of nanoreinforced fibers/polymer matrices from a manufacturing and cost perspective.

- Quantify nanoreinforced structure-property relations experimentally.

- Study material failure modes and energy absorption characteristics under different loading conditions

- Development of a multiscale materials model based upon micromechanics models and experiments for nanocomposites.

Accomplishments

- Selected readily available low-cost thermoset resins (vinyl ester, polyester) as the primary matrix materials in this investigation; other polymer resins (*e.g.*, epoxy, polypropylene) may be considered as part of supplemental investigations associated with this work (Year 1).

- Selected Applied Science, Inc. PR-24 vapor grown carbon nanofibers (VGCNFs) as the primary nanoreinforcement for use in this examination (Year 1).

- Selected E-glass unidirectional and woven fabric plies as the primary traditional continuous fiber reinforcement phase in this investigation because of their widespread use in automotive applications (Year 1).

- Fabricated nanophased resin test specimens comprised of thermoset (vinyl ester, polyester) resins and varying weight fractions of VGCNFs using a combination of mechanical mixing, sonication and high shear mixing and dispersing agent (Year 1, 2).

- Evaluated the dispersion of nanoreinforcements within polymer resins using scanning electron microscopy (SEM) and transmission electron microscopy (TEM) (Year 1, 2).

- Evaluated VGCNF surface functionalization and use of dispersants in order to enhance nanofiber dispersion in and interaction with the thermoset matrices, as well as to minimize VGCNF agglomeration (Year 1, 2).

- Fabricated continuous fiber E-glass laminates and sandwich composites with nanophased thermoset using vacuum-assisted resin transfer molding (VARTM) (Year 1).

- Performed three-point bend experiments for two-phase (nanoreinforced) resin test specimens comprised of polyester reinforcement with varying weight fractions of CNFs (0.0%, 0.5%, 1.0%, 1.5%, 2.0%, 3.0%) (Year 1).

- Established a student exchange between MSST and T-CAM, where two MSST minority undergraduate students fabricated CNF/ polyester three-point bend test specimens and compression test specimens using T-CAM experimental facilities (Year 1).

- Used SEM to assess damage morphology and failure mechanisms for nanophased resins (Year 1).

- Performed dynamic mechanical analysis (DMA), thermo-gravimetric analysis (TGA), standard coupon and split Hopkinson bar testing to assess the thermal/ mechanical properties of nanophased polymer resins (Year 1, 2).

- Initiated development of a multiscale-materials modeling strategy that employs a combination of micromechanics models, three-dimensional (3D) finite elements (ABAQUS, GENOA), and validation experiments for nanocomposites (Year 1, 2).

- Established a partnership with AlphaStar, Inc. for the modeling of nanocomposites using the finite-element code, GENOA (Year 1, 2).

- Submitted and published two refereed journal articles and two conference papers (Year 1, 2).

Future Direction

- Continue ongoing dynamic mechanical analysis (DMA), thermo-gravimetric analysis (TGA), and standard coupon and split Hopkinson bar testing of VGCNF/ vinyl ester resins to assess the thermal and mechanical properties of nanophased polymer resins.

- Conduct structure-property tests for three-phase composite systems (nanophased resin, E-glass plies) in order to assess the mechanical behavior and failure of the structural nanocomposites.

- Determine weight fractions of nanoreinforcements that lead to optimal nanophased resin and structural nanocomposite properties.

- Determine material failure modes and energy absorption characteristics for structural nanocomposites subjected to static and dynamic loading conditions. Perform flexure, tension, fatigue, fracture, and dynamic tests of structural nanocomposites.

- Validate micromechanical model for determining effective properties of nanophased resins using structure-property data.

- Incorporate effective nanophased resin properties from micromechanical models into 3D finite- element models of three-phase composites. Validate numerical models using structure-property data.

Introduction

A multiscale design methodology is being employed to investigate the effects of nanoreinforcements on the mechanical properties of fiber-reinforced composites for automotive structural applications. Critical issues being addressed include: selection of key combinations of fibers (glass, carbon, natural, etc.), matrix materials (thermoset, thermoplastic) and relatively cost-effective nanoreinforcements (vapor grown carbon nanofibers, nanoclay particles, etc.); fabrication of fine scale and coupon scale material samples for static and dynamic testing; and development of a multiscale materials modeling strategy for assessing high-performance nanocomposites that accounts for the influence of material processing parameters on mechanical properties of the material under static and dynamic loads. A literature review of recent experimental and modeling activities related to nanoreinforced composites, particularly those involving glass fibers coupled with thermoset resins (e.g., vinyl ester, polyester, as well as epoxy) was performed (cf., Odegard, et al., 2001; Ghoniem, et al, 2003; Thostenson, et al., 2004; Buryachenko, et al., 2005; Gates, et al., 2005; Odegard, et al., 2005; Valavala and Odegard, 2005; Hussein, et al.,

2006; Liu and Brinson, 2006; Fischer, et al., 2007). Such material systems are of particular interest to the Automobile Composites Consortium (ACC). A dialogue has been initiated with the ACC in order to solicit guidance and feedback on relevant aspects of the research, including identification of additional industry partners to participate in cost-share relationships with MSST, T-CAM and the DOE. A summary of year two accomplishments is included in the following discussion.

Determination of Composite Fiber-matrix Systems and Nanoreinforcements

Because of their widespread use and relatively low cost, two commercially available thermoset resins (U.S. Composites, Inc. polyester and Ashland Co. vinyl ester) were selected as the primary matrix materials in this investigation; other polymer resins (e.g., epoxy and polypropylene) are being considered as part of supplemental investigations associated with this work (cf., Zhou, et al., 2007; Ingram, et al., 2008). Applied Science, Inc. PR-24 vapor grown carbon nanofibers (VGCNFs) (typical diameters, 60–200 nm; typical lengths, 20–100 μm) were selected as the primary nanoreinforcement for use in this examination.

VGCNFs are relatively inexpensive and possess excellent mechanical properties. Because of prevalent use in automotive applications, E-glass unidirectional and woven fabric plies are being used as the primary traditional continuous fiber reinforcement phase in this investigation.

Investigation of the Effects of Different Mixtures of Nanoreinforced Fibers/ Polymer Matrices on Manufacturing Vinyl Ester Nanocomposite Formulation

In year two, nanophased resin test specimens comprised of a thermoset vinylester (VE) resin and varying weight fractions of VGCNFs were fabricated at MSST using a combination of mechanical mixing, sonication, high shear mixing, addition of dispersing agents, and cure. Vinyl esters possess superior mechanical properties compared to unsaturated polyesters. Derakane 441–400 (Ashland Co.), with a relatively low styrene content (33%), was selected as the candidate matrix. In order to assess the effect of nanoreinforcement surface-modification on mechanical properties of the nanocomposite, two different grades of VGCNFs were used: (1) PR-24-XT-LHT (Applied Sciences, Inc.), which is a pristine (unmodified) VGCNF similar to the one used previously with unsaturated polyesters (year one), and (2) PR-24-XT-LHT-OX (Applied Sciences, Inc.), which is a surface-oxidized VGCNF with mainly carboxylic-type functional groups on the nanofiber surface. Nanoreinforcement functionalization is an established methodology for the enhancement of dispersion and load transfer capabilities of the resin-embedded nanoreinforcements.
In order to investigate the effect of nanocomposite formulation, mixing/processing, and curing conditions on the mechanical properties of the VGCNF/ VE nanocomposites, a factorial design of experiments approach is being employed. The goal of this work is to establish nanocomposite formulation and processing conditions resulting in optimal mechanical properties. A total of 48 different combinations of processing and configuration parameters were considered in this study. The individual factors (independent variables) considered in this study include:

1. Nanofiber "loading" level (0.25, 0.50, 0.75, and 1.00 phr). Here, "phr" stands for "parts per hundred resin," which is a standard basis for formulations common in the resin industry. Essentially, 1.0 phr suggests that a mixture contains one part of a given constituent (by weight) for every 100 parts of resin (by weight). VGCNF loading levels in excess of 1.00 phr were not considered in this examination due excessive viscosity of the resin/ nanoreinforcement mixture. Relatively low viscosity nanophased resins are desirable because of potential use in future vacuum-assisted resin transfer molding (VARTM) or other resin infusion process.

2. Nanofiber type (pristine and oxidized). The effect of different nanofiber surface chemistries on the dispersion characteristics and overall mechanical properties are being investigated. The oxidized nanofibers (PR-24-XT-LHT-OX) were used as received. Additional VGCNF surface functionalization is planned for year three.

3. Use of chemical dispersing agents (i.e., dispersants or surfactants) to facilitate nanofiber dispersion within the resin. A preliminary study was conducted using several readily available inexpensive dispersing agents (BYK-9076, BYK-9077, BYK-996, and Disperbyk-191 from BYK Chemie Co.). Based upon this study, BYK-9076 was selected as the most effective surfactant for use in the experimental design. The effect of a dispersing agent on nanofiber dispersion quality and ultimate mechanical properties of the nanocomposite is being investigated.

4. Mixing method (ultrasonication, high-shear mixing, and coupled high-shear mixing/ ultrasonication). One of the key steps in the fabrication of polymer nanocomposites is the incorporation of nanoreinforcements into the matrix by means of a suitable mixing method. The efficiency of the mixing method in dispersing and distributing nanofibers in the matrix plays a crucial role in achieving optimal nanocomposite properties. VGCNFs tend to agglomerate, due to high van der Waals interactions. Ideally, such agglomerates and VGCNF clusters must be separated into individual nanofibers during mixing. This can be achieved, though not completely, by

different means: ultrasonication, shearing action of special blades, etc. In this study, a novel high shear mixer is used alongside the more traditional ultrasonicator used in year one.

The VGCNF/VE nanocomposite formulations considered in this study are shown in Table 1. Due to rigorous mixing of nanofibers into the resin, excessive void formation is a concern. Hence, a surfactant (BYK-A515) and antifoam (degassing) agent (BYK-A555) were used as an integral part of each formulation to aid degassing of the mixture. A promoter, cobalt naphthenate 6% (North American Composites Co.), was used in each formulation to facilitate the resin curing reaction. One phr of methyl ethyl ketone peroxide (MEKP) was used as the curing agent (hardener); this amount provides a gelling time of 30–50 minutes, which is necessary for degassing of the mixture and pouring it in the mold.

Table 1. Formulation of nanocomposites

Ingredient	Weight (g)
Derakane 441–400 (vinyl ester resin)	100
Cobalt naphthenate 6%	0.20
BYK-A 515	0.20
BYK-A 555	0.20
BYK-9076[a]	1:1 ratio with VGCNF
VGCNF[b]	0.25/0.50/0.75/1.00
MEKP	1.00

[a]BYK-9076 was not used in all configurations
[b]Pristine and oxidized nanofibers were used in different configurations

Vinyl Ester Nanocomposite Specimen Preparation

VGCNF/VE test specimens were fabricated for use in dynamic mechanical analysis (DMA), four-point bending, and tension and split Hopkinson bar experiments. The following procedure was used in specimen preparation:

1. Individual ingredients were weighed and added to a 240 ml cup in the following order: resin, promoter, air release agents, dispersing agent (if used), and VGCNFs. Prior to the addition of nanofibers, the initial mixture was blended by hand to ensure that the promoter, air release agents, and the dispersing agent were uniformly distributed within the resin.
2. The liquid resin mixture was then processed in one of several ways depending on the configuration: (a) five minutes in a mechanical stirrer at 1500 revolutions per minute (rpm), followed by one hour sonication at an amplitude of 20% in continuous mode (no pulse). The cup was mounted on a special vortex mixer that shakes the cup for a uniform power input and was kept cool by a high-speed fan; (b) 15 min. in a Silverson high-shear mixer. The cup was immersed in an ice bath during mixing to avoid overheating of the liquid resin; and (c) 15 min. of high-shear mixing followed by one hour of sonication in the same manner as described above.
3. The hardener was then added to the mixture and mixed by hand for five minutes.
4. The mixture was degassed for 5–15 min. using a vacuum pump until all the air bubbles were removed. The degassing time varied for each configuration due to of differences in the viscosity of each mixture. Care was to taken to avoid removing an excessive amount of styrene during degassing.
5. The resin was gently poured into specimen molds and cured in an oven at elevated temperatures (five hours at 60°C and two hours at 120°C). It should be noted that the presence of a dispersing agent had a minor effect on the curing reaction (i.e., the exposed surface of these specimens in the mold appeared somewhat "tacky"). This issue will be addressed in year three.

The dispersion of nanoreinforcements within the cured resin for each configuration is being evaluated using a combination of scanning electron microscopy (SEM) and transmission electron microscopy (TEM); this assessment will continue into year three of the project.
As mentioned in an earlier report, vacuum assisted resin transfer molding (VARTM) has been established as a viable technique to fabricate continuous fiber E-glass laminates with

nanophased thermoset resins involving a variety of different nanoreinforcements (cf., Chisholm, et al., 2005; Chowdhury, et al., 2006, Zhou, et al., 2006). VARTM may be used to produce high quality composite parts and is an attractive alternative to autoclave processing. One key concern, however, is that a gradient in the distribution of VGCNFs may result due to filtering by continuous fiber plies in the vicinity of the infusion ports used in the VARTM process. The issue will be investigated in year three; continuous fiber composites with VGCNF/ VE resins fabricated using the VARTM technique will be destructively sectioned and examined using TEM and/or SEM imaging to assess the degree of VGCNF filtration.

Experimental Structure-Property relations for Nanoreinforced Materials

Dynamic Mechanical Analysis (DMA) of VGCNF/VE Nanocomposites

Dynamic mechanical analysis (DMA) and thermo-gravimetric analysis (TGA) testing of VGCNF/VE nanocomposites are currently being performed to assess the thermal properties of nanophased thermoset resins. The nanocomposite storage modulus (measure of material stiffness), loss modulus (measure of material toughness and energy dissipation capability), and tan delta (measure of damping) were selected as mechanical responses for the comparison between different material and fabrication conditions. The tests were conducted in a DMA Q800 instrument in single cantilever mode at a fixed frequency of 10 Hz and with a heating rate of 5°C/min. The temperature scan was from room temperature to 160°C.

At the time of this report, a total of 17 VGCNF/VE samples that were prepared using ultrasonication alone as the primary mixing technique had been tested. These specimens include: 1) one neat VE specimen (0 phr VGCNF); 2) four specimens were prepared using 0.25, 0.50, 0.75, and 1.0 phr of pristine (unoxidized) VGCNFs, respectively; 3) four specimens were prepared using 0.25, 0.50, 0.75, and 1.0 phr of pristine (unoxidized) VGCNFs and BYK-9076 dispersant, respectively; 4) four specimens were prepared using 0.25, 0.50, 0.75, and 1.0 phr of oxidized VGCNFs, respectively; and 5) four specimens were prepared using 0.25,

0.50, 0.75, and 1.0 phr of oxidized VGCNFs and BYK-9076 dispersant, respectively. The testing of other specimens prepared using high-shear mixing and coupled ultrasonication/ high-shear mixing is ongoing.

Figure 1 contains a plot of the measured storage modulus as a function of temperature for neat VE resin and pristine VGCNF/VE nanocomposites (no dispersing agent). As can be seen from the figure, the storage modulus (and nanocomposite stiffness) increased significantly as the weight fraction of pristine VGCNFs increased from 0 to 0.5 phr. At room temperature, the storage modulus for a nanocomposite specimen with 0.50 phr VGCNF was roughly 22% higher than the neat resin. As the weight fraction of nanofibers is further increased (0.75 and 1.0 phr), however, the improvement in storage modulus *decreased* to roughly 12% over the neat resin. The apparent degradation in storage modulus that occurs once the weight fraction of VGCNFs exceeds some optimal value is likely due to relatively poor nanofiber dispersion. For example, Figures 2 and 3 show typical SEM images of highly clustered VGCNFs in the VE resins for specimens containing 0.50 and 0.75 phr nanofibers, respectively. These regions act as potential stress raisers within the matrix, while providing relatively little in the way of stiffness increase. These results suggest that inclusion of relatively small amounts of nanoreinforcements can have a noticeable effect on nanocomposite material properties, provided that the nanofibers can be dispersed properly.
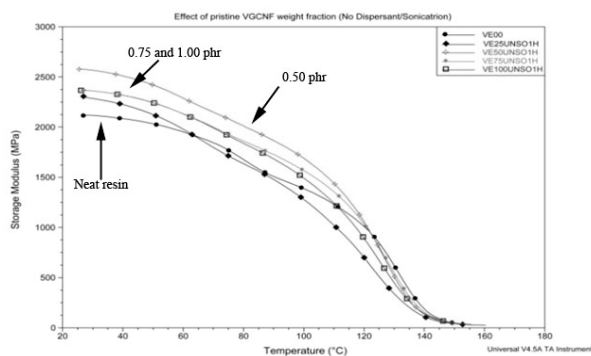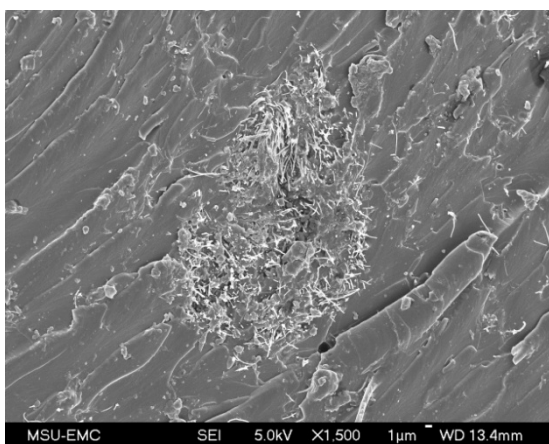

Figure 1. Effect of pristine VGCNF weight fraction on storage modulus (no dispersing agent).
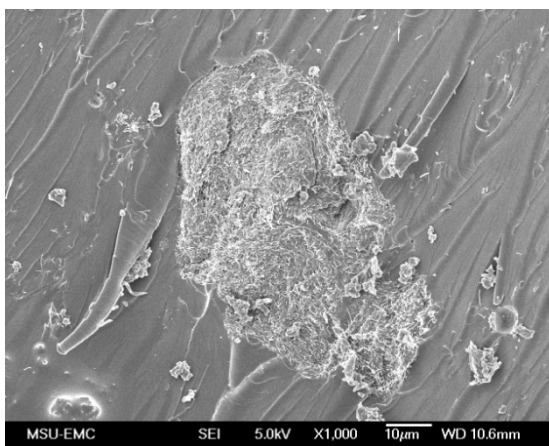
Figure 2. SEM image of a cluster of carbon nanofibers in the VE matrix (0.50 phr pristine VGCNF/ no dispersing agent/ ultrasonication).


Figure 3. SEM image of a cluster of carbon nanofibers in the VE matrix (0.75 phr pristine VGCNF/no dispersing agent/ ultrasonication).

Figure 4 contains a plot of the measured storage modulus as a function of temperature for neat VE resin and pristine VGCNF/ VE nanocomposites where a dispersing agent was employed to facilitate nanofiber dispersion (the ratio of dispersing agent to VGCNF was 1:1 for each configuration). Similar to the results presented in Figure 1, the storage modulus increased with increasing weight fraction of VGCNFs. At room temperature, the storage modulus for nanocomposite specimens with 0.25, 0.50, and 0.75 phr VGCNFs were each roughly 17% higher than the neat resin. In contrast to the preceding results, however, the greatest improvement in storage modulus (~25%) occurred for 1.0 phr weight fraction of nanofibers.
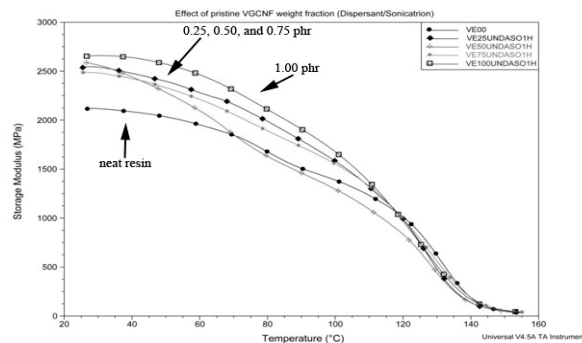
Figure 4. Effect of pristine VGCNF weight fraction on storage modulus in the presence of the dispersing agent.

Figure 5 contains a plot of the measured storage modulus for 1.0 phr VGCNF/VE resin specimens fabricated with and without a dispersing agent. Included in the figure is the measured storage modulus for the neat resin. As can be seen from the figure, the use of small amounts of dispersant can improve the mechanical properties of the nanocomposite through improved dispersion of nanofibers. One concern, however, is that the dispersing agent may have a negative effect on the properties of the neat resin. This issue will be addressed in year three.
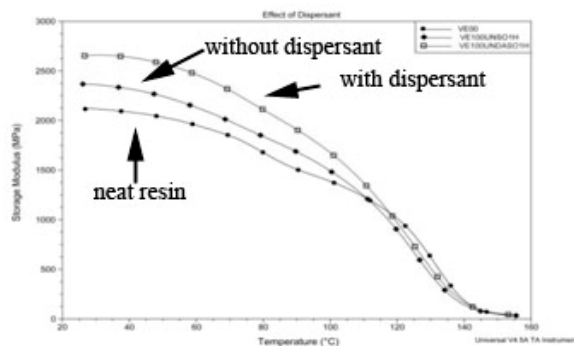
**Figure 5.** Effect of dispersing agent on storage modulus (1.0 phr pristine VGCNF).

Figure 6 contains a plot of the measured loss modulus as a function of temperature for neat VE resin and pristine VGCNF/VE nanocomposites (no dispersing agent). As can be seen from the figure, the loss modulus for the neat resin generally increased with increasing temperature up until the temperature approached the glass transition temperature (~140°C). In addition, a characteristic "hump" or local maxima in loss modulus can be observed at around 80°C. This suggests that the
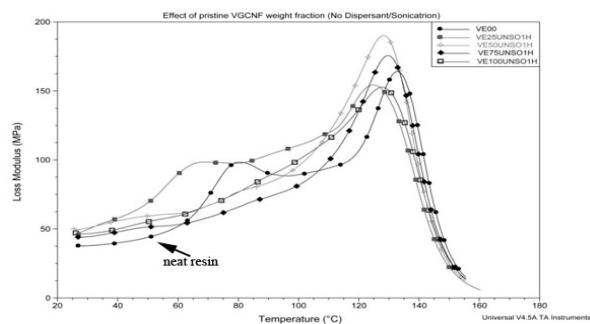
Figure 6. Effect of pristine VGCNF weight fraction on loss modulus (no dispersing agent).

neat resin is better able to dissipate energy in the vicinity of this temperature. In the absence of a dispersing agent, the inclusion of VGCNFs only has a modest effect on the loss modulus. For the 0.25 phr VGCNF nanocomposite, the loss modulus was slightly larger than that of the neat resin with a local maxima occurring at around 60°C. As the nanofiber weight fraction is increased, however, the difference in loss moduli of the nanocomposite specimens and the neat resin was minimal. Moreover, at higher weight fractions of nanofibers, no local maxima were observed at lower temperatures. While the nanocomposite loss moduli (energy dissipating capability) at moderate temperatures were slightly larger than that of the neat resin, the relative improvement was small in comparison to the improvement in storage modulus (stiffness).

When a dispersing agent is used in the nanocomposite processing, however, the relative improvement in loss modulus is more pronounced. Figure 7 contains a plot of the measured loss modulus as a function of temperature for neat VE resin and pristine VGCNF/VE nanocomposites fabricated using a dispersing agent. At moderate temperatures, the nanocomposite loss moduli were all somewhat larger than that of the neat resin. In addition, the 0.5 phr specimen demonstrated an appreciable increase in loss modulus and consistent with the neat resin, retained a local maximum value in the vicinity of 60°C. These results suggest that the nanophased resins are better able to dissipate energy (and have greater stiffness) than the neat resin. As mentioned previously, one concern is that the bulk properties of the resin are affected by the presence of the dispersant. In order to investigate whether the
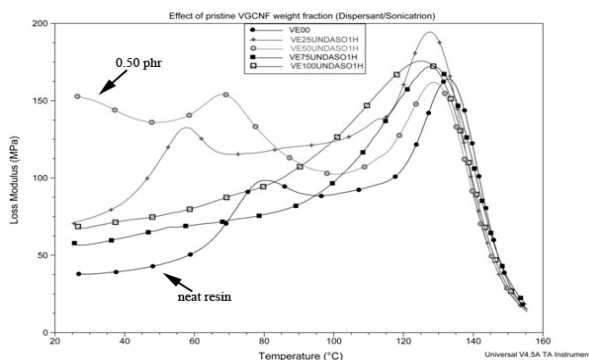

Figure 7. Effect of pristine VGCNF weight fraction on loss modulus in the presence of dispersing agent.

improvement in loss modulus was due to better dispersion of nanofibers or due to a change in properties of the modified resin (VE plus dispersant), additional DMA tests are planned for year three involving the modified resin with no nanoreinforcements.

Figures 8 and 9 show SEM images of two typical regions within a 1.00 phr pristine VGCNF specimen prepared using a dispersing agent. While VGCNF clusters are not completely eliminated (cf., Figure 9), the distribution of individual nanofibers is somewhat more uniform throughout the matrix. This is an indication of relatively better dispersion of nanofibers in the presence of the dispersing agent.

Figures 10 and 11 show the effect of different nanofiber weight fractions on a material's tan delta behavior (ratio between loss and storage modulus) for specimens prepared with and without a disperant, respectively. As can be seen in the
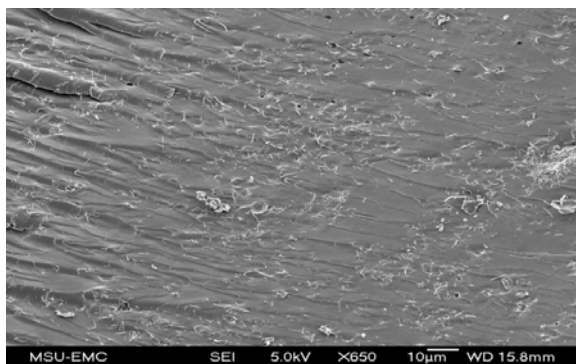

Figure 8. SEM image nanocomposite region with well-dispersed nanofibers (1.00 phr pristine VGCNF/ dispersing agent/ ultrasonication).
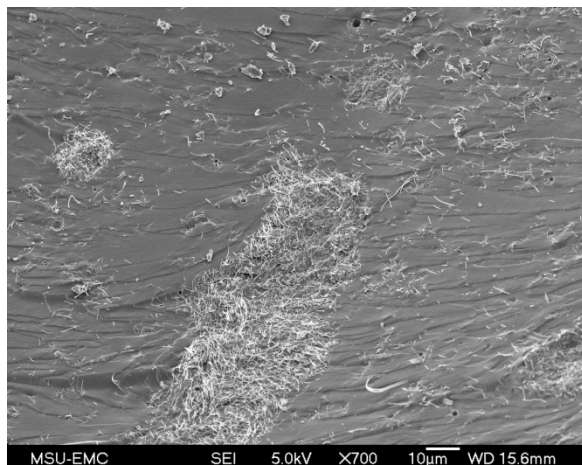
Figure 9. SEM image of a nanofiber cluster surrounded by well-dispersed nanofibers (1.00 phr pristine VGCNF/dispersing agent/ultrasonication).
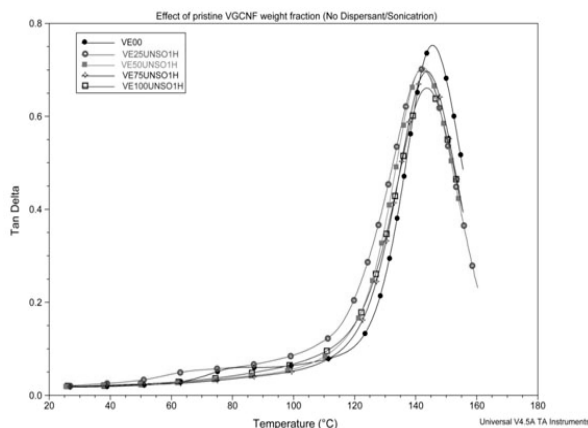
Figure 10. Effect of pristine VGCNF weight fraction on tan delta in the absence of dispersing agent.
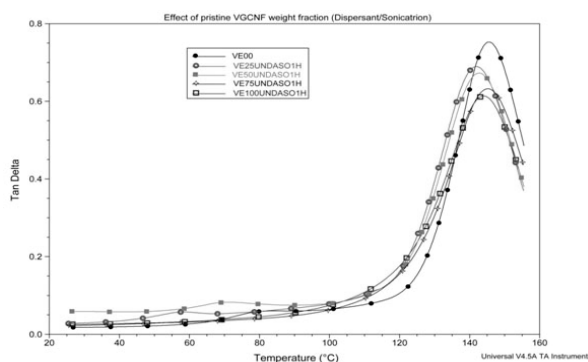
Figure 11. Effect of pristine VGCNF weight fraction on tan delta in the presence of dispersing agent.

figures, the location of the peak tan delta values (an indication of material's glass transition temperature) is not changed appreciably. This suggests that the glass transition temperature and damping behavior of the nanocomposites are almost independent of the nanofiber weight fraction and degree of nanofiber dispersion.

A similar set of DMA experiments were performed using specimens fabricated with oxidized VGCNFs. In general, such specimens would be expected to possess superior mechanical properties due to enhanced interaction with the thermoset resin in comparison to those obtained from specimens using unoxidized (pristine) nanofibers. Oxidized VGCNFs, however, tend to absorb moisture and clump together. As a consequence, oxidized nanofibers were somewhat difficult to disperse in the VE resin using ultrasonication alone. Ongoing efforts suggest that oxidized VGCNFs can be well dispersed in VE using a combination of high shear mixing and sonication. This work will continue in year three.

For comparison purposes, however, DMA tests were performed on oxidized VGCNF/VE specimens fabricated using ultrasonication alone. Figure 12 contains a plot of the measured storage modulus as a function of temperature for neat VE resin and *oxidized* VGCNF/VE nanocomposites (no dispersing agent). In contrast to the results obtained for pristine (unoxidized) fibers, at room temperature the storage moduli for 0.25 and 1.00 phr nanocomposites were slightly lower than that of the neat resin (i.e., no improvement in stiffness). At room temperature, the storage modulus for a nanocomposite specimen with 0.75 phr VGCNF was roughly 13% larger than that of the neat resin (recall that 0.50 phr of unoxidized VGCNFs yielded a 22% improvement in storage modulus; cf., Figure 1) . These results are likely a consequence of poor dispersion of oxidized VGCNFs within the matrix. SEM imaging of these specimens will be used in year three to assess nanofiber dispersion. Of course, the efficient breakup of nanofiber clumps is crucial for achieving optimal material property enhancement.

Surprisingly, the use of a dispersing agent in the fabrication of oxidized VGCNF/VE specimens had very little effect on the measured storage modulus (cf., Figure 13); here the ratio of dispersing agent to VGCNF was 1:2 for each
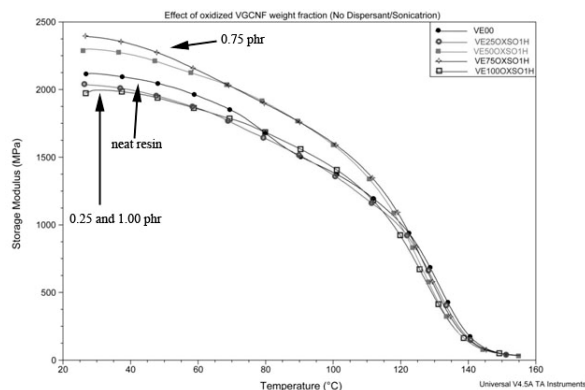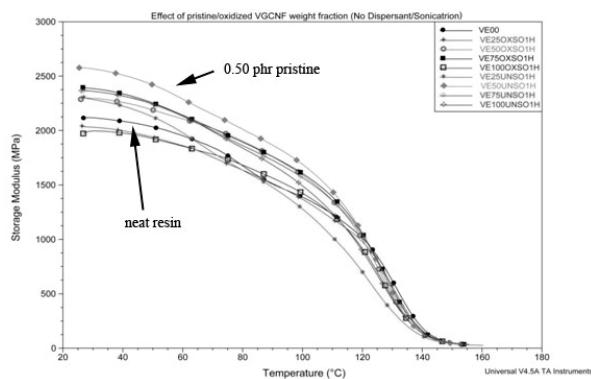
Figure 12. Effect of oxidized VGCNF weight fraction on storage modulus (no dispersing agent).
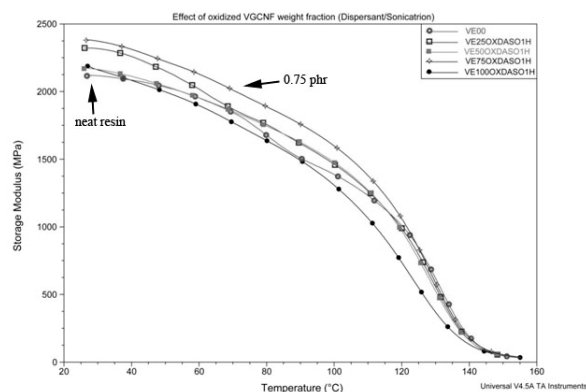
Figure 13. Effect of oxidized VGCNF weight fraction on storage modulus in the presence of dispersing agent.

configuration. As can be seen from the figure, the greatest improvement in storage modulus (~12%) occurred for 0.75 phr VGCNF. As an aside, an investigation aimed at determining the optimal weight fraction of dispersing agent will be performed in year three.

Unexpectedly, the property enhancement associated with the use of oxidized VGCNFs was not as pronounced as for unoxidized (pristine) VGCNFs. For example, Figure 14 compares the measured storage moduli for nanocomposite specimens prepared using pristine and oxidized nanofibers with no dispersant. Note that specimen containing 0.50 phr pristine VGCNFs resulted in the greatest improvement in storage modulus. These results underscore the coupled influence of nanofiber surface functionalization and dispersion on mechanical properties. Future work will focus on obtaining optimal dispersion of oxidized


Figure 14. Effect of oxidized and pristine VGCNF weight fraction on storage modulus (no dispersing agent).

VGCNFs using coupled high-shear mixing and sonication, as well as characterization of nanofiber dispersion using a combination of SEM and TEM.

Figures 15 and 16 show the effect of oxidized nanofiber weight fraction on nanocomposite loss modulus for specimens fabricated with and
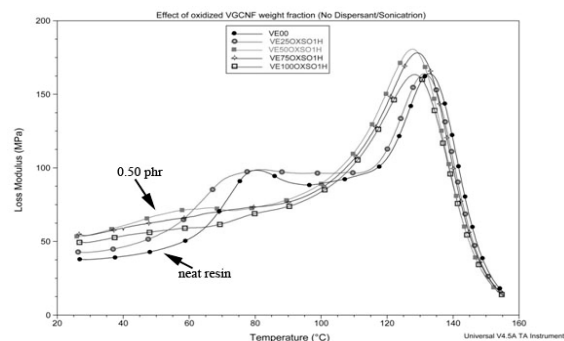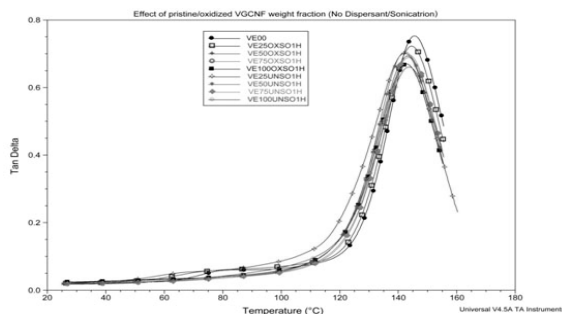

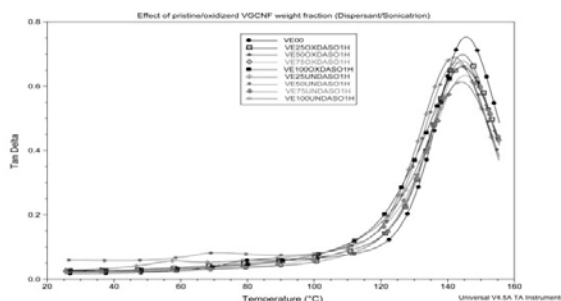**Figure 15.** Effect of oxidized VGCNF weight fraction on loss modulus (no dispersing agent).
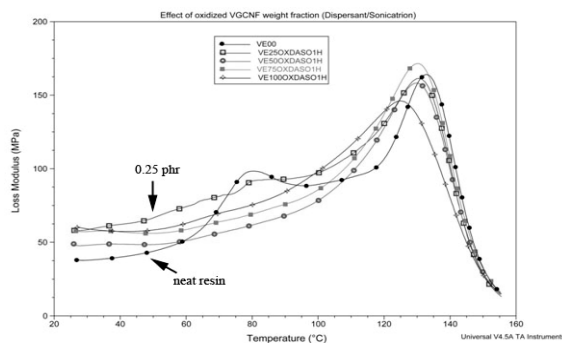
Figure 16. Effect of oxidized VGCNF weight fraction on loss modulus in the presence of dispersing agent.

without a dispersing agent, respectively. In both cases, the change in the loss modulus is relatively small for all nanofiber weight fractions. Similar to the case with pristine nanofibers, the measured tan delta behavior for oxidized nanofibers is not changed appreciably for different nanofiber weight fractions (cf., Figures 17 and 18).

Figure 17. Effect of pristine/oxidized VGCNF weight fraction on tan delta (no dispersing agent).

Figure 18. Effect of pristine/oxidized VGCNF weight fraction on tan delta in the presence of dispersing agent.

Recall that the preliminary results presented here are for specimen prepared using ultrasonication alone. Ongoing work suggests that significant additional enhancements in nanocomposite properties are possible using a combination of high-shear mixing and ultrasonication, coupled with the use of a dispersing agent. This work will be completed in year three.

Assessment of Nanocomposite Material Failure Modes and Energy Absorption Characteristics under Different Loading Conditions

Once optimal levels of VGCNFs have been determined for the candidate thermoset and thermoplastic resins, the static and dynamic failure

behavior of test specimens comprised of three-phase composites will be investigated using a number of standard tests, with an emphasis on energy absorption/ crash applications. The goal of this work is to establish relationships between composite processing, constituent morphology, properties, and macroscale performance. The effects of nanoreinforcements on macroscale physical properties (stiffness, toughness, energy absorption, etc.) will be examined using a combination of three-point bend tests (American Society for Testing and Materials (ASTM) D790), tensile tests (ASTM D3039), fatigue tests, crush tests, fracture tests, Hopkinson bar tests and other experiments involving specimen geometries and lay-ups of interest to the ACC. A combination visual inspection, light microscopy, TEM and SEM will be used to assess damage development and failure of structural nanocomposite specimens. The motivation for this work is to fabricate cost-effective nanoreinforced composite materials suitable for automobile primary structural applications. The majority of these activities will be performed in year three of this project.

Structure-property tests are being developed for three-phase composite systems (nanophased resin, E-glass plies) in order to assess the mechanical behavior and failure of the structural nanocomposites. These activities will continue into year three of the project.

## High Strain Rate Behavior of Nanofiber Reinforced Resins

In order to understand the dynamic response of the two-phase (nanofiber reinforced) VE resin system, split Hopkinson bar (SHB) compression tests were performed at strain rates ranging from 600/s–1800/s. The strain-rate dependent stress-strain response of neat VE resin was measured and compared to that of VE reinforced with 0.5 and 1.0 phr unoxidized VGCNFs. The ratio of dispersing agent to nanofibers was 1:2. The nanofibers were dispersed using a high-shear mixer for 15 minutes and an ultrasonication mixer for one hour. The specimens then cured at 60°C for six hours, followed by a two-hour post cure at 120°C. In year three, a comprehensive test matrix will be executed to investigate the effect of nanofiber functionalization and weight fraction,

mixing technique (sonication, high-shear mixing, coupled sonication/ high-shear mixing), dispersant and strain rate on the stress-strain response of VGCNF/ VE nanocomposites.

The nanofiber dispersion within the samples was assessed via TEM. For example, Figure 19(a) shows a typical dispersion of VGCNFs in a VE resin at 6,700X and 8,000X magnification respectively. It is clear from the figures that while the nanofibers appear to be well wetted by the VE resin with little nanofiber entanglement, the distribution is still not uniform.

The SHB tests were performed with the neat VE resin, as well as 0.5 phr and 1.0 phr VGCNF reinforced VE at three different strain rates: 600/s, 1200/s, and 1800/s. Moreover, in order to investigate the effect of dispersant on the stress-strain response of the neat resin, an additional set of specimens were prepared using neat VE plus 1.00 phr dispersant (i.e., no VGCNFs). Five tests were performed for each material configuration at each strain rate and the resulting stress-strain responses were averaged at increments of constant strain. For example, Figure 20 shows the typical dynamic stress-strain response for three neat VE SHB specimens loaded at 600/s; included in the figure is the nominal response with error bars. All of the SHB tests exhibited similar repeatability. Hence, the SHB results shown in this report only include the average response for each series of tests and the error bars are omitted for the sake of clarity and ease of viewing.

Figures 21(a–c) show the average compressive stress-strain response for each of the four material configurations at target strain rates 600/s, 1200/s, and 1800/s, respectively. Not surprisingly, the measured results were highly strain-rate dependent. One key result, however, was the presence of a small amount of dispersant (1.00 phr) significantly affecting the properties of the neat resin. For example, Figure 21(a) shows the compressive stress strain response for all four material configurations subjected to a strain rate of 600/s. As can be seen from the figure, the apparent yield stress and plateau stress for VE specimens prepared with a dispersing agent were significantly lower than those of the neat resin. This confirms that dispersants, while facilitating
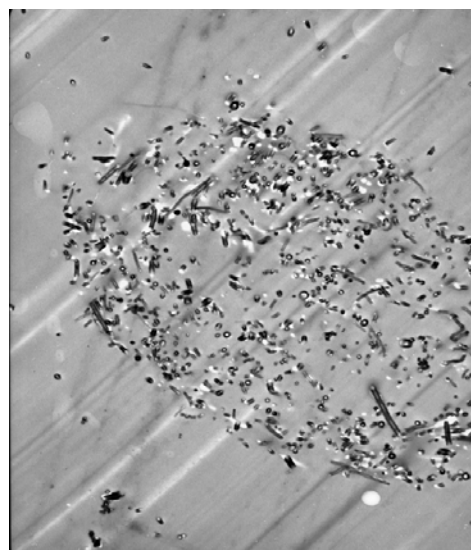

(a)
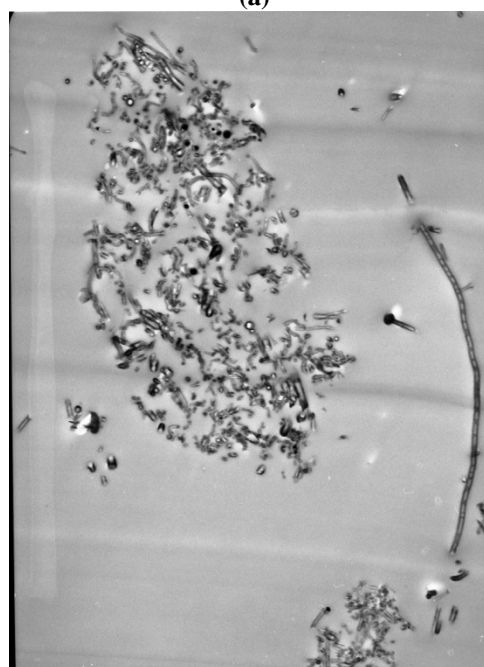
(b)

Figure 19. (a) TEM images of VGCNF dispersion for 0.5 phr VGCNF in VE resin at 6,700X magnification. (b) TEM images of VGCNF dispersion for) 1.0 phr VGCNF in VE resin at 8,000X magnification.

the distribution of nanofibers, alter the bulk properties of the VE resin. Since the SHB nanocomposite specimens discussed here were all prepared using a dispersant, then the nanocomposite stress-strain responses should compare to those of the VE resin plus dispersing agent. At a strain rate of 600/s, the measured
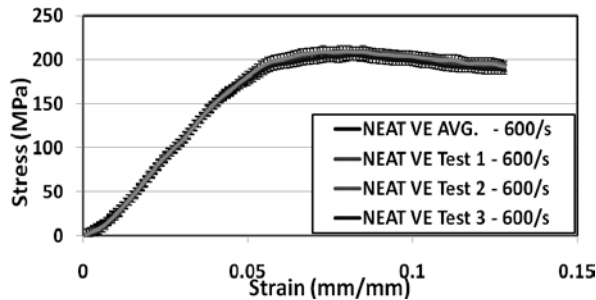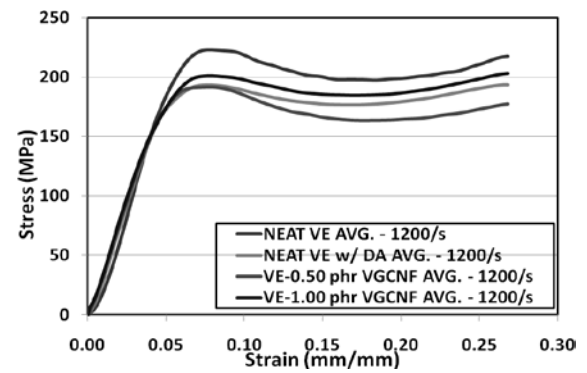
Figure 20. Stress-strain response of neat VE resin at a strain rate of 600/s.

apparent yield and plateau stresses increased with the increasing weight fraction of VGCNF. This suggests that at the given strain rate, the 1.00 phr VGCNF/VE nanocomposite demonstrated the highest yield strength and energy absorption capability relative to the resin modified with dispersant. At a target strain rate of 1200/s, the 1.00 phr VGCNF specimens also produced apparent yield and plateau stresses in excess of those of the resin [cf., Figure 21(b)]. Interestingly, at this strain rate the initial stress-strain response for the 0.50 phr specimen was similar to that of the modified resin, whereas the plateau stress was somewhat below that of the modified resin. In addition, the apparent yield and plateau stresses for the neat resin (no dispersant) were significantly larger than those of the nanocomposite specimens. This underscores the importance of investigating the effect of all constituents over a wide range of loading conditions. In contrast to the previous results obtained of lower strain rates, at 1800/s the 0.50 phr specimens yielded both the highest apparent yield and plateau stresses [cf., Figure 21(c)]. The 1.00 phr specimens produced somewhat lower values, followed by two VE specimens. Note that at 1800/s, the effect of dispersant on the stress-strain response was much less than at lower strain rates. The underlying physical mechanisms behind these phenomena are not obvious. Clearly, the presence of dispersing agent and varying amounts of VGCNFs activate, or inhibit, microstructural rearrangements as a function of strain rate. Temperature effects and/or thermal softening may also play a key role; the specimens tested at 1800/s were noticeably hot to the touch.
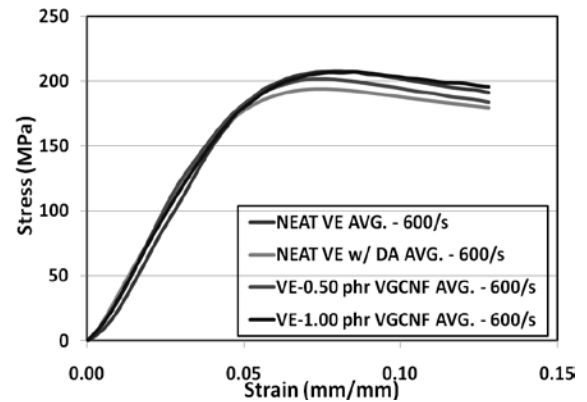

(a)

(b)
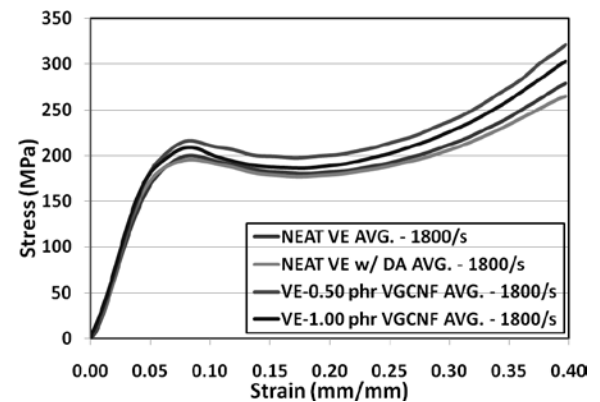
(c)

Figure 21 Average stress-strain response for neat VE resin, neat VE resin with dispersing agent, 0.5 phr VGCNF reinforced VE, and 1.0 phr VGCNF reinforced VE at strain rates of (a) 600/s, (b) 1200/s, and (c) 1800/s

As an aside, a series of preliminary tests were conducted at intermediate strain rates between the final target strain rates. A transition in apparent failure mechanism was observed as the strain rate

was increased. Tests conducted at strain rates between 500–650/s typically exhibited ductile deformation, but specimens tested at strain rates in the range 700–950/s typically failed, due to brittle fracture [cf., Figure 22(a)]. However, at strain rates in the range of 1000–1800/s, specimens tended to exhibit more ductile failure [cf., Figure 22(b)]. Again, this may be due the internal temperature rise in the specimens during the higher strain rate tests.

(a)

(b)
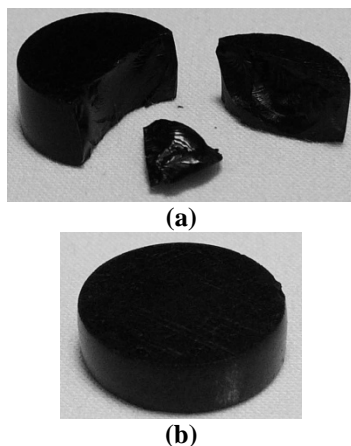
Figure 22. Alternating failure mechanisms for tests at (a) lower intermediate strain rates ~800/s and (b) higher strain rates between 1000–1800/s.

Once ongoing DMA tests are completed that will identify the optimal combination of fabrication and processing parameters (i.e., dispersing agent, unoxidized/ oxidized fibers, high shear mixing, ultrasonication, and nanofiber weight fraction), an additional series of quasi-static tests (tension compression, flexure, etc.) and SHB tests will be performed.

Development of Multiscale Materials Model Based upon Micromechanics and Experiments for Nanocomposites

Materials property data obtained from structure-property tests are being used in the development and validation of representative volume element (RVE) based micromechanical models of the two-phase (nanoreinforced) resins. The multiscale modeling methodology developed in this work involves both nanoscale and mesoscale homogenizations. The former is required to establish effective properties of the nanoreinforced matrix (here the characteristic size of a typical nanoreinforcement may be several orders of magnitude smaller than a typical glass fiber diameter). One key issue is the establishment of an empirically validated material model (and appropriate homogenization technique) for predicting effective properties of the two-phase matrix; a variety of methods (molecular dynamics, finite elements, *etc.*) are currently being considered.

Three-dimensional finite-element (FE) models of two-phase resin systems are being developed to establish effective properties of the nanoreinforced matrix. Effective nanophase resin properties obtained from FE simulations are being compared to those obtained using analytic micromechanics solutions (e.g., Mori-Tanaka method and similar effective medium idealizations; cf., Mura, 1991; Nemat-Nasser and Hori, 1993). Effective property data from these simulations, as well as from bulk structure property tests performed by T-CAM, will be employed in a RVE-based FE model of the fiber system/enhanced resin subjected to both load control and displacement control boundary conditions. Standard homogenization techniques (cf., Mura, 1991; Nemat-Nasser and Hori, 1993) will be employed to determine the effective properties of the three-phase composite systems (i.e., nanophased polymer matrix, traditional continuous fiber system architectures), with an initial focus on E-glass plain-weave woven fabric laminates. Modeling and simulation activities will continue into the third year of the project.

Conclusions

The goal of this investigation is to exploit expertise in polymer chemistry, composite materials processing and computational solid mechanics to design, synthesize, test and analyze cost-effective multiscale engineered nanocomposites for automobile primary structural applications. One key challenge is to establish empirically validated, multiscale methodologies, based on the morphologies and geometries of real heterogeneous materials, to obtain structure-property relationships over a wide range of length scales.

A crucial aspect of the work is that structure-property relations will be experimentally validated using a combination of fine-scale and macroscale tests. This study should facilitate the development of engineered multiscale materials designed by providing insight into relationships between nanomaterial fabrication/processing, chemical and physical characteristics and interaction and evolution of structure across disparate spatial scales that leads to improved macroscale performance.

Presentations/Publications/Patents

1. J. Ingram, Y. Zhou, S. Jeelani, T. Lacy, and M. F. Horstemeyer, 2008, "Effect of Strain Rate on Tensile Behavior of Polypropylene and Carbon Nanofiber Filled Polypropylene," *Materials Science & Engineering A*, 489 (1), 99–106.

2. Y. Zhou, S. R. Akanda, S. Jeelani, and T. E. Lacy, 2007, "Nonlinear Constitutive Equation for Vapor-Grown Carbon Nanofiber-Reinforced SC-15 Epoxy at Different Strain Rate," *Materials Science & Engineering A*, 465 (1), 238–246.

3. Y. Zhou, M. Shaik, S. Jeelani, T. Lacy, and M. Horstemeyer, "Experimental Study on Thermal and Mechanical Properties of Clay Modified Carbon Fiber Reinforced Epoxy," in the *Proceedings of the ASC 23rd Annual Technical Conference*, Memphis, TN, September 9–11, 2008.

4. Y. Zhou, S. Jeelani, and T. Lacy, "Strain Rate Dependent Behavior of Carbon Nanofiber Filled Polypropylene," in the *Proceedings of the 49th AIAA/ ASME/ ASCE/ AHS/ ASC Structures, Structural Dynamics, and Materials Conference*, Schaumburg, IL, April 7–10, 2008.

References

1. V. A. Buryachenko, A. Roy, K. Lafdi, K. L. Anderson, and S. Chellapilla, 2005, "Multi-scale mechanics of nanocomposites including interface: Experimental and numerical investigation," *Composites Science and Technology*, **65**, 2435–2465.

2. N. Chisholm, H. Mahfuz, V. K. Rangari, A. Ashfaq, and S. Jeelani, 2005, "Fabrication and mechanical characterization of carbon/SiC-epoxy nanocomposites," *Composite Structures*, **67**, 115–124.

3. F. H. Chowdhury, M. V. Hosur, and S. Jeelani, 2006, "Studies on the flexural and thermomechanical properties of woven carbon/nanoclay-epoxy laminates," *Materials Science and Engineering A*, **421**, 298–306.

4. F. T. Fisher, R. D. Bradshaw, and L. C. Brinson, "Fiber waviness in nanotube-reinforced polymer composites: I. Modulus predictions using effective nanotube properties," submitted to *Composites Science and Technology,* 2007.

5. T. S. Gates, G. M. Odegard, S. J. V. Frankland, and T. C. Clancy, 2005, " Computational materials: Multi-scale modeling and simulation of nanostructured materials, *Composites Science and Technology*, **65**, 2416–2434.

6. N. M. Ghoniem, E. P. Busso, N. Kioussis, and H. Huang, 2003, "Multiscale modeling of nanomechanics and micromechanics: an overview," *Philosophical Magazine*, 83 (31–34), 3475–3528.

7. A. Hussain, M. Hojjati, M. Okamoto, and R. E. Gorga, 2006, "Review Article: Polymer-Matrix Nanocomposites, Processing, Manufacturing, and Application: An Overview," *Journal of Composite Materials*, 40(17), 1511–1575.

8. J. Ingram, Y. Zhou, S. Jeelani, T. Lacy, and M. F. Horstemeyer, 2008, "Effect of Strain Rate on Tensile Behavior of Polypropylene and Carbon Nanofiber Filled Polypropylene," *Materials Science & Engineering A*, 489 (1), 99–106.

9. H. Liu and L. C. Brinson, 2006, "A hybrid numerical-analytical method for modeling the viscoelastic properties of polymer nanocomposites," *Journal of Applied Mechanics*, **73,** 758–768.

10. T. Mura, 1991, *Micromechanics of Defects in Solids, Second Edition*, M. Nijhoff Publ., The Hague.

11. S. Nemat-Nasser and M. Hori, 1993, *Micromechanics: Overall Properties of Heterogeneous Materials*, North-Holland, Amsterdam.

12. G. M. Odegard, T. S. Gates, L. M. Nicholson, and K. E. Wise, 2001, "Equivalent-Continuum Modeling of Nano-Structured Materials," NASA/TM 210863, 1–30.

13. G. M. Odegard, T. C. Clancy, and T. S. Gates, 2005, "Modeling of the mechanical properties of nanoparticle/polymer composites," *Polymer*, 46, 553–562.

14. E. T. Thostenson, C. Li, and T.-W. Chou, 2004, "Nanocomposites in context," *Composites Science and Technology*, 65, 491–516.

15. P. K. Valavala and G. M. Odegard, 2005, "Modeling techniques for determination of mechanical of polymer nanocomposites," *Review Advance Material Science*, **9**, 34–44.

16. Y. Zhou, F. Pervin, V. Rangari, and S. Jeelani, 2006, "Fabrication and evaluation of carbon nano fiber filled carbon/epoxy composite," *Materials Science and Engineering A*, **426**, 221–228.

17. Y. Zhou, S. R. Akanda, S. Jeelani, and T. E. Lacy, "Nonlinear Constitutive Equation for Vapor-Grown Carbon Nanofiber-Reinforced SC-15 Epoxy at Different Strain Rate," accepted for publication in *Materials Science & Engineering A*, 2007.